

HIGH EFFICIENCY COPPER INDIUM GALLIUM DISELENIDE (CIGS) THIN FILM SOLAR CELLS

A Thesis Submitted to

The Maharaja Sayajirao University of Baroda

For the Degree of

Doctor of Philosophy

In

Applied Physics

By

Mr. Ray Jayminkumar Rajanikant

Under the Supervision of

Dr. C. J. Panchal

**Applied Physics Department
Faculty of Technology and Engineering
The M. S. University of Baroda
Vadodara-390001
January 2013**

APPLIED PHYSICS DEPARTMENT

Telephone No.: (0265) 2434188
Fax No.: (0265) 2423898



Faculty of Technology & Engineering
M S University of Baroda,
Kalabhavan
VADODARA-390 001
GUJARAT STATE, INDIA

CERTIFICATE

This is to certify that the thesis entitled "**High Efficiency Copper Indium Gallium Diselenide (CIGS) Thin Film Solar Cells**" submitted by **Ray Jayminkumar Rajanikant** to **The Maharaja Sayajirao University of Baroda, Vadodara** for the award of degree of **Ph.D. in Applied Physics** is bona fide and the work has been carried out by him in this department.

C. J. Panchal
17/1/2013

Dr. C. J. Panchal
Research Guide,

Date: 17th January, 2013

C. J. Panchal
17-1-13
Head,
Applied Physics Department

Head
Applied Physics Department
Faculty of Technology & Engineering
The Maharaja Sayajirao University of Baroda,
Vadodara-390 001.

A. N. M.
Dean,
Faculty of Technology and Engineering
Faculty of Tech. & Engg.
M. S. University of Baroda,
Baroda.

Dedicated to
My Parents
and
My Friends

CONTENTS

	Acknowledgement	IV
	Abstract	VII
1	Introduction	
1.1	Need for Renewable Energy	1
1.2	History of Photovoltaic	4
1.3	Solar Cell Based on Copper Indium gallium diselenide (CIGS)	7
1.3.1	Device Structure of CIGS Thin Film Solar Cell	7
1.4	Solar Cell Device Operation	10
1.5	Stability and Defect Chemistry of CIGS	14
1.6	Present Study	16
1.7	Organization of the Thesis	17
2	Thin Film Fabrication and Characterization Techniques	
2.1	Thin film Fabrication Techniques	19
2.1.1	Thermal and Flash Evaporation	23
2.1.2	RF Magnetron Sputtering	25
2.2	Characterization Techniques	26
2.2.1	X-ray Diffraction	26
2.2.2	Electron Microscopy	28
2.2.3	AFM Analysis	32
2.2.4	Transmission and Reflection Measurements	34
2.2.5	Electrical Measurements	35
2.2.6	Current-Voltage (I-V) Measurements	39
2.2.7	Spectral Response Measurements	41
3	Molybdenum Back-Contact Layer: Growth and Optimization	
3.1	Need of Molybdenum Back-Contact Layer	43
3.2	Thin Film Preparation	44
3.3	Effect of Working Pressures	44
3.3.1	Structural Characterization	44
3.3.2	Morphological Characterization	48
3.3.3	Electrical and Optical Characterization	49
3.4	Effect of RF Power	50
3.4.1	Structural Characterization	50
3.4.2	Morphological Characterization	52

	3.4.3	Electrical and Optical Characterization	52
	3.5	Laser Scribing of Molybdenum Thin Film	54
	3.6	Conclusions	62
4		Copper Indium Gallium Diselenide (CIGS) Absorber Layer: Growth And Optimization	
	4.1	Synthesis of CIGS Material	63
	4.1.1	Structural Characterization	66
	4.1.2	Compositional Characterization	67
	4.2	Thin Film Preparation	68
	4.3	Effect of Substrate Temperature	68
	4.3.1	Structural Characterization	68
	4.3.2	Microstructural and Chemical Characterization	69
	4.3.3	Optical Characterization	72
	4.3.4	Electrical Characterization	74
	4.4	Effect of CIGS Thin Film Thickness and Rapid Thermal Annealing (RTA)	76
	4.4.1	Structural Characterization	76
	4.4.2	Micro-structural and Chemical Characterization	78
	4.4.3	TEM Characterization	81
	4.4.4	Optical Characterization	83
	4.4.5	Electrical Characterization	87
	4.5	Conclusions	89
5		Cadmium Sulphide (CdS) Buffer Layer: Growth And Optimization	
	5.1	Need of CdS Buffer Layer	90
	5.2	Thin Film Preparation	91
	5.3	Effect of Substrate Temperature	91
	5.3.1	Structural Characterization	91
	5.3.2	Morphological Characterization	94
	5.3.3	Compositional Characterization	94
	5.3.4	Optical Characterization	95
	5.3.5	Electrical Characterization	97
	5.4	Conclusions	98
6		Aluminum Doped and Intrinsic Zinc Oxide (ZnO) Window Layer: Growth And Optimization	
	6.1	Need of ZnO Window Layer	99

6.2	Aluminum Doped Zinc Oxide (Al-ZnO) Thin Film Preparation	100
6.3	Effect of RF Power	101
6.3.1	Structural Characterization	101
6.3.2	Optical Characterization	103
6.3.3	Morphological Characterization	106
6.3.4	Electrical Characterization	107
6.4	Effect of Working Pressure	107
6.4.1	Structural Characterization	107
6.4.2	Optical Characterization	109
6.4.3	Morphological Characterization	111
6.4.4	Electrical Characterization	111
6.5	Intrinsic Zinc Oxide (i-ZnO) Thin Film Preparation	112
6.5.1	Structural Characterization	114
6.5.2	Optical Characterization	114
6.5.3	Morphological Characterization	116
6.6	Conclusions	117
7	Fabrication of CIGS Thin Film Solar Cell Device and Its Characterization	
7.1	Simulation of CIGS solar cell	118
7.1.1	Model Description	120
7.1.2	Simulation Parameters	122
7.1.3	Results and Discussions of Simulation	124
7.2	Fabrication of CIGS Thin Film Solar Cell Device	126
7.2.1	Effect of Thermally Evaporated CdS Film Thickness on the performance of CIGS solar cell	127
7.2.2	Effect of Flash Evaporated CdS Film Thickness on the performance of CIGS solar cell	131
7.2.3	Effect of i-ZnO Film Thickness on the performance of CIGS solar cell	136
7.3	Conclusions	143
8	Summary and Future Outline	144
	References	146
	List of Symbols	152
	Abbreviations	153
	List of Publications	154

Acknowledgement

My deepest gratitude goes to my parents, Shri Rajanikant Shivabhai Ray and Smt. Daxaben Rajanikant Ray, for supporting me in whatever I do. My sister Priyanka Patel and her family, Dhara, Siya, Tejaskumar Patel, Japlaben Patel, Vinubhai Patel, and Manjuben Patel, for always giving their best to stay in touch and who make my breaks, from work, so enjoyable. I also thankful to my other family members Yogeshbhai Patel, Kanubhai Patel, Dipikaben Patel, Shrushti, Tinabhai, Belaben Patel, Jagdishbhai Patel, Navneetbhai Patel, Tarlikaben Patel, Riteshbhai Patel, Femiben Patel, Nayanbhai Patel, Krupa, Harshadbhai Patel, Hemuben Patel, Beena, Vandana, Krupa and sweet little Khushbu for giving me enormous support during my whole research work.

Successful accomplishment of any work needs proper method and right direction. This becomes accessible through proper guidance and supervision. Again, while accomplishing a difficult task is wide-ranging and sometimes unanticipated difficulties may arise which might make one to lose one's courage and slacken one's dedication. Under such a kind of circumstances a person not only giving guidance but also giving encouragement and moral support is required to be at hand. During the period of my work, I was in the midst of unexpected obscurity. Though, I never slacken my dedication and lose my courage when such a situation meets. It is only because of my Ph.D. guide, Dr. C.J. Panchal, who has extended me moral support at that hour of need. Thanks for supporting my research ideas, for giving me the leeway to do independent work, for letting me travel and present my work, and of, course, for teaching me.

My sincere thanks to Prof. A.N. Mishra (Dean, Faculty of Technology and Engineering), The M.S. University of Baroda, and Dr. D.R. Joshi (I/C-Head, Applied Physics Department) for their timely administrative and academic help since my Ph.D. registration under the department.

I express my sincere gratitude to Dr. M.S. Desai, for helping me into understanding the physics, and invaluable comments and suggestions for improving research methodology, research article and thesis writing. I would also like to thank Prof. V.N. Potbhare, Dr. N.D. Chavda, Dr. Bharti Rehani and Dr. P.K. Mehta for valuable suggestions with

enthusiastic environment during research work. Also I am very much thankful to my post-graduation faculty members, Prof. D. Laximnarayan, Mr. P.B. Patel, Dr. S.S. Patel, Dr. Urmesh Trivedi, Dr. R.R. Desai, Mr. A.B. Patil and lastly my school teachers Bhartiben Patel, Anjana Patel and Jayaben Patel.

I am also very much thankful to Mr. Arvind L. Patel (Director, The Sahjanand Laser Technology Ltd., Gujarat) for providing the laser scribing facility.

I am deeply indebted to my colleague Dr. Vipul Kheraj, Dr. Nitinkumar Shah, Dr. Keyur Patel, Gopal Bhatt, and Palak Patel, who were and are with me, with a true moral support at difficult times and making me pass through difficult situations with great ease during many stages of my research work. Also they are responsible for creating in me the optimism and carry out this work with great ease and precision with technical advices.

Without the full support of my boosters, Kaushik Raval, Smit Shah, Rahul Trivedi, Jigar Shah, and Nishant Shah, I do not believe I would have finished this journey as sanely or with the degree of confidence I currently feel. They supported me by all means, as teachers, as friends and as philosophers, and made it unforgettable by their goodwill. Lastly, Bring in the angels from the heavens Chiku, Darpita Patel, Kavita Chigare, Hemali Tanna and Anshumala Singh.

Friends are the angels that lift us up when our wings have forgotten how to fly. I also wish to express my gratitude to all my closest ones Ravi Travadi, Ankit Patel, Jigar Soni, Usha Parihar, , Romesh Sachdeva, Narinder Sharma, Deepti Sharma, Ankit Shah, Anand Kaneria, Ketan Modha, Bharat, Hinal Patel, Apexa Patel, Hussain Rangooni, Sneha Patel, Punita Patel, Amit Patel, Kinjal Patel, Dhaval Patel, Ashwini Karnik, Sandip Dhanani, Vijay Padhiyar, Nirav Shah, Ankit Pathak, Nisha Prajapati, Devang Shah, Nishant Barot, Sohan Chauhan, Laxmi Tomar, Gautam Patel, Vipul Katariya, Bhavesh Khunt, Ashish Patel, and Minal Soni.

I express my warmest thanks to all my hostel friends, Mayur Patel, Rajesh SV, Hemant Mande, Harishbhai Talele, Salimbhai, Vrushabh, Anoop Markande, Ashok Vishwakarma, Sanjay Verma, Ekbaal, Vinod Bhoi, Parimal Patel, KB, Manish Jaiswal, Naveen Agrawal,

Washimbhai, Navin Bunekar, Mothuku Shyam Sundar, Murlibhai Sharaff, Subbramanyam, Dushyant Reddy and Lakshminarayan Balappagol.

I would like to thanks to all my friends, with whom I travel most in the earlier stage of my Ph.D., Sohil Darji, Bhavesh Patel, Alpesh patel, Munnabhai, Kalpesh Patel, Rajesh, Chintan, Shambhukaka, Maheshbhai Patel, Kashyapbhai Patel, and Nishant.

I am very much graceful to the departmental members Raffic A. Dudhwala, Yogesh Power, Nilesh Rathwa, P.B. More, and Bhavesh Patel for helping me a lot in the technical and non-technical issues of my Ph.D. work.

I am very much thankful to Jalaram trust, Vadodara, and University grant commissions (UGC) for providing the financial support during my post graduation study and Ph.D., respectively.

I also thankful to Prof. Marc Burgelman, Pennsylvania State University, for providing the software package AMPS-1D.

Ray Jayminkumar Rajanikant

Abstract

The generation of electrical current from the solar radiation is known as the photovoltaic effect. Solar cell, also known as photovoltaic (PV) cell, is a device that works on the principle of photovoltaic effect, and is widely used for the generation of electricity. Thin film polycrystalline solar cells based on copper indium gallium diselenide (CIGS) are admirable candidates for clean energy production with competitive prices in the near future. CIGS based polycrystalline thin film solar cells with efficiencies of 20.3 % and excellent temperature stability have already been reported at the laboratory level. The present study discusses about the fabrication of CIGS solar cell. Before the fabrication part of CIGS solar cell, a numerical simulation is carried out using One-Dimensional Analysis of Microelectronic and Photonic Structures (AMPS-1D) for understanding the physics of a solar cell device, so that an optimal structure is analyzed.

In the fabrication part of CIGS solar cell, Molybdenum (Mo) thin film, which acts as a 'low' resistance metallic back contact, is deposited by RF magnetron sputtering on organically cleaned soda lime glass substrate. The major advantages for using Mo are high temperature, (greater than 600 °C), stability and inertness to CIGS layer (i.e., no diffusion of CIGS into Mo). Mo thin film is deposited at room temperature (RT) by varying the RF power and the working pressure. The Mo thin films deposited with 100 W RF power and 1 mTorr working pressure show a reflectivity of above average 50 % and the low sheet resistance of about 1 Ω/\square .

The p-type CIGS layer is deposited on Mo. Before making thin films of CIGS, a powder of CIGS material is synthesized using melt-quenching method. Thin films of CIGS are prepared by a single-stage flash evaporation process on glass substrates, initially, for optimization of deposition parameters and then on Mo coated glass substrates for device fabrication. CIGS thin film is deposited at 250 °C at a pressure of 10^{-5} mbar. The thickness of the film was kept 1 μm for the solar cell device preparation. Rapid Thermal Annealing (RTA) is carried out of CIGS thin film at 500 °C for 2 minutes in the argon atmosphere. Annealing process mainly improves the grain growth of the CIGS and, hence the surface roughness, which is essential for a multilayered semiconductor structure.

Thin layer of n-type highly resistive cadmium sulphide (CdS), generally known as a “buffer” layer, is deposited on CIGS layer by thermal and flash evaporation method at the substrate temperature of 100 °C. The CdS thin film plays a crucial role in the formation of the p-n junction and thus the solar cell device performance. The effect of CdS film substrate temperature ranging from 50 °C to 200 °C is observed. At the 100 °C substrate temperature, CdS thin film shows the near to 85 % of transmission in the visible region and resistivity of the order of greater than $20 \times 10^9 \Omega\text{cm}$, which are the essential characteristics of buffer layer.

The bi-layer structure of ZnO, containing 70 nm i-ZnO and 500 nm aluminum (Al) doped ZnO, act as a transparent front-contact for CIGS thin film solar cell. These layers were deposited using RF magnetron sputtering. i-ZnO thin film acts as an insulating layer, which prevents the recombination of the photo-generated carries and also minimizes the lattice miss match defects between CdS and Al-ZnO. The resistivity of i-ZnO and Al-ZnO is of the order of $10^{12} \Omega\text{cm}$ and $10^{-4} \Omega\text{cm}$, respectively. Al-ZnO thin films act as transparent conducting top electrode having transparency of about 85 % in the visible region. On Al-ZnO layer the finger-type grid pattern of silver (Ag), 200 nm thick, is deposited for the collection of photo-generated carriers.

The thin film based multilayered structure Mo / CIGS / CdS / i-ZnO / Al-ZnO / Ag grid of CIGS solar cell is grown one by one on a single glass substrate. As-prepared CIGS solar cell device shows a minute photovoltaic effect. For the further improvement of the cell we have varied the thickness of the buffer layer i.e. CdS. In addition, the deposition of CdS is carried out using flash evaporation method to improve the CIGS/CdS junction. Heat soak pulses of about 200 °C are also applied for 20 sec for the further upgrading the junction. To protect the CIGS/CdS junction from the high-energy sputtered particles of ZnO, a fine mesh of stainless steel is placed just before the sample holder to enhance the performance of the solar cell. The influence of the thickness of i-ZnO and CdS has been checked. The maximum V_{oc} and J_{sc} of about 138 mV and 1.3 mA/cm^2 , respectively, are achieved using flash evaporated CIGS layer and flash evaporated CdS thin film. Further improvement of current performance can be done either by adopting some other fabrication method to obtain a denser CIGS absorber layer or replacing the CdS layer with some other efficient buffer layer.

Chapter 1

Introduction

1. INTRODUCTION

The energy is a key for the life cycle of mankind. Mankind is using energy in many ways to improve its living standards. The world energy consumption is increasing, which is related to growing population. The modern world had facing the difficulty with the traditional energy sources i.e. fossil fuels because of the limited resources of them and it is non-renewable. Environmental point of view, a burning of fossil fuels causes' air and water contamination. These problems with conventional fossil fuels draw our attention to alternative non-renewable energy sources like solar energy, wind energy, Bio gas, hydropower, tidal waves etc. Because of the wide availability and ease of use the utilization of solar energy and wind energy are the current trend of the world in the area of non-renewable energy sources. Due to the geographical limitation the wind energy not have been used extensively compare to the solar energy. Solar cell is a kind of device that converts the solar energy to the electrical energy, also called as photovoltaic (PV) device. Silicon based PV technology dominates the PV market today. This is mostly due to a well-established knowledge on silicon material science and engineering, an available abundant supply of silicon raw material, and the advantages of low ecological impact but high efficiencies. However, the low optical absorption ($\sim 10^2 \text{ cm}^{-1}$), and a complicated manufacturing process lead to a high installation cost for silicon-based PV technology.

At present with silicon several materials available in the market which has a tendency to generate appreciable electrical energy from the solar energy. They are as amorphous silicon (a-Si), cadmium telluride (CdTe), copper indium (gallium) diselenide (CI(G)S), TiO_2 based di-sensitized, copper zinc tin selenide (CZTS) etc. The present thesis mainly dealing with fabrication and characterization of CIGS thin film solar cells.

1.1 NEED FOR RENEWABLE ENERGY

The world of today is dependent on energy sources that are generated mainly from fossil fuels, nuclear power or hydropower. The energy that comes from fossil fuels, which includes coal, lignite, petroleum and natural gas is non-renewable conventional source of energy. It is not gracious to the environment, too. The increased use of fossil fuels increases carbon expelling and accelerates global climate change. The energy produced using these fossils

fuels responsible for ecological problems like global warming, air pollution, and depletion of forests etc. The emission rate of carbon dioxide particularly in the developing countries has jumped by about 25 % in recent years. These emissions continue to decline in many countries and cities of the world. Due to that air becomes poisonous that directly affected many kind of plants and bird-life, many of them lost the visibility rapidly. Therefore, there is an urgent need to discourage the use of conventional sources of energy. It is essential that the uses of renewable resources to protect the future of the earth and the quality of life on the earth.

The renewable sources of energy like solar, wind, tidal waves, biogas, hydropower, etc., hold a great potential. Modern science, technology, research and development have to play a significant role in popularizing an increased use of non-conventional sources of energy both in industrial and domestic sectors. The use of some renewable sources like hydropower, tidal waves, and biogas are not evenly distributed across the world. Wind energy is limited to a few regions, but the solar energy available widely. Life on earth, we can say, is because of Sun - a source of solar energy. A simple model assumes that the sun is circular and behaves as a black-body whose surface is maintained at temperature about 6000 K. This surface temperature is kept constant by energy generated through continuous nuclear fusion of hydrogen into helium in the interior of the sun. The interior temperature is, approximately 10^7 K. Because of interior temperature, the surface (photosphere) radiates electromagnetic radiation in all directions of space. The spectral distribution is changed considerably when the sunlight penetrates through the earth's atmosphere. Even for a clear sky the light intensity is attenuated by at least 30 % due to scattering by molecules, aerosols, and dust particles and adsorption by its constituent gases like water vapor, ozone or carbon dioxide.

Figure 1.1 shows three curves related to solar spectral irradiance. The upper curve, which represents the solar spectrum outside the earth's atmosphere, is the air mass zero condition (AM 0). This condition can be approximated by a 5800 K black-body radiation. For a typical cloudless atmosphere and zero zenith angle, the irradiance reaching the outer atmosphere is reduced to approximately 1050 W/m^2 direct beam radiation (AM 1.5D), or 1120 W/m^2 global irradiation (AM 1.5G), on a horizontal surface at sea level [1] as shown in Fig. 1.1. Some key technologies for harnessing the power from the sun are briefly reviewed in the following subsections.

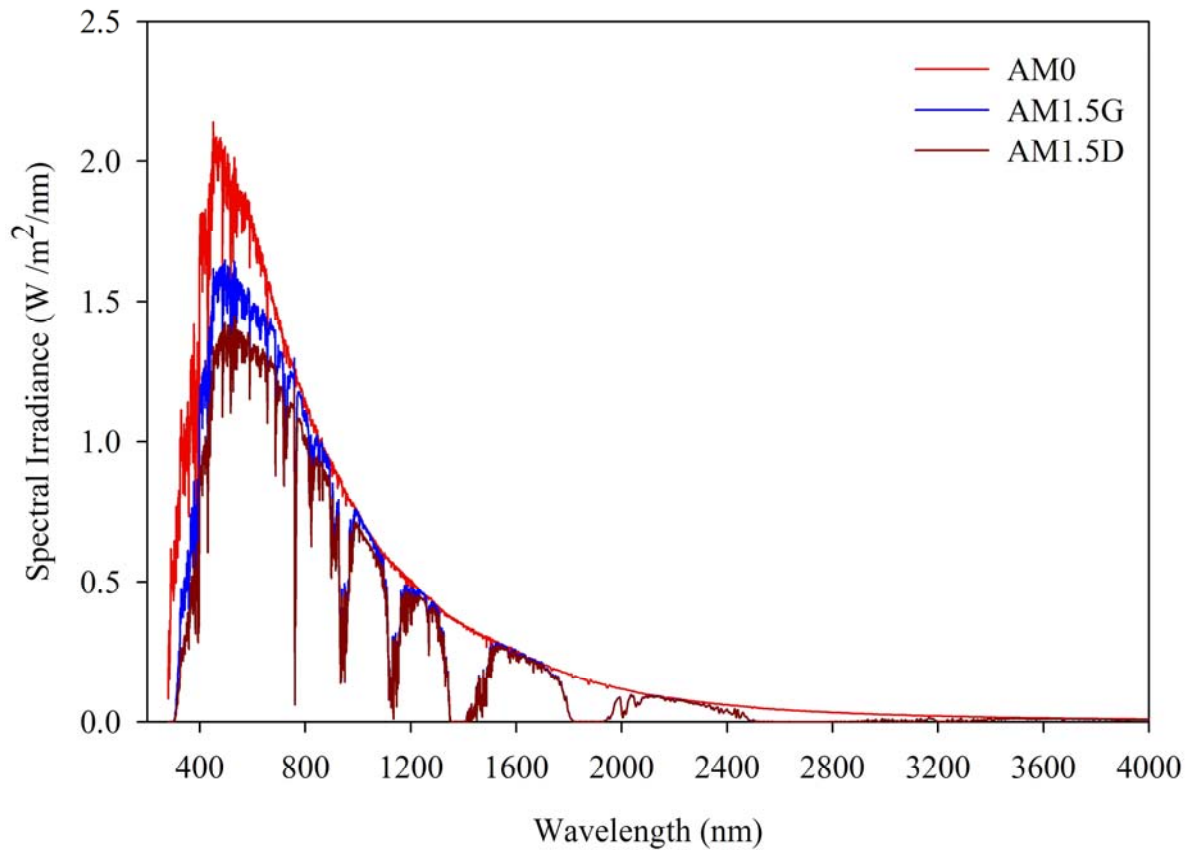


Fig. 1.1 Spectrum of solar radiation available on the earth.

What is photovoltaic?

The word photovoltaic stands for two words. “Photo” for light and “voltaic” for the name of the Italian scientist Alessandro Volta. Photovoltaic is a safe, clean, and reliable technology that can convert sunshine (solar power) directly into electric current. In a semiconductor, if the electron gets energy larger than its band gap energy, then this can lead to the creation of electron-hole pairs. In a semiconductor device, such as a p-n diode, these electron-hole pairs may be separated by the built-in electric field producing either voltage or electric current, or both, depending on the external circuit. While the creation of electron-hole pairs in a p-n junction device can enhance conduction (photo-enhanced conduction), the process can also generate a voltage. Such voltage generation when radiant energy strikes a junction device is known as a photovoltaic effect, and single unit devices are referred to as photovoltaic cells.

About 1000 watt (1 kilowatt) per square meter solar energy is available on a bright summer day at noon. This amount of solar energy, if converted perfectly to electricity, could power up approximately ten 100-watt bulbs, or two furnace motors, or several 60 cm television sets. The drawbacks are that it is not high noon and summer all the time, and photovoltaic cells do not work at 100 % efficiency. At present they work at about 15 % efficiency, with the best performance being about 25 %. A photovoltaic (PV) system consists

of a number of interconnected components designed to accomplish a desired task, which may be to feed electricity into the main distribution grid, to pump water from a well, to power a small calculator or one of many more possible uses of solar-generated electricity. The design of the system depends on the task it must perform. Solar cell technology is fairly mature and may become very important if the environmental concerns related to the greenhouse effect force us to switch from coal and oil to solar energy.

Importance of photovoltaic

The need for a small as well as large-scale use of photovoltaic device both in space and on earth has grown rapidly. Electrical power generation from the Photovoltaic devices have proven themselves to be durable, efficient, and dependable compare to finite fossil fuel supplies and combustion by-products. Photovoltaic systems have an additional advantage that they can survive in the harsh physical rigours of space – high vacuum, hard radiation and great temperature differentials. Their virtues have been proven in applications on earth, as they have survived dirt, dampness, chemical smog, wind, and hail.

Photovoltaic is a rapidly evolving technology. New cell design concepts, new materials from which to make cells, steadily increased efficiencies, and simplified production are leading to low-cost, long-lived cells. Photovoltaic device use the fundamental properties of matter itself to produce power quietly, safely, and with virtually no operation and maintenance costs. Because photovoltaic systems are modular and can be produced in size and type to fit almost any need, they permit local, decentralized installation at the point of need, and can, in very simple fashion, be designed to match the output to the user's purposes.

1.2 HISTORY OF PHOTOVOLTAIC

The Photovoltaic effect was first discovered by a French physicist Becquerel in 1839 [2]. The German scientist Heinrich Hertz experimented with selenium electrodes and this led to the development of the first primitive PV cell. These cells had only about 1~2 % efficiency. In 1954 Bell labs came up with the first silicon solar cells with efficiency of 6 % [3]. The space race between the United States and the Soviet Union led to the use of solar cells as a power source in space. PV systems were selected for space use because they were light-weight, which kept operational costs down and because they could produce power for long periods of time. The main driving force behind the use of photovoltaic for terrestrial power supplies came in 1973 with the notorious oil shock. Since then all possible options for cost reduction have been explored, which was recognized as the major obstacle to the widespread use of photovoltaic.

Today, the majority of solar cells are made of crystalline silicon. Silicon produces devices with highest efficiency 24.5 % [4], that are also very stable. Silicon's availability is huge, but crystalline Si cells require an expensive production process. Silicon is fragile, and it is an indirect band-gap material having a low absorption coefficient, 10^2 cm^{-1} . Because of these characteristics, production of relatively thick cells is essential. A typical Si-cell thickness is approximately 300 μm , more than 100 times the thickness of a typical polycrystalline thin-film cell. Although not commercially established like Si solar cells, the thin-film polycrystalline solar cells, such as CdTe and CIGS, have a great advantage of significantly lower in production cost. Lower cost comes not only from lesser semiconductor material usage, but also from lower deposition temperatures (by $\sim 1000 \text{ }^\circ\text{C}$) and from higher forgiveness towards non-uniformities, which allows usage of less pure materials. Even though thin film cells have obvious advantages, still 90 % [5] of the world-wide PV market belongs to silicon. In the United State of America (USA), however, the production of silicon and its thin film based solar cells in 2006 was roughly equal. The progress towards higher thin film efficiency and production growth has been strongly connected with the understanding of the materials and devices. Fig. 1.2 shows the reported timeline of solar cell energy conversion efficiencies [6].

In India, knowing for fastest growing economy in the world, the solar photovoltaic cells, indigenously produced at Bharat Heavy Electrical Limited (BHEL) and Central Electronics Limited (CEL) are being increasingly used under the Rural Electrification Programme in the remote villages where it is not possible to carry the electric lines. For that amorphous silicon cell was the base for the power generation, capable of 10 to 100 KW. In July 2009, India unveiled a US\$19 billion plan to produce 20 GW of solar power by 2020. Under the plan, the use of solar-powered equipment and applications would be made compulsory in all government buildings, as well as hospitals and hotels. In November 2009, it was reported that India was ready to launch its National Solar Mission under the National Action Plan on Climate Change, with plans to generate 1,000 MW of power by 2013 [7].

Recently, in April 2012, at the India Solar Investment & Technology Summit (ISIT) event in Gujarat, the state's 214 MW Charanka photovoltaic park was also opened at the event and now represents Asia's largest photovoltaic power plant. When fully built-out, the Charanka Solar Park will host 500 MW of solar power systems using state-of-the-art thin film technology, and should be finished by the end of 2014 [8].

Best Research-Cell Efficiencies

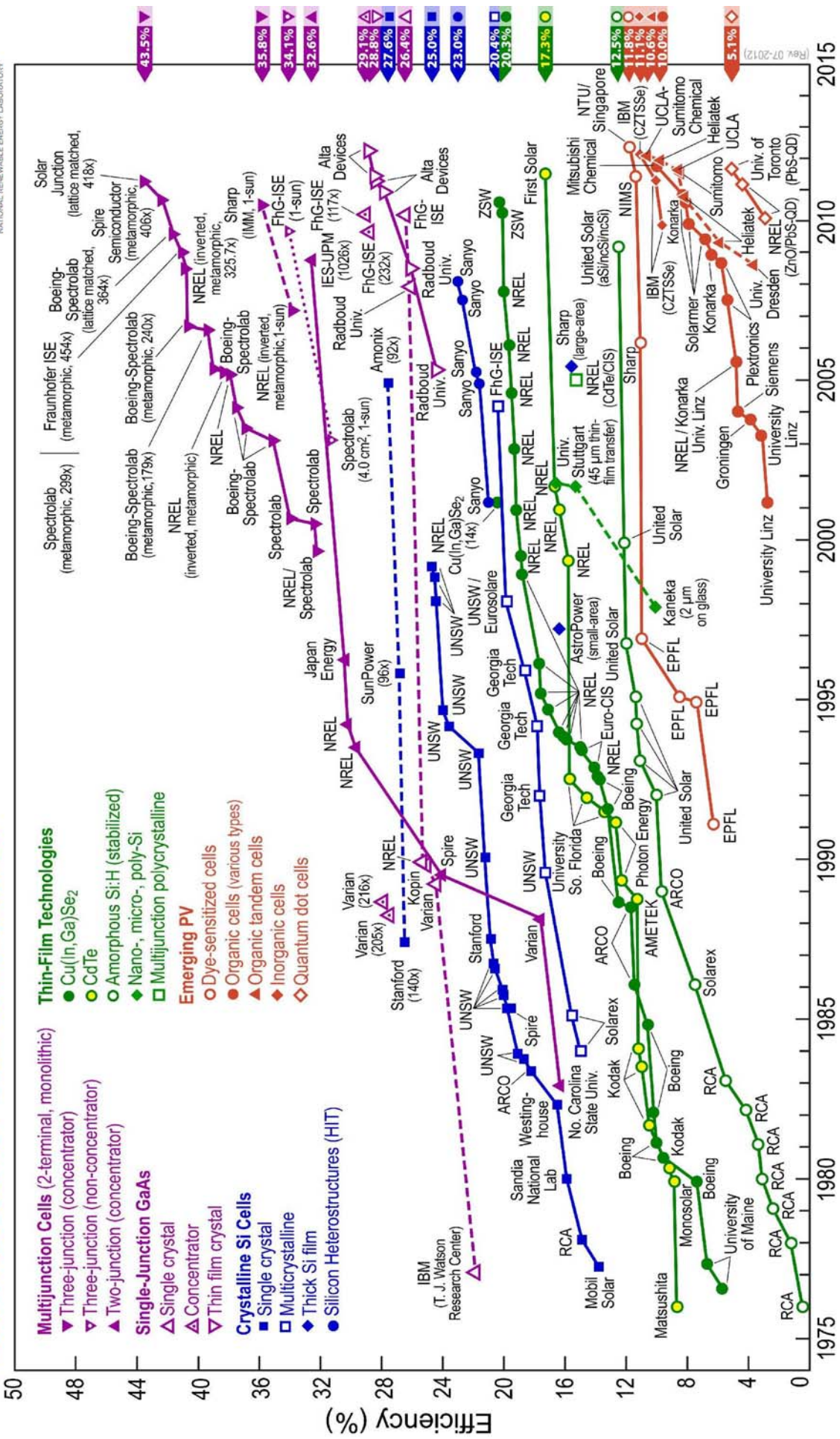


Fig. 1.2 Reported timeline of solar cell energy conversion efficiencies.

1.3 SOLAR CELL BASED ON Cu(In,Ga)Se₂ (CIGS)

CIGS based solar cell belong to the I-III-VI (I= Cu, III= (In, Ga), and VI= Se) family. These chalcopyrite semiconductors are promising materials for the fabrication of thin film solar cells because of their high absorption coefficient ($\alpha \approx 10^5 \text{ cm}^{-1}$), suitable direct band gap ($E_g \approx 1.15 \text{ eV}$), and long term stability. However, the device properties of CIGS based solar cells are critically influenced by their stoichiometric compositions and defect chemistry, which in turn are strongly related to the film growth parameters. Despite a lack of information in this regard, conversion efficiencies of polycrystalline CIGS/CdS/ZnO thin film solar cell devices have steadily increased to values above 20 % [9]. A key issue to be addressed for further improvement of these solar devices is the correlation between the performance of these devices and the material properties (i.e. growth, structural, optical and electrical) of the CIGS absorber thin films.

1.3.1 Device Structure of CIGS Thin Film Solar Cell

A schematic of a typical CIGS thin solar cell is shown in Fig. 1.3. Light enters the cell through the anti-reflection (AR) coating, transparent conductive oxide layer (TCO), Al-ZnO (AZO) and i-ZnO thin films, passes through the CdS buffer layer, and enters the absorber CIGS layer. The p-n junction is formed by p-type CIGS layer and n-type CdS layer. The substrate used for this kind of solar cell device structure is soda-lime glass, which has a low price, ease of availability and well match thermal expansion coefficient with CIGS material. In addition, sodium from such a substrate diffuses into CIGS and has beneficial effects. It replaces substitution defects where a Cu atom is replaced with In (In_{Cu}) that act as compensating donors. It also catalyzes the dissociation of molecular oxygen. Oxygen atoms passivate selenium vacancies V_{Se} on the grain boundaries, which would otherwise act as recombination centers. The details descriptions of the defect and recombination centers are discussed at a later stage. CIGS devices have also successfully been deposited on flexible substrates, such as plastic or metal foils [10]. Although devices with these substrates do not obtain the same efficiencies as the glass substrate ones, they extend the application possibilities.

Back-contact

The metal back-contact material is needed at the beneath of absorber layer, whose role is to collect the photo-generated carriers, here holes, from the absorber and deliver them to the external circuitry. In standard solar cells, the requirements for back-contact material are: low

resistivity, not to impede the flow of majority carriers, holes, and, in CIGS cells, to allow diffusion of Na from the substrate to the CIGS. So far, the best cells have been produced with molybdenum (Mo) as a back-contact. The back-contact material becomes more important and more interesting as the cells become thinner, because the carrier generation profile shifts closer to it.

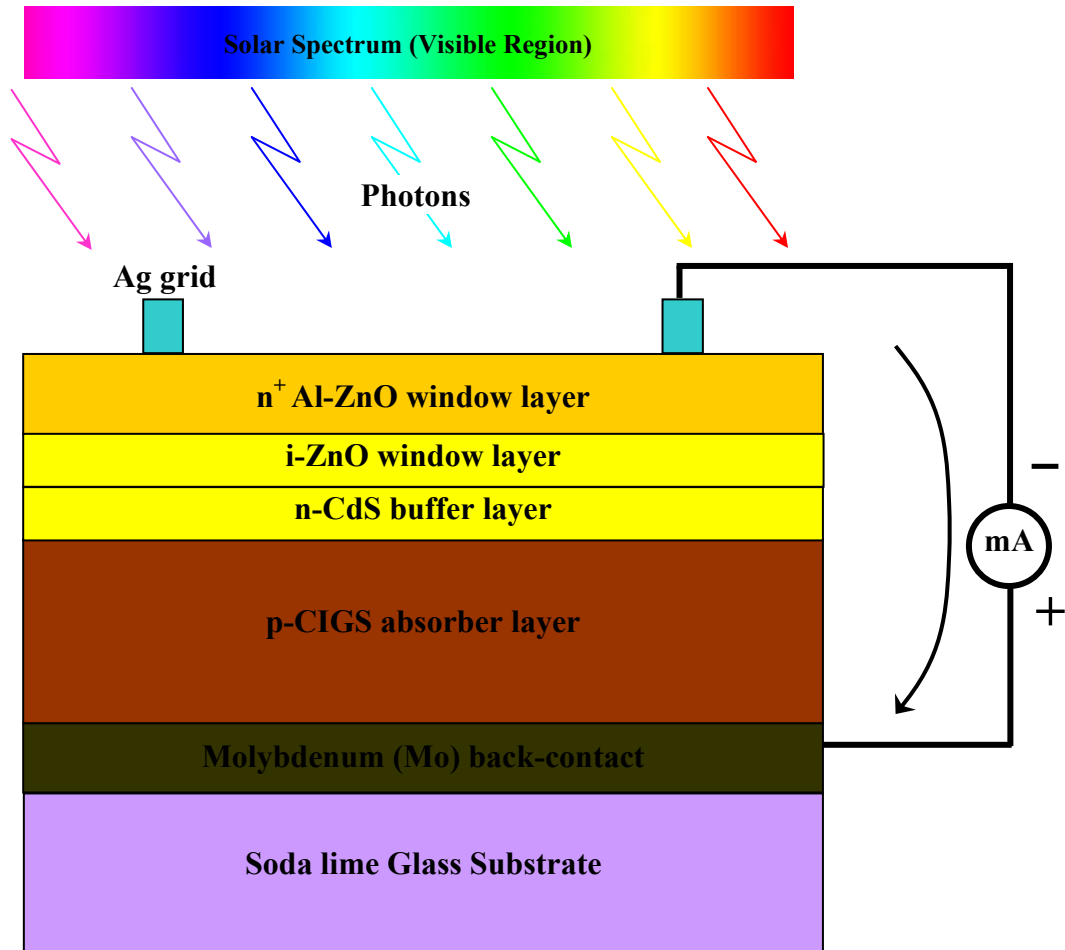


Fig. 1.3 Schematic of a typical CIGS thin film solar cell device structure.

Absorber layer

The absorber layer is the most important active layer in the photovoltaic device. CuInSe_2 (CIS) is a I-III-VI compound with a chalcopyrite structure. It is a direct band-gap semiconductor material and has a large absorption coefficient ($\alpha \sim 10^5 \text{ cm}^{-1}$). Most of the incident sunlight is absorbed close to the p-n junction. As a result, the cells based on CIS can be made thin and with low cost. To produce efficient devices, it is important to match the band-gap of the absorber layer to the solar spectrum. The ideal band-gap for the solar spectrum is 1.4 eV [11]. CIS has a lower-than-optimal band gap of 1.02 eV, and, because of that, the best CIS cells have achieved efficiencies of 15 % [12]. The band-gap can be increased by partial substitution of the In cation with other group III elements such as Al or

Ga, or by replacement of Se with S. The record device [13] was produced with a 30 % In substitution with Ga. This device had a band gap of CIGS is 1.15 eV and an efficiency of 20.3 % [9]. The electrical properties of CIGS depend very strongly on the stoichiometry [14]. Doping of CIGS comes from native defects, mainly from V_{Cu} (copper vacancies) that act as shallow acceptors.

Buffer layer

CIGS solar cells with a buffer layer generally have superior characteristics compared to those without buffer layer. Such a layer can provide good junction formation, lower interface recombination, and decrease leakage. Solar cells containing cadmium sulphide (CdS) have been most efficient for a long time, but CdS introduces current loss at wavelengths below 520 nm (corresponding to photon energies above the CdS band gap). There have been many attempts to substitute CdS with an alternative buffer layer. A thorough review of alternatives is given in Ref. [15]. However, until recently, all of the devices with alternative buffer layers performed inferior to the ones with CdS, although ZnS(O,OH) was close when deposited on the same substrate. Recently, a cell with CdZnS buffer was produced [16] having same efficiency as the record CdS/CIGS cell and a potential to surpass it.

Window layer

The bi-layer of zinc oxide (ZnO) is referred to as a “window layer” or a transparent conductive oxide (TCO). For most photons to be absorbed by CIGS, it is very important for the TCO to have a large band gap (3.3 eV) and therefore be transparent for most of the solar spectrum. On CdS a thin layer around 60 nm of i-ZnO is deposited mainly for reducing the lattice mismatch between CdS and AZO.

Ag top contact grid

For the proper collection of the photo-generated carries (electrons from the ZnO layer) the layer of Silver (Ag) is deposited on AZO layer with finger type geometry. The deposition of Ag is carried out by thermal evaporation and the thickness of Ag layer is kept about 200 nm.

p-n junction

The p-n junction in a typical CIGS cell is formed between the p-type CIGS and n-type CdS. The energy band diagram for such a cell is shown in Fig. 1.4. The CIGS band gap is 1.15 eV and its thickness is 1 μ m. The difference in electron affinities between CIGS and CdS results in a band-gap discontinuity. The conduction-band offset ΔE_c between CIGS and CdS is positive by convention, meaning that CdS conduction-band minimum is higher than that of

CIGS. Wei and Zunger [17] calculated the theoretical valence-band offset between CdS and CIGS. The conduction-band offset for 1.15 eV CIGS can be deduced from their calculations to be $\Delta E_c = 0.3$ eV, a value within the optimal range. An offset larger than 0.5 eV creates a strong barrier for light-generated electrons, thus limiting the current transport.

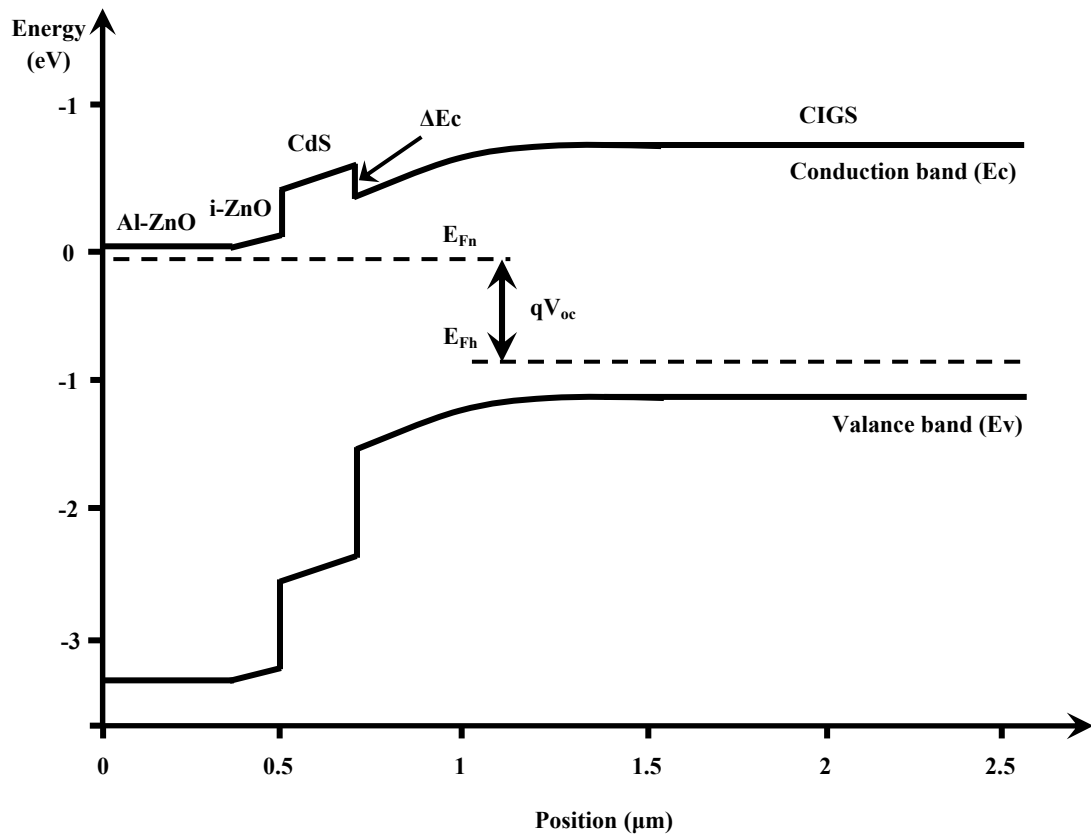


Fig. 1.4 Energy band diagram of a typical CIGS thin film solar cell.

1.4 SOLAR CELL DEVICE OPERATION

The general device operation for solar cells is well described in the textbooks for example by Green [23] and by Fonash [18]. The solar cell performance is commonly described in the terms of four current-voltage (I-V) parameters: efficiency, η , short circuit current, I_{sc} , open circuit voltage, V_{oc} , and the fill factor, FF. In Fig. 1.5 the ideal current-voltage characteristics of a solar cell in dark and under illumination is shown.

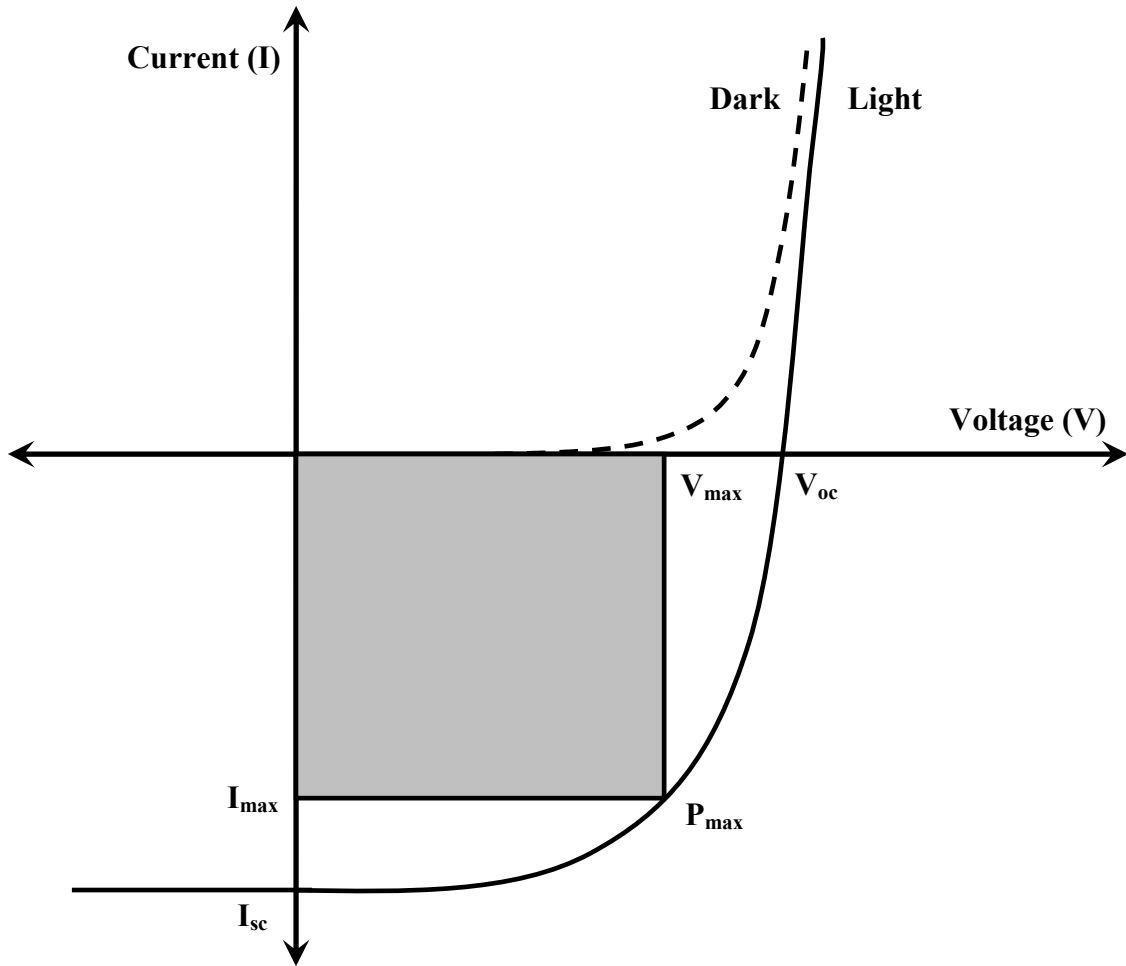


Fig. 1.5 Current-voltage (I-V) characteristics of a solar cell in dark (dotted line) and under illumination (solid line) open circuit voltage (V_{oc}), short circuit current (I_{sc}) and maximum power point (P_{max}) are indicated.

Efficiency

The energy conversion efficiency is defined as,

$$\eta = \frac{V_{max} \times I_{max}}{P_{in}} = \frac{V_{oc} \times I_{sc} \times FF}{P_{in}} \quad (1.1)$$

where P_{in} is the total radiation incident on the solar cell, V_{max} and I_{max} is the maximum voltage and current extract from the solar cell respectively. The I-V parameters are commonly measured under Standard Test Conditions (STC) [19]. Under these conditions the solar cell temperature is 25 °C and the total irradiance is 1000 W/m² with a spectral distribution according to a standard Air Mass (AM) 1.5 spectrum [19]. In the following the definitions and limitations of the three I-V parameters I_{sc} , V_{oc} and FF will be described.

Short circuit current

The current obtained from a solar cell in short circuit conditions is called the short circuit current, I_{sc} . In general terms the I_{sc} can be described by Equation 1.2,

$$I_{sc} = I(V = 0V) = \int_0^d G(x) - R(x,0)dx \quad (1.2)$$

where $G(x)$ is the photo-generation of carriers as a function of the position in the absorber film, d is the absorber thickness and $R(x,V)$ is the recombination at position x and applied voltage V . In short circuit conditions the applied voltage is 0 V. The photo-generation of carriers at the junction, G , is first of all limited by the light reaching this layer. The initial light intensity is reduced due to reflectance from the complete device structure and absorption in the stacked individual layers depending upon the energy band gap. CdS, ZnO, and AZO layers are responsible in the case of CIGS thin film solar cell structure as shown in Fig. 1.3. The reflectance from the complete device can be reduced significantly by an anti-reflective coating like MgF_2 . Another limitation of the photo-generation, G , is the absorption of light in the absorber layer, CIGS thin films in the case of CIGS based solar cell.

By comparing the integrated photo-generation (absorption) with the actual obtained quantum efficiency (QE) an estimate of the integrated recombination, R , as a function of wavelength is obtained. An astonishingly large fraction of the photo-generated carriers are contributing to the short circuit current. This implies that the recombination at short circuit conditions is rather small. I_{sc} is also commonly expressed as a current density J_{sc} (mA/cm^2).

Open-circuit voltage

The voltage across an unloaded (open) solar cell is called the open circuit voltage, V_{oc} . that is basically the energy difference between the Fermi levels of the front and back contact. Theoretically this difference is limited by the band gap of the absorber layer. In practice the V_{oc} will, however, be much lower because of various recombination processes. Commonly the V_{oc} reaches a level corresponding to 50-60 % of the band gap energy. In Fig. 1.6, a band edge diagram of a CIGS based solar cell under open-circuit conditions and illumination is shown. The dashed lines indicate the three main recombination processes. Recombination in the neutral bulk (A) and at the CIGS/Mo interface (A'), recombination in the space charge region (SCR) (B), and interface recombination (C). The horizontal dotted lines indicate that tunneling can enhance the latter two recombination mechanisms.

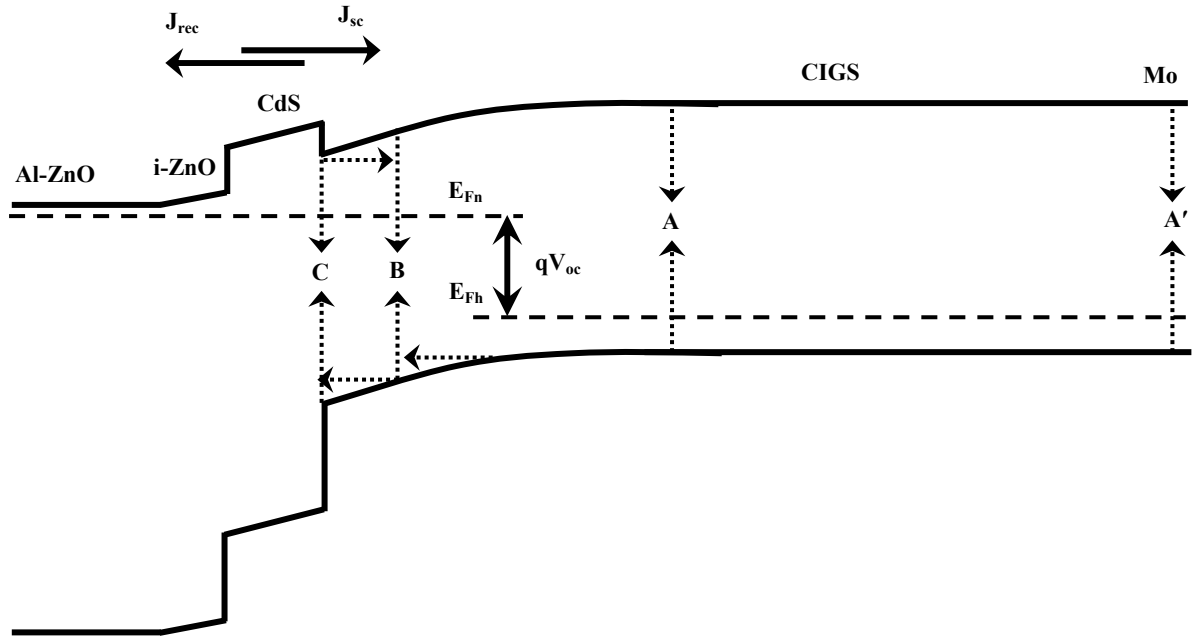


Fig. 1.6 Band edge diagram for a standard CIGS solar cell under open circuit conditions and illumination. (A') Illustrates recombination at the CIGS/Mo interface, (A) recombination in the neutral bulk, (B) recombination in the space charge region (SCR) and, (C) recombination at the CIGS/CdS interface. The thin dashed horizontal arrows indicate that the latter two can be enhanced by tunneling. $J_{rec}=J_{sc}$ at open circuit conditions. E_{Fn} , E_{Fh} are the Fermi energies for electrons and holes respectively.

The voltage dependence of the recombination currents A-C can be described by [20],

$$j_{rec} = j_0 \left(e^{\frac{qV}{nkT}} - 1 \right) \quad (1.3)$$

where V is the applied voltage, kT/q is the thermal voltage, n the diode quality factor and the reverse saturation current, j_0 , is in general thermally activated and may be expressed as [21],

$$j_0 = j_{00} e^{\frac{E_A}{nkT}} \quad (1.4)$$

where E_A is the activation energy of the recombination process and j_{00} is a pre-factor. Since the recombination processes (A-C) are all contribute to the total recombination current but commonly one dominates at $V \approx V_{oc}$. At open circuit conditions, the net current is zero and the total recombination current (J_{rec}) will exactly compensate the J_{sc} . Combining Equation 1.3 and 1.4 gives the following expression for the V_{oc} :

$$V_{oc} = \frac{E_A}{q} - \frac{nkT}{q} \ln \left(\frac{j_{00}}{j_{sc}} \right) \quad (1.5)$$

From Equation 1.5, it can be seen that the V_{oc} becomes equal to the activation energy if the temperature is reduced towards 0 K. An analytical expression of j_{00} can be found for the

different recombination processes in Fig. 1.6, and thus their limitation of V_{oc} [21]. The dominating recombination process for CIGS based solar cells is believed to be recombination process B, recombination in the SCR [20, 22]. Except for recombination losses, the V_{oc} is also affected by “parasitic losses” like series resistance, R_s , and shunt conductance, G_{sh} .

Fill factor

The fill factor, FF, is a measure of how “square” the output I-V characteristics are and is defined as,

$$FF = \frac{V_{max} \times I_{max}}{V_{oc} \times I_{sc}} \quad (1.6)$$

Ideally, the FF is a function only of the V_{oc} [23]. A typical value for a CIGS solar cell is 75-78 %.

1.5 STABILITY AND DEFECT CHEMISTRY OF CIGS

The performance of polycrystalline CIGS based solar cells depends on the native defect chemistry of the CIGS absorber layer. The CIGS is a quaternary alloy belonging to the I-III-VI class of semiconductors with a direct band-gap of 1.15 eV and an absorption coefficient of $\sim 10^5 \text{ cm}^{-1}$. The CIGS-based solar cells are simple to produce and they also exhibit features like chemical stability, stability with time, and doping versatility [24]. The absorbing layer is the key element of solar converters, which is produced mainly from the p-type semiconductor [24]. CIGS crystallizes in the chalcopyrite structure as shown in Fig. 1.7, which is primarily a diamond like lattice with a face centered tetragonal unit cell. This tetrahedron cell of two Cu and In or Ga atoms has a selenium as a center atom. In turn, each metallic atom is surrounded by a tetrahedron of chalcogen atoms.

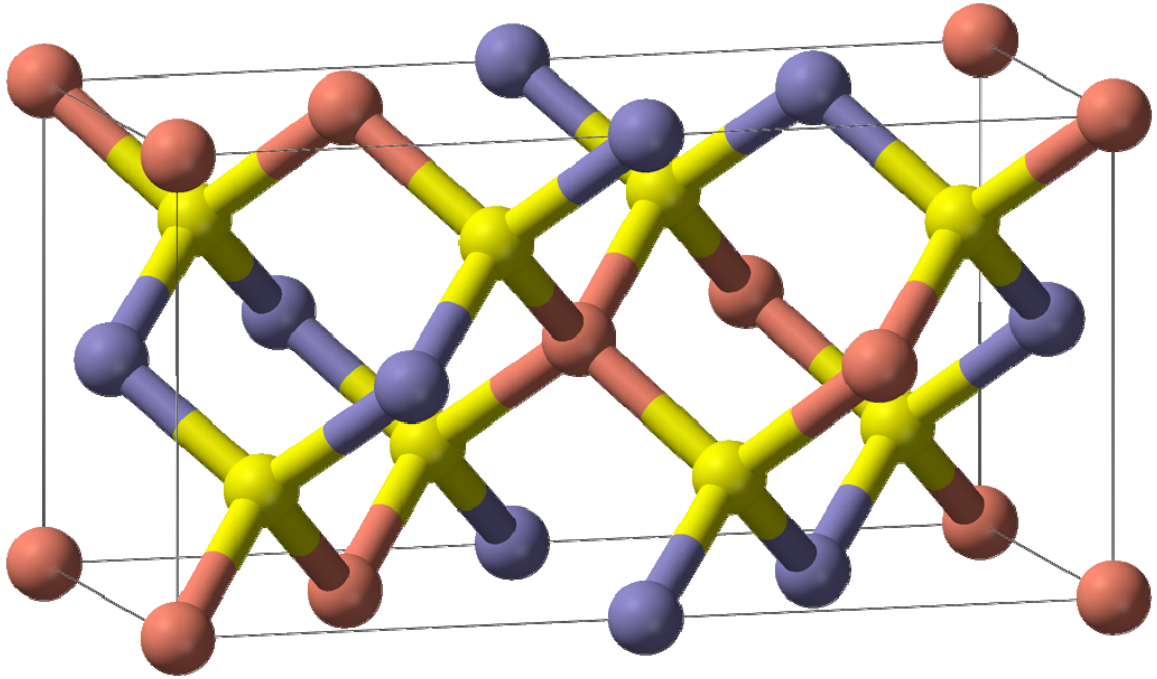


Fig. 1.7 Atomic structure of CIGS unit cell (Red = Cu, Yellow = Se, Blue = In/Ga).

The electrical properties of Cu ternary semiconductors are basically determined by native defects. A high degree of compensation between native donors and acceptors as determined for CIGS seems characteristic [25]. The possible electrically active intrinsic defects are vacancies, interstitials and antisite defects. Depending on these defects, the material can have either n-type or p-type conductivity. For CIGS, the electrically active intrinsic defects are Copper vacancies (V_{Cu}) and Copper on Indium or Gallium antisite defects (Cu_{In} or Cu_{Ga}) in a p-type material and the defects that make the material n-type are Selenium vacancies (V_{Se}) and Indium on Copper antisite defects (In_{Cu}). Copper rich material is generally p-type and highly conductive. This kind of material is not preferred mainly because of the formation of Copper Selenide (Cu_2Se). Cu_2Se being highly conductive, shorts out the junction. Adding more Indium than copper reduces the formation of Cu_2Se but it causes other defects like V_{Cu} and In_{Cu} which are compensating in nature. Hence, the Copper to Indium ratio ($Cu/(In+Ga)$) is always maintained around unity. Samples with p-type conductivity are grown if the material is Cu-poor and is annealed under high Se vapor pressure, whereas Cu-rich material with Se deficiency tends to be n-type [26]. CIGS films when suitably manufactured tend to be p-type because of the low energy of formation of Copper vacancies which give the material its conductivity [27]. The band gap of $CuIn_{(1-x)}Ga_xSe_2$ varies according to the equation [28],

$$E_g = 1.011 + 0.664x - 0.249x(1-x) \quad (1.7)$$

Depending on the $[Ga] / [In+Ga]$ ratio, the band gap of CIGS can be varied continuously between 1.02 eV and 1.72 eV [29]. Employing CIGS together with CIS extends the spectral range to the IR region [24]. The addition of about 30 % Ga in CIS increases the band gap to 1.4 eV. This has a closer match with the air mass (AM) 1.5 solar spectrum. Addition of Gallium not only increases the band gap but also has other beneficial effects. The addition of Ga improves the adhesion of the film to the Mo substrate [30]. The carrier concentration in the absorber is also reported to increase with addition of gallium. Moreover, defect chemistry, electron and hole affinities, film morphologies and lattice constants are also affected by the addition of Ga.

The addition of Ga in the film can be done in a way that the concentration of Ga is the same throughout, resulting in homogenous films with uniform band gap everywhere. The Ga profile in the absorber can also be varied resulting in graded band gap structures. By using graded compositional profiles, i.e. higher gallium concentration towards the back contact, a back-surface field (BSF) is achieved since a higher concentration of gallium mainly increases the conduction band level in the CIGS layer. A reduced back-contact recombination has earlier been demonstrated by the use of such a BSF [31]. Band gap grading creates a quasi-electric field due to the conduction band bending, moving the electrons towards the junction, and thereby increasing the probability of their collection. Further, graded band gap structures could be developed which could result in an improvement in V_{oc} without reduction in I_{sc} [24]. Though it is beneficial to add Ga to improve the properties of CIS, there is a limit to which it serves favorable. Higher Ga content of 40 % has a detrimental effect on the device performance, because it negatively impacts the transport properties of the CIGS absorber film [32]. The current, high-efficiency devices are prepared with band gaps in the range 1.20–1.25 eV, this corresponds to a $[Ga] / [In+Ga]$ ratio between 25 and 30 % [32].

1.6 PRESENT STUDY

The aim of this work is to fabricate multilayered structure of CIGS thin film solar cell on a glass substrate. The proposed solar cell device is already shown in Fig. 1.1. The overall performance of the solar cell depends on the properties of the individual thin film layers. Each individual thin film layer thus optimize as it plays an important role in solar cell device performance. Thin films, for solar cell device fabrication, are grown by different physical vapor deposition (PVD) techniques. Prepared thin films are characterized to ensure the best structural, optical, electrical, compositional, and surface properties. The solar cell device is then prepared by sequentially depositing each layer. The performance is analyzed by the I-V

measurement in the dark as well as light. The spectral response of the prepared cell is also measured. Before the solar cell fabrication part we check the solar cell performance by simulation using AMPS-1D program and finally it is to be checked with the obtained experimental results.

1.7 ORGANIZATION OF THE THESIS

Chapter 2: The experimental procedure of growing thin films and the techniques required for its characterization are discussed in this chapter. The physical vapor deposition (PVD) technique is used for the fabrication of thin films. Various thin film characterization techniques used for the study of the structural, compositional, electrical, and optical properties of the films are discussed. This chapter also includes some of the experimental facility indigenously developed and automated at our lab to study various properties of thin films and solar cell device.

Chapter 3: This chapter deals with the growth of metallic back-contact, molybdenum (Mo), thin films. The preparation of molybdenum thin films is carried out by RF magnetron sputtering under different growth conditions. The effect of various growth conditions like the sputtering power and the working pressure, on the structural, electrical and optical properties of the thin films is studied. The low resistive ($1 \Omega/\square$) and desirable adhesion with the glass substrate achieved. Additionally the laser scribing of the molybdenum thin film were done and optimized, the best scribing condition, which will be used for the module preparation.

Chapter 4: This chapter contains optimization of the absorber layer (CIGS) as an active layer in the solar cell device structure. CIGS, absorber layer, deposited by the flash evaporation technique and selenised using evacuated argon pressure controlled RTA furnace. The growth, structural, electrical, and optical properties of the CIGS thin film by varying the substrate temperature and thickness of the film is discussed in detail.

Chapter 5: The n-type cadmium sulphide (CdS), also called the buffer layer, is optimized. CdS thin films are grown by the thermal evaporation technique on glass substrates. The effect of substrate temperature and thickness on the

structural, electrical, and optical properties of CdS thin film are investigated and discussed in this chapter.

Chapter 6: The window layer (n^+ -type), bi-layer of i-ZnO and Al- ZnO, is optimized by growing its thin films by RF magnetron sputtering technique at different working pressure and RF power. Optimization part includes the electrical conductivity, optical transmission in UV and visible region, grain growth and surface morphology of both i-ZnO and AZO thin films. All these properties are very sensitive to the working pressure and rf power. The best values of them are used to grow device quality thin films of i-ZnO and AZO.

Chapter 7: This chapter deals with the simulation and fabrication of the solar cell device. The simulation is done by using one dimensional simulation program called an analysis of microelectronic and photonic structures (AMPS-1D). In the simulation the effect of CIGS film thickness is demonstrated in the form of current-voltage (I-V) characteristics and spectral response analysis. In the fabrication part of CIGS solar cell the variation in the thickness of CdS layer is been considered. As it plays an important role in the performance of solar cell. The spectral response of the same is also analyzed.

Chapter 2

Thin Film Fabrication and
Characterization
Techniques

2. THIN FILM FABRICATION AND CHARACTERIZATION TECHNIQUES

The role of individual thin film is vital in any multilayered thin film device structure. The defect free thin film is the prior criteria for healthier performance of the thin film device. This chapter discusses the thin film deposition methods in brief. Thin film characterization techniques used to investigate the structural properties viz. X-ray diffraction (XRD), Scanning electron microscopy (SEM), Transmission electron microscopy (TEM), and Atomic force microscopy (AFM) are also discussed. The optical characterization technique utilized to study the transmission and reflection of the grown thin films. In the electrical measurements of thin films, Van der Pauw method, four-point probe method, and Hall-effect are elaborated.

2.1 THIN FILM FABRICATION TECHNIQUES

Methods of making or depositing the thin film can be divided into two parts: one is physical vapor deposition (PVD) and other one is chemical vapor deposition (CVD). Thermal or flash evaporation (resistive heating), e-beam evaporation, sputtering are the examples for PVD, while Low Pressure CVD, Plasma Enhanced CVD (PECVD), Laser Enhanced CVD (LECVD), Metal-organic CVD (MOCVD) are the examples of CVD. Depending upon the application the vacuum system is attached with the deposition method. In the present thesis we are using thermal evaporation, flash evaporation, and RF magnetron sputtering. These different PVD techniques are described in the subsequent sections.

In PVDs the atoms or molecules, of the evaporable material, energized from a thermal vaporization source or from the ionization process, reach the substrate. Successful vapor transport process from the source to substrate is done by reducing the number of gas collisions, and enabling high energy particles to be used as part of the deposition process. This course of action requires a good vacuum near to 10^{-6} mbar. A vacuum could be described as where within an enclosed volume there is less gas particle per unit volume than is present in a similar volume in the atmosphere surrounding the enclosed volume. The word vacuum is derived from the Latin word “vacua” meaning empty. If we empty the chamber of gas, we produce a vacuum. This can be used for our advantage. Less gas particle in particular area gives a less obstacle for atoms or molecules of the material in the vapor transport process from source to substrate. This physical process is known as a “mean free path”. In the simple manner the mean free path is the average distance between the successive

collisions of vaporized material with the present gas atoms. The length of the path depends on the molecular diameter of the gas particle, the density of molecules, and their average velocity. The vaporized phase of the material collected on to the substrate, this collection of the material is named as a thin film. The process of making the thin film can be divided into few steps namely, thermal accommodation, binding, surface diffusion, nucleation island growth with coalescence, and continued film growth.

In the thermal accommodation process impinging atoms must lose enough energy thermally to stay on surface. More than one atoms attach with each other by two types of surface bond. One is physisorption (physical adsorption) in which the Van der Waals type the attachment is observed between the atoms. This type of the bonds is weak bonds. The second one is chemisorption (chemical adsorption) deals with the chemical bonds between the atoms and they are strong bonds. Within or after the binding process the atoms are move around on the surface. The process of an atom moving around on the surface is known as surface diffusion. The higher the energy the atoms arrive with on the surface the more and faster they move around on the surface. The atoms continue to move until they reach a position that minimizes the total energy.

As more atoms arrive, they undergo the same process, and attached with the atoms which are already sticking to the surface and so the nucleated particles will grow. Once the nuclei reach a critical size, it gets stable and fixed. There are various mechanisms for the further growth of the nuclei shown in Fig. 2.1 [33]. Van der Merwe mechanism describes the method where the atoms cover the whole surface before a second layer is grown. If the nuclei grow as hemispheres and a thin film is formed once the hemispheres have grown large enough to touch each other, then it is referred to as the Volmer-Weber mechanism. If the growth process is a combination of the two by first covering the surface and then growing by hemispheres, it is referred to as the Stranski-Krastanov mechanism. In roll coating onto polymer surfaces, the growth will be by the Volmer-Weber mechanism.

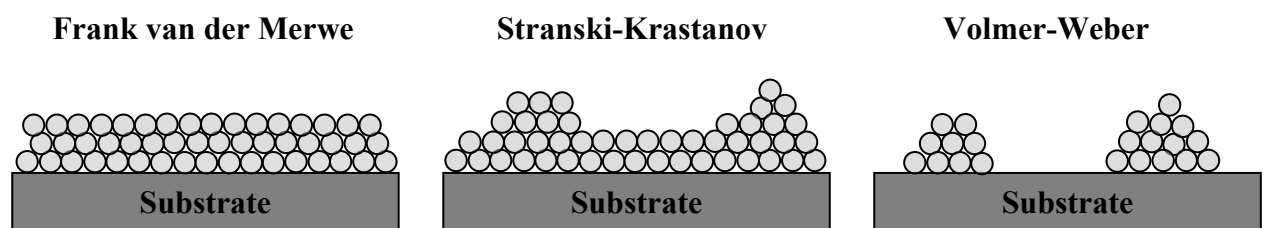


Fig. 2.1 A schematic diagram for the different vacuum based growth techniques of thin film.

In all the above listed mechanism the substrate roughness will lead to preferential nucleation. Nucleation will start in the valleys between peaks. Hence, defects in the surface

can generate defects in the subsequent coating. Figure 2.2 describes the surface dependency during the nucleation process.

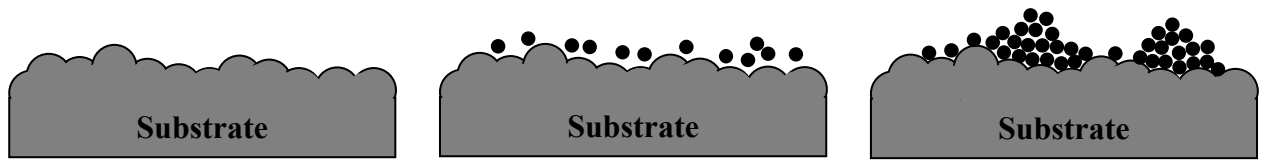


Fig. 2.2 Substrate dependence nucleation of atom and finally the effect of it on thin film growth.

As the randomly positioned nuclei increase in size into islands, there will be some that come into close proximity. Once the spacing between any two nuclei or islands gets to within a critical distance, they will move toward each other and coalesce into a single entity (Fig. 2.3). With the arrival of more atoms, the nuclei and islands continue to grow and coalescence continues. When larger islands coalesce, the area they move from is denuded of material and so new nuclei will form and grow. With the continued growth, there will be coalescence of several nuclei and islands into more complex shapes. Eventually, this will result in a network of interconnected islands.

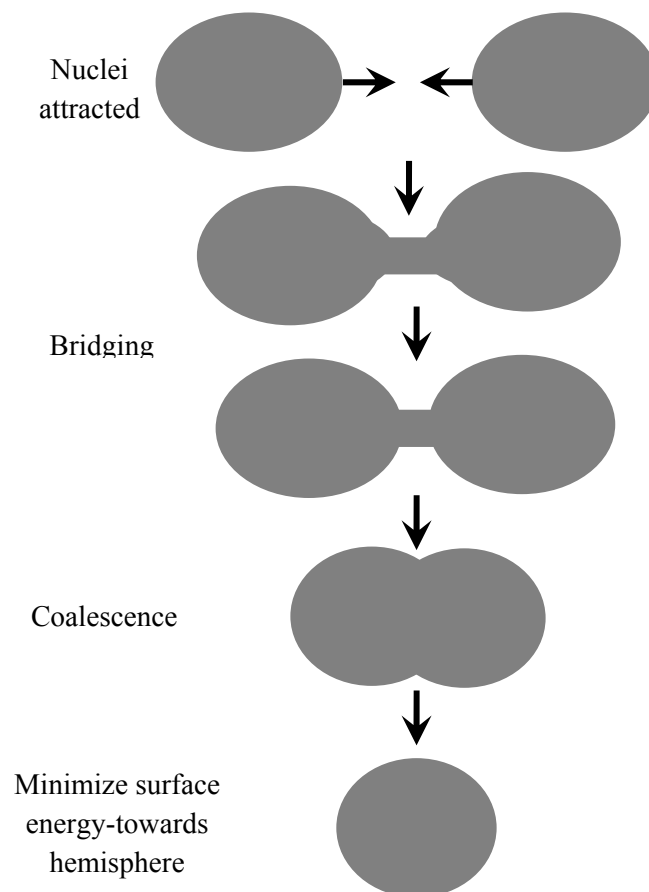


Fig. 2.3 Schematic of coalescence of a couple of nuclei of thin film.

The network will expand and undergo further coalescence, increasing the conduction paths for more efficient conduction and thus reducing the resistance. The surface will become more completely covered apart from some isolated holes as shown in Fig. 2.4. Depending on the conditions, the coating might be quite thick before the last of the holes is filled in.

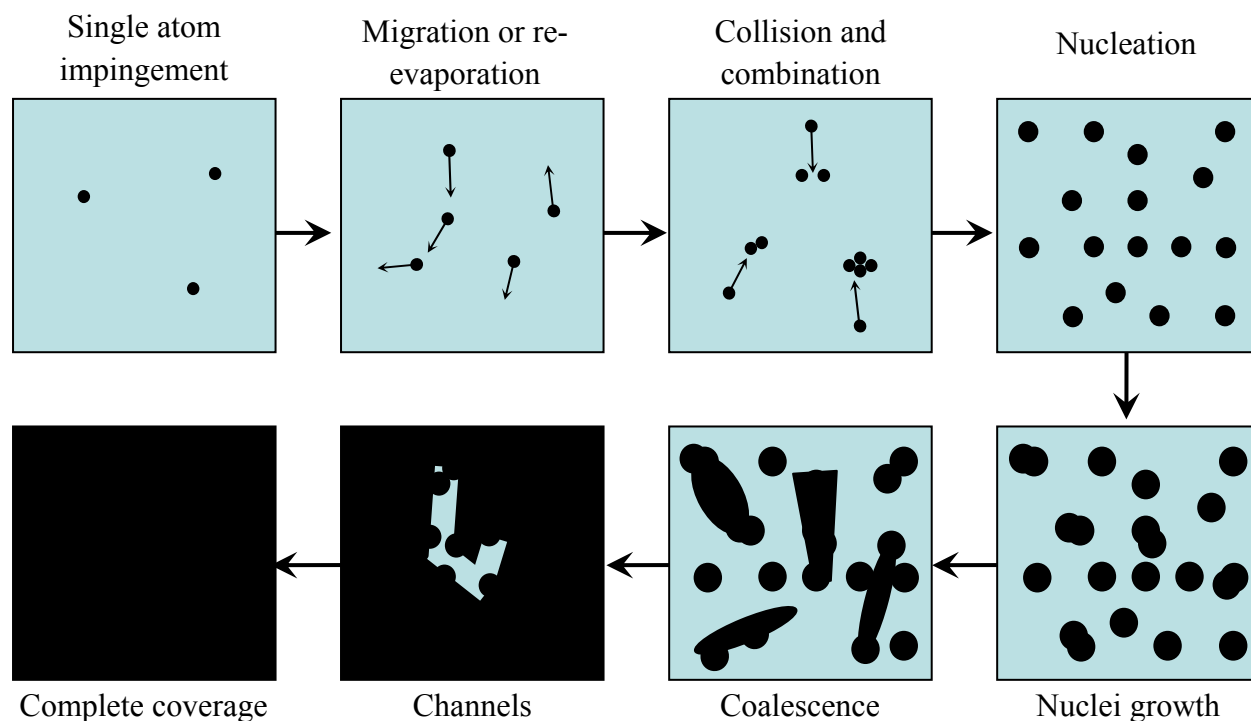


Fig. 2.4 Schematic showing the different stages of nucleation and initial growth of thin film.

Various kind of deposition techniques were used in general for making the thin film of a particular material. That is highly depends on the melting or sublimation temperature of the material. In the present work for the deposition of CIGS powder and CdS powder, flash and thermal evaporation was used. For the deposition of Molybdenum and intrinsic as well as Al doped ZnO, RF magnetron sputtering was used. Thermal evaporation, flash evaporation, and RF magnetron sputtering are discussed in details in the next section.

Substrate preparation

Thin film growth and adhesion is fundamentally related to the substrate surface conditions. It is therefore crucial to thoroughly clean the substrate before the deposition process. In industry this is often done by using the etching chemicals or plasma etching. Here we are used the soda lime glass substrate. To remove the impurities from the glass surface first we placed it in the 5 % dilute H_2O_2 solution. Afterward, a hot bath of acetone, trichloroethylene and methanol is provides followed by drying it by nitrogen flow. Dried clean glass substrate is kept in clean environment at ~ 40 °C temperature before used it for the evaporation.

2.1.1 Thermal and Flash Evaporation

Thermal vaporization requires that the surface, and generally, a significant volume of the material must be heated to a temperature where the material gets melt and an appreciable vapor pressure built up. A Common technique for melting or evaporating/sublimating the material was resistive heating. Different types of evaporation sources are used for the resistive heating [34].

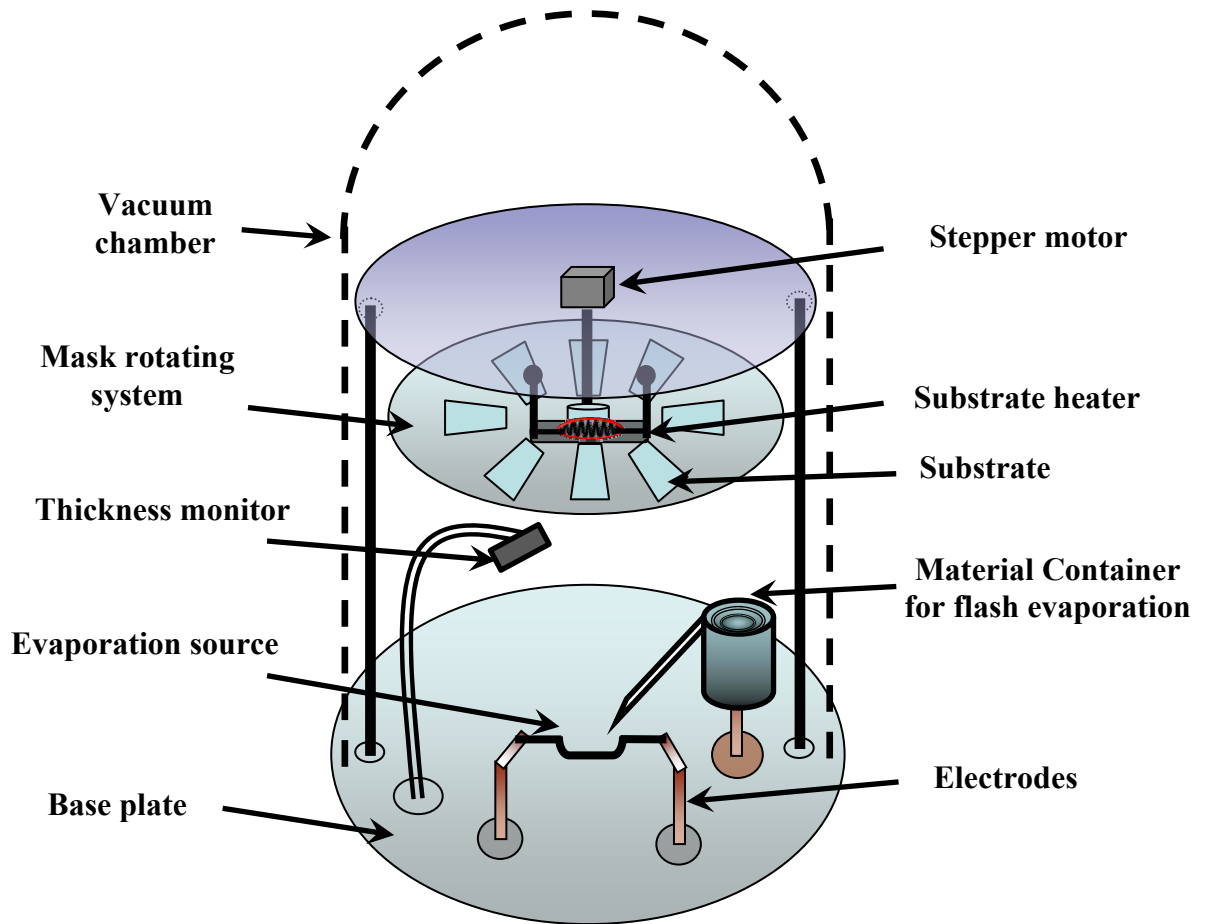


Fig. 2.5 Schematic of the specially designed vacuum chamber for thermal and flash evaporation which has multiple substrates holder with rotation facility.

Fig. 2.5 shows a typical schematic of thermal and flash evaporation setup. The thickness of the thin film is measured by Quartz crystal thickness monitor. The substrate temperature is provided by the 1000 W halogen tube, placed just above the substrate holder. The substrate holder is made such a way that in a single evacuation operation, multiple number of the thin film can be made.

By observing the setup as shown in Fig. 2.5, there is a minor difference between thermal and flash evaporation. In the thermal evaporation the evaporation source is preloaded with the material, but in the flash evaporation technique there is a separate container which is loaded with the material. At the time of the deposition the material is fall on the evaporation

source slowly and gets vaporized. Molybdenum Baffled Box type evaporation source is used for the deposition CdS and CIGS material. Flash evaporation technique is more useful for the evaporation of the ternary or quaternary alloys and compound, which is made up of elements having a different vapor pressure and melting temperature values. Because of the instant vaporization of the material the spitting of the material is very less. While in the thermal evaporation method, only single elements or binary alloys and compounds can be evaporated.

Post-deposition annealing

To increase the stability, compactness and grain size of the thermal or flash evaporated thin film, there is a need for rapid post-annealing. In our study a specially designed rapid thermal annealing (RTA) furnace was used. The schematic and photograph of RTA furnace, is shown in the Fig. 2.6.

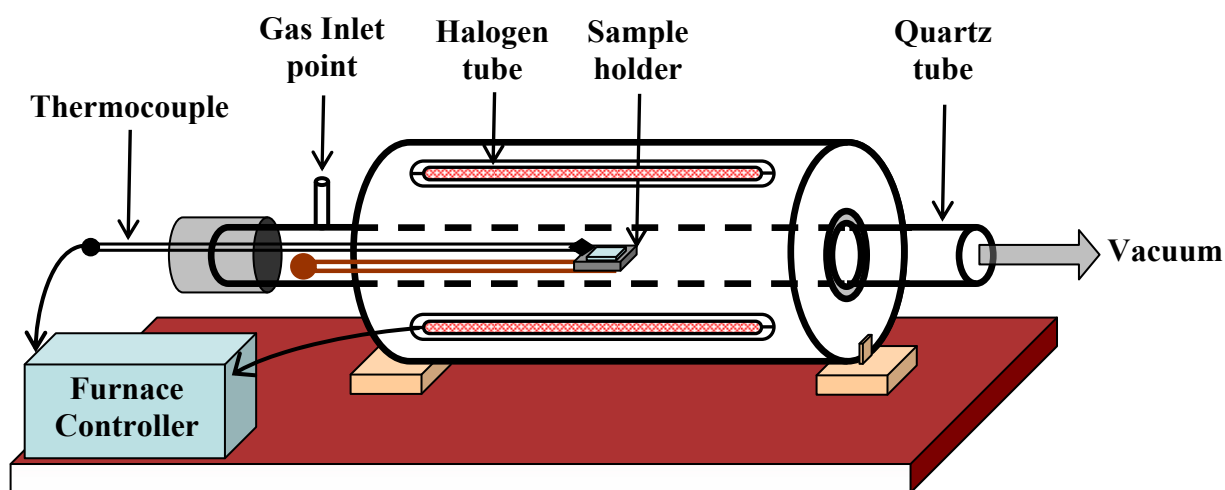


Fig. 2.6 Schematic of the vacuum based RTA furnace.

The quartz tube is placed in a circular cylinder with circularly arranged six halogen tubes (1000 W each). One end of the tube is connected to the vacuum system and the in other one there is an arrangement for the sample loading/unloading and thermocouple. The thermocouple and the halogen tube are connected to the furnace controller, which consists of PR502 (Selec Controls, Mumbai, India) programmable temperature controller and locally made solid state relay (SSR). Gas inlet point is available for providing the reactive annealing process.

2.1.2 RF Magnetron Sputtering

Sputtering is a widely used and well known technique for the erosion of any kind of surfaces and the preparing thin films of them. Sputtering is mainly used for patterning the

semiconductor wafers, cleaning surfaces, depth-profiling measurement, and a number of applications [35].

The simplest kind of plasma device, a diode sputtering, is simply an anode and a cathode arrangement having a specific distance between them inside a vacuum system. Under the right conditions, with enough voltage across the electrodes and the appropriate gas pressure, the gas will breakdown into a plasma discharge. In this discharge, the potential of the plasma is spatially uniform, slightly higher than the potential of anode. Near the cathode, there is a very large electric field. Ions are accelerated rapidly across the electric field and strike the cathode. As part of this collision (which can cause sputtering), occasional electrons, known as secondary electrons, are emitted from the surface. These electrons are accelerated back across the electric field and gain significant energy. This energy can be used used, through the collisions with gas atoms, to form more ions to sustain the discharge process. The secondary electrons are the primary source of energy to the plasma discharge, and each secondary electron must generate a significant number ions.

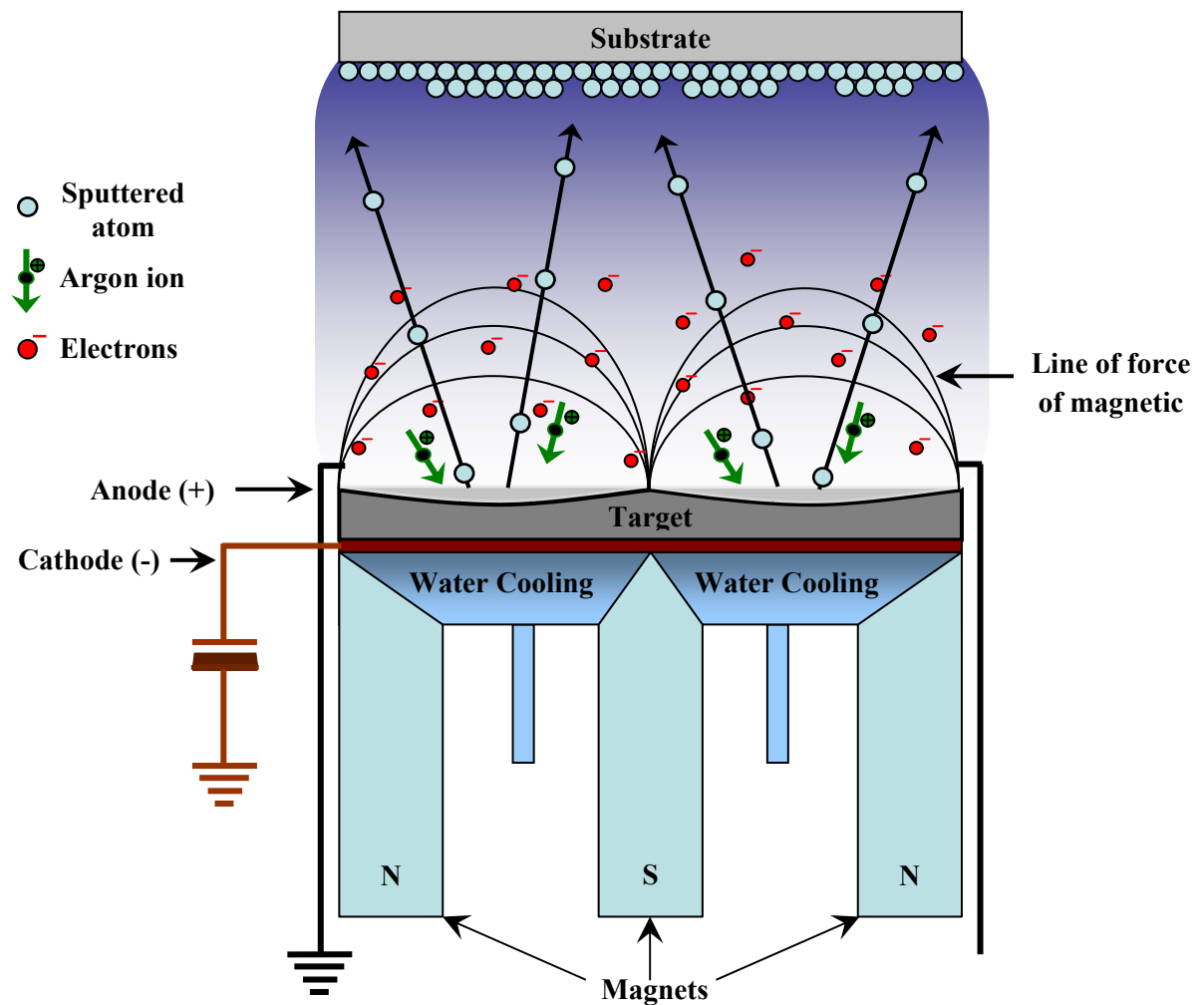


Fig. 2.7 Schematic of RF magnetron sputtering system with water cooled arrangement below the cathode.

In the case of the insulating material there is no plasma because of the least generation of secondary electrons from the insulating surface. Radio frequency (RF) sputtering gave the solution for that. The cathode and anode are electrically reversed in RF sputtering for the elimination of charges that builds-up on an insulating surface by providing the equal number of ions and electrons. This allows insulators to be sputtered. Due to the cyclic motion of the generated electrons while sputtering of insulator by RF, that makes it complex and highly system dependent. Confining the generated secondary electrons, i.e. plasma, at particular area by using the magnets resolve this problem. The schematic of the RF magnetron sputtering system is shown in Fig. 2.7.

A magnetron uses a static magnetic field that is configuring at the cathode plate. The magnetic field is located parallel to the cathode surface. Secondary electrons emitted from the cathode due to the ion bombardment are constrained by the magnetic field to move further in a direction perpendicular to both the electric field (normal to the surface) and the magnetic field. This is known as an $E \times B$ drift, which is also the basis for the Hall Effect. This drift causes electrons to move parallel to the cathode surface in a direction 90 degrees away from the magnetic field. We used RF power supply of 600 W from HÜTTINGER Elektronik, Germany and circular magnetron cathode from Angstrom Sciences Inc, USA.

2.2 CHARACTERIZATION TECHNIQUES

2.2.1 X-ray Diffraction

X-ray diffraction (XRD) is a powerful non-destructive diagnostic tool in analyzing the crystalline phases of thin-films and determining the structural properties of these phases such as the preferred orientation and average grain size. X-ray diffractometry (θ - 2θ scan deometry) using a Bruker D8 advance with Cu $K\alpha$ radiation ($\lambda = 1.540562 \text{ \AA}$) was used in this thesis. The machine was typically operated at a voltage of 30 kV and current 30 mA. A standard setting for continuous scans is at an angular speed of 1° min^{-1} and a step size of $0.02^\circ \text{ s}^{-1}$ in a 2θ range of $0^\circ - 100^\circ$. Schematic of X-ray diffractometer and the diffracted X-ray beam from the lattice spacing is show in Fig. 2.8 (a) and (b) respectively.

Principle of θ - 2θ scans

A real three-dimensional crystal consists of many sets of atomic planes. These atomic layers are spaced a distance (d) and are named as d -spacing. An atomic plane can be distinguished by its miller indices (hkl), and the d -spaces between (hkl) planes denoted by d_{hkl} . When X-ray beams irradiate the sample surface at certain angle of incidence, these planes of atoms scattered the incident X-rays beam. There is a constructive interference from specular

reflectance of X-rays at particular values of d-spacing and the angle of incidence θ_{hkl} onto the (hkl) planes, resulting in a diffraction peak. The condition of the constructive interference is given by the Bragg law [36]:

$$n_i \lambda = 2d_{hkl} \sin \theta_{hkl} \quad (2.1)$$

Where the integer n_i is known as the order of the reflection, and λ is the X-ray wavelength. X-ray diffractometer is based on the Bragg Equation 2.1. For diffraction to be observed, the angle between the surface of the sample and the incident X-rays must be at the Bragg angle θ_{hkl} , and the reflected intensity is measured by detector as a function of $2\theta_{hkl}$. In this case, X-rays are incident on the samples over a range of angles θ , while reflections are detected over the range of angles 2θ . This XRD scan mode is known commonly as the θ - 2θ scans. Figure 2.8 (a) shows a schematic representation of X-ray diffractometer. Polycrystalline thin-films consist of many grains distributed in various orientations. The diffraction occurs from any grain or particles must follow the Bragg law.

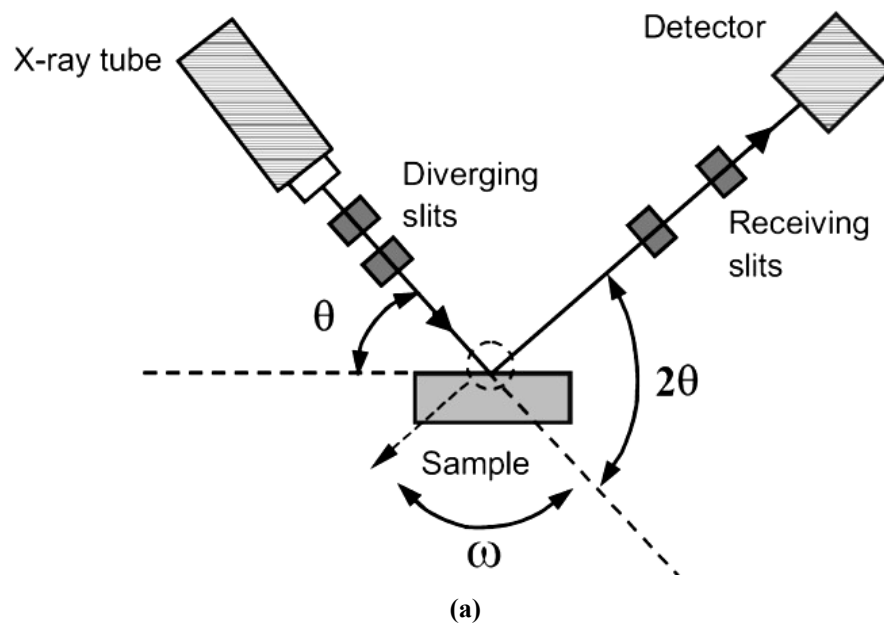


Fig. 2.8 Schematic of X-ray diffractometer (a) and interaction between atomic places having a finite d-spacing of material and X-ray beam (b).

The most random distribution of orientations occurs in powder samples consisting of a many small crystallites with random orientations. As a result, the powder diffraction pattern can be taken as a reference for all possible diffraction peaks. In the following Chapters, diffraction data from the Joint Committee on Powder Diffraction Standards (JCPDS) are used determine their structural properties.

Determination of average crystallite size

The width of diffraction peak, in a θ - 2θ scan, is related to the average crystallite size of the crystals present in the sample. Under an ideal diffraction condition, namely a perfect infinitely thick crystal and an incident beam of parallel monochromatic radiation, XRD peaks become narrow lines located at the Bragg angles. The infinite number of parallel atomic planes leads to the destructive interference and complete cancellation of scattered X-rays over all angles, except for the Bragg angles. This is because an X-ray reflected at the surface can always be cancelled by an X-ray reflected from a plane deeper in the crystal, which happens to be exactly out of phase due to the additional path length. However, if the crystal is so thin that the deeper atomic planes do not exist, then there will be incomplete cancellation of scattered X-rays, leading to broader XRD lines. The incomplete cancellation of scattered X-rays can also be observed when the sample itself a polycrystalline. This broadening of the diffraction peak helps to determine the average crystalline size (D), Scherrer's formula [36] is use to calculate it, and is given by,

$$D = k\lambda / \Delta(2\theta) \cos\theta \quad (2.2)$$

where λ is the X-ray wavelength, and $\Delta(2\theta)$ is the FWHM in radians, θ is the peak position in degrees. k is a constant close to 1. The size D is effectively an average coherence length of the crystal structure. It is not necessarily a measured size of an entire grain since defects, such as dislocations in the lattice structure, may divide each grain into sub-grains, or crystallites, and result in a value of D , which is far smaller than the average grain dimensions measured by transmission electron microscopy (TEM) or Scanning electron microscopy (SEM).

2.2.2 Electron Microscopy

Beyond crystalline phases of thin-films, the surface topography and morphology, including grain size and shape, existence of compounds, evidence of film voids, micro-cracking or lack of adhesion, etc., are prior observation. In addition to that, somewhat more difficult to obtain are the cross-sectional views of multilayer structures where interfacial regions, substrate interactions, and geometry and perfection of electronic devices with associated conducting

and insulating layers may be observed using the electron microscopy. The electron microscopy is based on the scanning of the secondary electrons generated from the sample surface, called a scanning electron microscopy (SEM). Chemical or elemental analysis of the sample can also be examined by just attaching extra X-ray detector with the SEM equipment. It works upon dispersion of X-ray produced from the atoms of the sample, so called as energy dispersive analysis of X-ray (EDS). Most of the latest SEM equipments now have an extra attachment for the EDS analysis.

SEM and EDS Analyses

The scanning electron microscope is the versatile tool for the observation of the micron size elements and surface of specified objects. The capabilities of surface-analysis instruments, especially spatial resolution, sample handling and treatment, speed of data acquisition, and data processing and analysis have been greatly enhanced during the past three decades. The applications of these instruments have now advanced from research and development to problem solving, failure analysis, and quality control and the instruments have become more reliable.

An electron microscope uses an electron beam (e-beam) to produce a magnified image of the sample. The three principal electron microscopes are: scanning, transmission, and emission. In the scanning and transmission electron microscope, an electron beam incident on the sample produces an image while in the field-emission microscope the specimen itself is the source of electrons. A scanning electron microscope consists of an electron gun, a lens system, scanning coils, an electron collector, and a cathode ray display tube (CRT). The electron energy is typically 10 - 30 keV for most samples, but for insulating samples the energy can be as low as several hundred eV. The use of electrons has two main advantages over optical microscopes: much larger magnifications are possible since electron wavelengths are much smaller than photon wavelengths and the depth of field is much higher. The basic model for the scanning electron microscope is shown in Fig. 2.9.

When an electron beam interacts with the sample, it gets absorbed, reflected, or transmitted and, may generate light, X-ray or electron (Backscattered, secondary). Typical depth of the electron beam is near to 1 μm . The energies produced from electron beam interaction with the sample give a wealth of information about the surface composition, and the physical structure of a sample. Electron beam microscope consists of an electron gun, a lens system, scanning coils, an electron collector, and a cathode ray display tube.

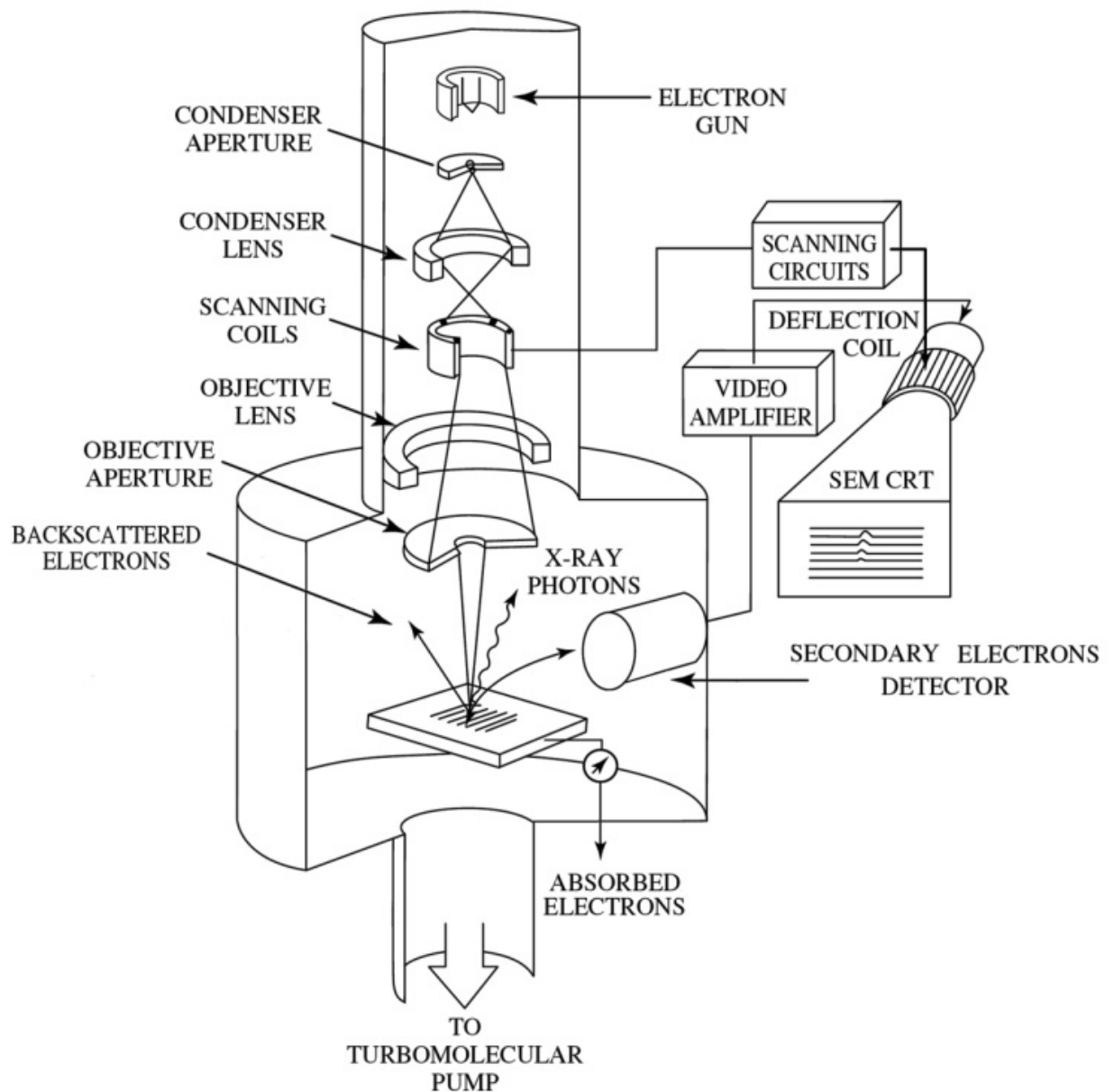


Fig. 2.9 Basic model for the scanning electron microscopy and different types of energies produced by the interaction of electron beam with the sample.

SEM can produce magnified image of the sample to study the surface topology using focused electron beam. The image in SEM is produced by detecting the secondary and/or backscattered electrons from the sample surface. The final image is created by scanning the sample in XY direction and collecting the number of electrons emitted from each spot on the sample simultaneously. The change in the contrast of image is directly related to the surface topology of the sample.

EDS provide elemental identification and quantitative compositional information by analyzing X-rays emitted by the sample when it interacts with an electron beam. The electron beam removes an inner shell electron from the sample, which cause a higher energy electron

to fill the shell and release energy as characteristic X-rays. All elements except hydrogen and helium can be detected but Sodium (Na) window in front of the detector can absorb low-energy X-rays so, it can not detect the element having the atomic number less than 11 (Na). EDS gives a quantitative analysis of elemental composition within a sampling depth of typically 0.5 to 5 nm, etching of the sample with the help of sputtering provides depth information.

TEM analysis

Lastly, and most complex of all, are diffraction patterns, the crystallographic information, and the high-resolution lattice images of both plain-view and transverse film sections. For that the TEM is required for these applications.

In principle a beam of electrons is transmitted through an ultra thin specimen, interacting with the specimen material as it passes through, shown in Fig. 2.10, an image is formed by the interaction process of the electrons of the specimen, transmitted through the specimen. The transmitted electrons collected on to the fluorescent screen, on a layer of photographic film, or to be detected by a sensor such as a CCD camera. The image is magnified by magnetic lances and focused onto an imaging device.

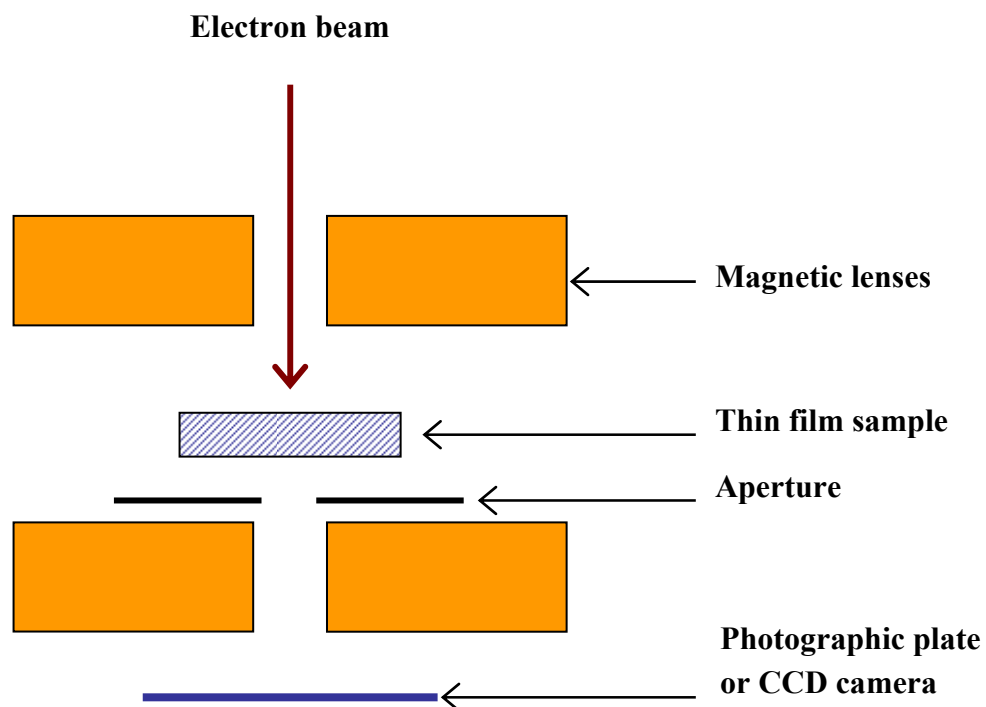


Fig. 2.10 Schematic diagram of TEM analysis, diffraction from the thin film sample collected on the photographic plate or a CCD camera.

TEMs have an imaging power with a significantly higher resolution than light microscopes, owing to the small de-Broglie wavelength of electrons. This enables the

instrument's user to examine fine detail - even as small as a single column or a row of atoms, which is tens of thousands times smaller than the smallest resolvable object in a light microscope. TEM is one of the major analytical methods in the scientific field, in both physical and biological science. There is an interesting distinction between the TEM and SEM. The former is a true microscope in that all image information is acquired simultaneously or in parallel. In the SEM, however, only a small portion of the total image is probed at any instant, and the image builds up serially by scanning the probe.

2.2.3 AFM Analysis

The atomic force microscope is a type of scanned-proximity probe microscopes. All of these microscopes work by measuring a local property – such as height, optical absorption, or magnetism – with a probe or “tip” placed very close to the sample [37]. The small probe-sample separation (on the order of the instrument’s resolution) makes it possible to take measurements over a small area. The AFM probe having a very sharp tip, less than 10 nm diameters, is at the end of a small cantilever beam. The schematic of the AFM operation is shown in Fig. 2.11. A piezoelectric scanner tube is used for scanning the probe across a selected area of the sample surface. The Inter-atomic forces between the sample surface and the probe tip cause the cantilever to deflect as per the sample’s surface topography (or other properties) changes. Depending upon the reflected laser light from the cantilever, a data of the laser position on the four-quadrant photo-detector is fed to a computer, which generates a map of topography and/or other properties of interest. The sample areas maximum about 100 μm square to less than 100 nm square can be imaged. Various modes are available to operate the AFM.

Contact Mode AFM: The AFM probe is scanned at a constant force between the probe and the sample surface to obtain topographical map. When the probe cantilever is deflected by sample surface topography, the scanner adjusts the position of the probe to restore the original cantilever deflection. Lateral resolution of <1 nm and height resolution of <1 Å can be obtained.

Intermittent Contact (Tapping Mode) AFM: In this mode, the probe cantilever is oscillated at or near its resonant frequency. The oscillating probe tip is then scanned at a height where it barely touches or “taps” the sample surface. The system monitors the probe position and vibrational amplitude to obtain topographical and other property information. Accurate topographical information can be obtained even for very fragile surfaces. Optimum resolution is about 50 Å lateral and <1 Å height.

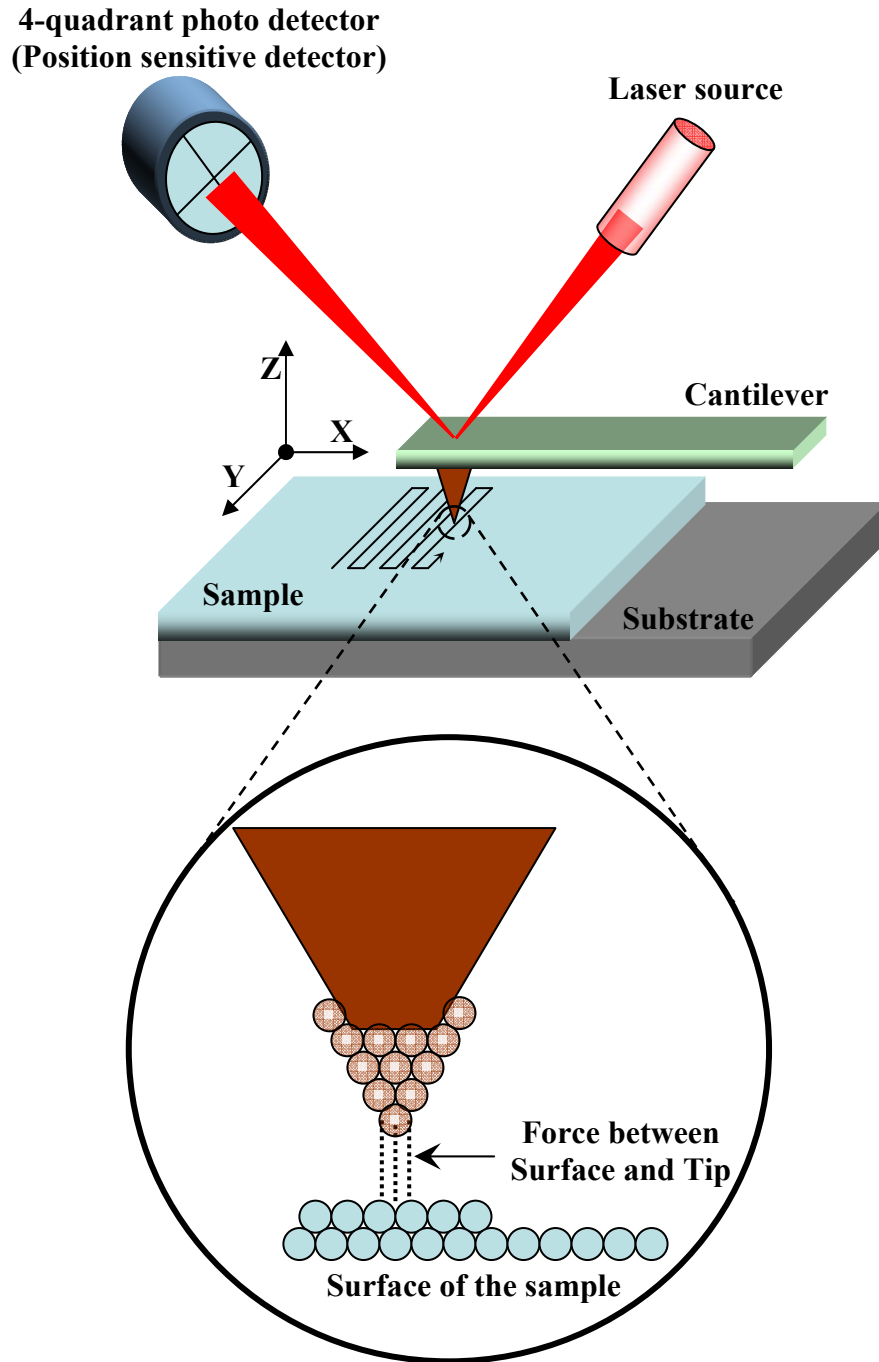


Fig. 2.11 Schematic diagram of AFM analysis. The deviations in the laser beam, due to the surface of the sample, imagine using the 4-quadrant position sensitive photo detector.

Magnetic Force Microscopy: The local variations in the magnetic forces at the sample's surface can be measured in the form of image. The probe tip is coated with a thin film of ferromagnetic material that will react to the magnetic domains on the sample surface. The magnetic forces between the tip and the sample are measured by monitoring cantilever deflection while the probe is scanned at a constant height above the surface.

2.2.4 Transmission and Reflection Measurements

Transmittance and reflection measurements of the samples are used to determine the band gap of semiconductor. The band-gap of the sample is determined by observing the wavelength at which the sample begins to absorb the transmitted light. In order to measure the absorption accurately, we must account for the entire light incident, reflected, transmitted or scattered by the sample. The schematic of optical characterization set up is shown in the Fig. 2.12.

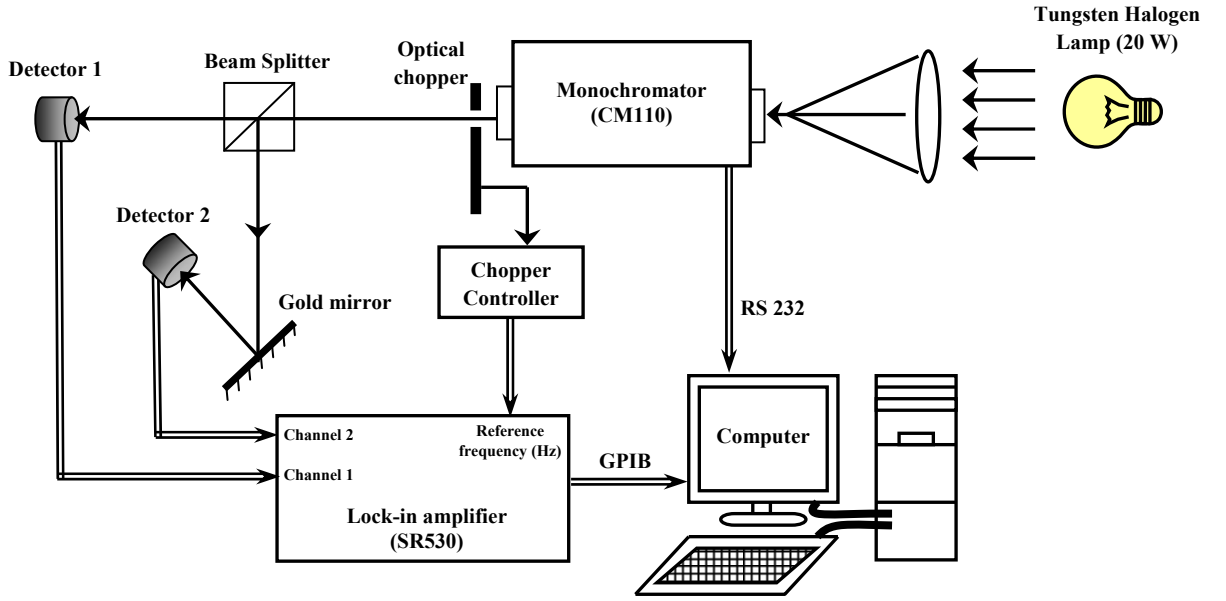


Fig. 2.12 Experimental set-up for transmission and reflection measurement of the thin film samples.

From the measurement of transmission and reflection of the thin films, the absorption coefficient (α) was calculated using the Lambert's law [38],

$$T = (1 - R)^2 \exp(-A) = (1 - R)^2 \exp(-\alpha t) \quad (2.3)$$

where, R is the reflectance, T is the transmittance, A is the absorbance, and t is the film thickness. For an absorbing material, the absorption coefficient is given by [39],

$$\alpha = \frac{1}{d} \ln \left(\frac{T}{[1 - R]^2} \right) \quad (2.4)$$

The absorption coefficient, α , for a direct transition is related to the band gap of a semiconductor and is given by [40]:

$$\alpha h\nu \propto (h\nu - E_g)^{\frac{1}{2}} \quad (2.5)$$

where $h\nu$ is the photon energy, and E_g is the energy gap. Using the above equation, the plot of $(\alpha h\nu)^2$ versus $h\nu$ gives the band gap of the material. For the band gap calculation of CIGS thin films we consider the reflection while for others i.e. CdS, i- and AZO only the transmission values are consider, as they are transparent.

2.2.5 Electrical Measurements

The van der Pauw technique of four-point probe measurement allows measurements of samples of arbitrary shape. Using four-point probe one can calculate the majority charge carrier density, n_s , and mobility, μ , of a semi-conducting sample as a function of temperature. The van der Pauw technique, due to its convenience, is widely used in the semiconductor industry to determine the resistivity of uniform samples [41]. The inventor, van der Pauw, uses an arbitrarily shaped, thin-plate sample containing four very small point-ohmic contacts placed on the periphery, extreme ends of the plate.

Resistivity Measurements

The van der Pauw configuration having a rectangular shaped sample is shown in Fig. 2.13. The objective of the resistivity measurement is to determine the sheet resistance, R_{Sh} . van der Pauw demonstrated that there are actually two characteristic resistances, R_A and R_B , related to the sheet resistance R_s through the van der Pauw equation,

$$R_A = \frac{(R_{21,34} + R_{12,43} + R_{43,12} + R_{34,21})}{4}, \text{ and} \quad (2.6)$$

$$R_B = \frac{(R_{32,41} + R_{23,14} + R_{14,23} + R_{14,32})}{4}$$

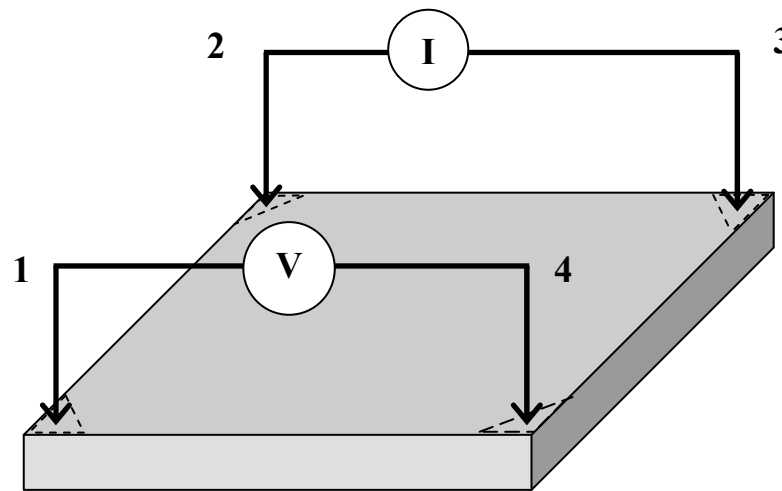


Fig. 2.13 Schematic of a van der Pauw configuration used in the determination of the two characteristic resistances R_A and R_B .

Using R_A and R_B , one can calculate the, R_{Sh} using the equation,

$$\exp(-\pi R_A/R_{Sh}) + \exp(-\pi R_B/R_{Sh}) = 1 \quad (2.7)$$

which can be solved numerically for R_S . The bulk electrical resistivity, ρ can be calculated using,

$$\rho = R_{Sh}d \quad (2.8)$$

For the measurement of resistivity and sheet resistance of CIGS and CdS thin film, we follow the Van der Pauw method. While for molybdenum (Mo) and ZnO thin film we used the four-point probe method.

In four-point probe method (Fig. 2.14), the separate current and voltage electrodes are used for eliminate the contact resistance between the electrodes and the material. In particular, in the case of thin films, the distance between the two probe(s) is very high compared to the film thickness (d), and hence the sheet resistance (Ω/\square) can be given as,

$$R_{sh} = k \frac{V}{I} \quad (2.9)$$

where, k is a constant dependent on the configuration and spacing of the contacts.

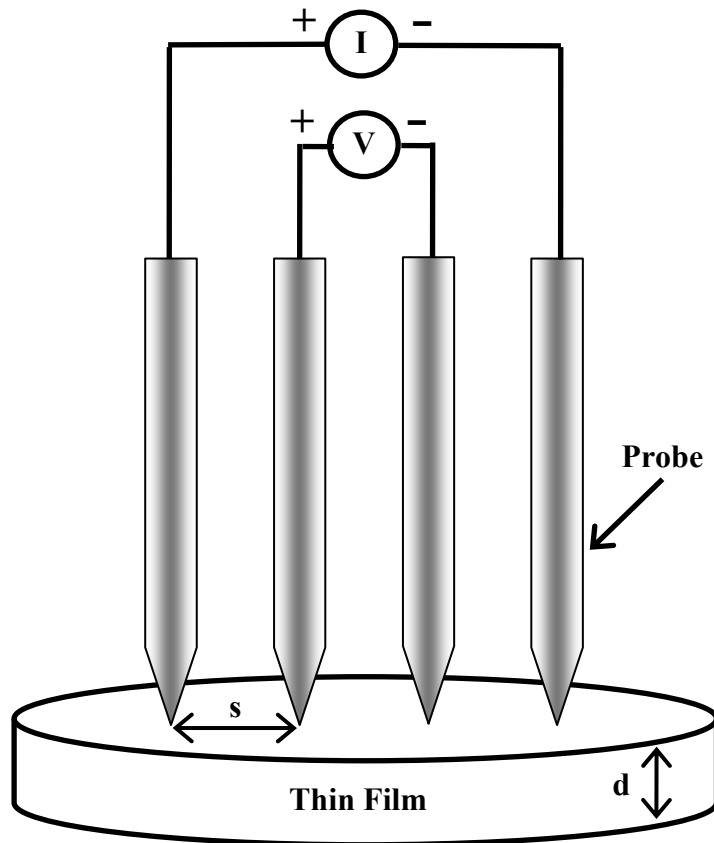


Fig. 2.14 Four-point probe arrangement for the measurement of sheet resistance of the thin film.

If the film is large in extent compared with the probe assembly and the probe spacing is large compared with the film thickness, then $k = \pi/\ln 2 = 4.53$. By using the Equations 2.8 and 2.9, we can find the resistivity of the thin film sample.

Hall-effect

A Hall-effect measurement, discovered by the Edwin Hall in 1879, is a valuable tool for material and device characterization [42]. Fundamentally, the Hall-effect can be observed when a combination of a magnetic field through a sample and a current along the length of the sample creates an electrical current perpendicular to both the magnetic field and the current. This creates a transverse voltage; perpendicular to both the magnetic field and the current (see Fig. 2.15). The fundamental principle is the Lorentz force, that is, the force on a point charge due to electromagnetic fields. The “right hand rule” allows determining the direction of the force on a charge carrier based on its direction of motion and the direction of the applied magnetic field.



Fig. 2.15 Illustration of Hall-effect, the hall voltage observed due to the Lorentz force.

Measuring the Hall-effect of the thin film the following equipments are required:

- Permanent magnet, or an electromagnet (500 to 5000 Gauss)
- Constant-current source with currents ranging from 10 μA to 100 mA; Must satisfy the, $I < (200R)^{-0.5}$, condition
- High input impedance voltmeter ranging from 1 μV to 1 V
- Sample temperature-measuring probe (resolution of 0.1 $^{\circ}\text{C}$ for high accuracy work).

The Hall voltage measurement consists of a series of voltage measurements with a constant current, I , and a constant magnetic field, B , applied perpendicular to the plane of the sample.

Conveniently, the van der Pauw sample geometry, as shown in Fig. 2.16, used for the Hall measurement.

To measure the Hall voltage V_H , a current I is forced through the opposing pair of contacts 1 and 3 and the Hall voltage $V_H (= V_{24})$ is measured across the remaining pair of contacts 2 and 4. From the hall voltage, the sheet carrier density n_s and hall mobility μ can be calculated. The procedure of the calculation is given below.

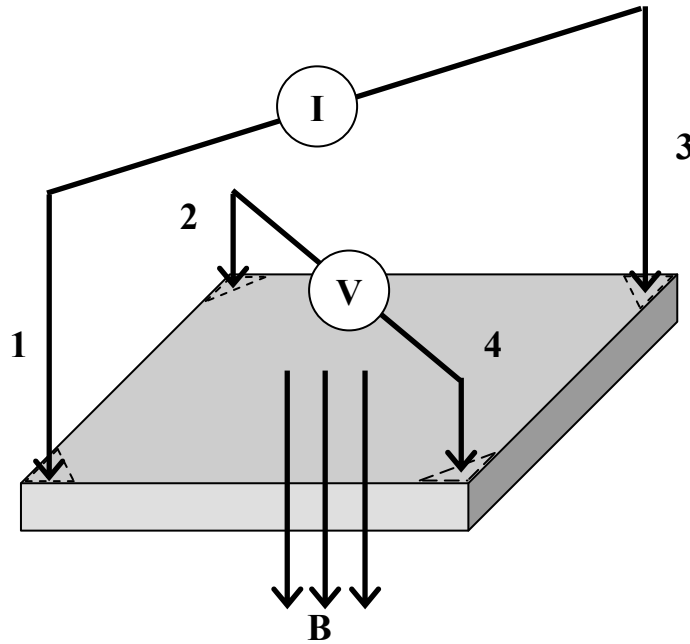


Fig. 2.16 Schematic of a Van der Pauw configuration used in the determination of the Hall voltage V_H .

Hall Calculations

Calculate the following (be careful to maintain the signs of measured voltages to correct for the offset voltage):

$$\begin{aligned} V_C &= V_{24P} - V_{24N}, \quad \text{and} \quad V_D = V_{42P} - V_{42N}, \quad \text{and} \\ V_E &= V_{13P} - V_{13N}, \quad \text{and} \quad V_F = V_{31P} - V_{31N} \end{aligned} \quad (2.10)$$

The sample type is determined from the polarity of the voltage sum $V_C + V_D + V_E + V_F$. If this sum is positive (negative), the sample is p-type (n-type). The sheet carrier density (in units of cm^{-2}) is calculated from,

$$p_s = |8 \times 10^{-8} I_B / [q(V_C + V_D + V_E + V_F)]| \quad (2.11)$$

If the voltage sum is positive. If negative than;

$$n_s = |8 \times 10^{-8} I_B / [q(V_C + V_D + V_E + V_F)]| \quad (2.12)$$

where B is the magnetic field in gauss (G) and I is the dc current in amperes (A). From the values of sheet carrier density (n_s) and sheet resistance (R_{sh}) the mobility (μ) of the sample is

$$\mu = 1/qn_sR_{sh} \quad (2.13)$$

where q = charge of the electron.

2.2.6 Current-Voltage (I-V) Measurements

We have developed the LabVIEW (Laboratory Virtual Instrument Engineering Workbench) controlled automation program for studying the solar cell I-V characteristics. The block diagram of experimental set-up used to measure solar cell I-V characteristics is shown in Fig. 2.17. The Metal Halide bulb (150 W) is used as an irradiation light source. Keithley 2420C source meter and 6^{1/2} digit Keithley 2000 multimeter are connected with computer using GPIB. The source meter and multimeter are configured in 4-wire configuration to eliminate the contact resistance value, which plays important role in terms of series resistance (R_s), and shunt resistance (R_{shu}) of the solar cell. The source meter capable to source and measure the voltage or current in the range of 200 mV to 60 V and 10 μ A to 3 A respectively. It can measure 1700 readings/second at 4-1/2 digits via GPIB. The light intensities at various distances from the source were measured with the help of solarimeter (CEL, India).

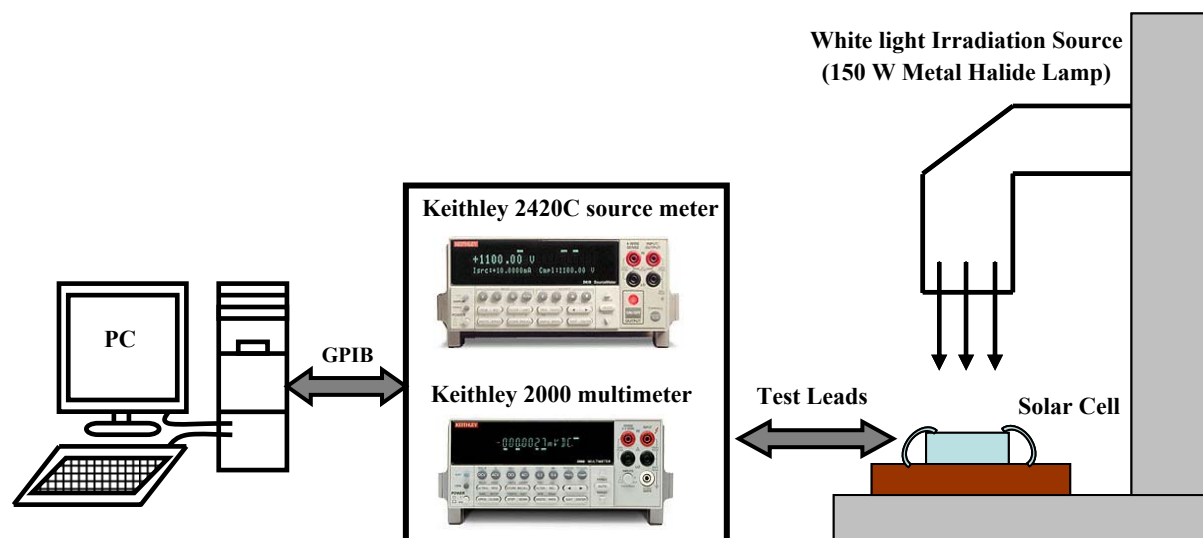


Fig. 2.17 The block diagram of the experimental set-up for the solar cell I-V characteristics measurement.

The basic idea of the developed LabVIEW program for the solar cell I-V characteristics is to minimize the direct irradiation time of metal halide bulb to the solar cell. As the irradiation time is more the temperature of the solar cell increases so, the V_{oc} of the solar cell decreases because of the widening the depletion region. The useful parameters like solar cell efficiency (η), fill-factor (FF), open-circuit voltage (V_{oc}), short-circuit current (I_{sc}),

series resistance (R_s), and shunt resistance (R_{shu}) were directly evaluated from the I-V characteristic of the solar cell in very short time compared to the manual measurement.

The LabVIEW program, shown in Fig. 2.18, is used for measuring the I-V characteristics of the solar cell. The LabVIEW program has two parts, one is the dark I-V measurements and the other one is illuminated I-V measurements. By selecting the dark I-V tab from the front panel of the LabVIEW program. In the dark I-V set the parameters i.e. the start voltage, stop voltage, voltage source delay, voltage source steps. By selecting the data save option we can save the data (in .txt format) as well as curves (in .jpg format). Before run the program, the solar cell placed in the dark environment. When the program run, according to the value of source voltage range, steps and delay the source meter source the voltage and measure the current and plot the I-V of the solar cell. The ideality factor, n , and reverse saturation current, I_0 of the solar cell found from those curves.

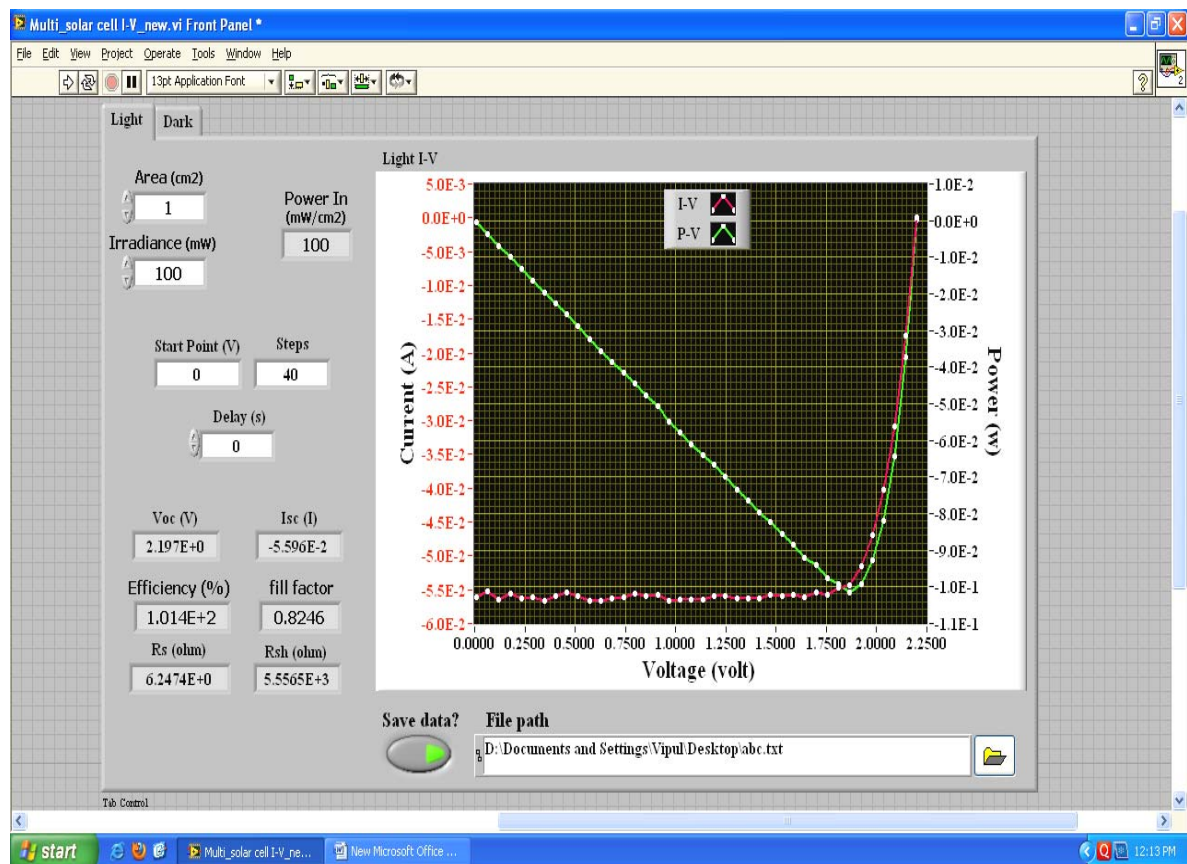


Fig. 2.18 The front panel of the LabVIEW program for the I-V measurements in light as well as dark environment.

For the illuminated I-V, the solar cell is kept under the solar irradiation source. As mention above we have used metal halide (150 W) as a light source. After adjusting the input power to the solar cell, i.e. whether AM 1.5 or AM 1, set it in the program and then set the parameters i.e. start voltage, voltage source delay, voltage source steps and the temperature of

the solar cell. Select the data save option and run the program. The graph of illuminated I-V and P-V was plotted and from those plots the program find the solar cell parameters i.e. like η , FF, V_{oc} , I_{sc} , R_s , and R_{sh} .

2.2.7 Spectral Response Measurements

Spectral response, i.e. Quantum efficiency (QE), measurements quantify the behavior of a device over a spectrum of light. In the generally, QE defined as ration of the optically generated electrons due to the monochromatic probe beam to the number of light photons incident.

$$QE(\lambda) = \frac{\text{No.of electrons collected}}{\text{No.of incident photons}} \quad (2.14)$$

A tungsten halogen lamp is used as the light source at the input slit of the monochromator. The output beam of monochromator is chopped with the optical copper and focused into a 0.4×0.4 cm area on the solar cell device. Using LabVIEW (Version 8.2) software, spectral response is measured in the range 350–1400 nm at 5 nm intervals at room temperature. Fig. 2.19 shows LabVIEW front panel for the measurement of spectral response.

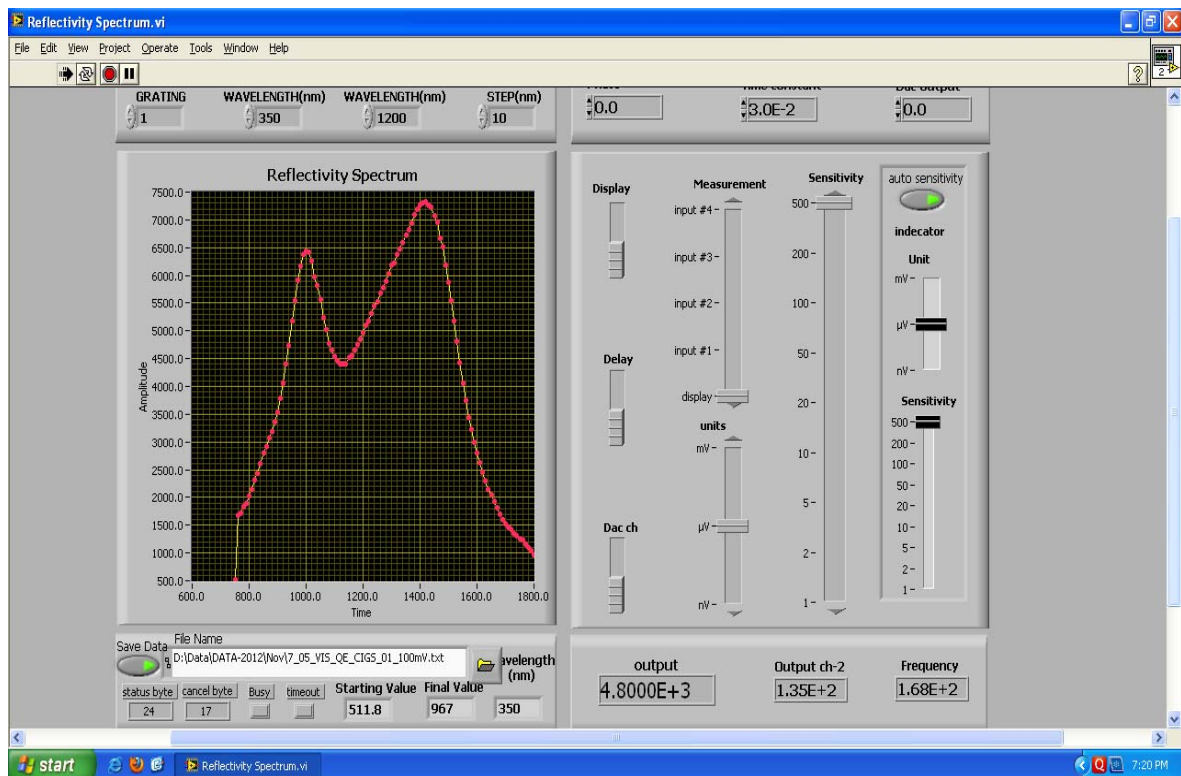


Fig. 2.19 The LabVIEW front panel for the measurement of spectral response of the solar cell.

In the measurement process, the computer records the currents produced by the test device and the monitor photodiode one by one for each wavelength in the test. Using the

power to current ratio previously recorded, it converts the monitor current to a beam power quantity. The ratio of test device current $I_{DUT}(\lambda)$ to beam power is the device responsivity.

$$QE(\lambda) = \frac{h \cdot c \cdot I_{DUT}(\lambda)}{e \cdot \lambda \cdot I_{STD}(\lambda) \cdot R_{STD}(\lambda)} \times 100\% \quad (2.15)$$

Where h is Plank's constant, c is the speed of light, e is the electron charge, $I_{STD}(\lambda)$ is the standard detector current, and $R_{STD}(\lambda)$ is the responsivity of the standard detector in W/A.

Chapter 3

Molybdenum Back-contact
Layer: Growth and
optimization

3 MOLYBDENUM BACK-CONTACT LAYER: GROWTH AND OPTIMIZATION

Molybdenum (Mo) thin films are most widely used as an ohmic back-contact for copper indium diselenide (CIS) and its alloy copper indium gallium diselenide (CIGS) based thin film solar cell. Radio frequency (RF) magnetron sputtering system is used to deposit Mo thin films on soda lime glass substrate. The deposition was carried out using argon (Ar) gas at different Ar controlled (working) pressures (1 to 10 mTorr) and at different RF powers (60 to 100 W). The influence of both the working pressure and the RF power on the Mo thin films was studied by investigating its structural, morphological, electrical, and optical measurements. The results reveal that a stress-free, low-sheet-resistance ($\sim 1 \Omega/\square$), and reflecting ($\sim 55\%$) Mo thin film grown at 1 mTorr working pressure and 100 W RF power.

3.1 NEED OF MOLYBDENUM BACK-CONTACT LAYER

Molybdenum (Mo) thin films are used as a back-ohmic contact widely in copper indium diselenide (CIS) and, its alloy, copper indium gallium diselenide (CIGS) thin film solar cells. The metallic back-contact, Mo, serves as substrate on which the absorber layer i.e., CIS/CIGS is deposited. Mo is more favorable as a back-contact layer in CIS and CIGS thin film solar cells because its diffusion into the absorber starts above 600 °C [43] and, in addition, it offers a resistance to alloying with copper and indium [44]. Studies on the deposition of the Mo thin films by radio frequency (RF) magnetron sputtering have been reported in the literature [45,46] and, recently, about 20 % energy conversion efficiency [47] has been reported for CIGS thin film solar cell. The adhesion property of the Mo thin film, which has direct impact on the film resistance, depends on the deposition parameters like RF power, working pressure, etc. Studies on the correlation between the working gas pressure and growth of the film have been reported in the literature [48, 49].

In the present work, the emphasis was to deposit Mo thin films using the RF magnetron sputtering to achieve a low resistive and a well adherent Mo thin film. In order to achieve the above requirements the RF power was varied from 60 to 100 W and the working pressure was varied from 1 to 10 mTorr. The structural, morphological, electrical, and optical properties of the Mo thin films were studied as a function of RF power and working pressure. Furthermore, the laser scribing of the molybdenum thin film having different thicknesses

were done and optimized the void free clean scribing condition, that will be use in future for the solar cell module preparation.

3.2 THIN FILM PREPARATION

Mo thin films were prepared on organically cleaned soda lime glass substrate (50 mm × 50 mm) by using the circular RF magnetron sputtering system, (Huttinger Elektronik 600 W, U.S.A.), at different working pressures and different RF powers. The distance between Mo target (2-inch diameter, 5 mm thick) and the substrate was 90 mm and the substrate's rotation was kept at ~ 40 rpm to obtain uniform film. The thickness was kept constant at 1000 nm for all deposition and it is measured in-situ by using a quartz crystal thickness monitor. The argon (Ar) gas was used as a sputtering gas, whose flow was controlled by the mass flow controller (MFC, AALBORG, Germany). The deposition of Mo thin films was carries out in vacuum coating unit (model - 15F6 HINDHIVAC, Bangalore, India).

The following process was used for the deposition of all Mo thin films. Initially, the chamber was evacuated to a base pressure close to 1×10^{-5} mbar. Then the Ar gas was introduced into the chamber using a needle valve. Using the Ar flow, we set the chamber pressure at a desired working pressure and, subsequently, by throttling the high vacuum valve the pressure was maintained at the desired value during the deposition process. Before initiating the actual deposition of Mo layer on soda lime glass substrate, the target was pre-sputtered for 5 minutes to remove surface contamination, if any. We have first grown Mo thin films by varying the working pressure from 1 to 10 mTorr and keeping the RF power constant at 100 W. Subsequently, the films were characterized to find out the optimum pressure; thereafter, the films were prepared at this optimum pressure by varying the RF power from 60 to 100 W. All prepared Mo thin films were characterized by GIXRD, AFM, four-point probe method, and optical reflectivity measurements.

3.3 EFFECT OF WORKING PRESSURES

3.3.1 Structural Characterization

The influence of the working pressure (1 to 10 mTorr) on the Mo thin films can be observed from the XRD spectra shown in Fig. 3.1, in terms of full width half maxima (FWHM) and the shifting of the 2θ value from its bulk value i.e., 40.05° . From the values of FWHM, the crystallite size (D), was calculated using the Scherrer's formula (Equation 2.2). The observed d-value of (110) plane for 1 mTorr is matched with the JCPDS data card 01-1208. By using

the d-value and the corresponding (hkl) value of the peak, the lattice constant, a, was derived from the relation [50],

$$d = \frac{a}{\sqrt{h^2 + k^2 + l^2}} \quad (3.1)$$

The variations in the value of a, and L is shown in Table 3.1. From the XRD spectra, shown in Fig. 3.1, the change in the FWHM of the (110) peak and the shifting of the 2θ value from its bulk value i.e., 40.05°, for the same peak are clearly noticeable.

The broadening of the FWHM and the shifting of 2θ value are both related to the structure defects in the films and so, indication of the stress present in the film. The stress is directly related to the lattice strain. The percentage of strain is determined from the lattice constant, a, [51],

$$\text{strain}(\%) = \frac{\Delta a}{a_0} \times 100 \quad (3.2)$$

where a_0 = bulk lattice constant of Mo = 3.1469 Å, and Δa = difference between the lattice constant of observed Mo thin film and the bulk Mo. Knowing the strain, we can estimate the isotropic stress [52],

$$\sigma = \frac{E}{2\nu_f} \times \frac{a_0 - a}{a_0} \quad (3.3)$$

where, E is the Young modulus and ν_f is the Poisson ratio.

For the calculation of the stress, we have used the bulk values of E and ν_f viz. $3.36 \times 10^{11} \text{ Nm}^{-2}$ and 0.298, respectively [53]. The values of crystallite size, D, lattice constant, a, percentage strain, estimated stress, 2θ angle and its corresponding d-values for Mo thin films grown at different working pressures are tabulated in Table 3.1. At lower working pressure (1 mTorr) the highest crystallite size, 14.3 nm, was observed, which shows the improvement in the crystallization of the Mo thin films.

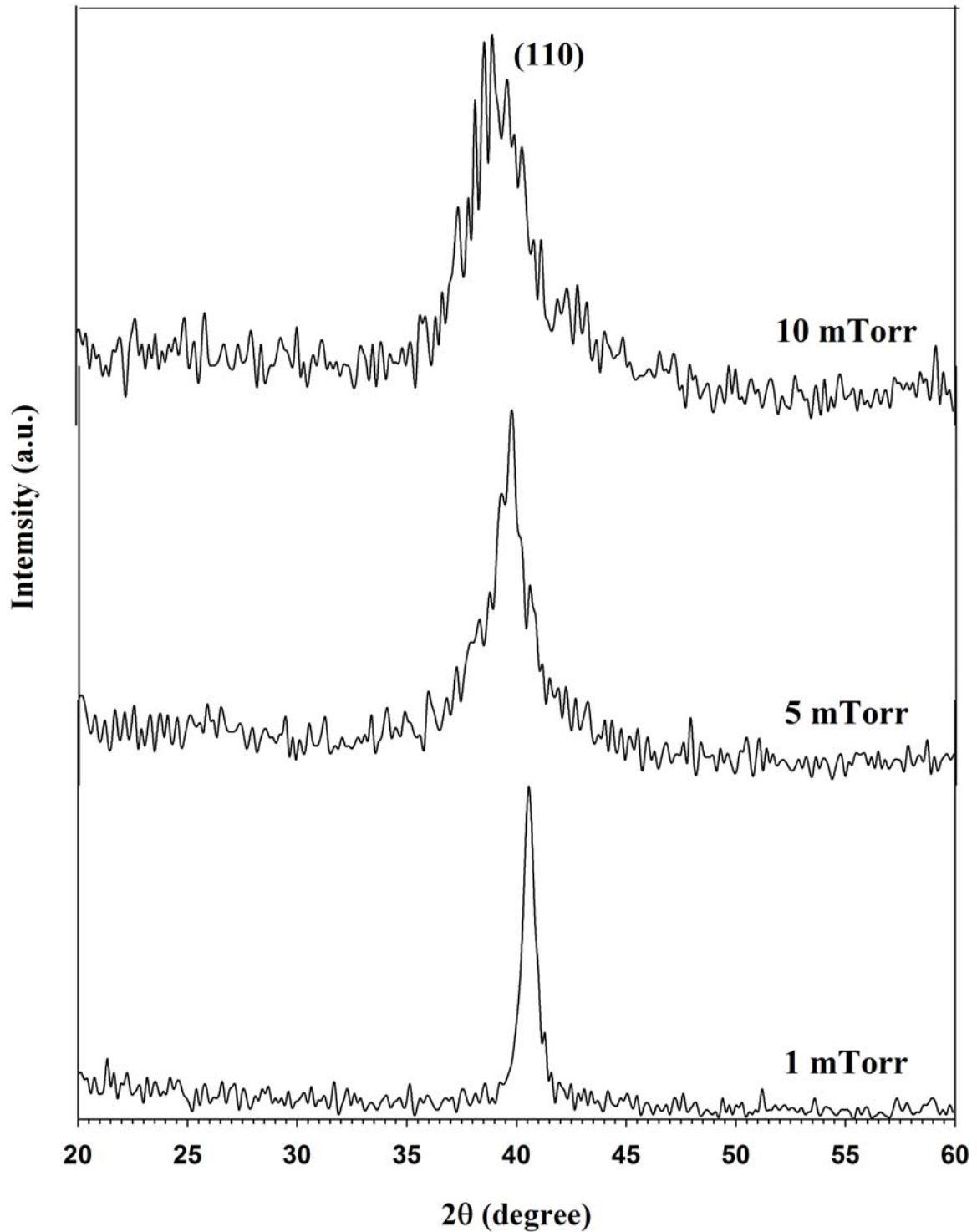


Fig. 3.1 The XRD spectra of the Mo thin films grown at different working pressures (from 1 to 10 mTorr) and a constant RF power (100 W) show that by increasing the working pressure the crystallinity of the Mo thin film degrades due to the decrease in the deposition rate.

During the deposition of the thin films, the strain or stress arises from the incomplete process of structural ordering occurring during the film growth and may be due to the substrate contamination. The grain growth process in the film mainly depends on the deposition or condensation rate and the deposition temperature.

Table 3.1 The 2θ value of the (110) plane, its corresponding d-value, crystalline size, L, and lattice constant, a, of Mo thin films grown at different working pressures by keeping the RF power constant at 100 W.

Working Pressure (mTorr)	d-value (Å)	2θ (degree)	Crystalline size, D, (nm)	Lattice constant, a, (nm)	Strain (%)	Stress ($\times 10^9$ Nm ⁻²)
1	2.22174	40.572	14.32	0.314	0.1562	0.88
5	2.27067	39.661	5.67	0.321	2.0427	-11.51
10	2.33142	38.586	3.77	0.329	4.7728	-26.90

By varying the working pressure, the deposition rate varies. At lower pressure, at 1 mTorr, the collisions of the sputtered particle with the gas will be reduced and therefore the deposition rate higher ~ 0.32 nm/s in our case. Owing to this, the sputtered particles with its improved energy reduce its arrival angle to the substrate. Thus, the possibility of the formation of inter-granule void reduces, which, in turn, results in the dense structure of the grains and hence the improvement in the crystallinity of the film [52]. The higher crystallite size, 14.32 nm, due to the dense microstructure of the film was observed at 1 mTorr working pressure shown in Table 3.1.

On the other hand, at a higher pressure, greater than 5 mTorr in our case, due to the multiple collisions of the sputtered particle with the gas, the deposition rate is reduced, ~ 0.23 nm/s at 5 mTorr and ~ 0.15 nm/s at 10 mTorr. This leads to a reduction in the energy of the sputtered particle as well as an increase in the average angle of arrival at the substrate. This results in the formation of porous grain growth and inter-granule voids. This deformation of the crystallinity of the film leads to an increase in the lattice constant and thus introduces strain in the film. In addition, the crystalline size reduces to 5.67 to 3.77 nm, as the working pressure increases from 5 to 10 mTorr respectively.

The stress values, as obtained by solving Equation 3.3, for different lattice constants of Mo thin films, which are grown at different pressures, are tabulated in Table 3.1. For pressures greater than 1 mTorr the value of lattice constant is lower than the bulk value, i.e. 0.314 nm, due to which the grains of the film experience a tensile force between them. The negative and positive signs in Table 3.1 indicate a compressive stress and a tensile stress, respectively. The stress in the film does not allow the grains to accumulate uniformly to the surface of the substrate. In our case, we experienced that at greater than 5 mTorr pressure, due to the considerably low deposition rate, the grains were not conglomerate together, and formed a surface having pinholes or scratch-like morphology.

3.3.2 Morphological Characterization

The study of the surface morphology of the RF magnetron sputtered Mo thin films was carried out using AFM. Figure 3.2 shows the AFM images of Mo thin films grown at different working pressures (1 mTorr to 10 mTorr) by keeping the RF power constant at 100 W. From the AFM images, we observe that the average grain size, and hence the surface roughness, decreases as the working pressure increases. As a result, the surface homogeneity is degraded and becomes porous. At 10 mTorr pressure, the ‘scratch-like’ appearance of the film surface having a surface roughness 1.87 nm was observed. This observation, as already analyzed by GIXRD measurements, is due to the lower deposition rate. By lowering the working pressure, viz. ~1 mTorr, due to the higher deposition rate, a uniform surface morphology is observed which has a higher surface roughness viz. 7.78 nm.

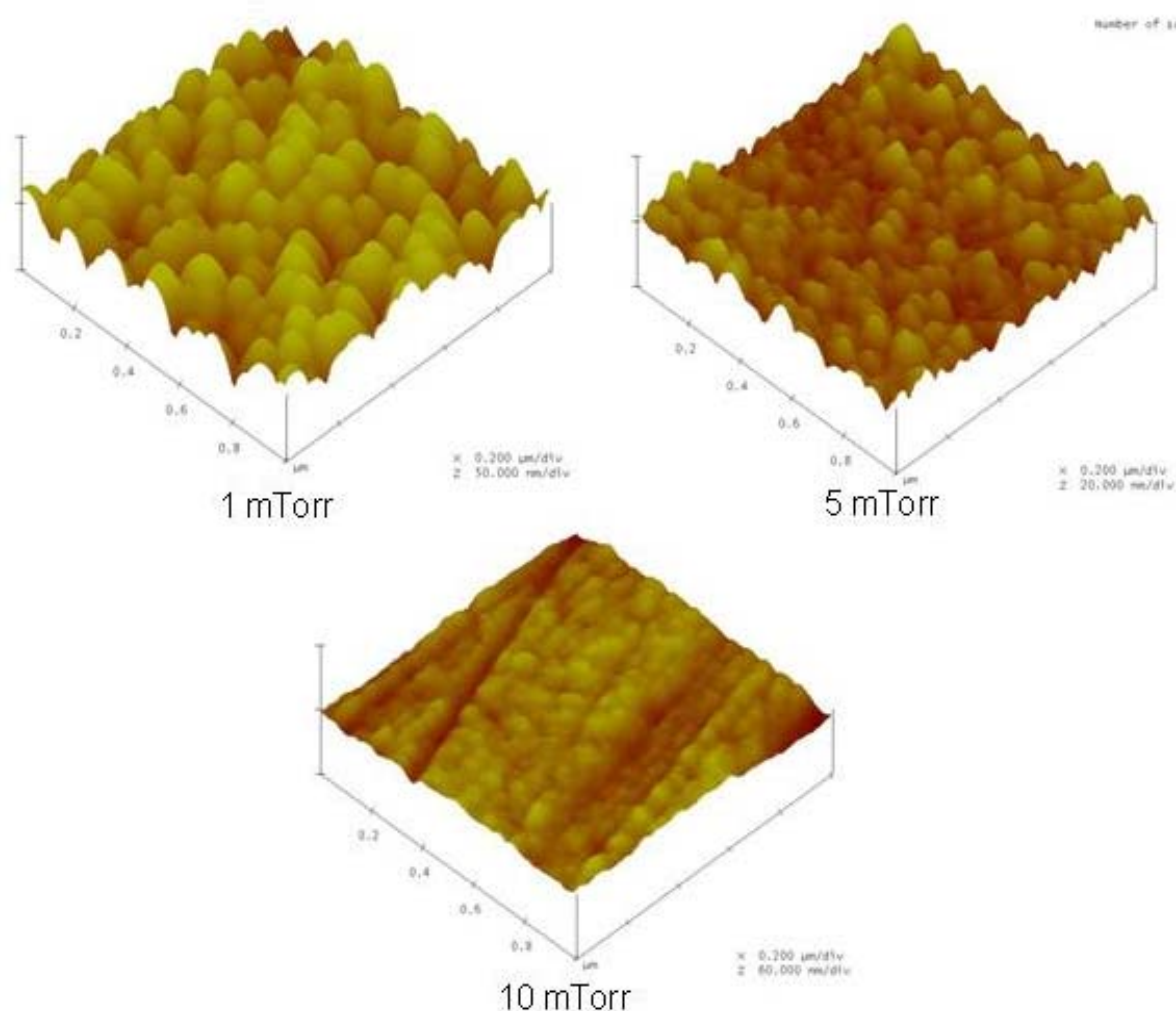


Fig. 3.2 The AFM images of Mo thin film at different working pressures from 1 to 10 mTorr shows that by reducing the working pressure from 10 to 1 mTorr, the uniformity in the grain coalescence improves significantly.

3.3.3 Electrical and Optical Characterization

The sheet-resistance is a crucial parameter in the application of the solar cell. Minimum sheet-resistance of Mo thin film gives minimum series resistance of the solar cell and that, in turn, improves the final efficiency of the solar cell. Figure 3.3 shows the sheet resistance, using the four-probe technique, of the Mo thin films deposited at different working pressures.

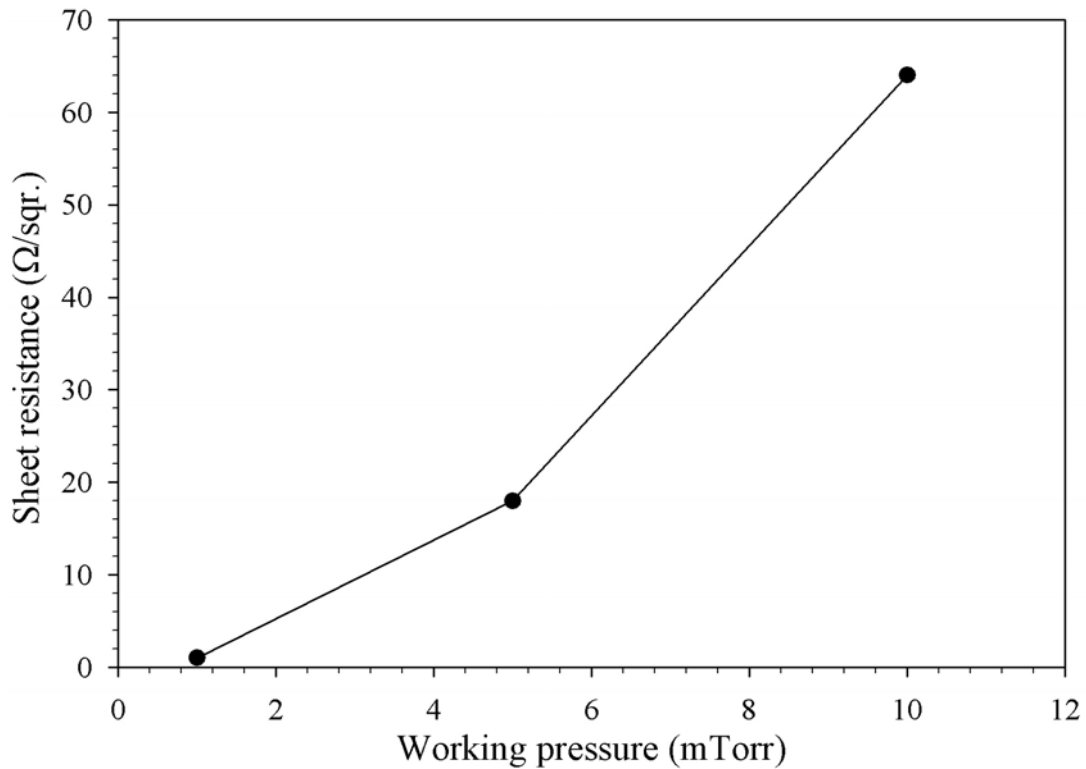


Fig. 3.3 The sheet-resistance of Mo thin films at different working pressures by keeping the RF power constant at 100 W, which shows that at lower working pressure viz. 1 mTorr, the sheet-resistance is lowest.

Increasing the sheet-resistance as increasing the working pressure is shown in Fig. 3.3. At higher sputtering pressure is a direct result of the sputtering induced porous structure that has a greater number of grain boundaries [54] (as observed from the AFM results) compared to the lower working pressure Mo thin film. As we move towards the lower pressure, the porosity reduces and hence the sheet-resistance decreases. The sheet-resistance at 1 mTorr working pressure and 100 RF power was $\sim 1 \Omega/\square$.

In the optical study, we have measured the reflectivity of the Mo thin film, shown in Fig. 3.4, for film grown at different working pressures by keeping the RF power constant at 100 W. The optical reflectivity plays an important role in the solar cell application. Highly reflective back-contact improves the absorption in the absorber layer. At 1 mTorr working pressure we observed highly reflective silvery white Mo thin films. By increasing the

working pressure isolated columnar crystallites, can be observed from the AFM images, reduces the optical reflectance. J.A. Thornton et al., [55] observed a similar kind of response of Mo thin film deposited at different working pressure.

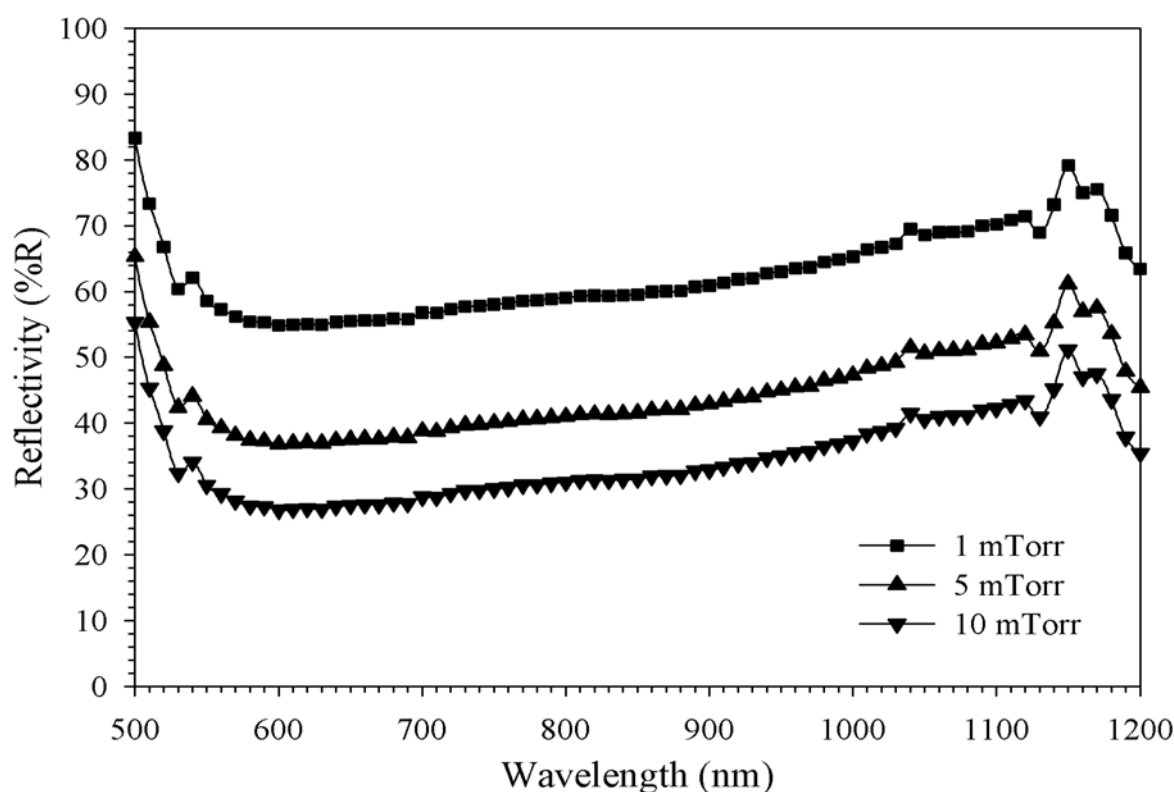


Fig. 3.4 The optical reflectivity of Mo thin films at different working pressures indicates that due to the improvement in the surface uniformity at lower working pressure viz. 1 mTorr, the surface scattering reduces and the reflectivity improves.

3.4 EFFECT OF RF POWER

3.4.1 Structural Characterization

After observing better structural, optical, and electrical properties of the Mo thin film grown at 1 mTorr working pressure, the RF power was varied from 60 to 100 W by keeping the working pressure constant at 1 mTorr. The XRD spectra of Mo thin films grown at different powers keeping the Working pressure at 1 mTorr are shown in Fig. 3.5.

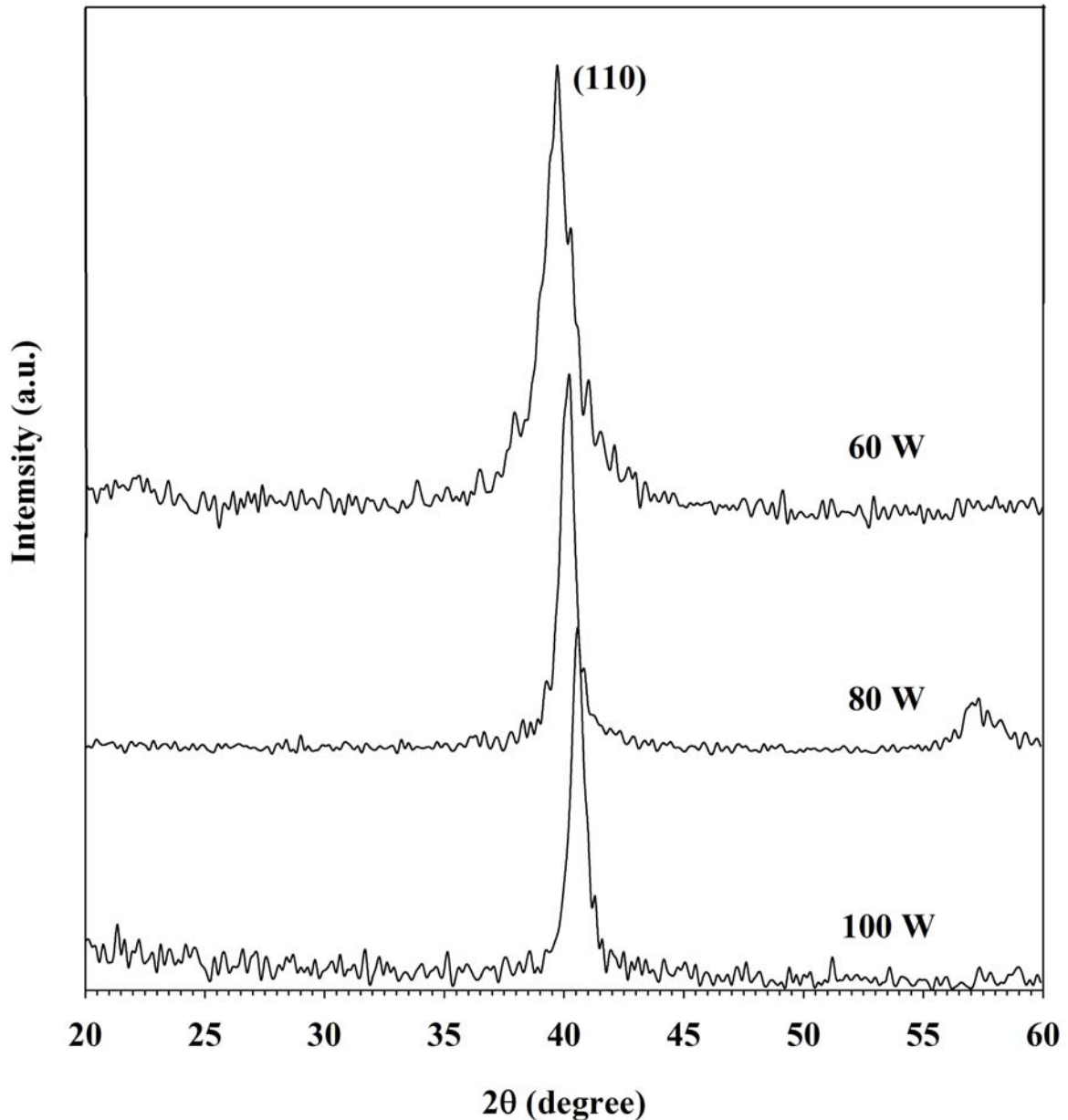


Fig. 3.5 The XRD analysis of the Mo thin films grown at different RF power by keeping the working pressure constant at 1 mTorr. At 100 W RF power and 1 mTorr working pressure, the negligible shift in the 2θ angle from its bulk value, 40.05° , this shows that a minimum strain is present in the Mo thin film.

The XRD spectra shown in Fig. 3.5 indicate a preferred orientation along the (110) plane and observed d-values matches with the JCPDS data card 01-1208. 2θ angle shift to a lower angle for the Mo film grown at lower RF power indicates the strain, and therefore, the stress introduced in the film. In addition, by reducing the RF power, the FWHM increases, which indicates that the crystalline size reduces to 8.47 nm due to the lower kinetic energy of the sputtered particles hence lower deposition rate. Table 3.2 shows the 2θ value of the (110) plane, its corresponding d-value, crystalline size, lattice constant, percentage of strain, and the estimated stress of Mo thin films grown at different RF power by keeping the Working pressure constant at 1 mTorr.

Table 3.2 The 2θ value of the (110) plane, its corresponding d-value, crystalline size, lattice constant, strain, and estimated stress of Mo thin films grown at different RF power by keeping the working pressure constant at 1 mTorr.

RF power (W)	d-value (Å)	2θ (degree)	Crystalline size, D (nm)	Lattice constant, a, (nm)	Strain (%)	Stress ($\times 10^{-9}$ Nm ⁻²)
100	2.22174	40.572	14.32	0.314	0.1562	0.88
80	2.24344	40.163	14.06	0.317	0.8100	-4.5
60	2.27387	39.603	8.47	0.321	2.1800	-12.29

By reducing the RF power from 100 W to 60 W, the deposition rate decreases from ~ 0.32 to ~ 0.28 nm/s respectively. Due to the reduced scattering of the sputtered atoms at lower power, at 60 W, with the gas atoms, the crystallinity degrades. Thus, the strain in the Mo film increases. At higher RF power (100 W) due to the increase in the deposition rate, ~ 0.32 nm/s, the crystallinity of the film improves and the strain reduces.

3.4.2 Morphological Characterization

The AFM morphology of Mo thin films grown at 1 mTorr working pressure and different RF powers viz. from 60 W to 100 W is shown in Fig. 3.6. At lower RF power, viz. 60 W, due to the lower deposition rate the grain growth is not uniform. The surface roughness of Mo thin films is 3.45 nm for 60 W RF power. As the RF power increases from 60 W to 100 W, the deposition rate increases, which leads to the improvement in the uniform grain growth and so, the surface roughness improves and reach to the 7.78 nm.

3.4.3 Electrical and Optical Characterization

The sheet-resistance of Mo thin film decreases as the RF power decreases. The sheet-resistance mainly depends on the surface morphology of the film. The AFM results confirm that the porosity increases as the RF power reduces from 100 W to 60 W, which increases the sheet-resistance of the Mo thin film shown in Fig. 3.7. At 1 mTorr working pressure and 100 W RF power we got the minimum sheet-resistance viz. $\sim 1 \Omega/\square$.

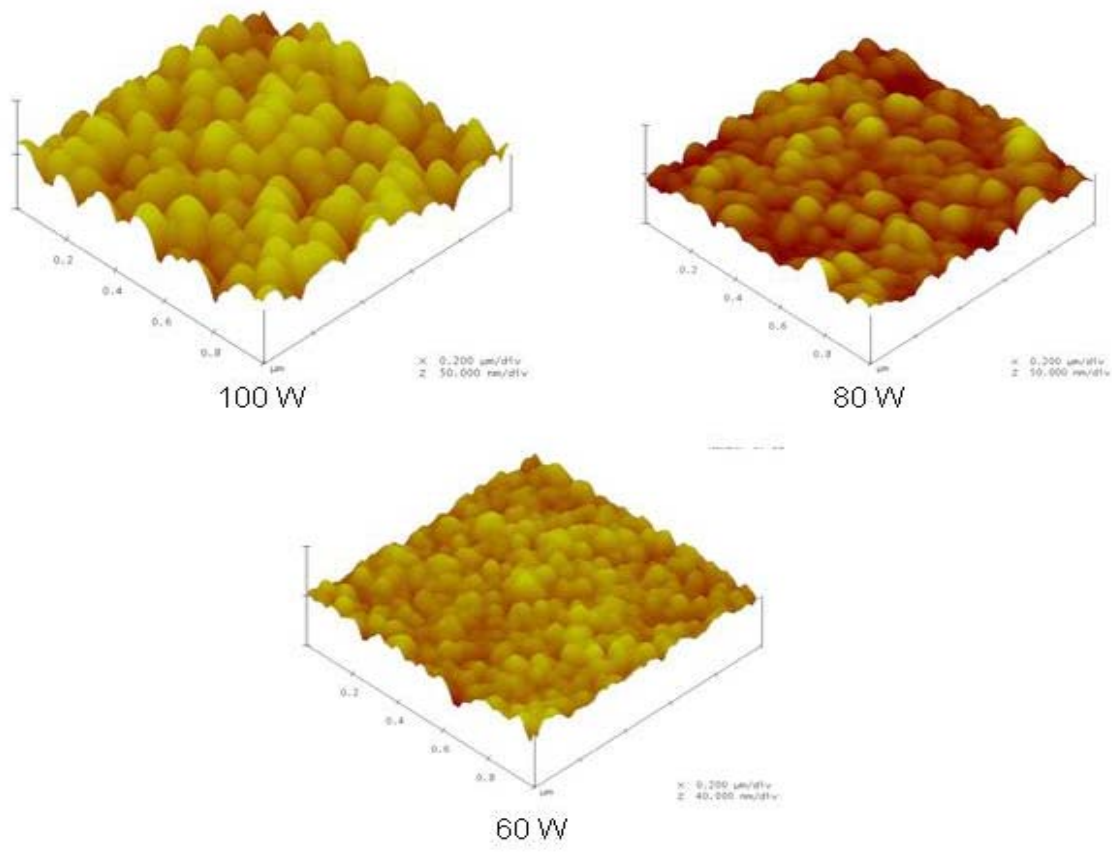


Fig. 3.6 The AFM images of Mo thin film at different RF power, by keeping the working pressure 1 mTorr, indicate that by increasing the RF power the film surface becomes dense and relatively uniform due to the increase in the deposition rate.

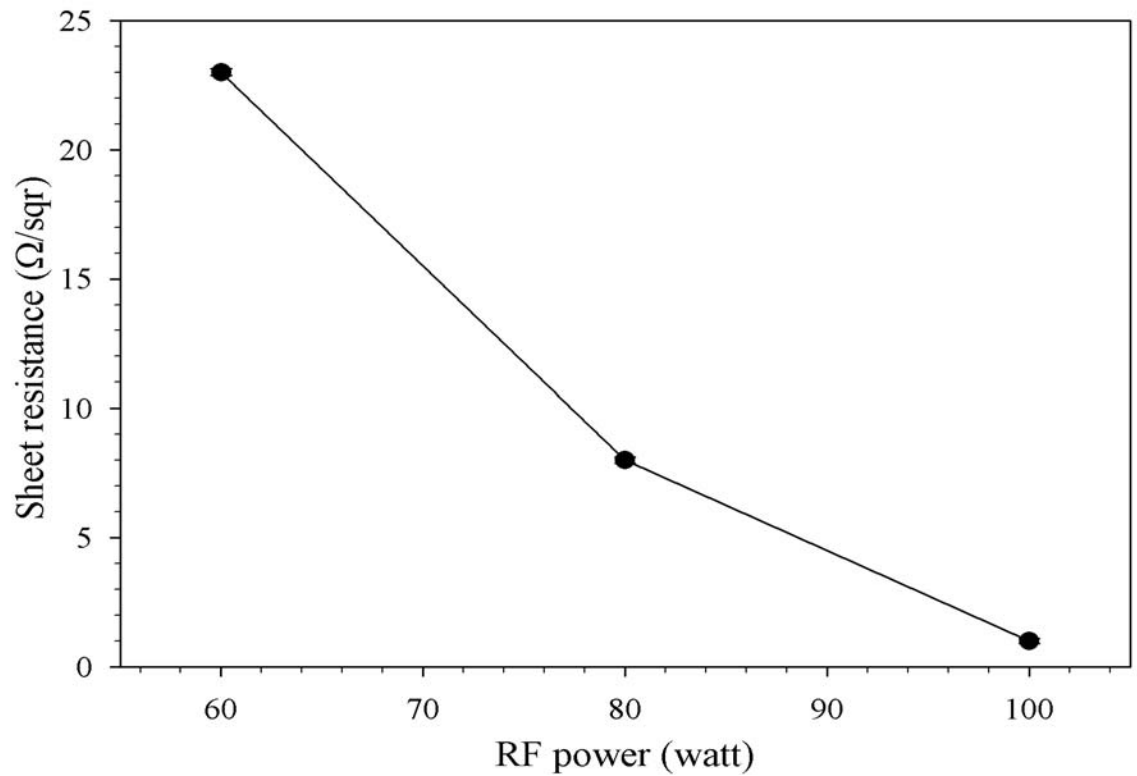


Fig. 3.7 - The sheet-resistance of Mo thin films deposited at different RF power by keeping the working pressure constant at 1 mTorr. At higher power the films shows a lower sheet-resistance because of the dense grain structure of the film.

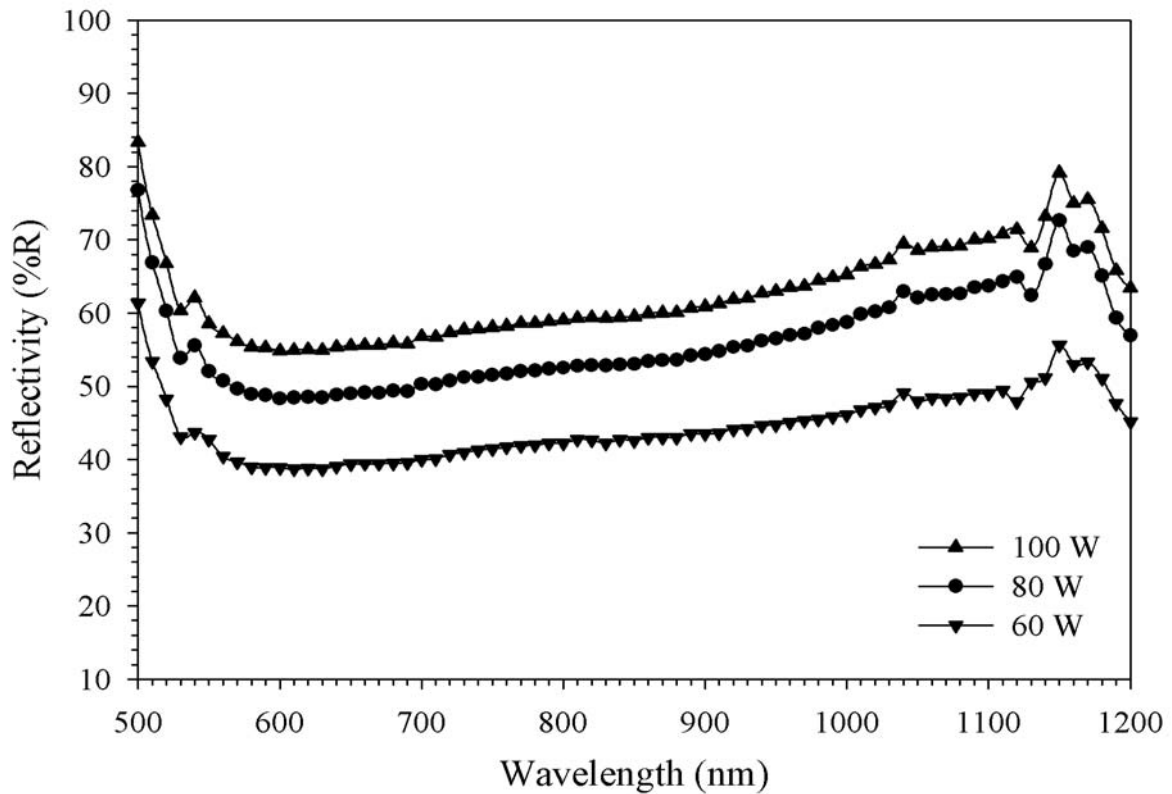


Fig. 3.8 - The optical reflectivity of Mo thin films grown at different RF power, by keeping a constant Working pressure at 1 mTorr, suggests that at a relatively higher RF power, due to a uniform surface structure, the reflectivity is higher compared with that at other RF power.

In the optical reflectivity, here, by reducing the RF power, the columnar crystallites isolates, observed from the AFM images, which reduces the optical reflectance shown in Fig. 3.8. Owing to a uniform distribution in the grains, the Mo thin film grown at 100 W RF power shows a higher reflectance (~ 55 %).

3.5 LASER SCRIBING OF MOLYBDENUM THIN FILM

The first step in manufacture of thin film solar cell is the deposition of molybdenum (Mo) as a back-contact layer on soda lime glass substrate and the next step is the isolative laser scribing of this layer for making a metal back contacts between the layers. However, the problems arise with a heat-affected zone around the scribed area due to the laser pulse beam [56]. The scribing should be done in such a way so that the scribed line should not contain bridges or process residue in the grooves that could cause an electrical connection and short-circuit the cell [57]. To increase the solar cell efficiency, the scribing of Mo layers desire minimum scribed area to have maximum active solar cell area [58] and so, minimize the dead area in the cell. Optimum operation for thin-film PV materials has been investigated by several PV manufacturers [59, 60, 61].

In this study, we present the results regarding the optimization of isolative laser scribing of sputtered-Mo thin-film deposited on soda lime glass substrate. The optimization process is performed by varying different laser parameters and thickness of the Mo thin-film in order to achieve lowest resistivity films. The result of successful scribing yields reliable, reproducible clean scribes without any presence of the buckling, ridges, or collars in the scribed areas.

Scribe Quality

However, the good results were extremely rare and seemed to occur within a process window of miniscule proportions. During the extensive experimentation only a handful of 40 μm scribes were achieved with good results. Nonetheless, the excellent quality of these scribes invite to speculation as to whether some alterations could be made to the system in order to achieve such scribes. Scribe results are often terrible, with big shards and cracks. The high energy scribe results that are referred to as good on the other hand are not square. Viewed from the top they have a typical pulse-to-pulse appearance of slightly overlapping circular holes. If the work-piece speed is too high the pulses will loose their overlap and bridges will occur. If the work piece slows down the “lips” that protrude into the scribe tend to flake up more readily.

In order to achieve a better quality of the scribe line we vary the laser power and pulse frequency for the different thickness of the Mo thin films. Ablation with a train of laser pulses per spot defines the scribe quality. Theoretically, the pulse train of the laser scribe the material is shown in Fig. 3.9. Some calculations were made in order to establish the geometrical situation [62] during the laser pulse.

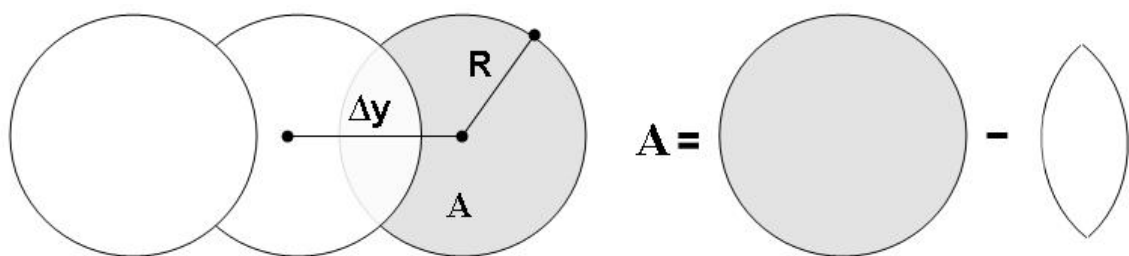


Fig. 3.9 Geometrical representation of exposed area.

Given that the laser spot has a radius, R , and is repeated with a frequency, f , onto a sample that is moving with the speed, v , one can express the surface area A of each consecutive pulse as the spot size minus the overlap of pulses (see Fig. 3.9). This area can be considered as the area of film removed per pulse [63].

$$A = \pi R^2 - 2 \left(R^2 \arccos\left(\frac{\Delta y}{2R}\right) - \frac{\Delta y}{2} \sqrt{R^2 - \frac{\Delta y^2}{4}} \right) \quad (3.4)$$

where Δy is the distance between consecutive pulse centres.

$$\Delta y = v \times \frac{1}{f} \quad (3.5)$$

Laser Scribing Process and Parameters

The processes of laser scribing of Mo thin-films were done using commercially available the laser system that has the multi diode pumped fiber laser (20 W average maximum power). Mo thin films used for the scribing have a different thickness from 60 nm to 800 nm. Mo thin films were deposited by RF magnetron sputtering at 1mTorr working pressure and 100 W RF power. The electrical property viz. sheet resistance of the Mo thin films was measured using four point probe method. The laser system, which was used for the scribing of Mo thin film, has a specification shown in Table 3.3. In our study we have kept the scribing speed constant at 500 mm/s in order to achieve fine scribed width. Scribing process of Mo thin film was optimized by varying both the laser power and the pulse frequency simultaneously. First keeping the maximum average power 20 W and varying the pulse frequency from 1 to 80 Hz to get the optimum pulse frequency and by using that, vary the average power up to minimum of 1 W. Different thickness of the Mo film shows different kind of scribe pattern. The smoothness of the scribed was observed using a polarization microscope (LABOURLUX 11, Leitz).

Table 3.3 Laser system parameters which are used for the scribing the Mo thin films.

Laser	Multi Diode Pump Fiber Laser
Nominal average power	20 W (optional 10 W)
Maximum peak power	>7.5 Kw
Power tunability	10 - 100%
Pulse repetition rate	20 - 80 KHz
Wavelength	1060 ± 10 nm
Pulse duration@20 kHz	<120 ns
Power stability	>95 %
Pulse energy@20 kHz	1 mJ
Beam quality	1.5 (M²)
Output beam diameter (1/e ²)	9 mm
Scribe speed	upto 1000 mm/s
Inbuilt guide (marking) laser	He-Ne laser (660 nm and 0.5 mW)

Optimization of Minimum Scribe Line Width

The scribed line width, which is an important parameter in the patterning of the semiconductor single- or multi-layers, is mainly dependent on laser power and pulse frequency. Laser power varies in this study from 20 W to 2 W and the pulse frequency varies from 1 Hz to 80 Hz. Figure 3.10 shows the obtained comparative results of the scribed line of Mo thin film (60 nm) by varying the laser power and pulse frequency. By increasing the laser power and laser pulse frequency the scribed line width increases. For higher laser power i.e. 20 W, the width of the scribed line was 240 μm at 1 Hz pulse frequency and 390 μm at 80 Hz pulse frequency, while at lower laser power i.e. 2 W, the width of the scribed line was near to 80 μm .

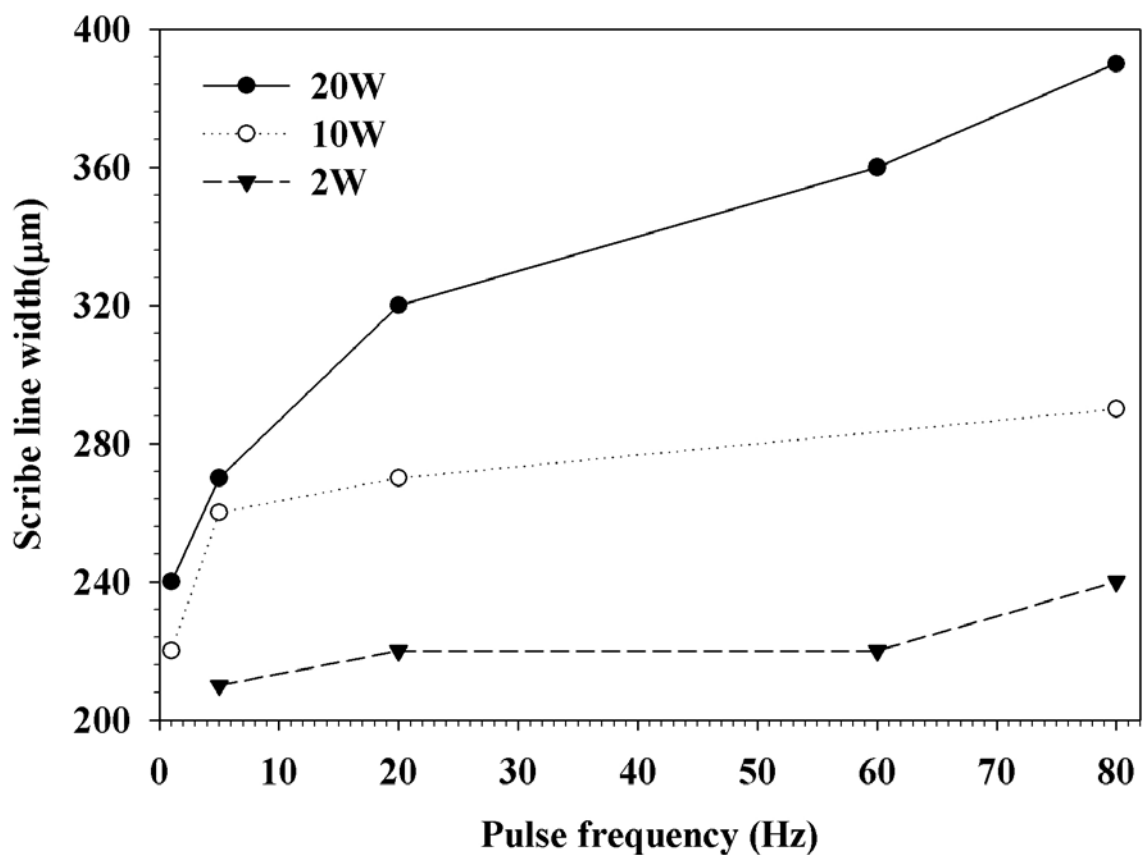


Fig. 3.10 The variation of the scribed line width of Mo thin film (60 nm) as a function of laser pulse frequency shows that as the laser power and the pulse frequency were set at minimum level, the scribe line width is lower.

The scribed line width should be kept minimum for its future use in patterning the different semiconductor devices. From Fig. 3.10, at 2 W laser power and 1 Hz pulse frequency we get the minimum scribe width i.e. 210 μm . The 210 μm is still a higher value. Therefore, by using the optimal laser parameters for 60 nm Mo film thickness i.e. 2 W laser power and 1 Hz pulse frequency we scribed the higher thickness of Mo thin film.

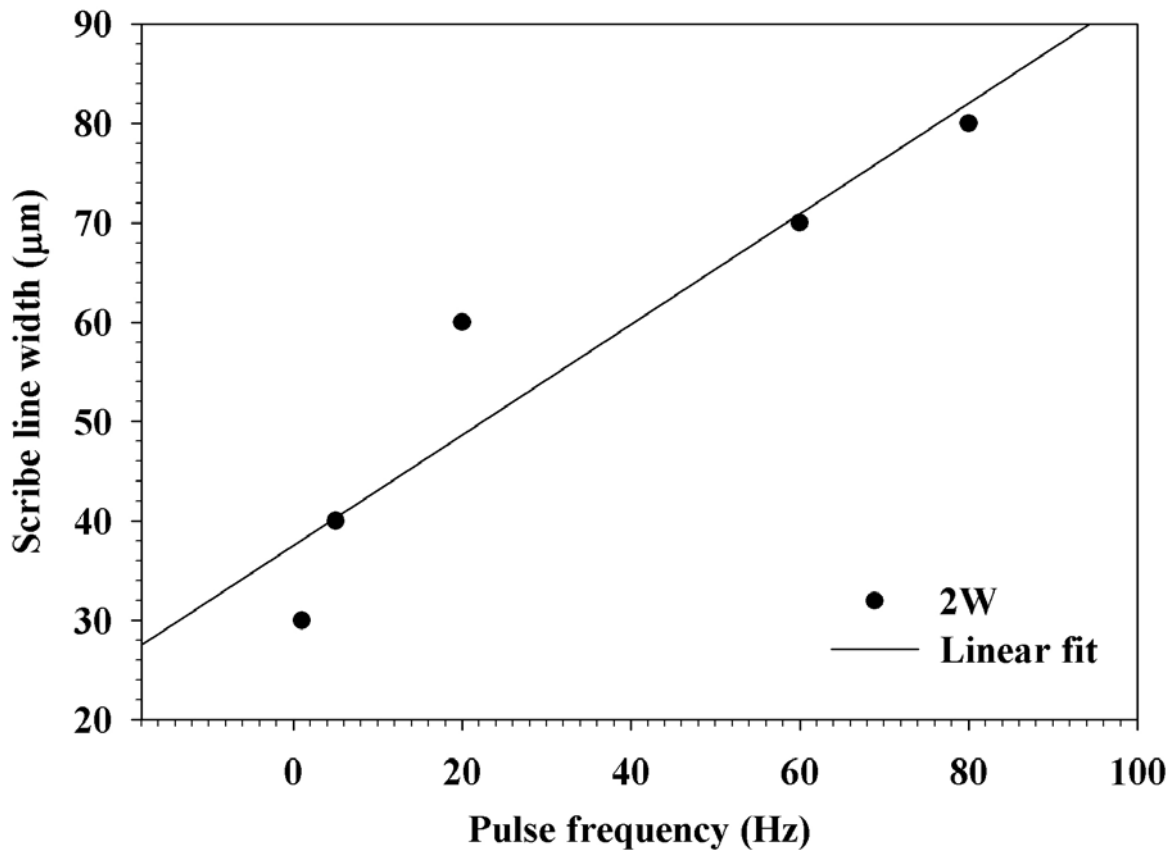
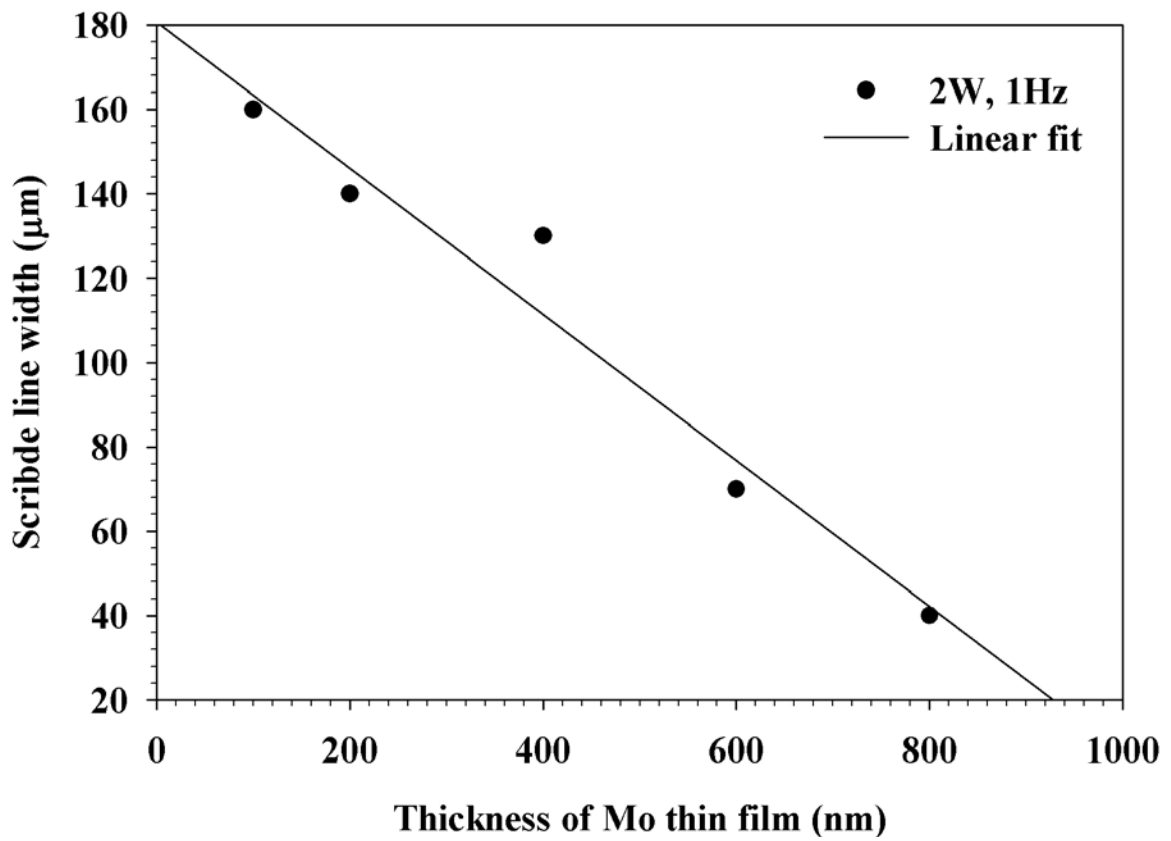


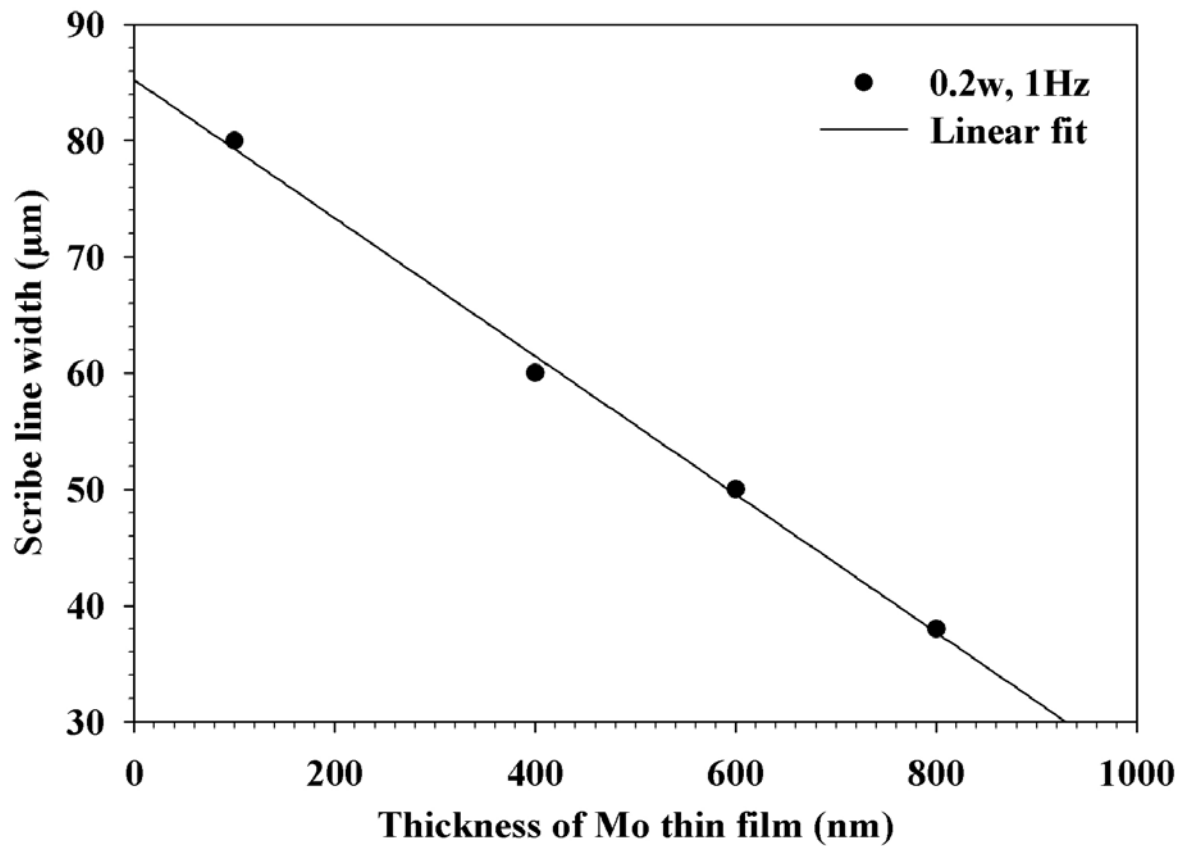
Fig. 3.11 The variation of the scribed line width of Mo thin film (800 nm) as a function of laser pulse frequency shows that as the pulse frequency was reduces; the scribe line width is decreases.

Figure 3.11 show the variation in the scribe line width as a function of pulse frequency. In this scribing, we found that as the pulse frequency reduces the scribe line width reduces. The minimum scribing width was 30 μm for 2 W laser power and 1 Hz pulse frequency. We had also scribed the different thickness of Mo thin films at 2 W laser power and 1 Hz pulse frequency and got a similar kind of variation. From that variation, we can say that as the thickness of the Mo thin films increases the scribed line width decreases, too, as shown in Fig. 3.12.

At low power (2 W) and low frequency (1 Hz) we have achieve the minimum scribe line width i.e. 40 μm (Fig. 3.12 (a)). In order to achieve lowest scribe line width without any presence of walls and collars in the scribed area, we scribe the higher thickness Mo films at 0.2 W laser power and 1 Hz pulse frequency, as shown in Fig. 3.12 (b). At 0.2 W laser power and 1Hz pulse frequency the minimum scribe line width is 38 mm. We also try the lower thickness of the Mo thin film for the 0.2 W laser power, but due to the lower thickness, the films experienced a stress, so, the scribe line was distorted or not uniform. Such scribe lines observed using the polarization microscope is shown in Fig 3.13.



(a)



(b)

Fig. 3.12 Scribed line thickness decreases as the thickness of the Mo thin film increases at 2 W laser power and 1 Hz pulse frequency (a), while at the same frequency and 0.2 W laser power the minimum scribe line width observed (b).

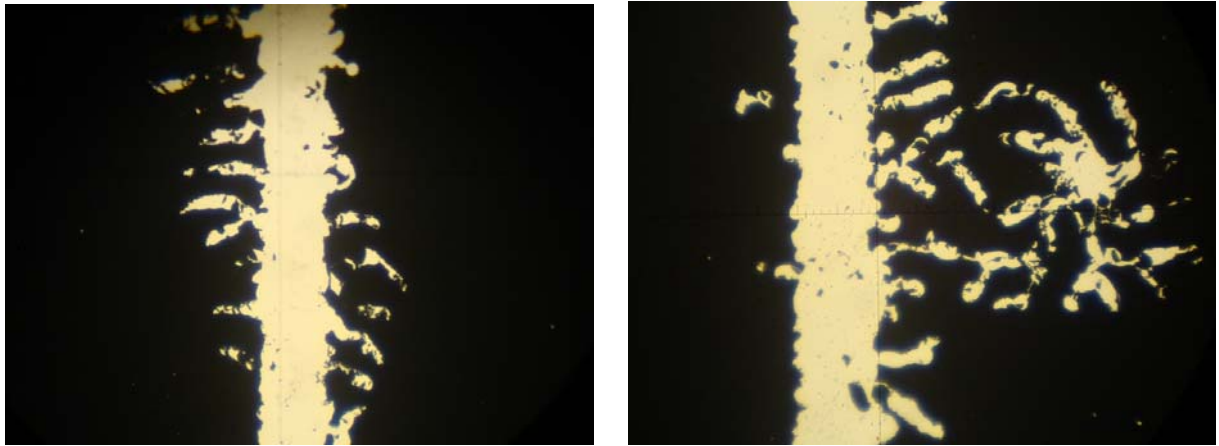


Fig. 3.13 – Stress introduced in the lower thickness of Mo thin films while scribing, that makes the non-uniform scribe line.

The obtained exposed area (scribe line width) of the scribe line of different thickness of the Mo thin films is shown in Fig. 3.14. On increasing the thickness of the Mo thin films, we see from the Fig. 3.14, that the scribe line width decreases. At higher thickness of the Mo thin films, we got the better scribe area as well as the minimum side edges. For 800 nm thin Mo films, the minimum scribe line width i.e. 80 μm was obtain (Fig. 3.14 (h)). The maximum scribe line width, i.e. 220 μm , with poor scribe area is observed at 60 nm thin Mo films (Fig. 3.14 (a)).

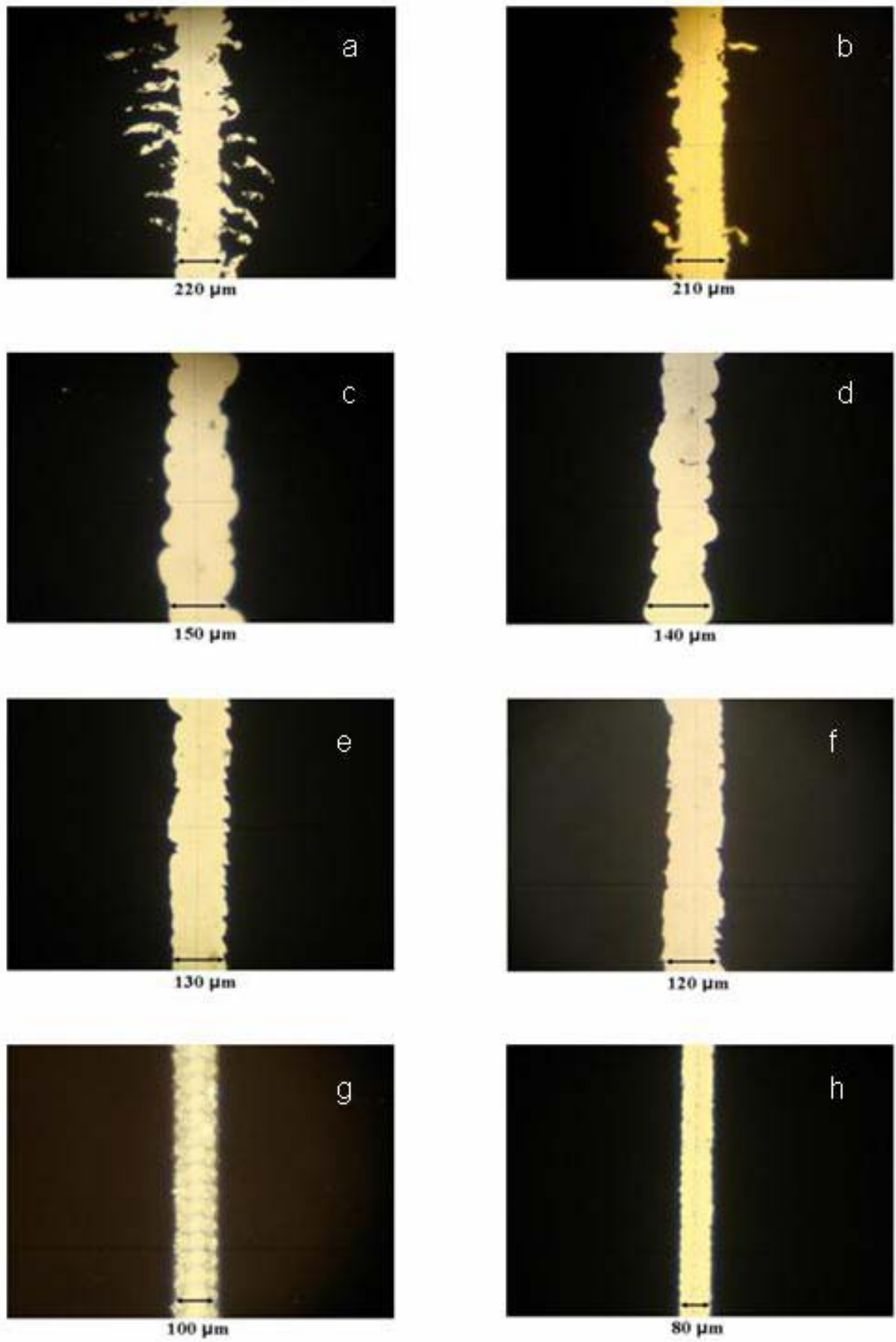


Fig. 3.14 Scribe line width of Mo thin films of different thickness, i.e. from (a) to (h) is 60 nm to 800 nm, results of an average laser power is 2 W and 1 Hz laser pulse frequency.

3.6 CONCLUSIONS

The Mo thin films were grown on soda lime glass substrate using RF magnetron sputtering system for its use as a back-contact in the CIGS thin film solar cell. The significant influence of Working pressure and the RF power was observed by the structural, morphological, electrical, and optical studies. The observations indicate that the metallic Mo thin films showed a better crystallinity, morphology, conductivity, and reflectivity at a lower working pressure (1 mTorr) and a higher RF power (100 W). The Mo thin film grown at 100 W RF power and 1 mTorr working pressure shows a sheet-resistance of $\sim 1 \Omega/\square$ surface roughness of 7.78 nm and near to 55 % reflectivity in the visible region. Apart from the growth of Mo thin film the laser scribing also performed which will use in future in the solar cells module preparation. Different thicknesses (60 nm to 800 nm) of Mo thin films were used for the laser scribing. Laser parameters have been determined that provide reproducible, good scribes, that do not present any unwanted bridges.

Chapter 4

**COPPER INDIUM GALLIUM
DISELENIDE (CIGS) ABSORBER
LAYER: GROWTH AND
OPTIMIZATION**

4. COPPER INDIUM GALLIUM DISELENIDE (CIGS) ABSORBER LAYER: GROWTH AND OPTIMIZATION

Copper indium gallium diselenide (CIGS) is a suitable material for solar cell applications due to its high absorption coefficient, $\sim 10^4 \text{ cm}^{-1}$, and a direct energy band gap value of $\sim 1.15 \text{ eV}$, which makes it conducive as an absorber over the nearly whole visible spectrum. This fact is clearly demonstrated by reported high conversion efficiencies close to 20 % for laboratory scale cells based on CIGS [9] and around 14.2 % for mini modules [64]. In the present study $\text{CuIn}_{1-x}\text{Ga}_x\text{Se}_2$ (CIGS) ($x = 0.3$) was synthesized by reacting its constituent elements in a quartz ampoule. The phase structure and composition of the synthesized pulverized material was verified using X-ray diffraction analysis (XRD) and energy dispersive analysis of X-rays (EDS). The CIGS thin films are depositing using the flash evaporation technique. The influence of substrate temperature, thin film thickness and the thermal annealing by rapid thermal process (RTA) are been consider to achieve the device quality CIGS absorber thin film. The morphology of the evaporated thin films was characterized using scanning electron microscopy (SEM) and atomic force microscopy (AFM), which clearly showed the improved surface observed after the RTA process. In addition, the optical and electrical properties of the evaporated CIGS films were characterized using transmission-reflection measurements and Hall-Effect method, respectively. Only the thicker RTA treated CIGS thin film shows the energy band gap valued near to 1.06 eV. The electrical measurement of the same CIGS thin films showed the p-type conductivity and resistivity in the order of $10^2 \text{ }\Omega\text{cm}$. The carrier mobility and the carrier density found to be in the range of 2 to 42 cm^3/Vs and 10^{16} to 10^{17} cm^{-3} respectively.

4.1 SYNTHESIS OF CIGS MATERIAL

The polycrystalline bulk CIGS [$\text{Cu}(\text{In}_{1-x}\text{Ga}_x)\text{Se}_2$: $x = 0.3$] was synthesized by direct reaction, above the melting point of it, of high-purity (99.99 %) elements Copper, Indium, Gallium, and Selenium, called a melt quenching process. In this kind of process the starting materials could be compound to be grown or pure elements. Accurately weighed elements, in their stoichiometry proportions, were sealed in a quartz ampoule, at a base pressure of 10^{-4} mbar. The sealed ampoule is then heated up in a furnace to a temperature above the melting point of

the compound to be grown. The melt is then allowed to stay at that temperature for a prolonged period of time in order to ensure the complete reaction between elements.

A schematic diagram of the specially formed ampoule used in the present study is shown in Fig. 4.1. The outer diameter and the inner diameter of the quartz ampoule used were 1.6 cm and 1.2 cm respectively. Quartz ampoules had a length of 12 cm. One end of the quartz ampoule was sealed by H₂/O₂ torch. This end of the quartz ampoule was normally made into a conical shape in order to facilitate nucleation of the melt at the early stage of crystallization. The quartz ampoule (with one end sealed) was first cleaned with trichloroethylene, acetone and then rinsed with de-ionized water. It was then etched 3 - 4 hours by using aqueous HCl and HNO₃ solution. After the etching, the quartz tube was then first rinsed with cold de-ionized water for many times and finally rinsed with boiling DI water.



Fig. 4.1 Vacuum sealed quartz ampoule containing constituent elements of CIGS material with 5 % excess selenium content.

Following the cleaning process, the quartz ampoule was dried by using torch flaming. Afterward the material was carefully filled in the ampoule and sealed at a base pressure of 10^{-4} mbar. Prepared quartz ampoule was then placed in the horizontal furnace and heated up to >1100 °C temperature. Fig. 4.2 shows the photograph of actual experimental setup of the ampoule preparation method.



Fig. 4.2 Photograph of experimental setup for the preparation of CIGS melt, containing the ampoule in the horizontal furnace.

At the initial stage of heating the rate of heating was kept $60\text{ }^{\circ}\text{C}/\text{hour}$ up to $450\text{ }^{\circ}\text{C}$ to avoid cracking of the ampoule. After that with rate of $100\text{ }^{\circ}\text{C}/\text{hour}$ the temperature was increases up to $\sim 1100\text{ }^{\circ}\text{C}$. The melt was then allowed to react for 8 hours at this temperature.

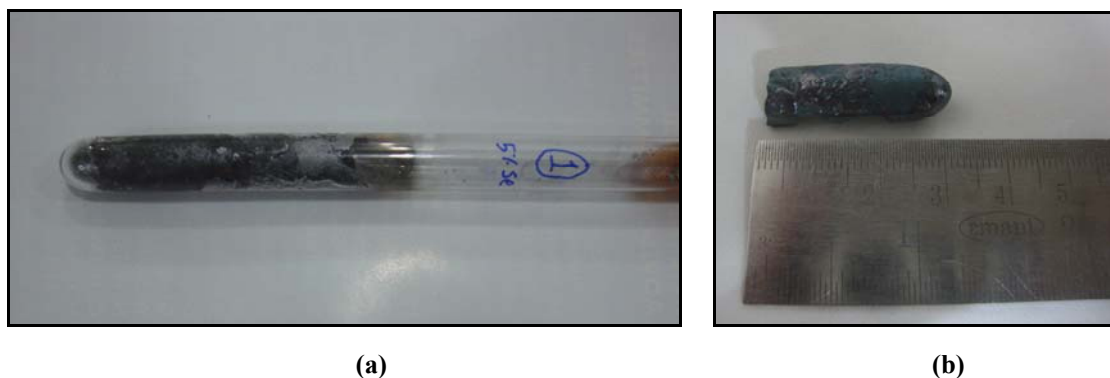


Fig. 4.3 Photograph of prepared CIGS ampoule (a), and resulting solid ingot of CIGS bulk material (b).

The melt was allowed to cool down after 8 hours reaction. The cooling rate was ser to $40\text{ }^{\circ}\text{C}/\text{hour}$ up to $800\text{ }^{\circ}\text{C}$ and $60\text{ }^{\circ}\text{C}/\text{hour}$ up to $200\text{ }^{\circ}\text{C}$. Afterward the furnace was shutdown. The resulting ampoule, as shown in Fig. 4.3 (a), was then carefully broken and the solid ingot, as shown as Fig. 4.3 (b), was powdered to a mean particle size of $\sim 100\text{ }\mu\text{m}$ using the process of grinding and then sieving. The prepared material was then undertaken for characterization

after the characterization and confirmation of the prepared CIGS powder, we used it for the thin film preparation.

4.1.1 Structural Characterization

The XRD of the synthesized CIGS powder is shown in Fig. 4.4. The preferred orientation of the particles is identified along certain crystallographic planes such as (112), (220)/(204), (312), (400), and (316), and the lattice parameters 'a' and 'c', in the prepared bulk compound, have been determined as $5.733 \pm 0.02 \text{ \AA}$ and $11.450 \pm 0.02 \text{ \AA}$, respectively, which conforms to the chalcopyrite (tetragonal) structure of CIGS based on JCPDS card 35-1102.

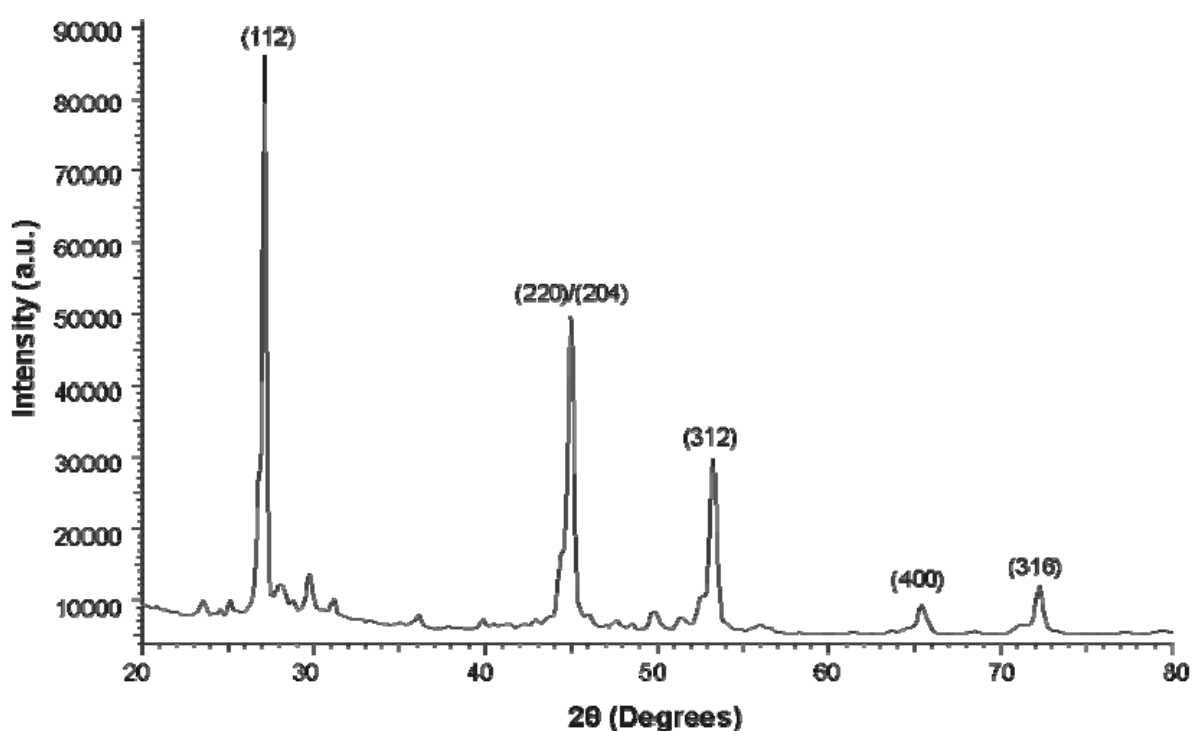


Fig. 4.4 XRD spectra of the synthesized CIGS powder showing tetragonal structure having a preferred orientation along the (112) direction.

The d-values with their corresponding crystallographic planes and 2θ -values are shown in Table 4.1. The lattice constant of the tetragonal system can be found by comparing the Equation 4.1 and 4.2 [65].

$$\frac{1}{d^2} = \frac{h^2 + k^2}{a^2} + \frac{l^2}{c^2} \quad (4.1)$$

This may be rewritten in the form,

$$\frac{1}{d^2} = \frac{1}{a^2} \left[(h^2 + k^2) + \frac{l^2}{(c/a)^2} \right] \quad (4.2)$$

Table 4.1 The d-values of the synthesized CIGS powder with its crystallographic planes and 2 θ values.

2 θ (degree)	d-value (Å)	(h l k)
27.070	3.29128	(112)
44.971	2.01411	(220)/(204)
53.264	1.71843	(312)
65.421	1.42545	(400)
72.295	1.30590	(316)

4.1.2 Compositional Characterization

The chemical composition of the prepared CIGS powder is identified from the EDS shown in Fig. 4.5. The pattern shows the purity of the synthesized powder. Not a single element other than Copper, Indium, Gallium, and Selenium were revealed and the data, shown in Table 4.2, shows the expected 1:1:2 stoichiometries of the elements of CIGS powder.

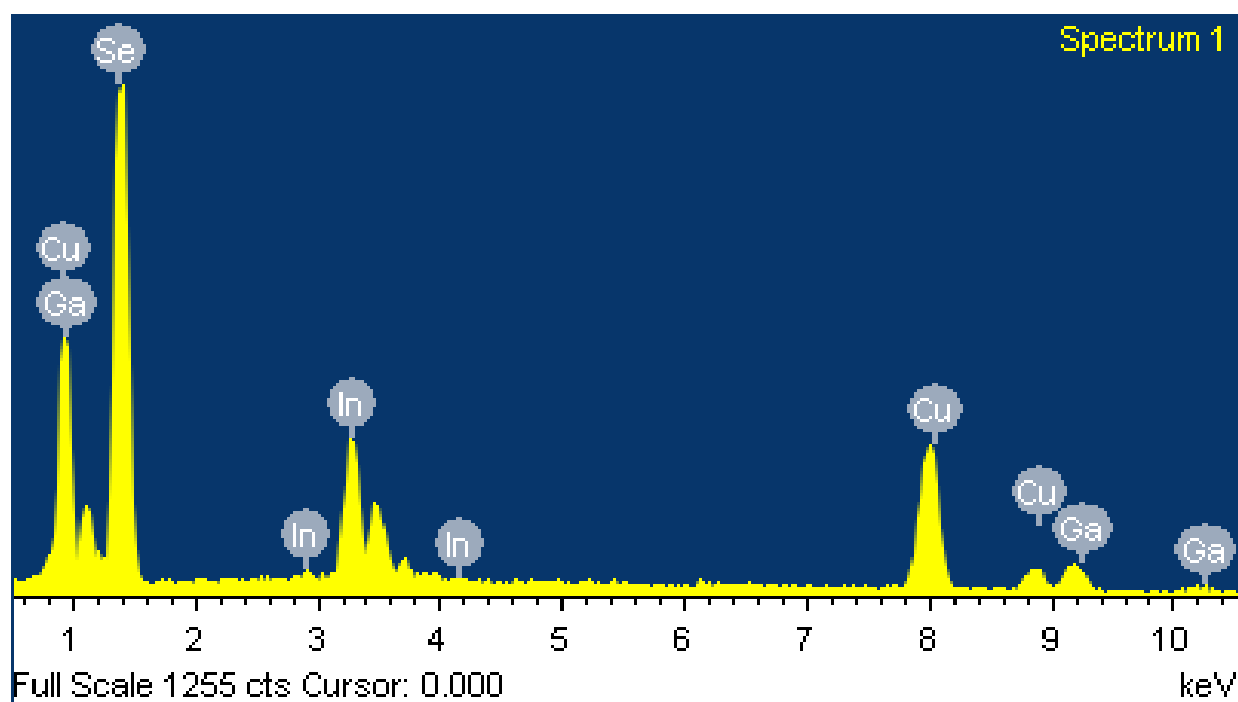


Fig. 4.5 The EDS pattern of the synthesized CIGS powder indicating the constituent elemental detection of CIGS powder.

Table 4.2 The composition, in atomic weight proportion, of the synthesized CIGS powder.

Elements	Cu K	Ga K	Se L	In L
at. wt. (%)	24.58	7.80	49.38	18.24

4.2 THIN FILM PREPARATION

Thin films of CIGS were deposited using the flash evaporation technique. For the optimizing the growth, structural, compositional, optical and electrical properties of CIGS thin film we used organically soda lime glass as a substrate. While preparing the solar cell device we used Molybdenum coated glass as a substrate. During the deposition of CIGS thin films the vacuum is kept constant around 10^{-5} mbar. The deposition rate is maintained near to 0.5 nm/s. The influence of substrate temperature (varied from 100 °C to 300 °C), the film thickness (varied from 300 nm to 1000 nm) and rapid thermal annealing at 500 °C of the CIGS thin films are studied.

4.3 EFFECT OF SUBSTRATE TEMPERATURE

4.3.1 Structural Characterization

CIGS thin films of thickness 300 nm, deposited at different substrate temperatures, were characterized using XRD analysis as shown in Fig. 4.6.

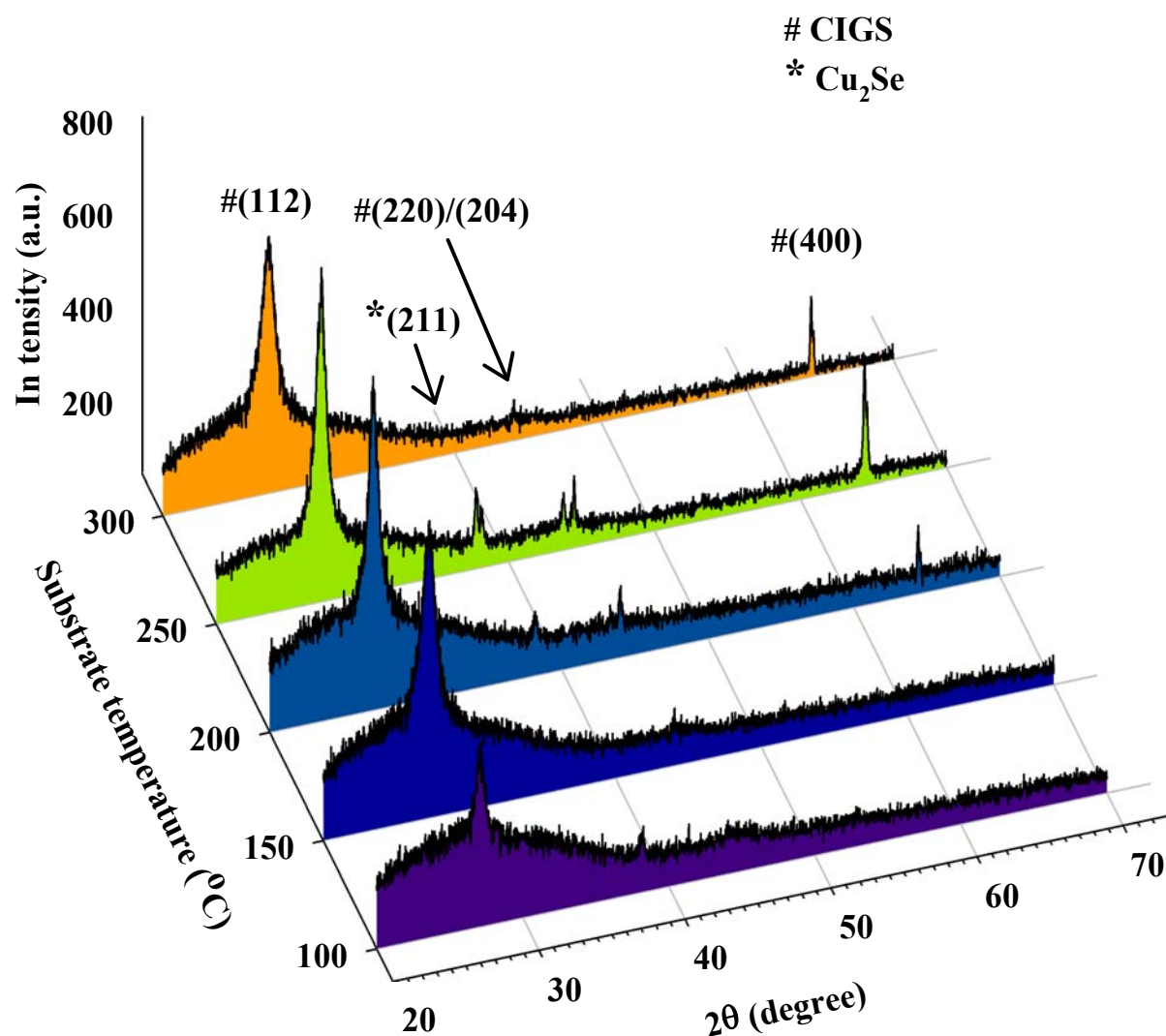


Fig. 4.6 XRD of CIGS thin films grown at different substrate temperature shows the major crystalline phase of (112) plane of CIGS and minor binary phase of (211) plane of Cu₂Se.

The analysis of the diffraction pattern suggests that CIGS thin films deposited at 100 °C shows poor crystalline structure. The major initialization of the crystalline phase was observed when the substrate temperature near to 150 °C. Thin films of CIGS deposited greater than 150 °C substrate temperature shows the major crystalline phase of (112) plane, parallel to the substrate, as expected being a chalcopyrite CIGS structure (JCPDS card 32-1105). Including (112) plane as a major crystalline phase, some binary phase is also detected as a (211) plane indicating the binary structure of Cu₂Se, which is responsible for lower efficient CIGS thin film solar cells [66].

The observed intensity of major crystalline phase i.e. (112) plane is improved by increasing the substrate temperature from 100 °C to 250 °C. Afterwards by further increasing the substrate temperature i.e. greater than 250 °C the intensity of major (112) is reduces, that shows there is decline in the crystallinity in the CIGS film. The possible reason behind this is deficiency of selenium in the film as it has high vapor pressure. A qualitative estimate of the mean size of the crystallites in CIGS thin films deposited at different substrate temperatures are calculated from the (112) X-ray diffraction peak broadening, full-width half maxima (FWHM), using the well-known Scherrer's formula. As the substrate temperature of CIGS thin film increases the FWHM decreases, therefore the mean crystalline size improves. At 250 °C the highest crystalline size of 50 nm was observed.

4.3.2 Micro-structural and Chemical Characterization

The microstructure analysis of the CIGS thin films deposited at different substrate temperature is studied using SEM and AFM. The chemical analysis is done by EDS analysis. Figure 4.7 shows the SEM images and Fig. 4.8 shows the AFM images of CIGS thin films grown at different substrate temperatures.

SEM images of CIGS thin films indicate that as the substrate temperature increases up to 250 °C, the particles of Cu-rich composition are increases. At 300 °C substrate temperature the surface of the films point out the dark circles around the Cu-rich particles, that may occur due to the selenium loss. Non uniform and lesser dense surface of identical grain of CIGS not sufficient for its use as an absorber layer in the solar cell. Further thermal treatment is needed for the improvement of CIGS thin film surface.

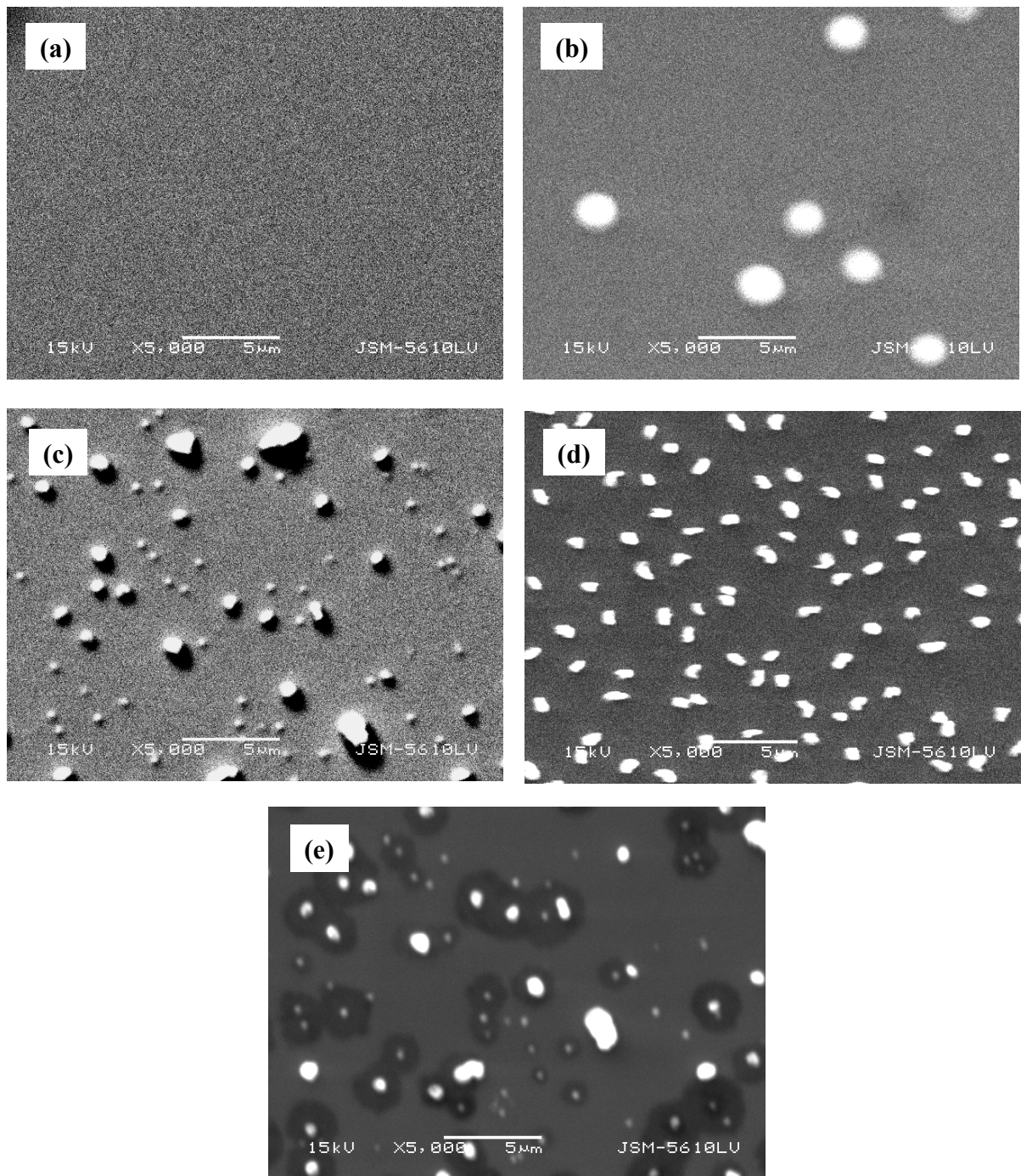


Fig. 4.7 SEM images of CIGS thin films grown at substrate temperatures: (a) 100 °C, (b) 150 °C, (c) 200 °C, (d) 250 °C, and (e) 300 °C.

The elemental analysis as per the Table 4.3 also shows the cu-rich composition observed in all CIGS thin film. At the end, the nearby composition of CIGS thin films is observed at 250 °C. This Cu-rich composition is also clearly observed as a minor binary crystalline phase in XRD measurements.

Table 4.3 The chemical composition of the CIGS thin films grown at different substrate temperature.

Substrate temperature (°C)	Cu (at. wt%)	In (at. wt%)	Ga (at. wt%)	Se (at. wt%)	Si (at. wt%)	O (at. wt%)
100	25.65	16.88	6.44	48.44	1.93	0.68
150	25.79	17.36	6.46	50.09	0.30	-
200	25.02	17.17	7.18	50.63	-	-
250	27.64	16.69	6.78	48.91	-	-
300	25.47	17.21	7.54	50.78	-	-

Figure 4.8 shows the AFM images of CIGS thin films grown at different substrate temperature. By visual inspection we can say that there is a clear influence of substrate temperature on morphology of the film. The surface diffusion energy of deposition atoms on the substrates is limited by the substrate temperature. At lower substrate temperature, due to the low kinetic energy, the surface diffusion energy is low. Thus, elements accumulate non-uniformly on the substrate and the roughness is increased. The average roughness measured was 2.8 nm and 10 nm of CIGS thin films grown at substrate temperature 100 °C and 150 °C respectively, as shown in Fig. 4.8 (a) and (b).

On increase in the substrate temperature, i.e. at 200 °C, due to higher kinetic energy and higher diffusion energy, the CIGS thin films experience a liquid-phase-assisted recrystallization process and the grains start to appear, which is clearly shown in Fig. 4.8 (c). By further increasing the substrate temperature from 200 °C to 250 °C, the roughness decreases from 14 nm to 12 nm for 200 °C and 250 °C, respectively, due to the improvement in the crystallization leading to the accumulation of the grains. The CIGS thin film grown at 250 °C substrate temperature shows the smoother and homogeneous surface as shown in Fig. 4.8 (d).

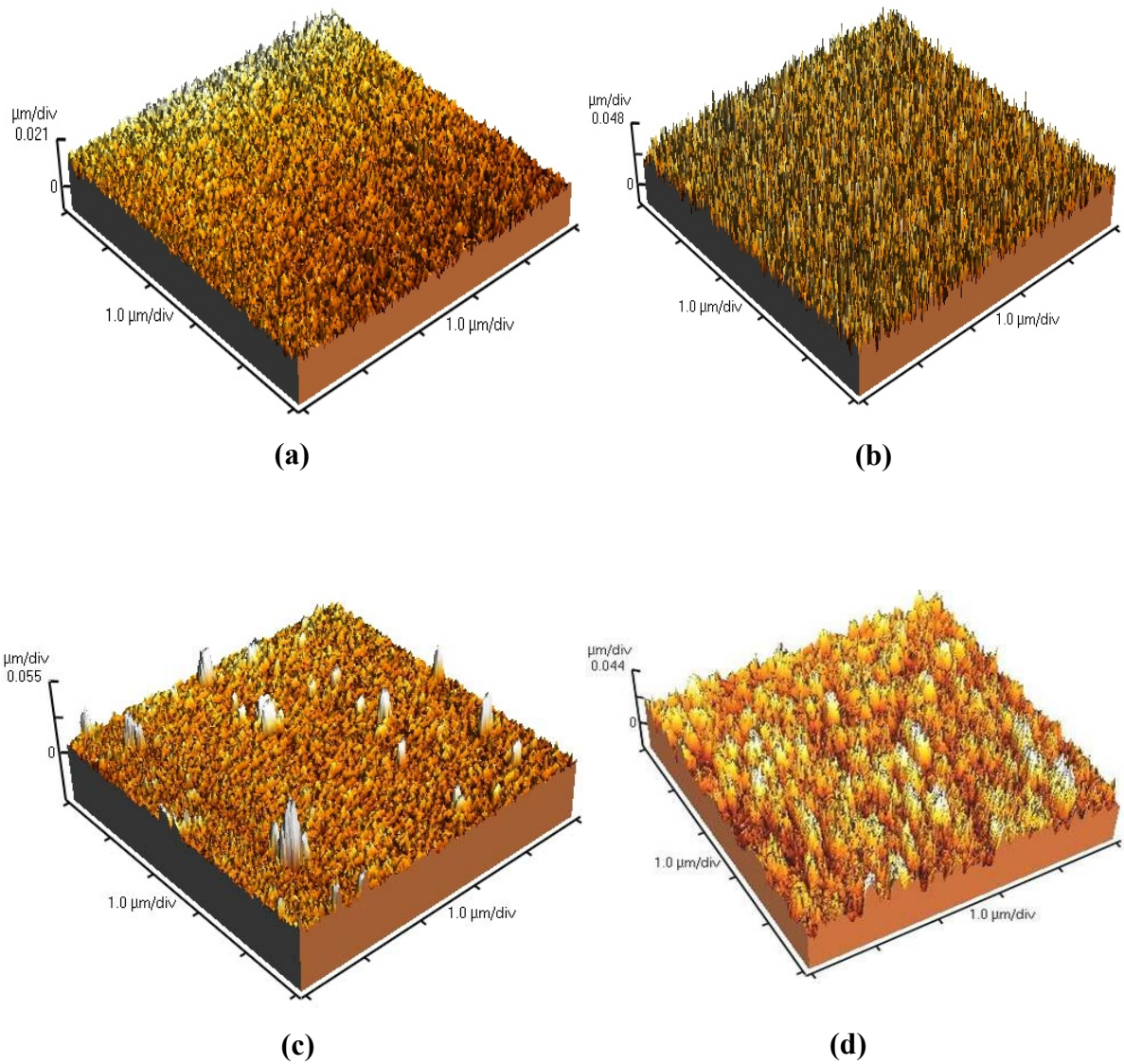


Fig. 4.8 AFM images of CIGS thin films grown at substrate temperatures: (a) 100 °C, (b) 150 °C, (c) 200 °C, and (d) 250 °C.

4.3.3 Optical Characterization

The energy band gap and absorption coefficient were found from the transmittance and reflectance spectra. The variations in the transmittance, from 40 % to 70 %, and reflection, from 5 % to 30 %, in the wavelength range from 900 nm to 1500 nm, depended upon the substrate temperature of the prepared CIGS thin films. The transmission and reflection spectra are shown in Fig. 4.9 (a) and (b) respectively. In all CIGS thin films, the transmission peak value was obtained within 1000 nm - 1200 nm, which shows that the absorption started within that range. The transmission decreases at higher wavelength due to the excess carrier generation. From the values of transmission and reflection (from Equation 2.4) the values absorption, α , can be found. It is greater than 10^4 cm^{-1} , which is the fundamental parameter need to be used in solar cell applications [67].

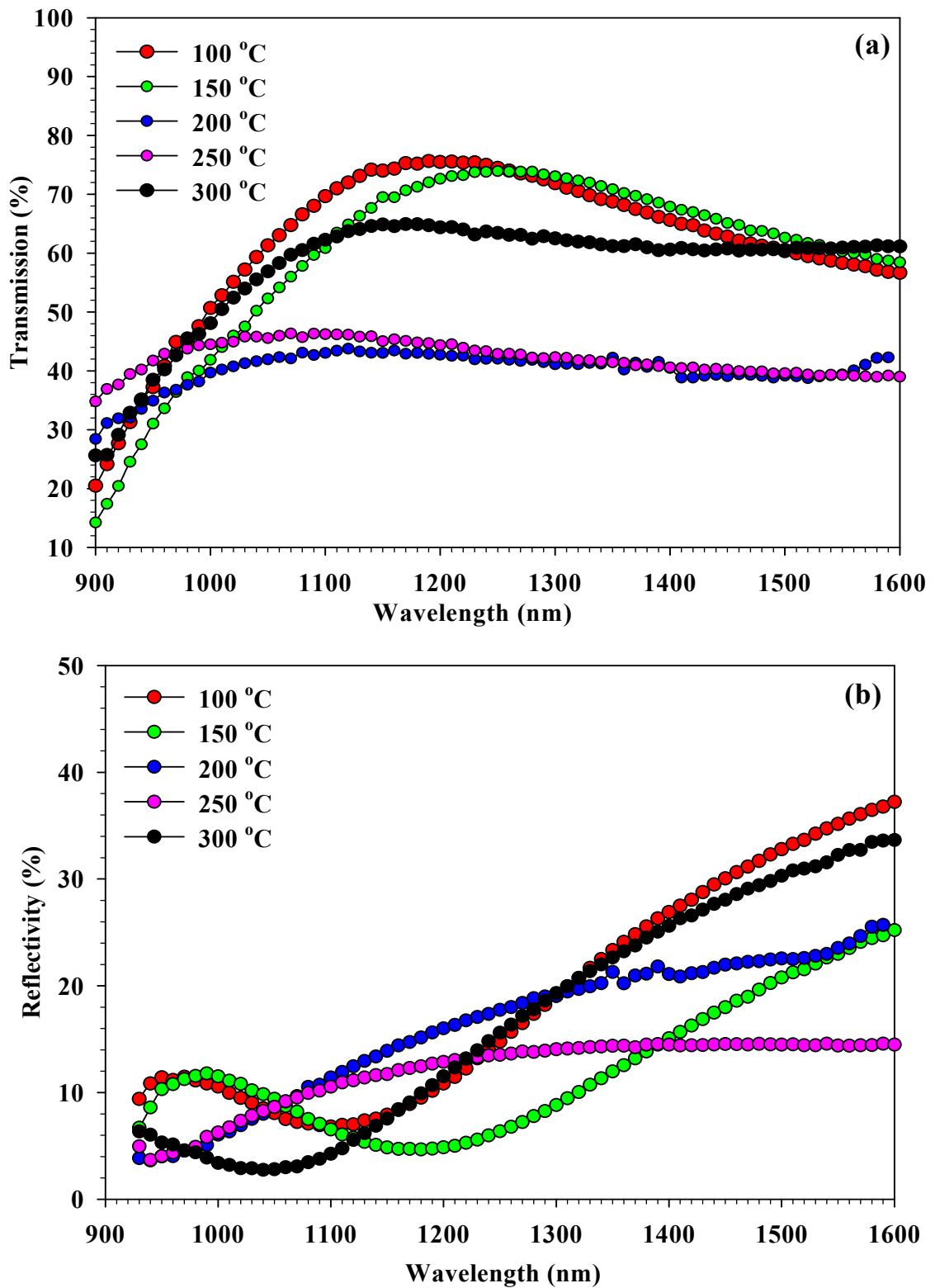


Fig. 4.9 (a) Transmission and (b) Reflection spectra of CIGS thin films grown at different substrate temperature.

Using the value of α , a plots of $(\alpha h\nu)^2$ versus the photon energy, $h\nu$, for films grown at different substrate temperatures are plotted as shown in Fig. 4.10.

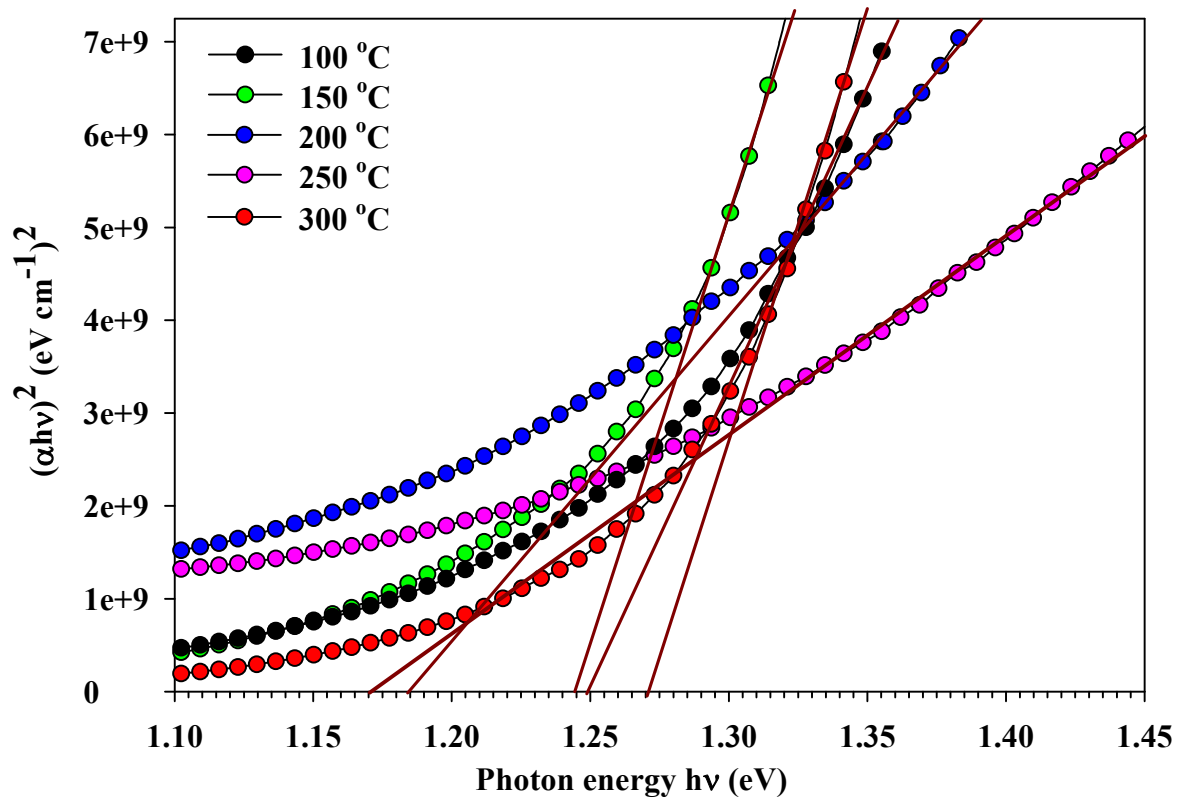


Fig. 4.10 Energy band gap values of CIGS thin films grown at different substrate temperature.

By extrapolating the linear portion of the curve to $(\alpha h\nu)^2 = 0$ we get the band gap energy. The energy band gap of films deposited at different substrate temperatures was in the range of 1.16 - 1.27 eV. By observing the energy band gap for the CIGS thin films deposited at different substrate temperatures, we can see that as the substrate temperature increases from 100 °C to 250 °C the energy band gap value reaches to 1.17 eV from 1.25 eV due to the improvement in the crystallinity. On further increasing the substrate temperature, the band gap value shifts to 1.27 eV, which may be due to the deformation of the crystallinity. The observed energy band gap is little bit higher compare to the bulk value of CIGS i.e. 1.12 eV. The reason behind this is the Cu-rich phase [68] observed clearly from XRD, SEM, and EDS analysis.

4.3.4 Electrical Characterization

Electrical characterization of CIGS thin films deposited at different substrate temperatures was carried out using van der Pauw technique for resistivity measurements and Hall-effect measurements for mobility and carrier concentration. The sample dimension is therefore kept 1 cm × 1 cm. The dot contact of a silver-paste applies at the edge of the sample before characterization. The type of electrical conduction in CIGS thin film was also verified using the hot-probe method.

The resistivity and the charge carrier density (hole density) for CIGS films, deposited at different substrate temperature, varied between $0.1 \times 10^{-1} - 6.6 \times 10^2 \Omega\text{cm}$ and $8.6 \times 10^{16} - 11.3 \times 10^{17} \text{cm}^{-3}$, respectively [69]. It was observed that as the substrate temperature was increased the resistivity of the film decreased. Higher resistivity and lower mobility at low temperature and lower resistivity and higher mobility at a higher temperature can be explained into two steps. Firstly, the surface diffusion energy of deposition atoms on the substrates is limited by the substrate temperature, which results in non-uniform accumulation of constituent atoms on the substrate and the roughness and grain boundaries increased at lower temperature. Secondly, due to the high surface diffusion energy at higher temperature, the CIGS thin films experience a liquid-phase-assisted recrystallization process, which results in the uniform accumulation of the constituent atoms. Therefore, the surface roughness as well as the grain boundaries decreases, and hence the resistivity of the thin film decreases. By increasing the temperature further, the resistivity started to increase due to the higher surface diffusion energy; the higher kinetic energy of the elements leading to non-uniformity of the surface and increase in the grain boundary. The variation of resistivity and mobility at different substrate temperature is shown in Fig. 4.11 (a). The carrier (hole) density is also influenced by the substrate temperature as shown in Fig. 4.11 (b). As the substrate temperature increases the carrier density increases due to the improvement in the crystallinity of the evaporated CIGS thin films and it decreases by a further increase in the substrate temperature due to the deformation of the crystallinity.

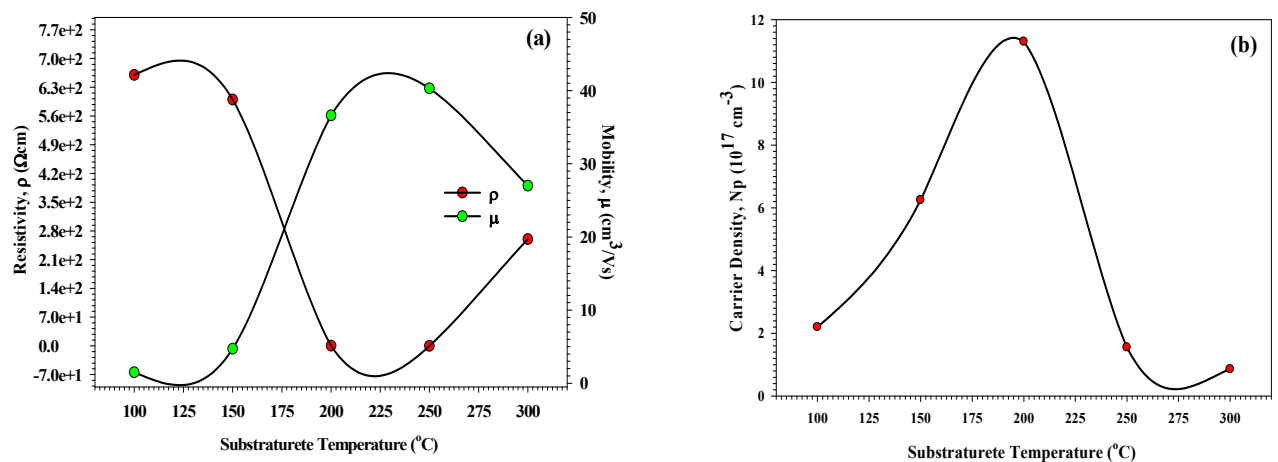


Fig. 4.11 (a) Resistivity, ρ , Mobility, μ , and (b) carrier density, N_p , of CIGS thin film grown at different substrate temperatures.

4.4 EFFECT OF CIGS THIN FILM THICKNESS AND RAPID THERMAL ANNEALING (RTA)

4.4.1 Structural Characterization

Structural wise all CIGS thin films, annealed and without annealed, shows that preferred orientation along the certain crystallographic planes such as (112), (220)/(204), (312), (400), and (316). This confirms the chalcopyrite phase as per the JCPDS data card 35-1102. Figure 4.12 (a), XRD patterns of CIGS thin films, without annealed, of different thickness grown at 250 °C substrate temperature, reveals that the thinner CIGS films have an extra minor Cu_{2-x}Se phase ($0 \leq x \leq 0.2$) (JCPDS 65-2982 and 06-0680) indicated by (200) peak. This is due to the CIGS films covers with a very thin layer of Cu_{2-x}Se surface layer [70]. H. Zachmann et al. characterized the CIGS thin film on polyimide substrate. They also observed thin Cu-rich surface layer on CIGS film [71]. Another study by J. Bekker states that before the selenization, there are CuSe and InSe phases present, which were found to be necessary for the incorporation of S into the partly selenized alloy in order to form good quality of absorber layer [72]. As the thickness approaches to greater than 800 nm, an extra minute Cu_{2-x}Se phase observed, this shows the preferable chalcopyrite phase formation of CIGS thin film [73].

CIGS thin films grown at 250 °C of different thickness are further annealed at 500 °C using RTA furnace for 2 min only. Rapid annealing treatment improves quality of the film. Many research groups check the effect of the thermal annealing of CIGS based thin films grown by different method [74,75,76]. There is appreciable improvement is observed from the annealing process, particularly in the (112) preferred orientation which is clearly observed from the Fig. 4.12. (b). In the XRD spectra for 400 and 600 nm thick annealed CIGS film, there is a minor Cu_3Se_2 phase (JCPDS 47-1745) is present along with the chalcopyrite CIGS phase, that is indicated as a (101) plane in Fig. 4.12(b). The binary compound products (crystalline phases) which are present in the thickness range below 600 nm. These binary compounds are not yet applicable for solar cell applications. When the thickness is raised to above 800 nm, Cu_3Se_2 phase disappears while peaks from $\text{CuIn}_{0.7}\text{Ga}_{0.3}\text{Se}_2$, (112) and (220)/(204) start to dominates, as shown in Fig. 4.12 (b). This shows that a single-phase tetragonal chalcopyrite structure of CIGS forms and dominates at 1000 nm thickness. Since further increment in thickness causes more Se-loss at the time of RTA process (at 500 °C) due to the fixed composition of compound material, so it is believed to be close to the optimal condition.

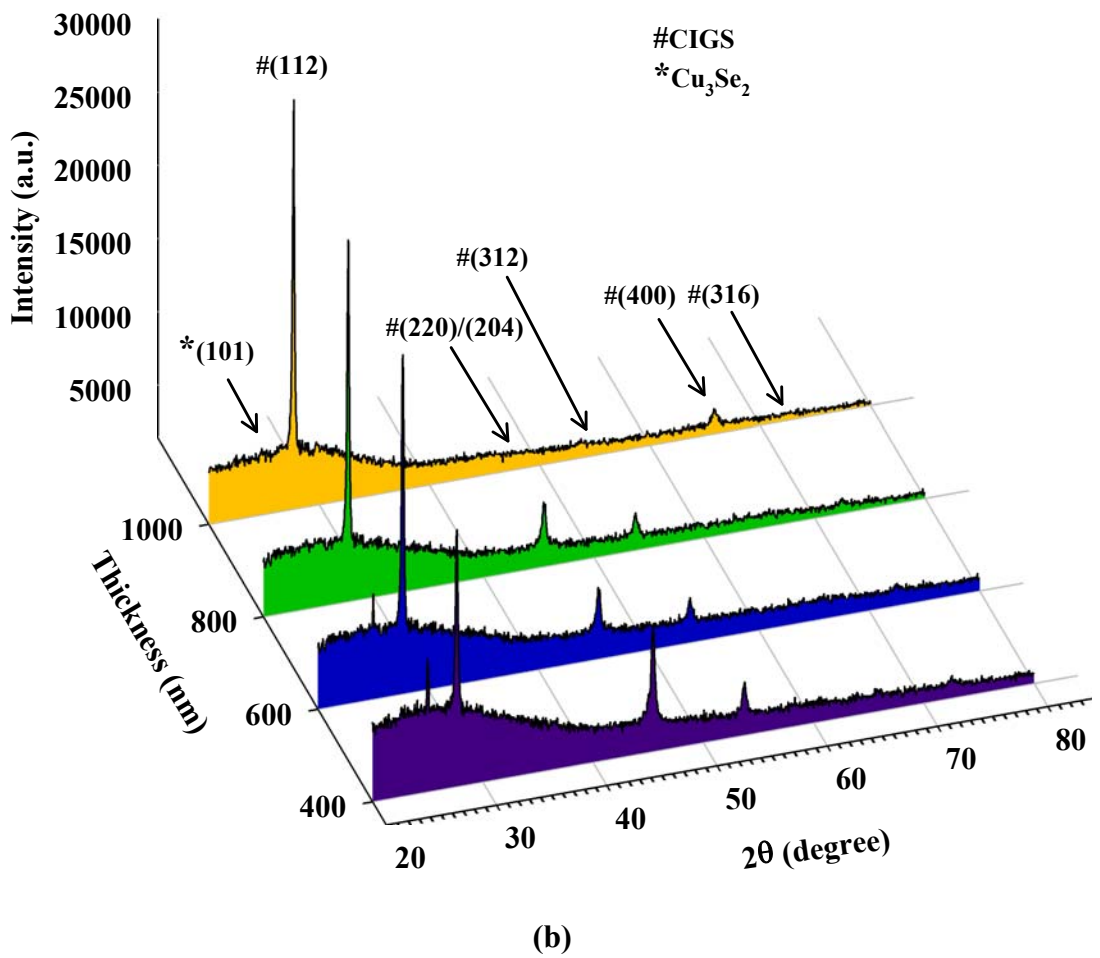
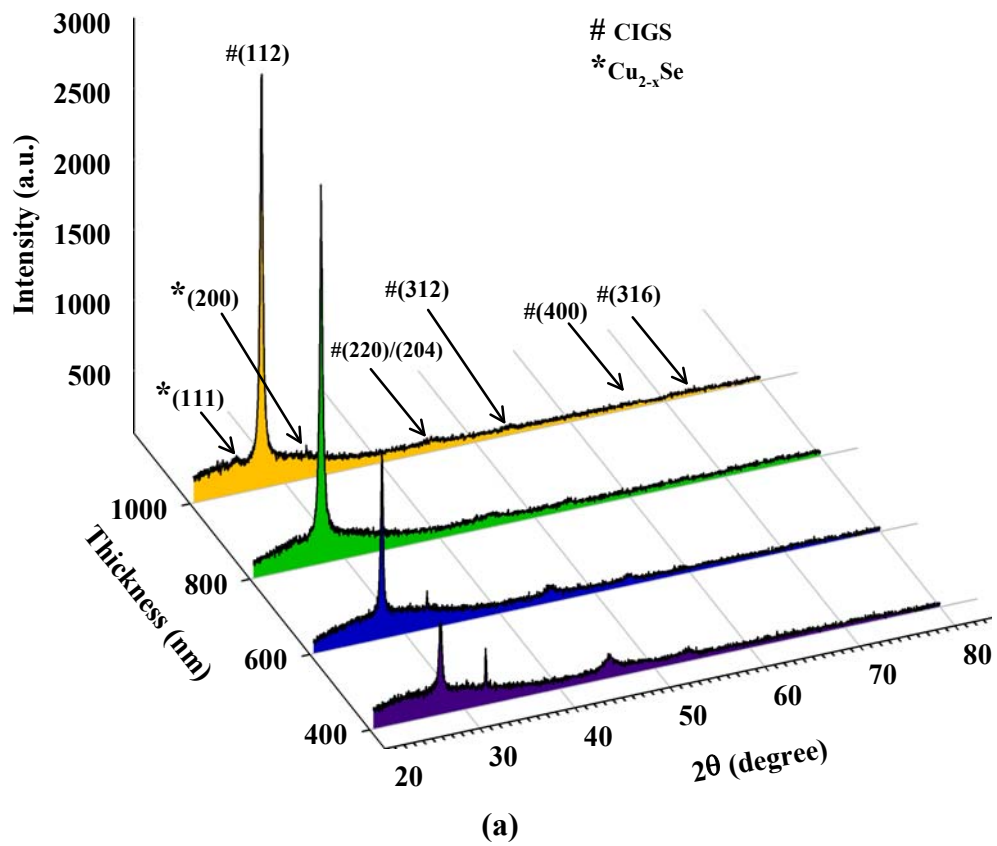


Fig. 4.12 XRD of CIGS thin films having a different thickness deposited at 250 °C substrate temperature (a) and, annealed at 500 °C (b).

As per the calculation for the crystalline size, it is observed for without annealed CIGS thin film that the crystalline size increases from 42 nm to 63 nm as the thickness of the CIGS film increases from 0.4 to 1.0 μm . The lattice parameters $a = 5.655 \pm 0.004$ nm and $c = 11.645 \pm 0.002$ nm, deduced by using Equation 4.2, matched with data presented by D. Liao et al. [77]. While annealed CIGS thin films shows have crystalline size is from 65 to 92 nm as the thickness increases from 0.4 to 1.0 μm . The lattice parameters $a = 5.645 \pm 0.003$ nm and $c = 11.628 \pm 0.005$ nm are deduced by using Equation 4.2 [76].

4.4.2 Micro-structural and Chemical Characterization

Surface morphology, observed using SEM, of without annealed CIGS thin films of different thickness (400 nm to 1000 nm) is shown in Fig. 4.13. CIS based thin films were known for its non uniform growth due to the non uniform distribution of elements. SEM shows that as the thickness of the CIGS film increases the morphology of the films improves. Smooth surface of CIGS film was observed at of 400 nm thickness. Non uniform and lesser dense surface was observed at 800 nm and at 1000 nm thickness the grains shows the uniform surface coverage with an identical grain of CIGS.

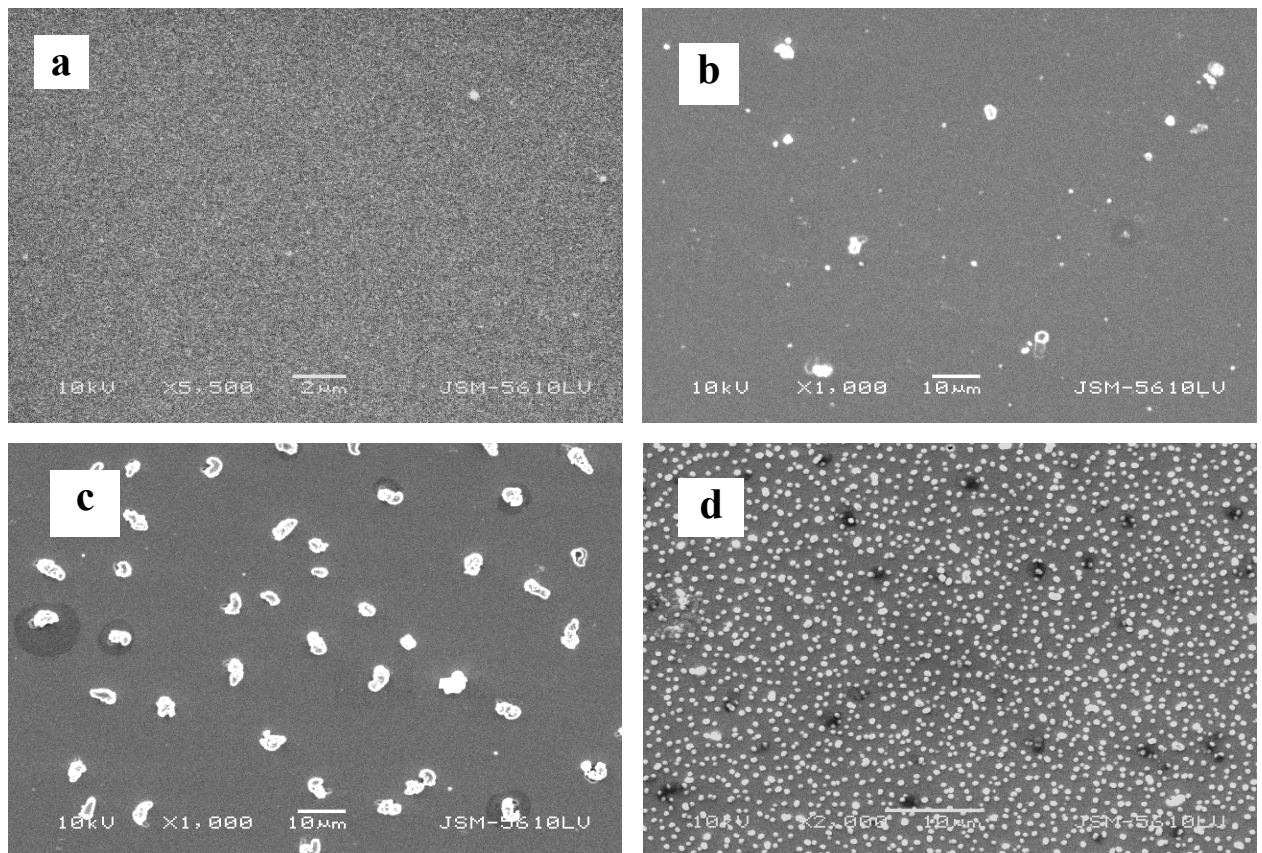


Fig. 4.13 Surface morphology of without annealed CIGS thin films of different thicknesses: (a) 400 nm, (b) 600 nm, (c) 800 nm, (d) 1000 nm.

The chemical analysis was carried out using EDS analysis. As shown in Fig. 4.13, at higher thickness of CIGS thin films the grain growth improves. The values of elemental composition present in film are tabulated in Table 4.4. The CIGS film having a thickness of 800 nm and 1000 nm, the CIGS grains appears clearly.

Table 4.4 Elemental composition of without annealed CIGS thin films of different thicknesses.

CIGS film thickness (nm)	Cu (at. wt%)	In (at. wt%)	Ga (at. wt%)	Se (at. wt%)	Si (at. wt%)	O (at. wt%)
400	25.65	16.88	6.44	48.44	1.93	0.68
600	25.79	17.36	6.46	50.09	0.30	-
800 (plane area)	25.02	17.17	7.18	50.63	-	-
800 (particle)	27.64	16.69	6.78	48.91	-	-
1000 (plane area)	25.47	17.21	7.54	50.78	-	-
1000 (particle)	26.64	17.85	7.37	48.14	-	-

Individual grains present at higher thickness shows the copper rich and selenium deficient composition and the plane area of the film shows stoichiometry composition. At lower thickness of CIGS, the deviation in the case of selenium was observed and also the impurity from the glass substrate has been detected. At lower thickness of CIGS, the deviation in the case of selenium was observed and also the impurity from the glass substrate has been detected. At the thickness of 0.4 μm the weight percentage of silicon and oxygen were 1.93 and 0.68, respectively, were observed.

As the thickness of the CIGS film increases the impurity was not detectable. For device-quality films the selenium composition is the key factor. Deficiency in the selenium, due to its highly volatile nature, leads to degrade the film quality [78]. Increment in the thickness of the film, observed improvement in the selenium shows its improved quality.

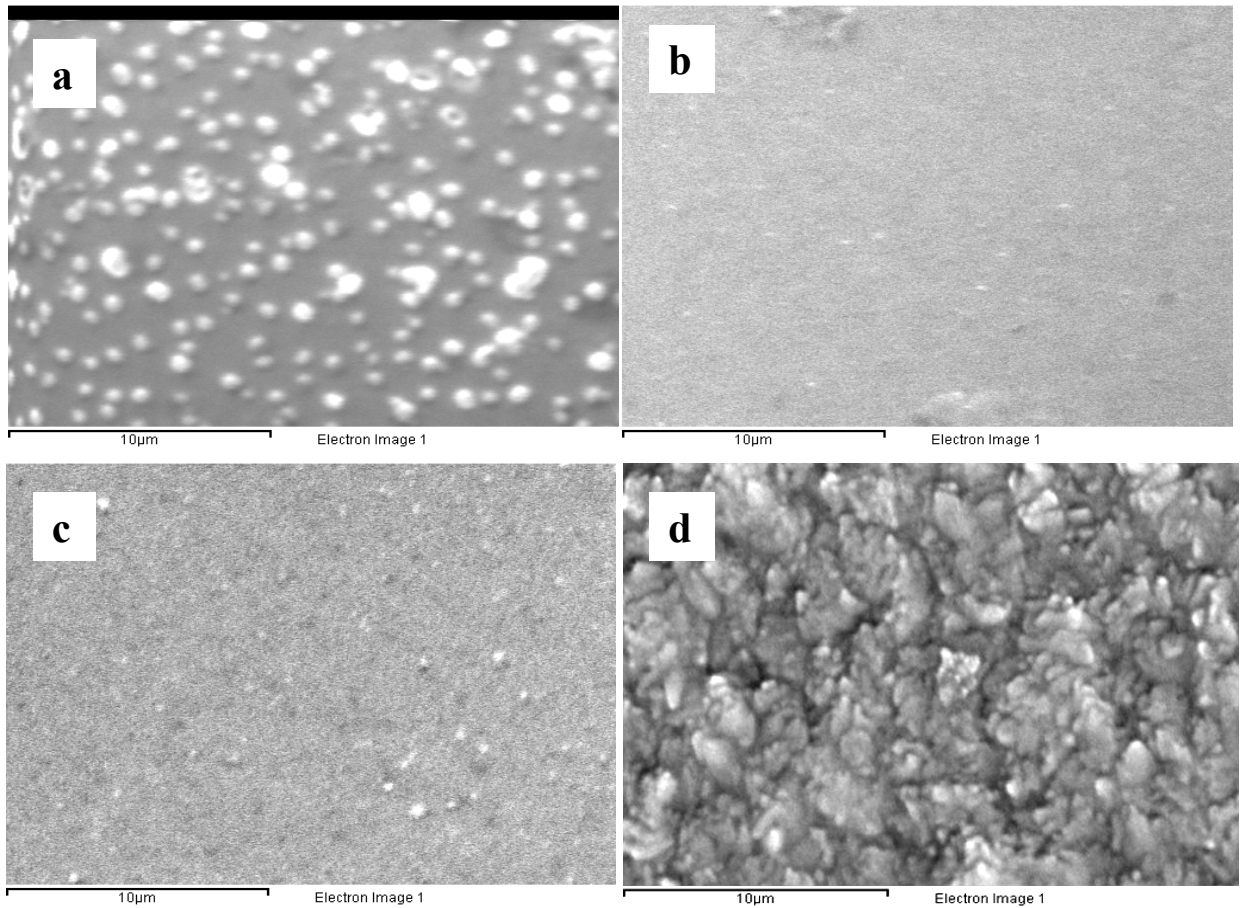


Fig. 4.14 SEM images of annealed CIGS thin films, indicating the rough morphology achieved at the higher thickness CIGS thin film

Table 4.5 Elemental composition of annealed CIGS thin films of different thicknesses

CIGS film Thickness (nm)	Cu (at. wt%)	In (at. wt%)	Ga (at. wt%)	Se (at. wt%)	O (at. wt%)
400 (particles)	35.98	10.66	5.19	45.97	2.20
400 (overall)	39.80	8.86	4.25	44.57	-
600	27.53	13.45	5.19	50.63	-
800	26.69	17.02	6.50	49.82	-
1000	24.50	19.07	6.59	49.74	-

The surface morphology and elemental compositional analysis of annealed, by RTA process, CIGS thin films of different thickness (400 nm to 1000 nm) is shown in Fig. 4.14 and Table 4.5. CIS and CIGS based thin films were known for its non uniform growth due to the non uniform distribution of elements. In our case (annealed CIGS thin films), the non uniform distribution of granules and uneven granule size was observed for 400 nm thickness

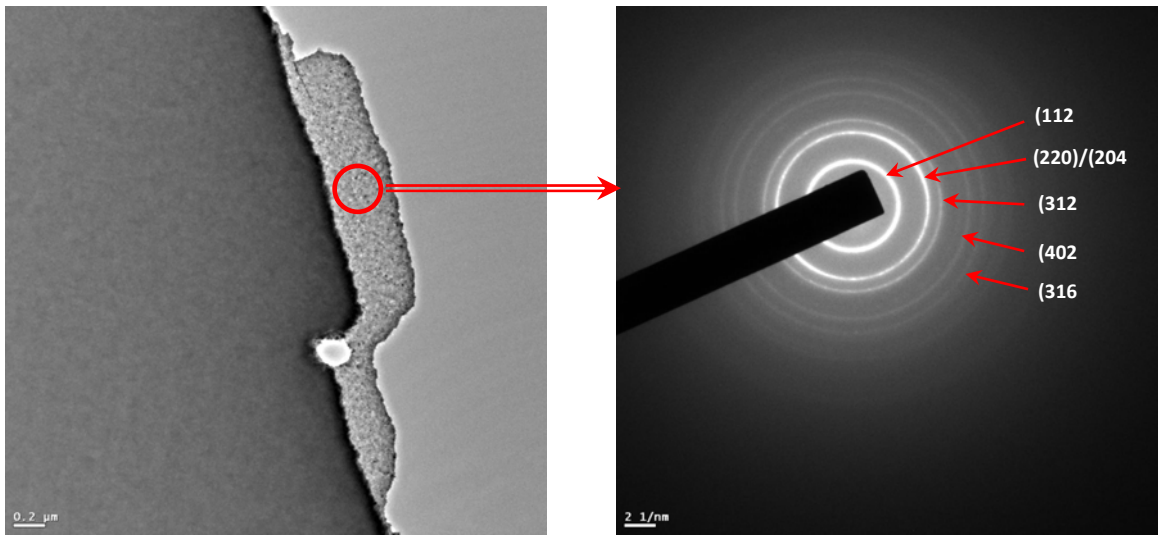
of CIGS thin film. These particles shows the copper (Cu)-rich composition, $\text{Cu}/(\text{In}+\text{Ga}) = 2.26$, and due to that overall composition gets disturb (non-stoichiometry). Similar kind of surface topography also observed by Cunha et. al. [79].

Up to 800 nm thickness we have observed the Cu-rich composition and the less rough film surface. In 1000 nm thickness of CIGS thin films the slightly Cu-poor, $\text{Cu}/(\text{In}+\text{Ga}) = 0.95$, and rougher surface is observed. Cu-poor surface is beneficial for improvement of the overall performance of the solar cell [80,81].

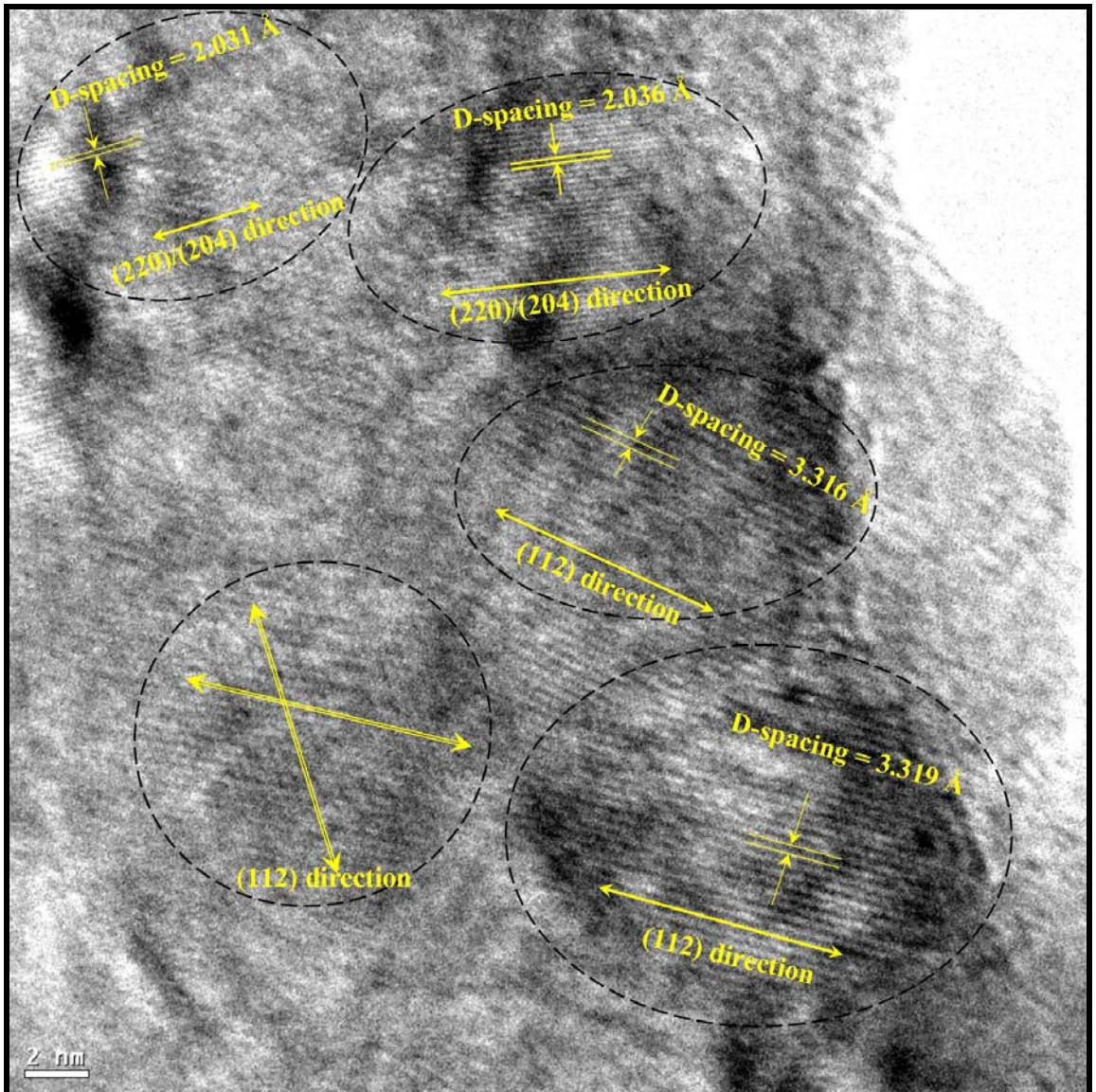
4.4.3 TEM Characterization

XRD analysis of CIGS thin films revealed that all films had (112) preferred orientation. Among all CIGS films 1000 nm thick annealed films shows the preferable structural properties. With the XRD measurement the TEM is also carried out of the CIGS thin film (1000 nm thick annealed) in order to confirm the structure of the film which was obtain from the XRD. A small portion of the CIGS film was taken out, by etched the film in 10 % dilute hydrofluoric solution, for measuring the selected-area-diffraction (SAD) pattern which is shown in Fig. 4.15 (a). The SAD pattern contains continuous sharp rings as expected for polycrystalline films. It can be seen that the three major characteristic peaks (112), (220)/(204) and (312) are present in the film. These obtained (hkl) indices of the diffracted rings well matched with the JCPDS data card 35-1105, for chalcopyrite $\text{Cu}(\text{In}_{0.7}\text{Ga}_{0.3})\text{Se}_2$ reflections. There are no reflections corresponding to elemental or secondary phases identified.

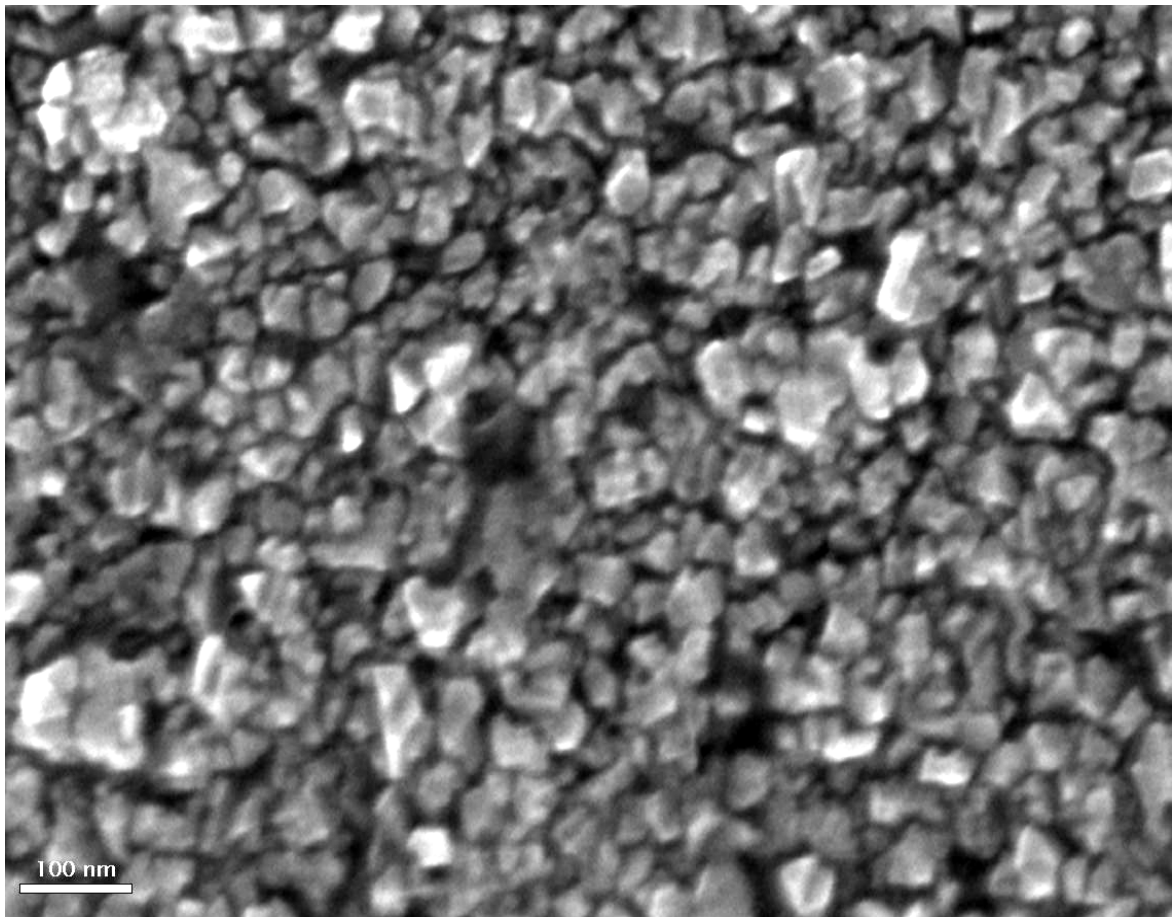
Figure 4.15 (b) shows the high resolution TEM image that clearly indicates growth of CIGS polycrystalline material phase having a different d-spacing. The measured d-values is $3.319 \pm 0.003 \text{ \AA}$ and $2.036 \pm 0.004 \text{ \AA}$, which confirms the growth of grains in (112) and (220)/(204) direction respectively [77]. The Fig. 4.15 (c) shows the image obtain from TEM of 1000 nm thick annealed CIGS thin film having a greater resolution compared SEM shown in Fig. 4.12 (d). The surface is clearly different than that less thick than 1000 nm CIGS films, where tiny minor grains form a very smooth surface. The surface of the CIGS film, Fig. 4.15 (c), demonstrates that a rough surface was formed after the RTA process and the grain size also had improvisation.



(a)



(b)



(c)

Fig. 4.15 (a) SAD pattern, (b) high resolution photograph, and (c) surface morphology annealed CIGS thin film.

4.4.4 Optical Characterization

Significant amount of transmission is reduced near to the end of visible range (900 nm- 1000 nm) indicates the improvement in the absorption as shown in Fig. 4.16 (a). In addition to that transmission as well as the spectral fringes both improves, above 1200 nm, as the thickness increases. That indicates the improved uniformity of the film. The spectral fringes observed from the reflection of the CIGS films are also improves as the thicknesses of the film increases (Fig. 4.16 (b)). The observed average transmission and reflection of CIGS of 1000 nm thick is ~ 70 % and ~ 20 %, respectively. Plot of $(\alpha h\nu)^2$ vs. $h\nu$, as shown in Fig. 4.17, gives the energy band gap values of the prepared CIGS thin films of different thicknesses. CIGS film having a 400 nm thickness does not show any significant band edge, which is in accordance with the selenium deficiency and non-stoichiometry as observed from the EDS analysis. For 800 nm thickness of CIGS thin film, two separate linear part of $(\alpha h\nu)^2$ plot is observed. That shows the non-uniform or mixed growth for CIGS thin film.

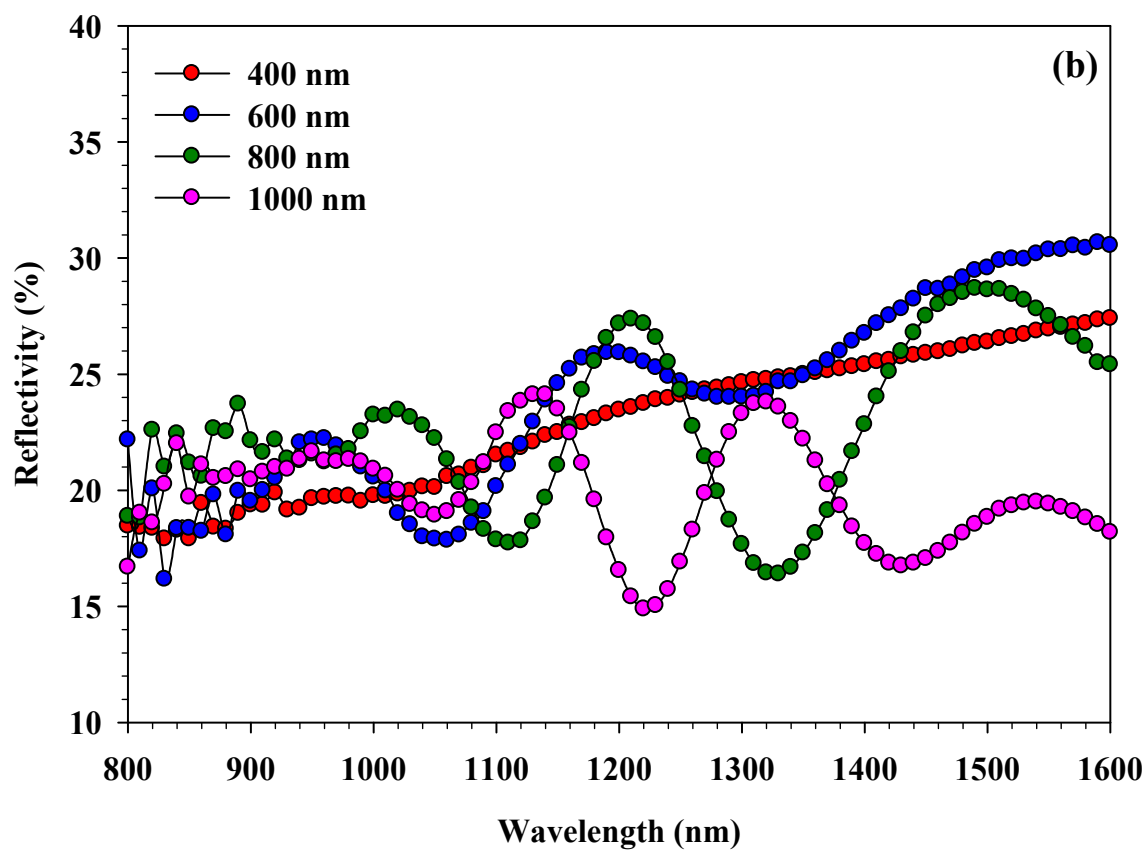
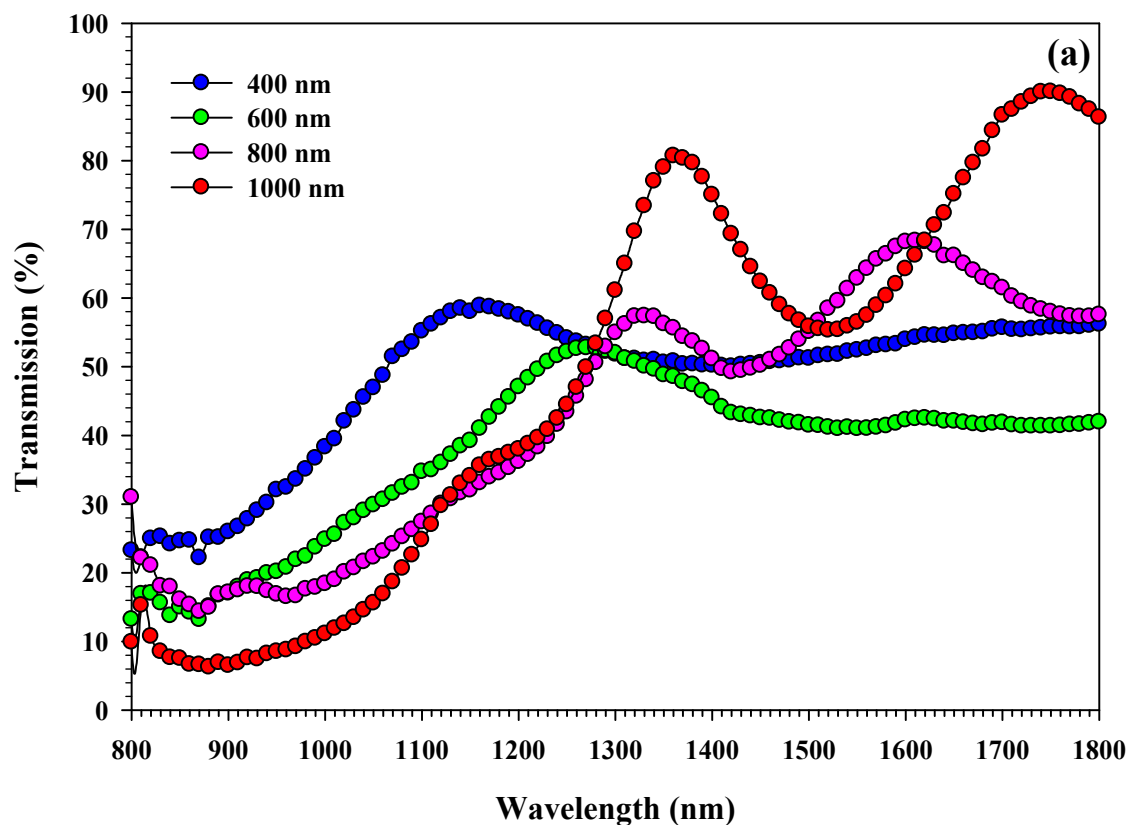


Fig. 4.16 (a) transmission and (b) reflection of without annealed CIGS films of different thicknesses.

This particular characteristic also observed from the SEM, as a non-uniform surface, and EDS as a composition difference between CIGS grains and plane area. At 1000 nm

thickness of CIGS, due to the uniform surface coverage by the CIGS grain growth the sharpness of the linear part of $(\alpha h\nu)^2$ plot is observed. The energy band gap value for 1000 nm thick CIGS film was 1.08 eV [82].

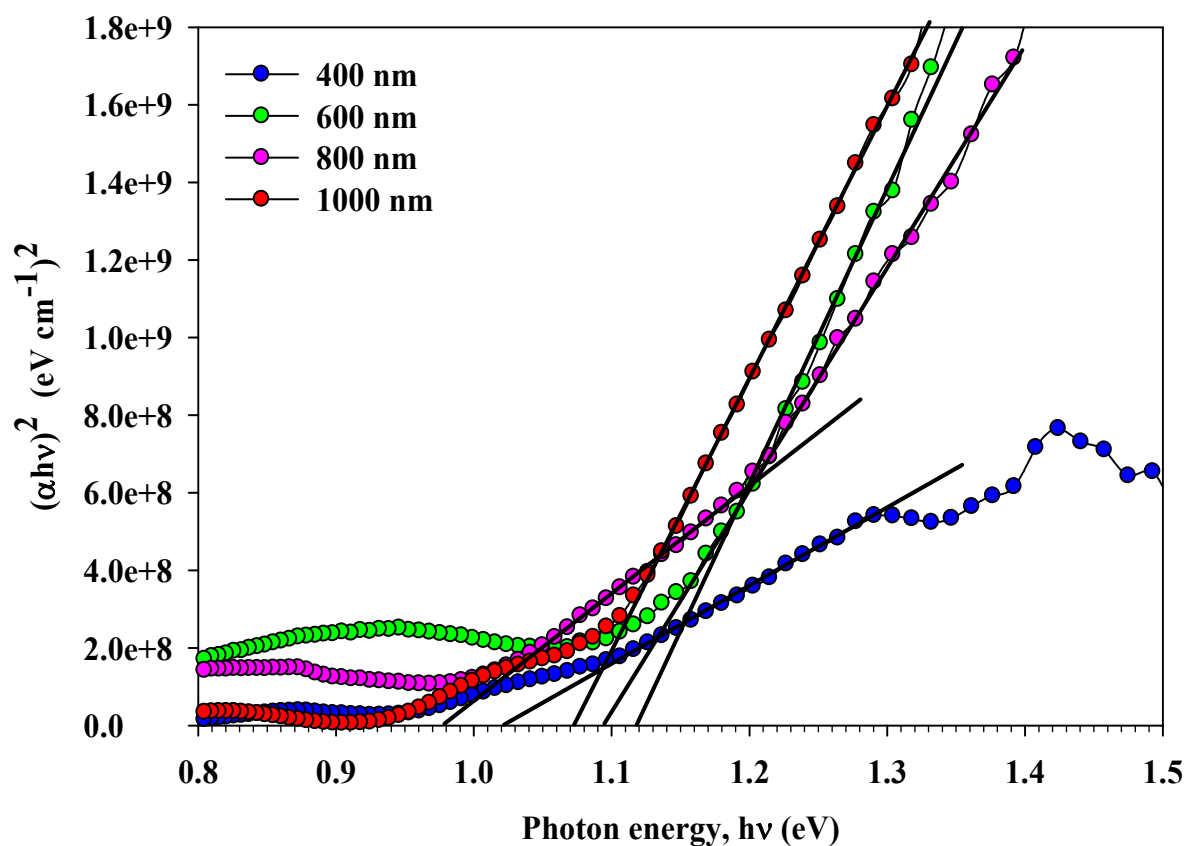


Fig. 4.17 Energy band gap of without annealed CIGS thin films for different thicknesses.

Transmission spectra (normal incidence) and reflection spectra in the wavelength range 800 to 1800 nm, as shown in Fig. 4.18 (a) were recorded for annealed CIGS thin films of different thicknesses. Lower transmission was observed in the region of 800 to 1100 nm. Above the 1100 nm the transmission increases rapidly. The transition of the spectrum is sharper for films grown at higher thickness, and the maximum level of transmission reached about 65 %. These changes are consistent with the physical properties of the samples observed by the SEM. The improved spectral fringes of reflection spectra indicate the uniform surface morphology of the CIGS thin film by annealing of 1000 nm thickness, which has the average reflection of about 25 %.

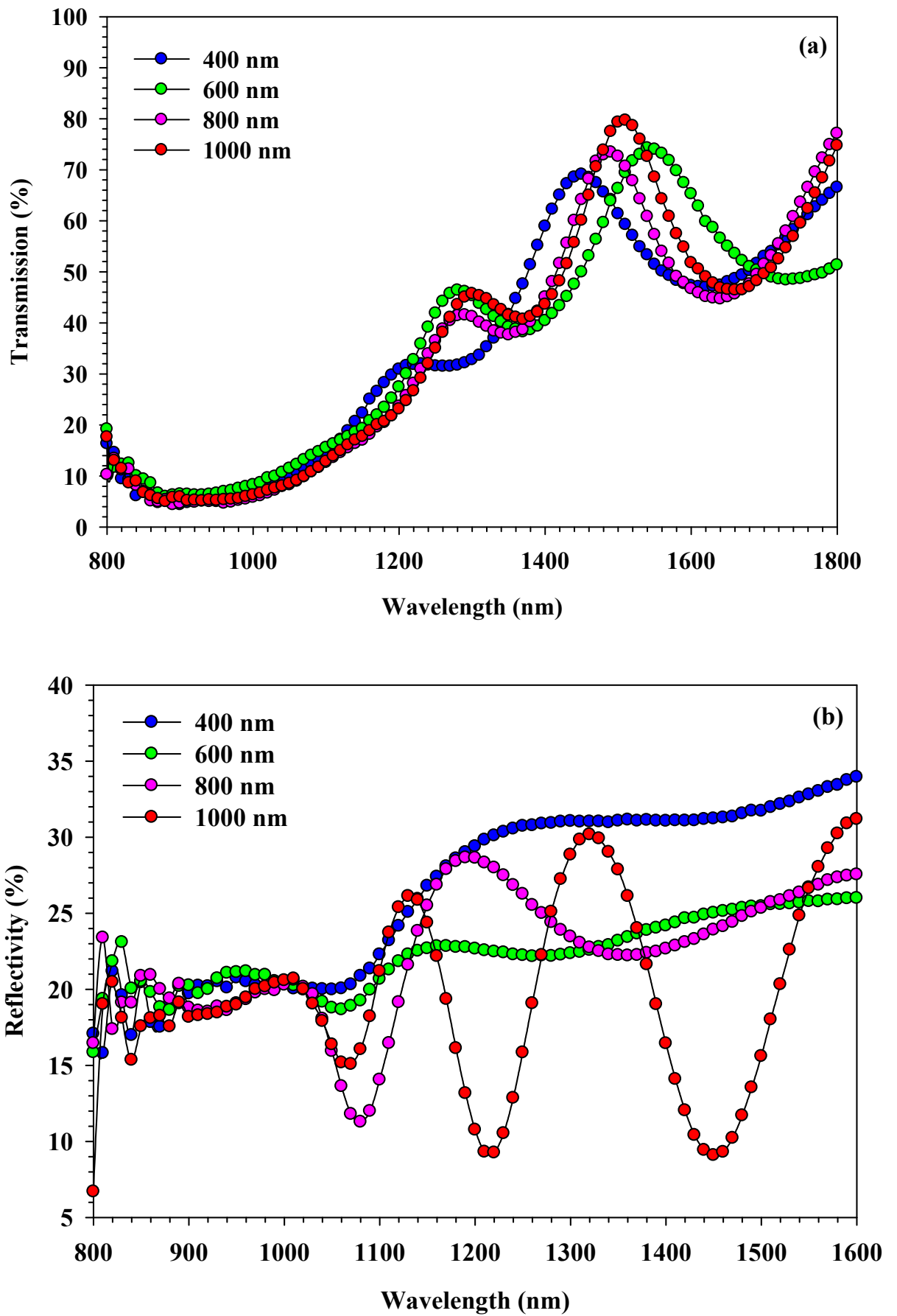


Fig. 4.18 (a) Transmission and (b) reflection of annealed CIGS thin films of different thicknesses.

The plot of $(\alpha h\nu)^2$ versus the photon energy, $h\nu$, for annealed CIGS thin films having a different thickness shown in Fig. 4.19. The low band gap can help charge separation, but is detrimental in terms of open circuit voltages. While, although the wide band gap increases open circuit voltages, it blocks photocurrent collection. The ideal band gap is in the range of 1.10 - 1.15 eV for CIGS thin film used for solar cell applications. The energy band gap value of 1.05 eV observed for most of the annealed CIGS thin films. While it is ~ 1.12 eV for without annealed CIGS thin film (Fig. 4.17). Decrease in energy band gap values on annealing process is consistent with the fact that the crystallinity of the polycrystalline thin films improves on annealing [83].

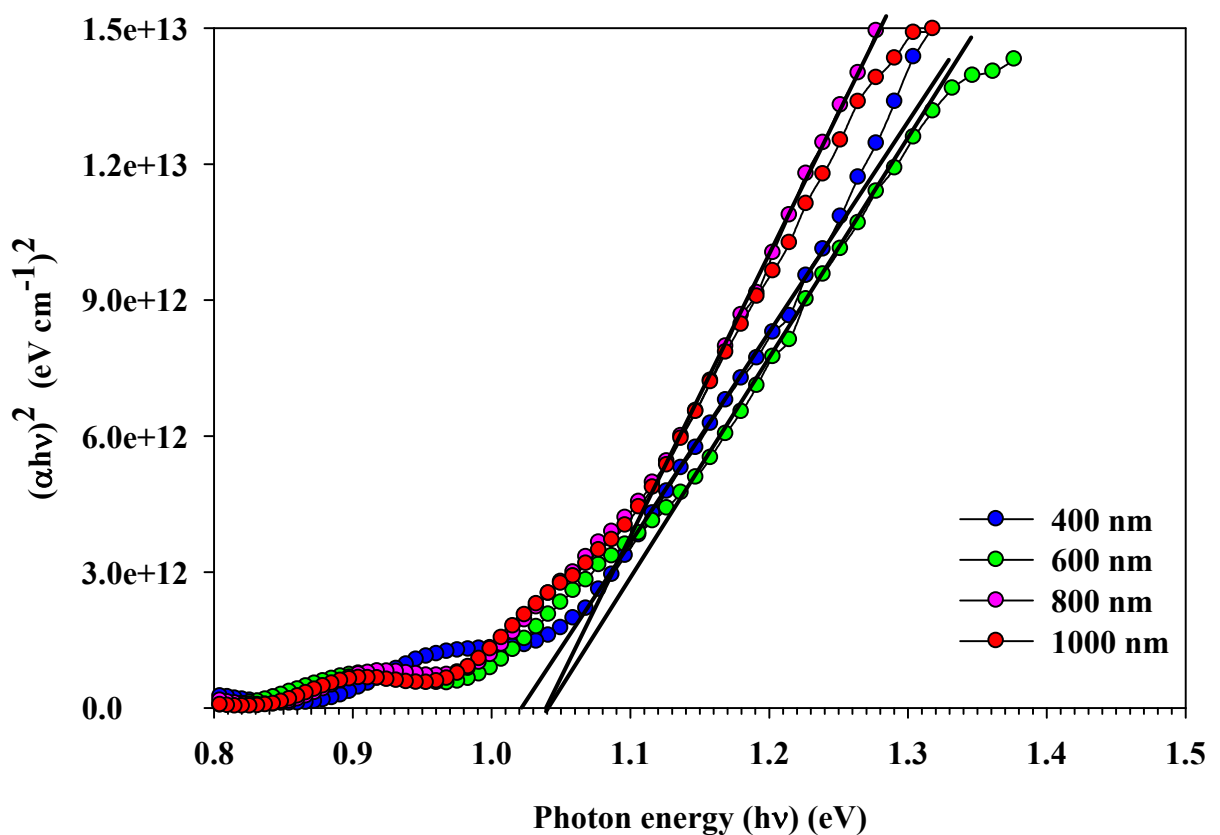


Fig. 4.19 Energy band gap of annealed CIGS thin films for different thicknesses.

4.4.5 Electrical Characterization

The conductivity of an absorber layer plays an important role in the conduction mechanism of solar cells. Change in the resistivity mainly observed due to microstructural or surface modification of the film and the film thickness variation. Variation in the resistivity of the without annealed CIGS films observed by changing with the thickness is shown in Fig. 4.20. This figure shows that resistivity was reduced as the thickness increases. With that the improvement in the mobility values were observed may be due to the improvement in the crystallinity of the film. The resistivity was in the order of $10^2 \Omega\text{cm}$, mainly due to the cu-rich

composition of the films surface that was clearly from SEM and EDS analysis of our previous work [73].

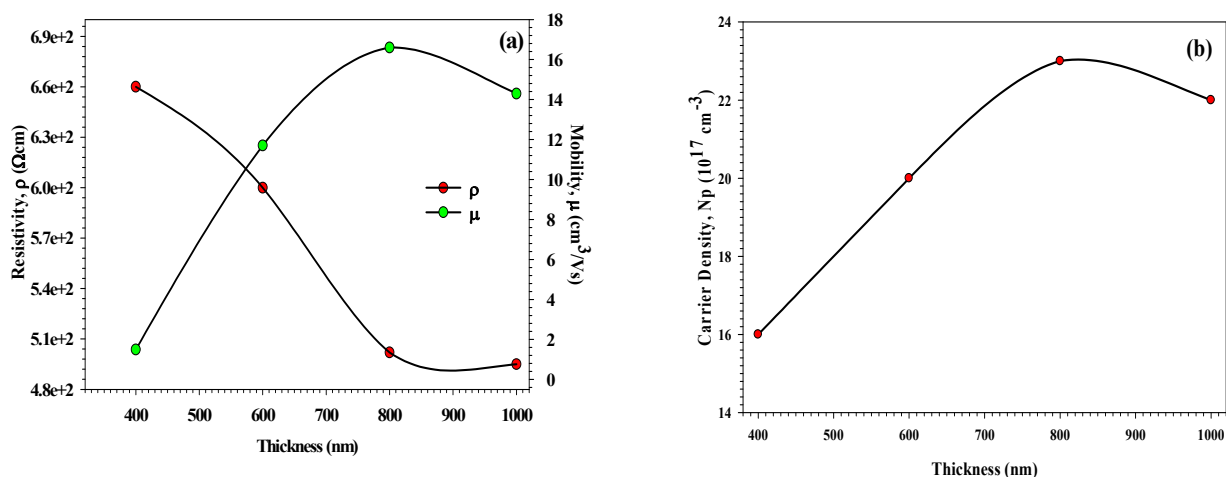


Fig. 4.20 (a) Resistivity, ρ , Mobility, μ , and (b) carrier density, N_p , of CIGS thin film of different thicknesses deposited at 250 °C.

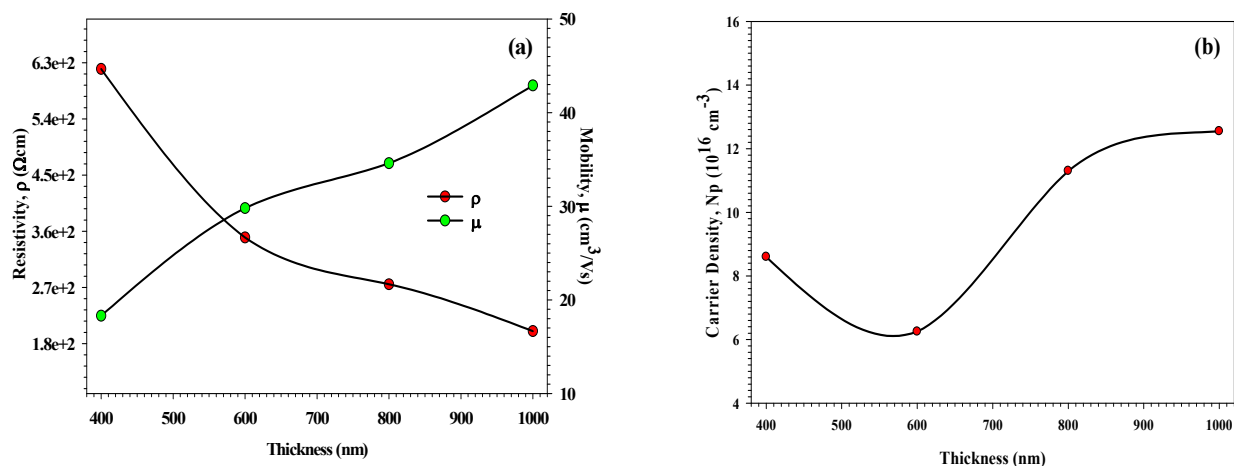


Fig. 4.21 (a) Resistivity, ρ , Mobility, μ , and (b) carrier density, N_p , of CIGS thin film of different thicknesses deposited at 250 °C and annealed at 500 °C.

Figure 4.21 shows the variation of resistivity and mobility of annealed CIGS thin film having a different thickness. This shows the significant reduction in the resistivity compare to the without annealed CIGS thin films. The reason for this may be found in an analysis of the SEM images. Higher temperature, the CIGS thin films experience a liquid-phase-assisted recrystallization process, which results in the uniform accumulation of the constituent atoms. Therefore, the grain boundaries decreases, and hence the resistivity of the thin film decreases. Improving the grain boundaries, reducing native defect centers and grain boundary defects [84], because of annealing, improves carrier mobility. All the samples' conductivity type was measured using hot probe method and exhibited p-type conductivity. That shows the device quality characteristics of prepared CIGS thin films [85].

4.5 CONCLUSIONS

CuIn_{1-x}Ga_xSe₂ (CIGS) (x = 0.3) was synthesized by melt quenching method successfully. Thin films of CIGS material are grown using the flash evaporation technique. The influence of substrate temperature, thin film thickness and the thermal annealing by rapid thermal process (RTA) are been investigated to achieve the device quality CIGS absorber thin film. RTA treated CIGS thin film shows device quality features, like the energy band gap valued near to 1.06 eV, p-type conductivity, resistivity in the order of 10² Ωcm, carrier mobility in the range of 2 to 42 cm³/Vs and the carrier density is of the order of 10¹⁶ to 10¹⁷ cm⁻³. These indicate its future use in the absorber layer in the thin film solar cell application.

Chapter 5

**CADMIUM SULPHIDE (CdS)
BUFFER LAYER: GROWTH AND
OPTIMIZATION**

5. CADMIUM SULPHIDE (CdS) BUFFER LAYER: GROWTH AND OPTIMIZATION

Cadmium sulphide (CdS) is a semiconductor compound of II–VI group. Thin film of CdS is widely used as a buffer layer in copper indium diselenide (CIS) hetero-junction based solar cells [86], transistors [87], photo detectors [88] and light emitting diodes [89]. Because of simple method of making thin film [90] by chemical bath deposition (CBD) [91] screen printing [92] and thermal evaporation [93] it is extensively used in the CIS based solar cells as a buffer layer. The buffer layer is used for reducing the interface recombination of the photo-generated carriers by means of improving the lattice mismatch between the layers. The optoelectronic properties of CdS thin films like, optical band gap, electrical resistivity, crystalline structure, and elemental composition etc., are to be considered for its use as a buffer layer. In the present study the CdS thin film were grown by thermal evaporation technique by varying the substrate temperature from 50 to 200 °C. The optoelectronics properties as listed above were optimized for its future use as a buffer layer in CIGS based solar cell.

5.1 NEED OF CdS BUFFER LAYER

As mentioned in chapter 1, buffer layer (n-type) is located between the CIGS absorber and intrinsic zinc oxide layer (i-ZnO). Fig. 1.4 and Fig. 1.6 clearly indicate the difference in the conduction band minima and valance band maxima between the CIGS and i-ZnO layers. The junction properties will improve by selecting the appropriate material, in the form of thin film, between CIGS and i-ZnO, which has the prior characteristics as following: less conductive for minimize the shunting of the photo-generated carries between the ZnO layer and the absorber layer [94]. Well matched lattice constant with the ZnO and absorber material to minimize the creation of defects at the junction. There is a belief that these lattice defects for the major recombination center for photo-generated carriers.

The literature survey for the suitable buffer layer for CIGS thin film solar cells shows that CdS is a kind of thin film that fulfills the maximal criteria and is used commonly for CIS, CIGS, CZTS based solar cells. Recently 20.3 % highest efficiency of CIGS thin film solar cell was reported using CdS as a buffer layer [9]. Apart from CdS many other materials

wildly available in the market and also used as a buffer layer like ZnS, ZnS(O,OH), In₂O₃, ZnSe etc.

5.2 THIN FILM PREPARATION

CdS thin films were grown by evaporating the CdS bulk material by thermal evaporation technique. Bulk of CdS material (99.995 % pure) is obtained from Sigma-Aldrich (U.S.A.). Thin films of CdS were grown on organically cleaned soda lime glass substrate by varying the substrate temperatures ranging from 50 to 200 °C. The thickness and deposition rate were observed in-situ using quartz crystal thickness monitor (DTM – 101, HIND HIVAC, Bangalore make). The deposition rate was kept near to 0.5 - 0.6 nm/s. The chromel-alumel thermocouple is used for the measurement of substrate temperature. We have used mica sheets as a mask for preparing CdS thin film of 1 cm² area.

The characterization part includes the structural characterization by an X-ray diffractometer (D8 Advance, Bruker make) in 2 θ range 20° - 70° at a scan rate 0.05° s⁻¹ with Cu K α (λ = 0.154 nm) radiation source and transmission electron microscope (TEM) (JEM-2100, JEOL make). The surface morphology and chemical analysis were carried out using scanning electron microscope (JEOL, JSM-5610LV) equipped with energy dispersive analysis of x-rays (EDS) facility. The optical measurement was carried out using the UV-VIS spectrophotometer (Shimadzu Analytical, India made) in the wavelength range 190 to 900 nm. The electrical characterizations were carried out using Hall-effect measurements at room temperature under normal light condition using programmable electrometer and nano-voltmeter, Keithley make.

5.3 EFFECT OF SUBSTRATE TEMPERATURE

5.3.1 Structural Characterization

X-ray diffraction (XRD) technique using CuK α radiation has been used for structural characterizations of CdS thin film deposited at different substrate temperature. Thin films of CdS can exist mostly in two crystalline modifications viz. the hexagonal (wurtzite) phase and cubic (zincblende) phase. For solar cell application, the hexagonal CdS thin films are preferable due to its excellent physical and chemical stability [95]. XRD spectra of CdS thin films deposited at different substrate temperatures are shown in Fig. 5.1.

The (002) plane of hexagonal structure was found to be the predominant phase at 2 θ = 26.7°. The preferred orientation of CdS films is observed due to the controlled nucleation process associated with the controlled deposition rate and substrate temperature. A

straightforward structural characterization of the as-deposited CdS film using XRD is difficult because of biphasic nature of CdS. The hexagonal phase of CdS films is more stable than the cubic phase [96]. To confirm the exact orientation of grown CdS grains TEM is carried out of the CdS thin film grown at 100 °C. The thickness of the film for TEM study was kept 70 nm; this enabled the films transparent to the electron beam. CdS thin film can be peeled off from the glass substrate using dilute hydrofluoric acid and set onto copper grid for TEM analysis. The typical selected area diffraction (SAD) of CdS thin film is shown in Fig. 5.2.

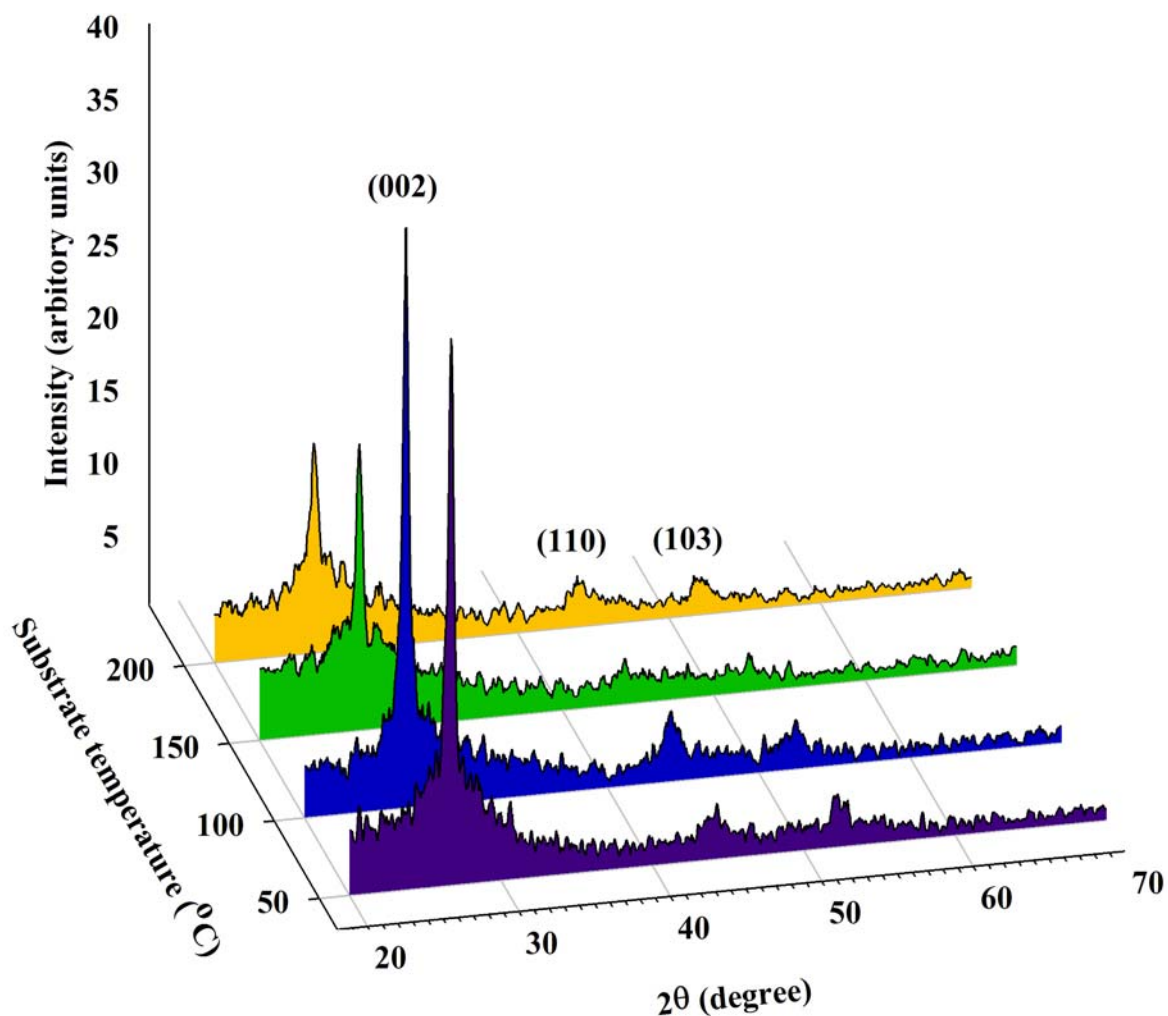


Fig. 5.1 XRD spectra of the CdS thin films deposited at different substrate temperatures ranging from 50 – 200 °C.

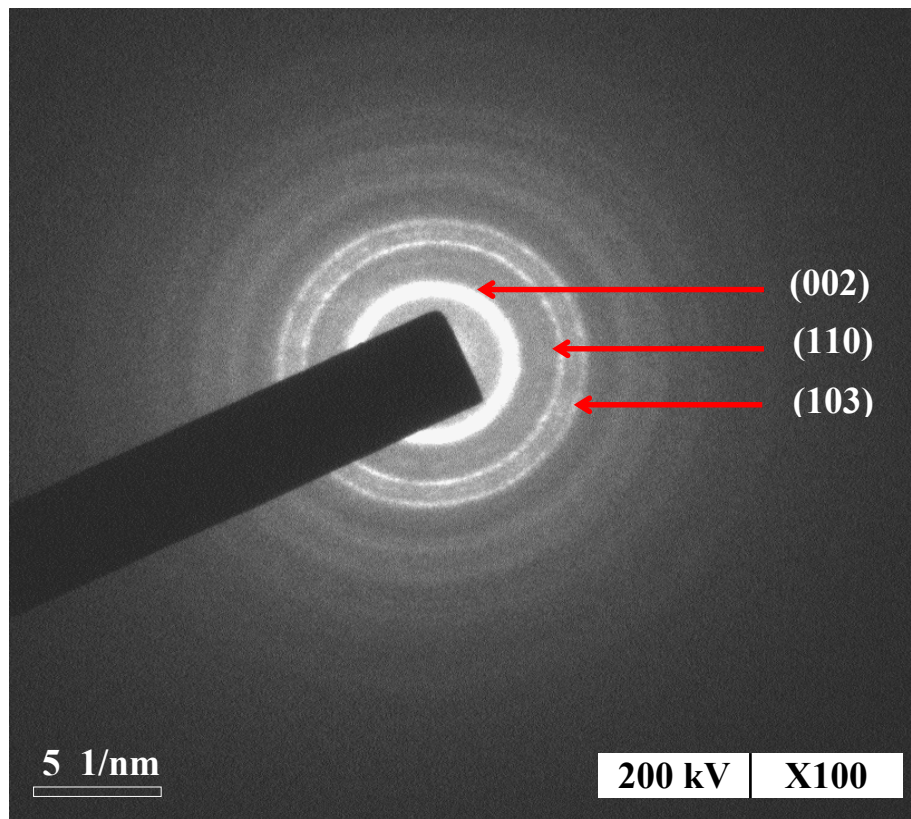


Fig. 5.2 SAD pattern of CdS film deposited at 100 °C indicated a (002) as a major crystalline plane.

The sharp and multiple numbers of circular continuous rings pattern indicate the polycrystalline nature of the films. The diameter of rings (D_{hkl}) in the SAD pattern is measured using the formula $d_{hkl} = 2\lambda L/D_{hkl}$, where L is the camera length and λ is the wavelength of the electron beam calculated from the accelerating potential. The calculated d -values corresponds to three characteristic major intensity peaks (002), (110), and (103) which matched well with those of the JCPDS data card 41-1049 of hexagonal α -CdS reflections. No secondary and cubic phase is observed from TEM. The very bright ring seen in SAD pattern due to the (002) plane indicates the preferred orientation along that direction. This agrees with the XRD study.

The crystalline size of CdS thin films deposited at different substrate temperatures are calculated from full-width half maxima (FWHM) of (002) peak, using the well-known Scherer's formula, after correction for the instrumental spectral broadening. The peak position of (002) plane, with its FWHM, along with the calculated values of the crystallite size, for films grown at different substrate temperature are shown in Table 5.1. The increase in the crystallite size was observed for increase in the substrate temperature up to 100 °C. On further increasing the substrate temperature the crystalline size reduces. The non-stoichiometry may be the reason due to the splitting of the compound or volatile nature of the CdS. The crystalline size for 200 °C is 30 nm.

Table 5.1 The 2θ values, FWHM and crystallite size, d , of (002) oriented CdS thin films grown at different substrate temperature.

Substrate Temperature (°C)	2θ (degrees)	FWHM (degrees)	Crystallite size, d , (nm)
50	27.31	0.4392	17
100	27.03	0.1742	51
150	27.05	0.1734	46
200	27.14	0.2765	30

5.3.2 Morphological Characterization

The surface morphology of the CdS thin films deposited at different substrate temperatures is studied using scanning electron microscope (SEM). Figure 5.3 shows SEM images of CdS thin films deposited at different substrate temperatures. All thin films look smooth, optically transparent, well adherent and light-yellow in color. The observation of SEM says that at substrate temperature 50 °C and 100 °C the surface of the film is smooth and homogeneous. But at 150 °C substrate temperature the cracking in the film is observed and it continues by further increase the substrate temperature up to 200 °C. The appearance of cracks in CdS thin films may be due to high tensile stress. A similar observation has also been reported by other workers for their CdS thin films [97] deposited using chemical bath deposition (CBD) method.

5.3.3 Compositional Characterization

The deviation from stoichiometry composition of CdS thin films was observed by the EDS. The stoichiometry composition greatly affects the optoelectronic properties like optical transmission, energy band gap, electrical resistivity etc. The observed values from compositional analysis of the CdS thin films deposited at different substrate temperatures is shown in Table 5.2. The ratio of cadmium to sulphur approaches to unity as the substrate temperature approaches 100 °C. The observed deviation in the sulfur content at the higher substrate temperature (at 150 °C) may be due to the volatile nature of sulfur. The deviation in the stoichiometry is clearly observed from the SEM images. Due to the high tensile stress observed at 200 °C (as shown in Fig. 5.3 (d)), the EDS could not be analyzed.

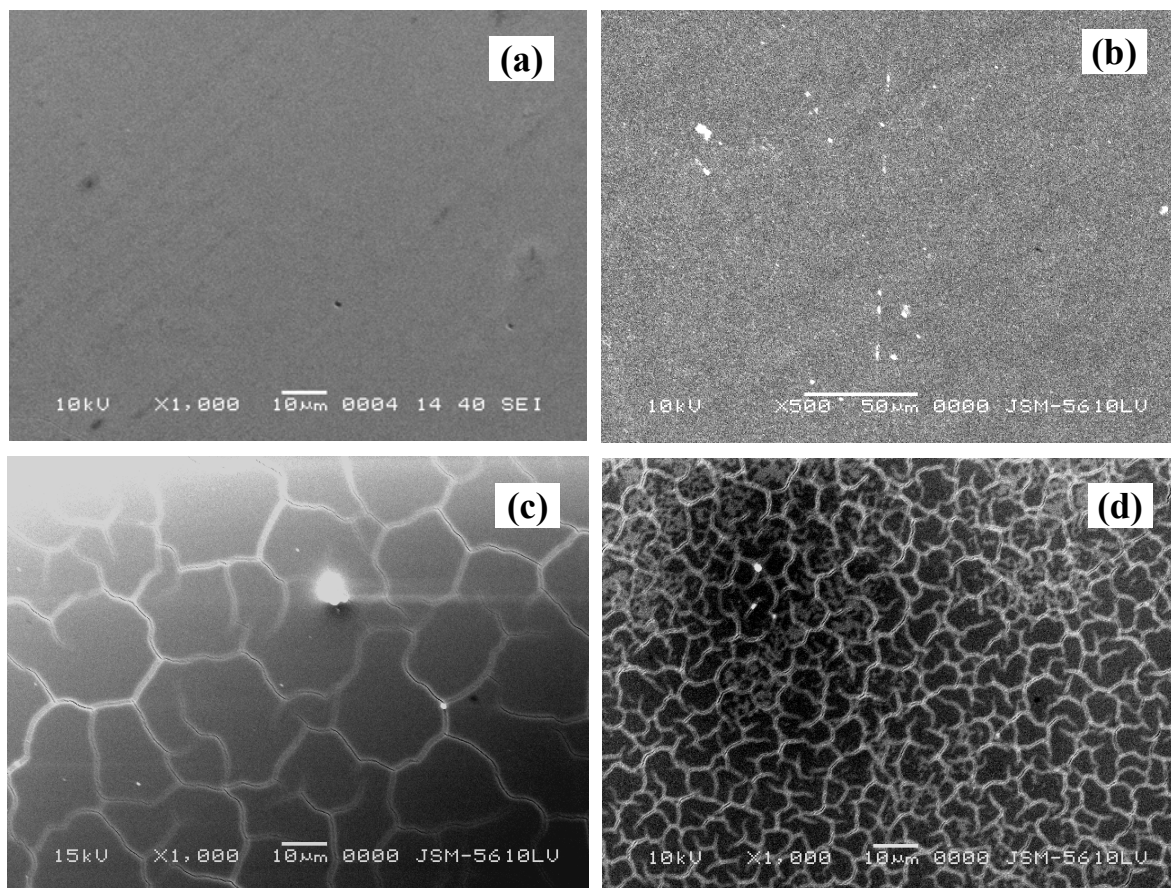


Fig. 5.3 SEM micrographs of CdS films deposited at different substrate temperature (a) 50 °C, (b) 100 °C, (c) 150 °C, and (d) 200 °C.

Table 5.2 EDS analysis of CdS thin films grown at different substrate temperatures.

Substrate Temperature (°C)	Elemental composition (at. wt. %)		Ratio Cd/S
	Cd	S	
50	49.09	50.91	0.96
100	49.93	50.07	0.99
150	49.33	50.67	0.97

5.3.4 Optical Characterization

For the optical characterization, we have measured the transmittance spectra of CdS thin films deposited at different substrate temperatures as shown in Fig. 5.4. All CdS thin film show average 80 % transmission in the visible region, which is essential to be for used as a buffer layer in the CIGS solar cell. By using the transmission spectra the energy band gap is calculated [98].

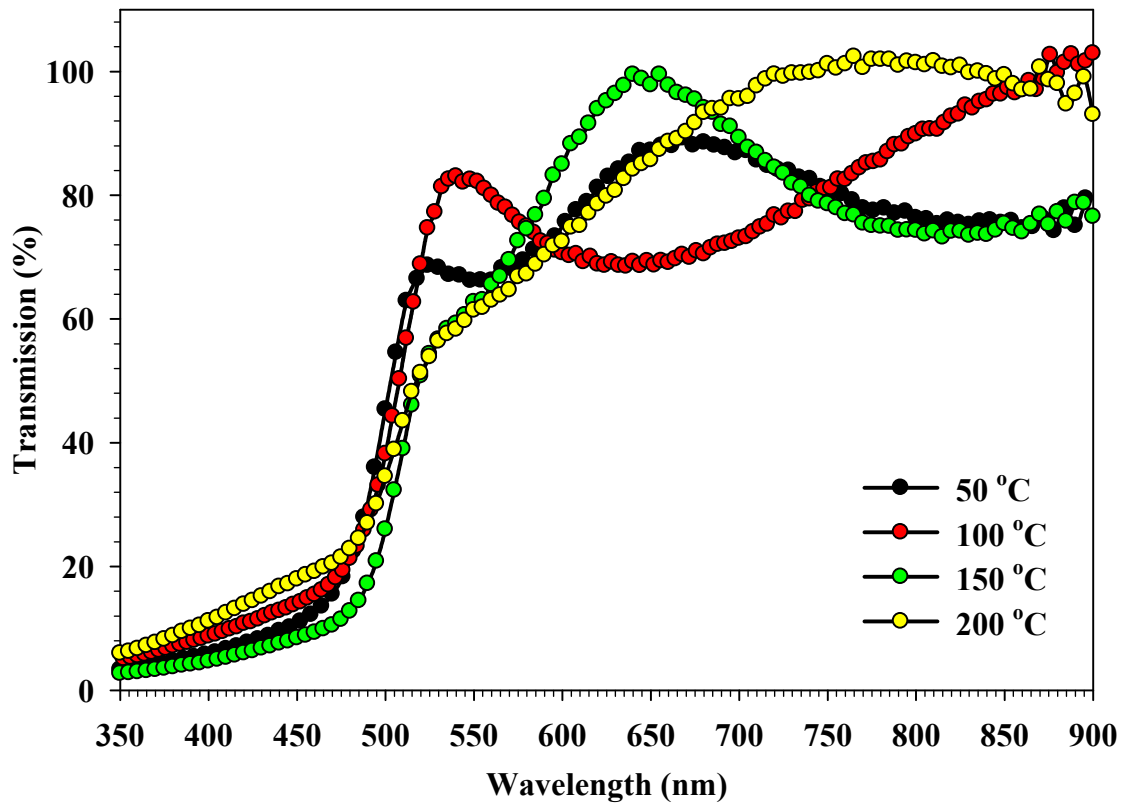


Fig. 5.4 Transmission spectra of CdS thin films grown at different substrate temperature indicating average 80 % transmission in the visible region.

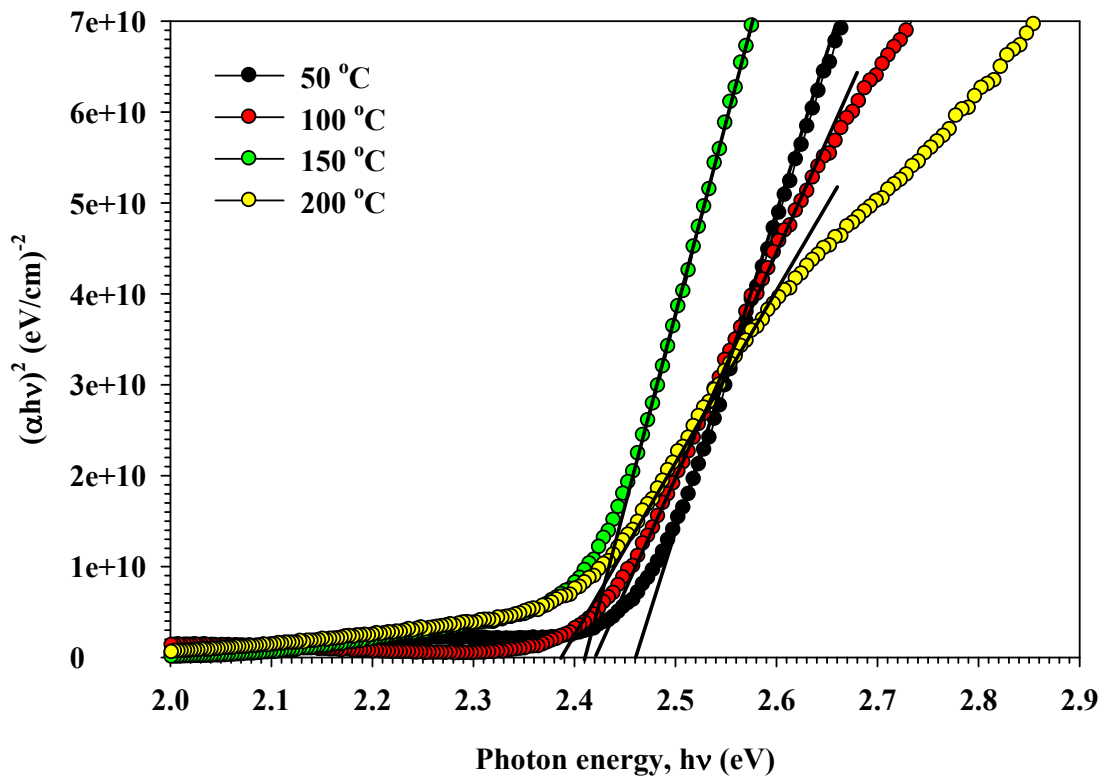


Fig. 5.5 Plots of $(\alpha h\nu)^2$ vs photon energy, $h\nu$ for CdS thin films grown at different substrate temperature reveals that the band gap decreases with the increasing the substrate temperature.

The plots of $(\alpha h\nu)^2$ versus photon energy $h\nu$ of CdS thin film grown at different substrate temperatures is shown in Fig. 5.5. The measured values of band gap are in the range 2.40 - 2.45 eV, which is in good agreement with the band gap values by many earlier works [99,100]. The reason for the variation in band gap of CdS films may be due to the various factors such as crystallite size, structural properties, stoichiometry deviations of the film etc. As the substrate temperature is increasing the band gap value is decreasing. At 50 °C the value of band gap is 2.46 eV while at higher substrate temperature, at 200 °C, it reaches at 2.39 eV. The noticeable reduction in the band gap can be related with the composition variation and surface morphology of the film surface. As the substrate temperature increases the compositional ratio of Cd and S is distorted due to that the crystalline size is significantly reduced and much deformation in surface morphology observed. At 100 °C substrate temperature the band gap value approaches the value of a single crystalline CdS (2.42 eV) [1].

5.3.5 Electrical Characterization

The electrical characterization includes the measurement of resistivity and mobility of the CdS thin film grown at different substrate temperature. Figure 5.6 shows the variation in the resistivity and mobility measured at room temperature. The value of resistivity is ranging from $1.3 \times 10^4 \Omega \text{ cm}$ to $7.9 \times 10^4 \Omega \text{ cm}$. The data show that the resistivity increased as the substrate temperature increased upto 100 °C, and then it decreases. The high resistivity of CdS films resulted from the good stoichiometry and the lack of defects. The observed order of resistivity is in the range of $\sim 10^4 \Omega \text{ cm}$, which is suitable for application of CdS films as a buffer layer in thin film solar cells based on CIGS. Similar kind of results of resistivity was observed for spray deposited CdS [101] and modified thermally evaporated CdS [102]. The electron mobility of CdS films increases with substrate temperature up to 150 °C and then afterwards it decreases. Similar behavior is reported by Kazamerski et. al. [103] for CdS films deposited using thermal evaporation technique.

The lower values of resistivity observed at the higher substrate temperature can be explained using Petritz's barrier model [104]. According to that, at lower substrate temperatures, the crystallites do not have sufficient thermal energy to grow large enough, while on higher substrate temperature provide enough thermal energy for growing larger crystallite of CdS, which ultimately decreased the inter-crystalline barrier and so the grain boundaries, therefore the resistivity values is low at higher substrate temperature.

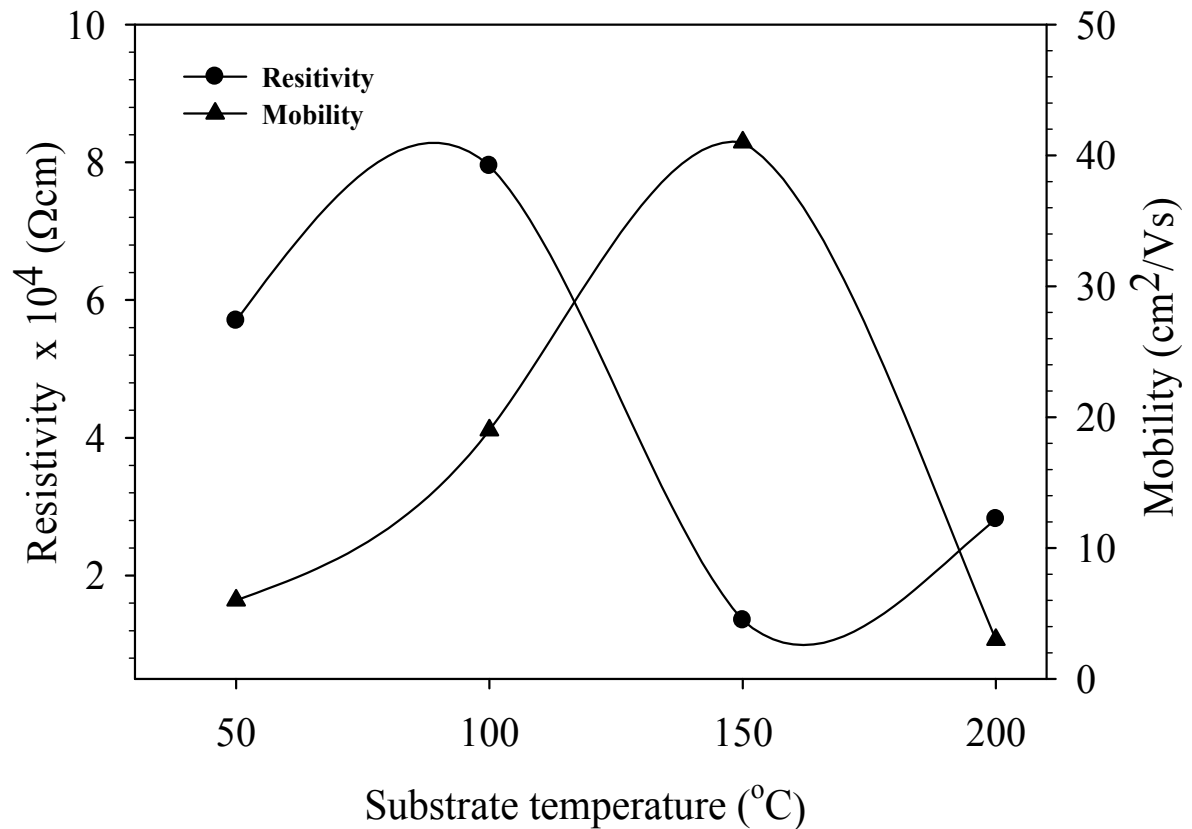


Fig. 5.6 Variation of Resistivity and mobility of CdS thin films deposited at different substrate temperatures.

5.4 CONCLUSIONS

Thin films of CdS were deposited on glass substrates at different substrate temperatures using thermal evaporation technique. The deposited CdS thin films showed good optical properties and adhered well to the substrates. The XRD and TEM of these films indicated that the deposited CdS film have hexagonal (wurtzite) structure. The highest crystallite size is found to be 51 nm for films deposited 100 °C substrate temperature. Analysis of SEM images indicates that above 100 °C substrate temperature the morphology has been distorted. With that the elemental composition is also distorted. The optical and electrical measurements show that the CdS thin film deposited at 100 °C have high transparency, energy band gap of 2.42 eV and high value of resistivity suitable for its' application as a buffer layer in CIGS thin film solar cell.

Chapter 6

ALUMINUM DOPED AND
INTRINSIC ZINC OXIDE (ZnO)
WINDOW LAYER: GROWTH AND
OPTIMIZATION

6. ALUMINUM DOPED AND INTRINSIC ZINC OXIDE (ZnO) WINDOW LAYER: GROWTH AND OPTIMIZATION

The optimization process of the RF magnetron sputtered Al-doped ZnO (AZO) thin films was carried out by studying its structural, optical, electrical, and morphological properties at different RF power and different working pressures for its use as a front-contact for the copper indium diselenide (CIGS) based thin film solar cell. The structural study suggests that the preferred orientation of grains is along the (002) plane having a hexagonal structure of the grains. The optical and electrical properties suggest that the films show an average transmission of 85 % and a resistivity of the order of 10^{-4} Ωcm . The morphology analysis suggests the formation of packed grains having a homogeneous surface. Also intrinsic ZnO (i-ZnO) thin films were grown by RF magnetron sputtering. The growth, structural, optical, and electrical properties of i-ZnO is studied.

6.1 NEED OF ZnO WINDOW LAYER

Thin films, which can be used as window layers in many optoelectronic devices, need to be transparent to the visible range of the light spectrum and be conductive enough. To date, the industry standard for transparent conducting oxide (TCO) is tin-doped indium-oxide (ITO). This material has a low resistivity of $\sim 10^{-4}$ Ωcm and a transmission greater than 80 %. However, in the field of solar cells, Al-doped ZnO (AZO) thin films have caught the attention for its use as a window layer because of its low cost and wide availability of its constituent raw materials compared to ITO. In the AZO thin films, the textured surface structure formation is easy compared to that in ITO [105], which increases the light trapping capability of the front surface of the solar cell and hence reduces the reflection losses. For the deposition of the AZO, the most commonly used technique is by radio frequency (RF) magnetron sputtering due to its high reproducibility [106, 107]. Besides, it permits the deposition to be carried out at low substrate temperatures, leading to smooth films with a good surface uniformity. Nowadays, there is an increasing interest in reducing the substrate temperature for many applications in order to minimize the inter-diffusion processes on prior deposited materials. Additionally, the use of flexible substrates such as plastic polymers replacing the conventional glass substrates becomes of great interest in the photovoltaic field as they contribute to cost reduction in the production processes [108].

In this study, we present the results regarding the optimization of AZO thin films deposited on soda lime glass substrate. The optimization process was performed by varying the RF power and working pressure and studying their influence on the structural, optical, morphological, and electrical properties, in order to achieve the highest transparency and lowest resistivity films. The outcome suggested its use as a window layer in the solar cell structure. To improve the performance of the CIGS based thin film solar cell a very thin layer of i-ZnO was placed between the CdS and AZO layer. The use of i-ZnO thin films in the CIS solar cells is to minimize the recombination of the photo-generated carriers at the CdS and AZO junction by means of reducing the lattice mismatch. Here we have used the optimized deposition parameter of AZO thin films for growing the thin i-ZnO thin films.

6.2 ALUMINUM DOPED ZINC OXIDE (Al-ZnO) THIN FILM PREPARATION

AZO thin films were optimized for the application of the Copper Indium Gallium diselenide (CIGS) thin film solar cells for the front-contact and with that i-ZnO thin films were optimized to reduce interface recombination of photo-generated carries using radio frequency (RF) magnetron sputtering system (HÜTTINGER Elektronik, 600 W, Germany). We have used a 50 mm diameter ceramic target of ZnO (doped with 2 % Al₂O₃) and i-ZnO. For the deposition of AZO thin films the vacuum chamber was first evacuated with a base pressure of 1×10^{-5} Torr using a vacuum coating unit (HINDHIGHVAC, model-15F6, Bangalore). By using the Ar gas flow (kept at 4 sccm constant), the pressure was controlled roughly and then by throttling the baffle valve a fine control on the chamber pressure was achieved. We have used mass flow controller (MFC) for the gas flow at constant rate made up from AALBORG, Germany. AZO thin films were grown on soda lime glass substrates. The glass substrates with a dimension of $50 \times 50 \text{ mm}^2$ were cleaned ultrasonically in a vapour of acetone, ethanol, and deionized (DI) water, followed by drying in blowing nitrogen. At the time of the deposition, we rotate the substrate at a speed of 40 rpm for the uniform coating of AZO thin film. Before the deposition, pre-sputtering was applied for 5 minutes at 5 mTorr pressure to remove the surface contamination of the AZO target. The source to substrate distance was kept 70 mm for all AZO deposition. The thickness of all AZO films was kept constant viz. 450 nm, which was measured in-situ by using the quartz crystal thickness monitor. No any external heat treatment applies during the time of the deposition. Structural, optical, and electrical properties of RF magnetron sputtered AZO thin films were analyzed using an X-ray diffraction (XRD) (D8 ADVANCE, Bruker AXS, USA), a UV-VIS spectrophotometer (Thermo Fisher Scientific, USA), and a four-point probe method using Keithley 2420C source meter, respectively. The best optimized condition of AZO thin film is also applicable

for making i-ZnO thin film. We kept the RF power constant at 100 W and the working pressure is 1 mTorr. Prepared i-ZnO thin films were characterized by same way as AZO thin films listed above in this section.

6.3 EFFECT OF RF POWER

6.3.1 Structural Characterization

The XRD spectrum of the AZO target is shown in Fig. 6.1. Through identifications of XRD, we found that all peaks presented in the spectra are from the ZnO crystal structure [109]. The XRD spectra of AZO thin films deposited at different RF power (80 W to 150 W) using AZO target is shown in Fig. 6.2. We have kept the working pressure constant at 10 mTorr.

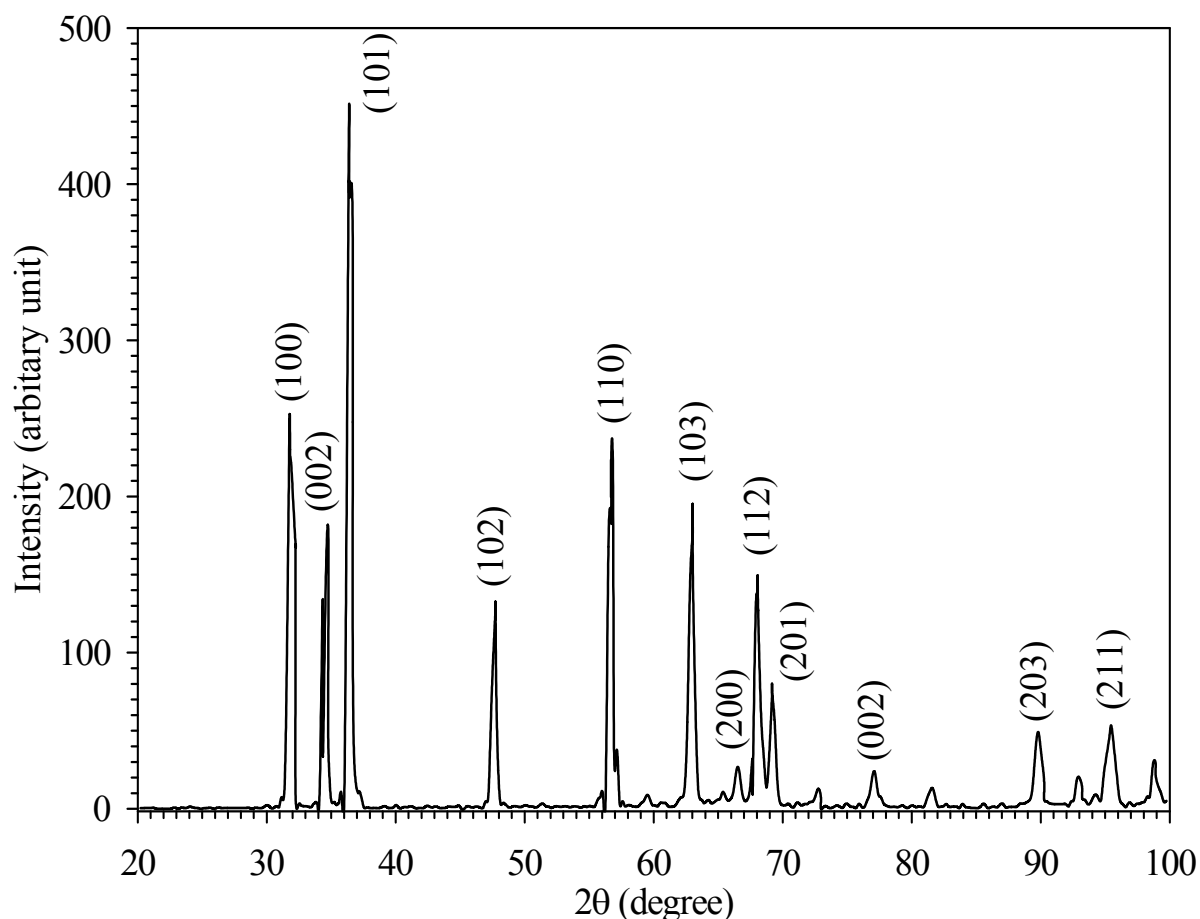


Fig. 6.1 The XRD spectra of the AZO target. The characteristic peaks well match with JCPDS data card 36.1451, confirm the wurtzite structure of ZnO.

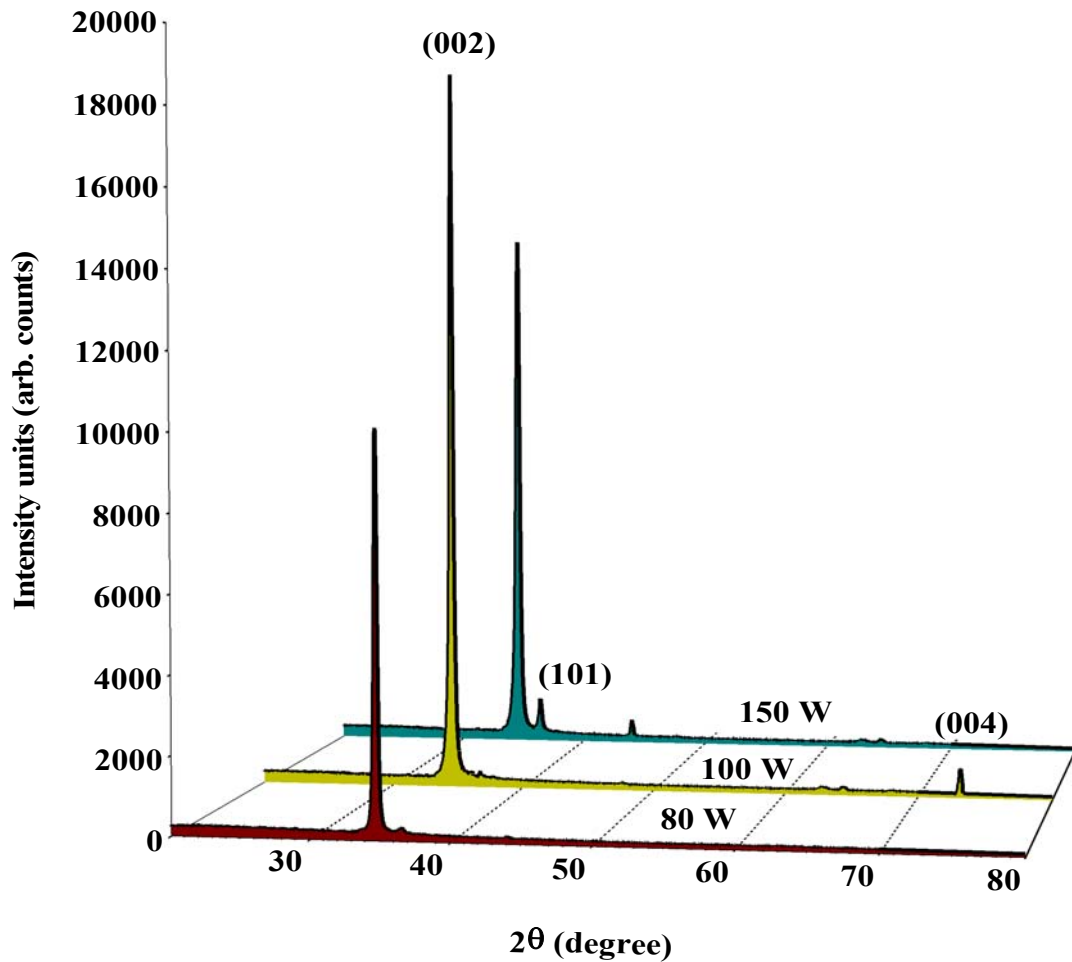


Fig. 6.2 The XRD spectra of the AZO thin films deposited at different RF power shows a preferred orientation along the (002) plane.

The XRD spectra revealed a strong preferred orientation of the (002) peak indicating that the films were orientated with their axes perpendicular to the substrate plane and having a hexagonal structure [109]. Small diffraction intensity from (101) and (004) planes are also present in the XRD spectra. As the RF power varies the deposition rate also varies with it. It was increased from 0.16 nm/s to 0.28 nm/s by varying the RF power from 80 W to 150W. From the XRD data, the average crystallite size (D) can be evaluated by the Scherrer's formula as follows [110],

$$D = \frac{0.9 \lambda}{\beta \cos \theta} \quad (6.1)$$

where, D is the crystalline size, λ is the X-ray wavelength (0.154 nm), θ is the Bragg angle, and β is the full-width at half-maximum (FWHM) of the AZO (002) diffraction peak. The crystallite size increases with increasing RF power. At 150 RF power, highest crystallite size of 10.18 nm was observed as shown in Table 6.1.

Table 6.1 The d-spacing, FWHM, and crystallite size of AZO thin films grown at different power keeping working pressure constant at 10 mTorr.

RF power (W)	d-spacing (Å)	FWHM (degree)	Crystallite size (nm)
80	2.56	0.95	8.50
100	2.55	0.85	9.66
150	2.56	0.79	10.18

In RF magnetron sputtering as the RF power increases the deposition rate increases because of the highly energetic ionized argon atoms bombarding on the target, which leads to an increase in the ejection rate of the sputtered atoms [111]. The XRD spectra of AZO thin films deposited at different RF power shows strong (002) diffraction peaks. Other peaks (004) with much less intensity were observed, indicating that the films are oriented with their c axis perpendicular to the substrate plane. The highest (002) peak value of AZO thin films was obtained at RF power of 100 W. The crystallite size of the AZO thin films was evaluated according to Scherrer's relation and found to be in range of 8.50 - 10.18 nm with the sputtering power ranging from 80 W to 150 W, and for highest value, 10.18 nm, was obtained at the power of 100 W. No Al₂O₃ related phase was found, which implied that Al atoms substitute Zn in the hexagonal lattice and Al ions may occupy the interstitial sites of ZnO or probably Al segregates to the non-crystalline region in grain boundaries and forms Al–O bond [112]. After 100 W, i.e. at 150 W in our case, we observed that the intensity of (002) peak decreases, due to deformation in the grains in the direction of (002) plane.

6.3.2 Optical Characterization

The influence of the RF power on the optical properties viz. transmission, energy band gap, E_g , and optical absorption, α , of the AZO films was analyzed. Figure 6.3 shows the transmission spectra of the AZO thin films deposited at different RF power i.e., from 80 W to 150 W. The average transmittance is ~80 % observed between 450 and 800 nm range (visible range). From the optical transmission data, the value of α , which provides the information of the band structure, is calculated from the lamberts law [113] and by using the transmission values the plot of $(\alpha h\nu)^2$ versus $h\nu$ is shown in Fig. 6.4 (a). The E_g can be obtained by extrapolating the straight-line portion of plots to the photon energy axis. The value of E_g for the as-deposited AZO films was in the range of 3.31 eV to 3.38 eV (Table 6.2). Figure 6.4 (b) shows the variation in α as a function of wavelength.

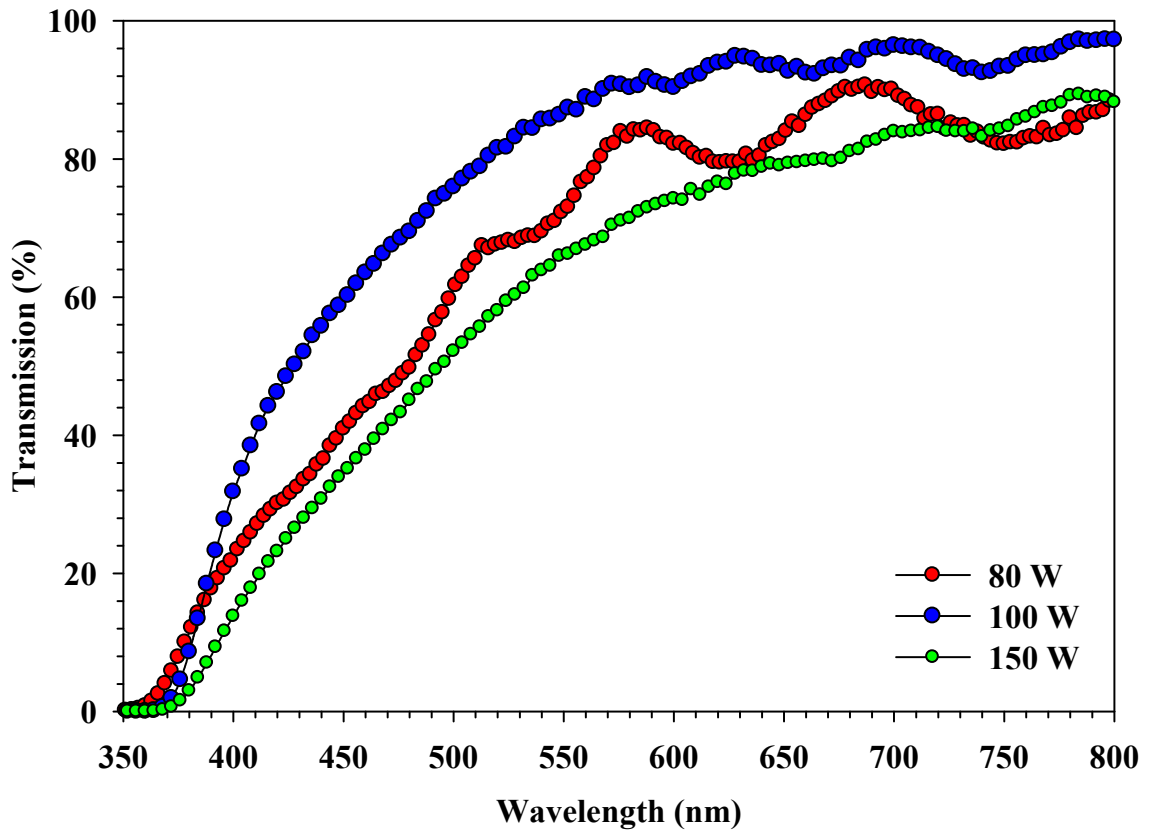
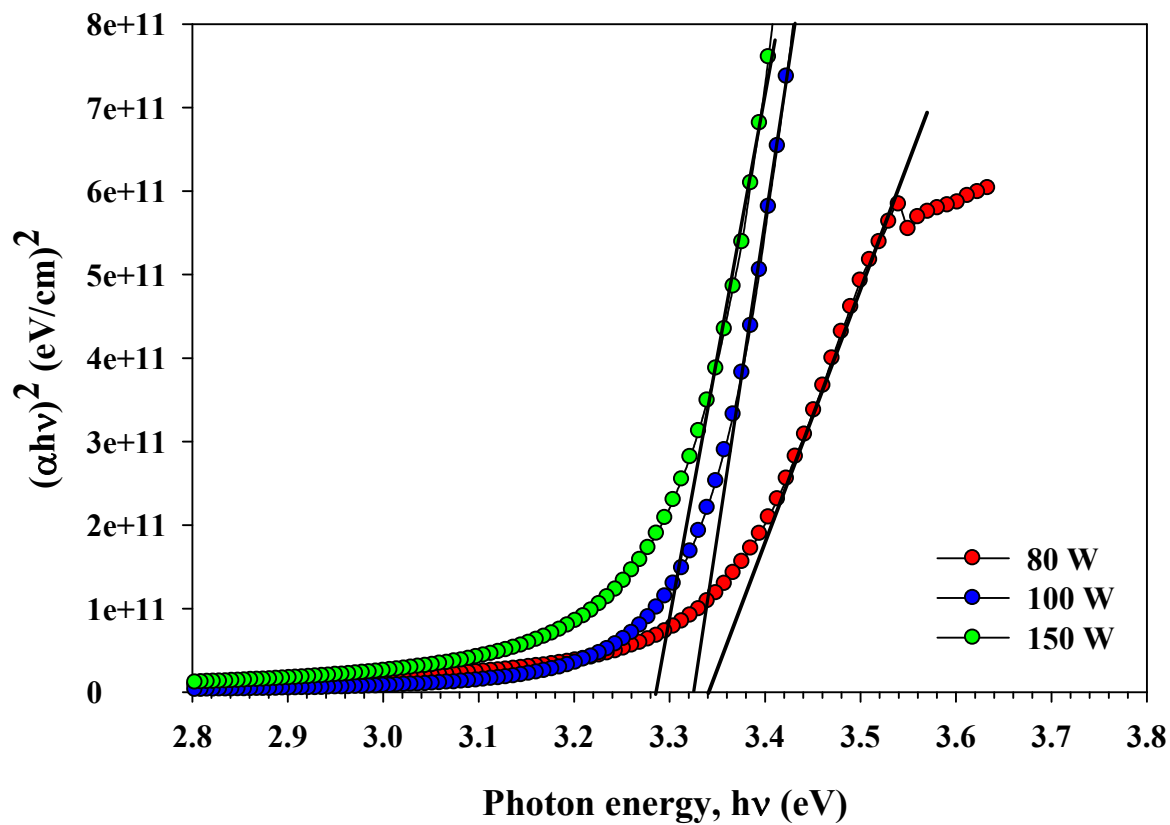
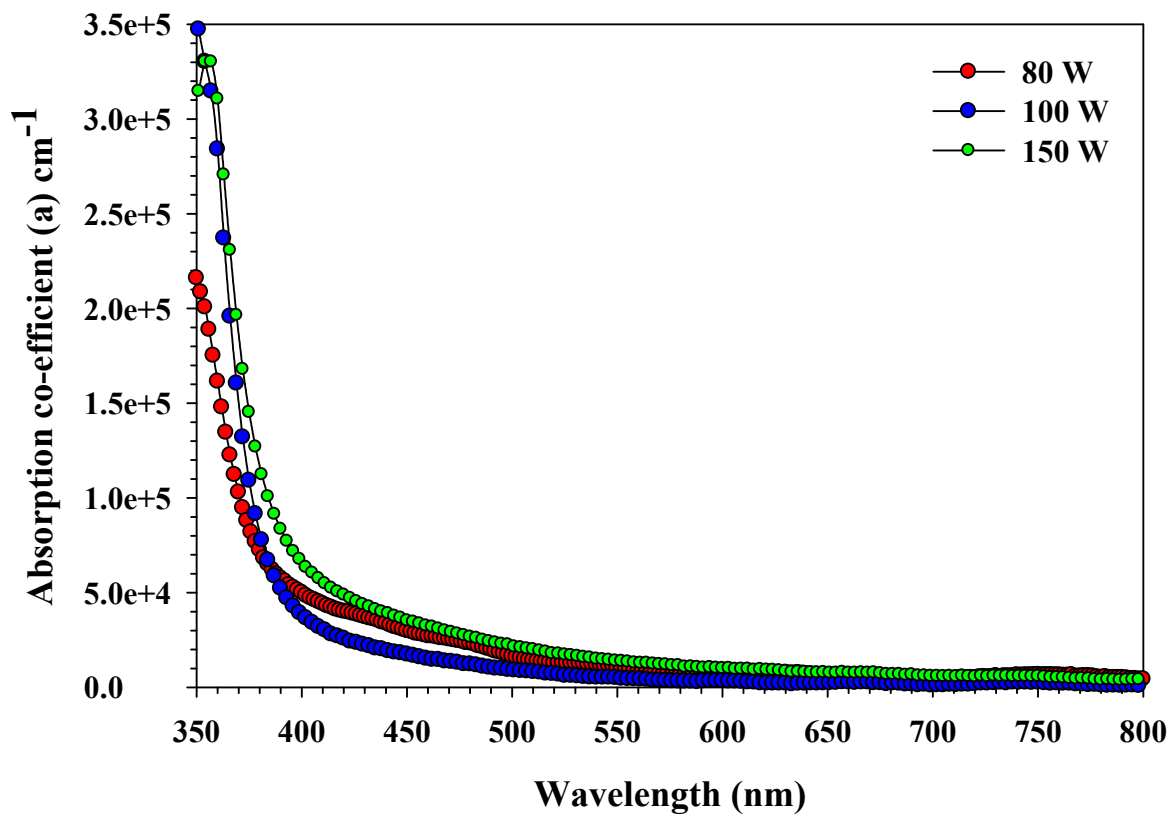


Fig. 6.3 The transmission spectra of the AZO thin films deposited at different RF power indicating an average transmission of 80 % over a visible region.

The transmission spectra of AZO thin film, Fig. 6.3, shows that at lower power, 80 W, there was a loss of transmission, which can be attributed to the limited solubility of the Al in the film. This is because of the reduction in the deposition rate at lower power. On increase the RF power, 150 W, due to the scattering of the light from the surface of the film, a loss of transmission observed. From the transmission spectra the calculated band gap values of our AZO thin films deposited at different power are higher than the value ($E_g = 3.25$ eV) of pure ZnO. It is generally believed that the Burstein-Moss effect [114, 115] plays a key role in this phenomenon: ZnO is a natural n-type material and the Fermi level would move into the conduction band when it is doped with Al. Since the states below Fermi level in the conduction band are filled, the absorption edge should shift to higher energies. With the sputtering power, increasing from 80 W to 150 W, as Fig. 6.3 shows, absorption edge shifts negligibly to shorter wavelength observed, which indicates an increase of carrier concentration, known as the Burstein–Moss shift [116].



(a)



(b)

Fig. 6.4 Plot of $(\alpha h\nu)^2$ versus $h\nu$ (a), and the variation in the absorption coefficient, α , (b) for AZO thin films deposited at different RF power.

The variation in the energy band gap and in the absorption coefficient is shown in Fig. 6.4 (a) and (b) respectively. It was observed from Fig. 6.4 (b) that, there was a negligible absorption of the photons in the visible region, which could be the important factor for its use as a window layer in solar cell.

6.3.3 Morphological Characterization

The surface morphology of the AZO thin film was observed using AFM. The morphology of the as deposited films indicates dense AZO grains, which is shown in Fig. 6.5. The surface morphology of the films i.e. the grain growth, depends upon the deposition flux, which increases, as the RF power increases. Due to that, the surface of the films becomes denser. The grain growth of the AZO thin films grown at different power is clearly observed from in Fig. 6.5. The surface roughness, as shown Table 6.2, increases from 17.73 nm to 36.77 nm as the RF power increases from 80 W to 150 W. The deformation of the grains observed at 150 W RF power is due to the higher deposition rate. The uniformity of the grains of AZO is found at 100 W RF power [116].

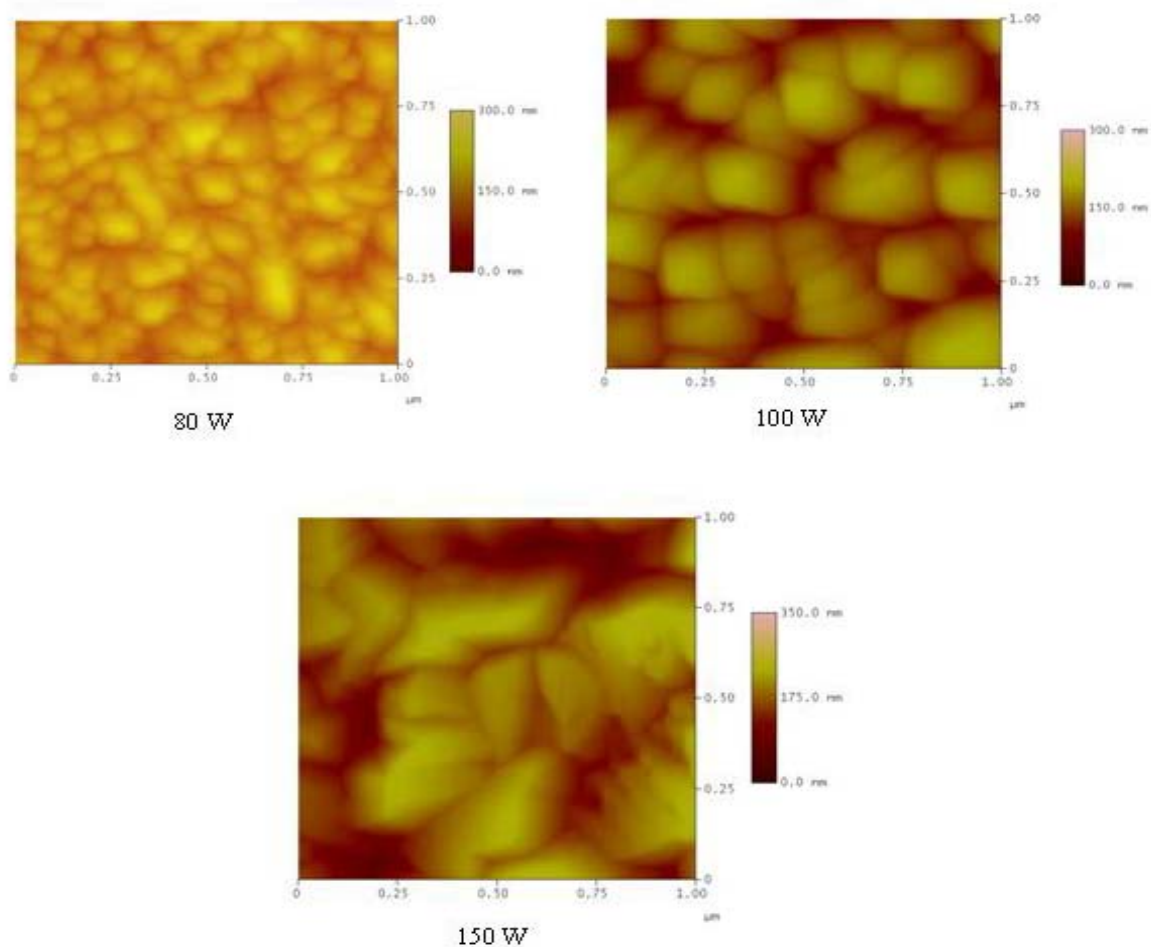


Fig. 6.5 The AFM images of the AZO thin films deposited at different RF power.

6.3.4 Electrical Characterization

For the use of AZO thin films as a window layer in the CIGS thin film solar cell, it has to behave as a metallic conductor. The sheet resistance (R_{sh}) and resistivity (ρ) of AZO thin films grown at different RF power were measured using the four-point probe method at room temperature. In addition, using the hot-probe method, we observed that all the AZO thin films showed n-type behavior.

Table 6.2 The variation in the values of energy band gap, sheet resistance resistivity and the surface roughness of AZO thin films, grown at 10 mTorr working pressure, as a function of RF power.

RF Power (W)	Energy band gap, E_g , (eV)	Sheet resistance, R_{sh} , (Ω/\square)	Resistivity, ρ , (Ωcm)	Surface roughness (nm)
80	3.35	50	1.5×10^{-3}	17.73
100	3.34	23	6.9×10^{-4}	26.14
150	3.32	16	4.8×10^{-4}	36.77

Traditionally, in the conduction mechanism of n-type ZnO, the intrinsic defects most commonly reported in the literature all the leading background donors in ZnO, namely the oxygen vacancy (V_o) and interstitial Zn (Zn_I) [117, 118]. For Al-doped ZnO films in our experiments, n-type conductivity will be enhanced by Al doping due to the contribution of extra free carriers via Al^{3+} ions substituting Zn^{2+} ions. The resistivity from four-point probe method was measured to be 1.5×10^{-3} , 6.9×10^{-4} , and 4.8×10^{-4} Ωcm , when RF power was 50, 100 and 150 W, respectively, tabulated in Table 6.2. It indicates that the resistivity decreases with increasing RF power. This, dependence of the resistivity on RF power, leads to an improvement in the nucleation, crystallinity, and the ionized donors, hence a better conductivity, of the films.

6.4 EFFECT OF WORKING PRESSURE

6.4.1 Structural Characterization

To study the effect of the working pressure, on the different properties of the AZO thin films, we have deposited the AZO thin film in the working pressure range of 2 to 20 mTorr at 100 W. By varying the working pressure, the deposition rate varies significantly. This is the key factor, which affect the properties of the thin films. In our case the deposition rate is higher (0.32 nm/s) for lower (2 mTorr) pressure and lower (0.15 nm/s) for higher pressure (20

mTorr). The XRD spectra of AZO thin film deposited at different working pressure (2 to 20 mTorr) at 100 W RF power is shown in Fig. 6.6.

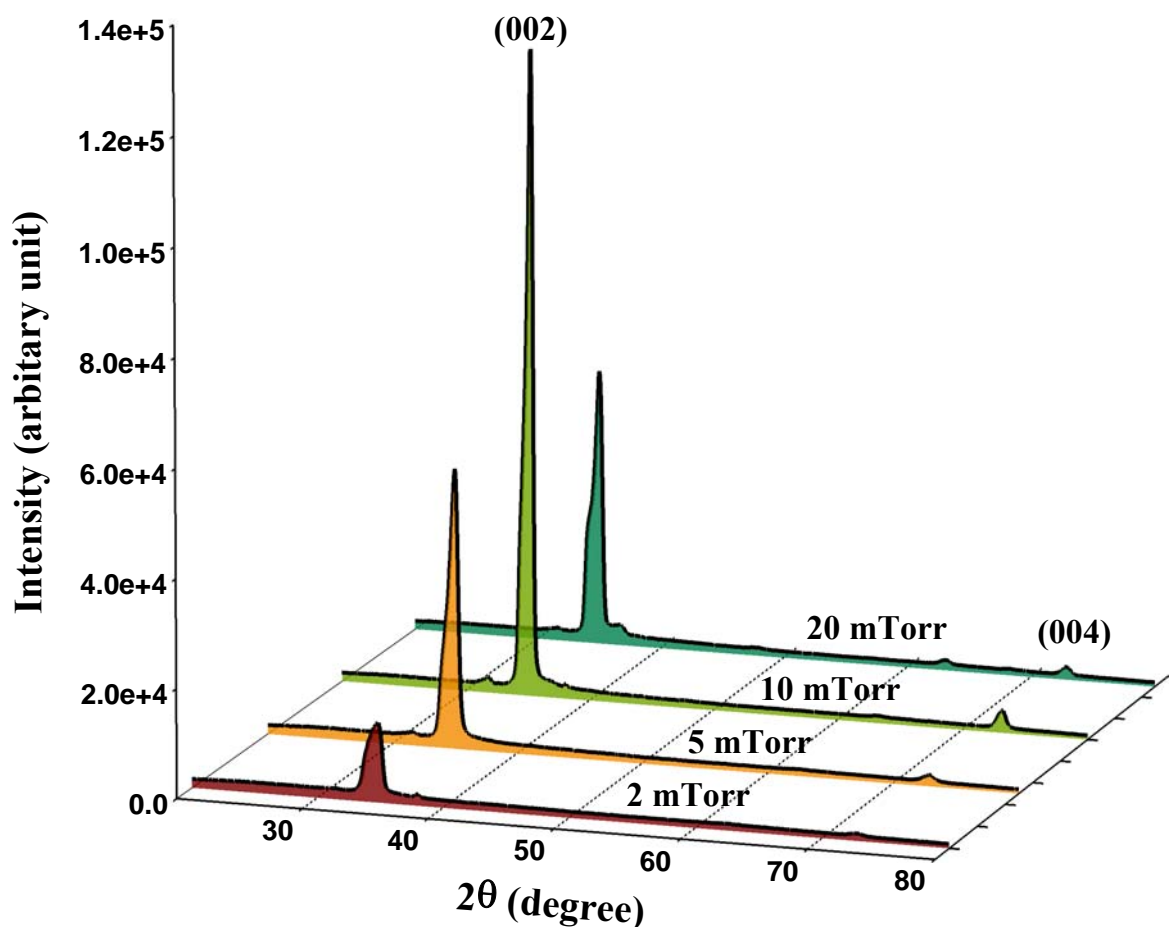


Fig. 6.6 The XRD spectra of the AZO thin films deposited at different working pressures.

All AZO thin films show a preferred orientation along (002) direction. The intensity of (002) peak is observed highest at 10 mTorr working pressure and the highest crystallite size viz. 9.66 nm are tabulated in Table 6.3.

Table 6.3 The d-spacing, FWHM, and crystallite size of the AZO thin films grown at different working pressure by keeping RF power constant at 100 W.

Working pressure (mTorr)	d-spacing (Å)	FWHM (degree)	Crystallite size (nm)
2	2.56	0.99	8.16
5	2.55	0.96	8.47
10	2.55	0.85	9.66
20	2.557	1.000	8.14

The XRD spectra of AZO thin films grown at different working pressures, Fig. 6.6, indicates that on increasing the working pressure from 2 mTorr to 10 mTorr the intensity of the (002) peak increases and by further increment in the working pressure i.e. at 20 mTorr the intensity decreases. In addition, other orientations, (101) and (004) are present in the XRD spectra. The improvement in the intensity of (002) peak up to 10 mTorr working pressure shows improvement in the crystallinity of the film, after that the intensity decreases. The crystallite size calculated from the Scherrer's formula is 8.16 nm for 20 mTorr working pressure and it is increased as the pressure increases and reaches at the maximum value of 9.66 nm. The variation in the crystallite size, FWHM, d-value and its corresponding 2θ value is tabulated in Table 6.3. The improvement in the crystalline quality of the films and the crystallite size show the enhancement in the possibility of Al doping in ZnO.

6.4.2 Optical Characterization

The optical transmission spectrum of AZO thin films grown at different working pressures is shown in Fig. 6.7. Using the transmission data, a plot of $(\alpha h\nu)^2$ vs. $h\nu$ and the variation in α as a function of wavelength are shown in Fig. 6.8 (a) and (b), respectively.

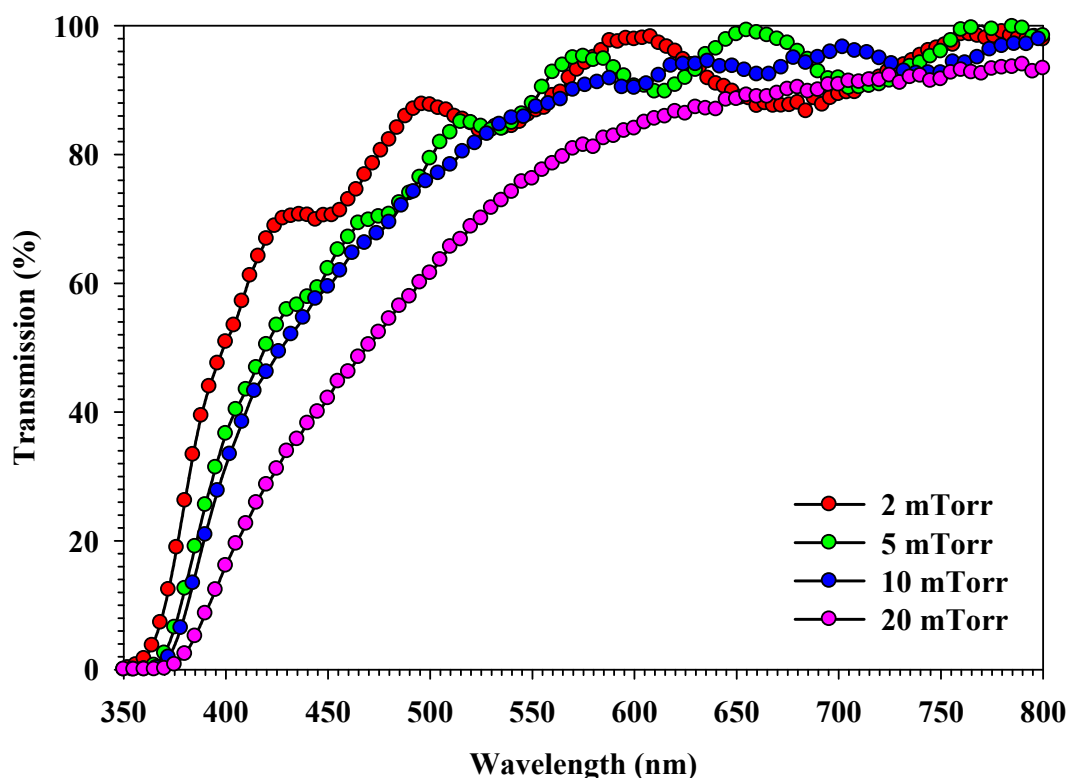


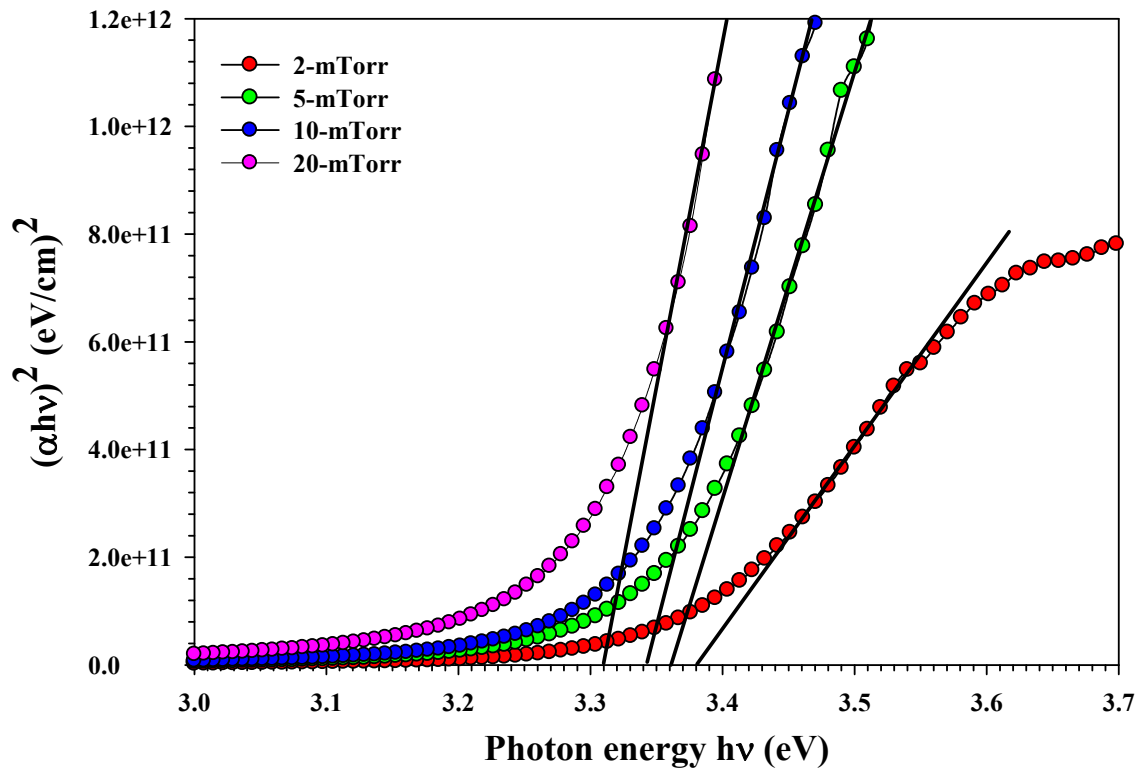
Fig. 6.7 The transmission spectra of the AZO thin films deposited at different working pressures.

The influence of the working pressure is clearly seen in the transmission spectrum of AZO thin films. The transmission is $\sim 85\%$ and the variation in the E_g is observed from 3.31

to 3.38 eV. The variation in the E_g as a function of working pressure is shown in Table 6.4. Looking at Fig. 6.7, the transmission spectra of AZO thin films deposited at different pressure, the drop of the transmittance towards the higher wavelengths indicates that the films were not fully oxidized but it contained metallic (Al) inclusions. It directly impacts on the energy band gap of the films. As the pressure increases from 2 mTorr to 20 mTorr the energy band gap decreases from 3.38 eV to 3.31 eV, which is shown in Fig. 6.8 (a). This behaviour can be explained by examining the dependence of the Al inclusion as a function of working pressure. The variation in the absorption coefficient is shown in Fig. 6.8 (b).

Table 6.4 The variation in the values of energy band gap, sheet resistance resistivity and the surface roughness of AZO thin films, grown at 100 W RF power, as a function of working pressure.

Working pressure (mTorr)	Energy band gap, E_g , (eV)	Sheet resistance, R_{sh} , (Ω/\square)	Resistivity, ρ , (Ωcm)	Surface roughness (nm)
2	3.38	50	1.5×10^{-3}	19.21
5	3.36	37	1.1×10^{-3}	23.29
10	3.34	23	6.9×10^{-4}	26.14
20	3.31	29	8.7×10^{-3}	22.70



(a)

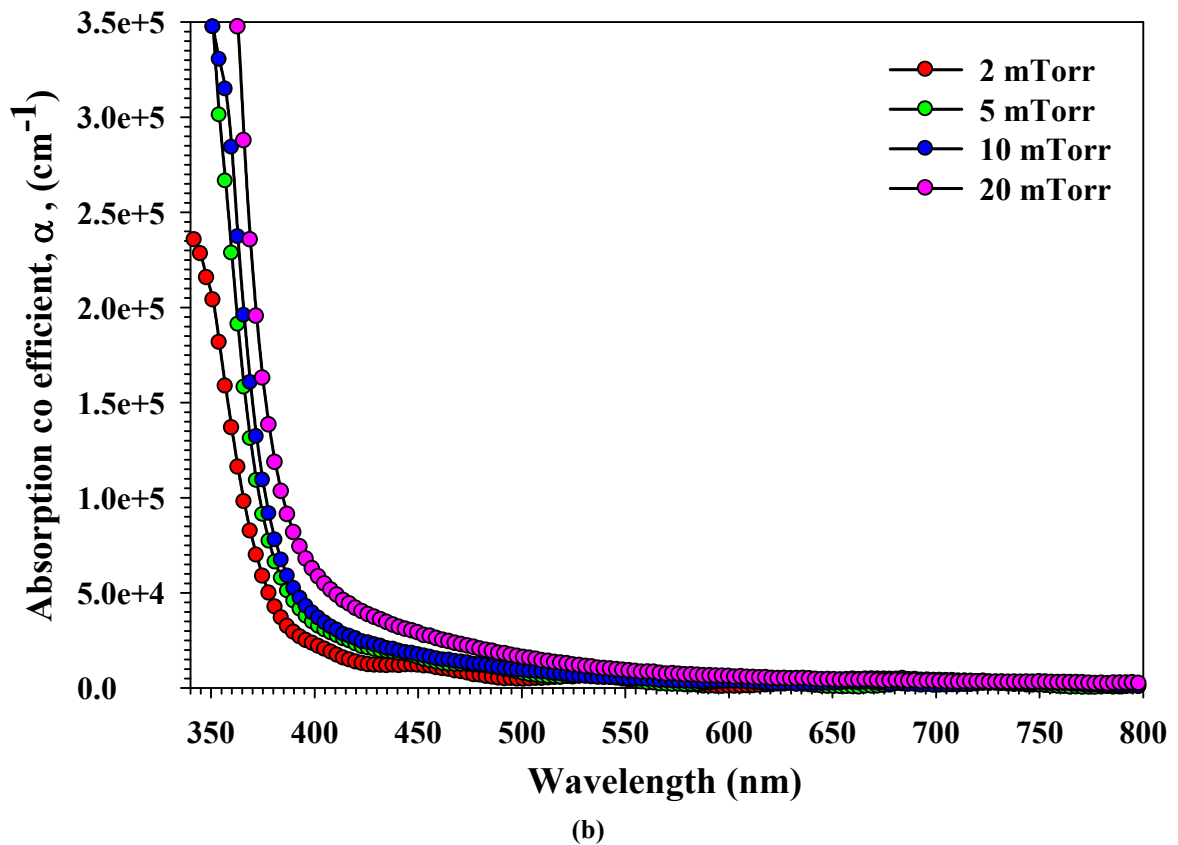


Fig. 6.8 Energy band gap values (a), Variation in the absorption coefficient, α , (b) for AZO thin films deposited at different working pressures.

6.4.3 Morphological Characterization

Figure 6.9 shows the AFM image of the AZO thin films grown at different working pressures at 100 W RF power. As shown from the AFM images, the morphology is influenced by the working pressure significantly. The grain growth depends upon deposition flux, which was higher at lower working pressure due to the less scattering probability of the sputtered and gas atoms. Therefore, as the bombardment of energetic particles increases, that leads to a non-uniform growth of the grains are observed from the AFM images of 2 mTorr pressure. Reduction in the gas pressure results in the decrease of energetic particle bombardment, which was responsible for the uniform grain formation. The increased surface roughness from 19.21 nm to 26.14 nm by increasing the working pressure 2 mTorr to 10 mTorr is likely an indicator of increased grain size, consistent with the X-ray diffraction data. The variation in surface roughness is tabulated in Table 6.4.

6.4.4 Electrical Characterization

The variation in the sheet resistance (R_{sh}) and the resistivity (ρ), from Table 6.4, suggests that its future use as a front top metallic contact in the CIGS thin film solar cell. As the pressure

increases from 2 mTorr to 10 mTorr the R_{sh} decreases from 50 to 23 Ω/\square . At 10 mTorr the resistivity was $6.9 \times 10^{-4} \Omega\text{cm}$. The decrease in the sheet resistance can be explained by the increment in the surface roughness of the film. As the roughness increases due to the increment in the average grain size and so, the grain boundary reduces, which decreases the sheet resistance.

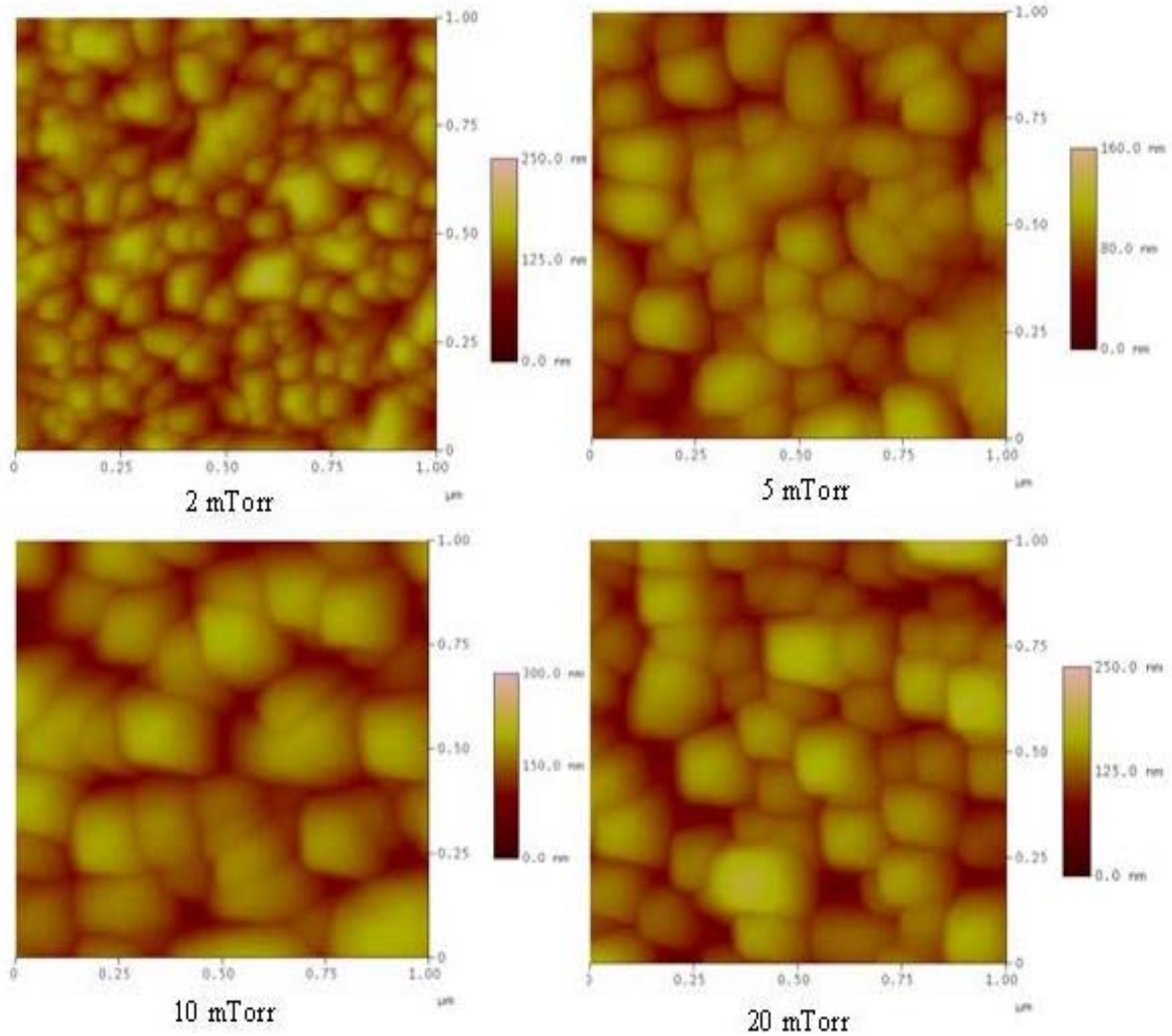


Fig. 6.9 The AFM images of the AZO thin films deposited at different working pressures.

6.5 INTRINSIC ZINC OXIDE (i-ZnO) THIN FILM PREPARATION

i-ZnO Target Preparation: High-quality sputtering targets are important in obtaining superior thin film properties. Transparent conducting oxide thin film targets can be divided into two types - metal targets and powder oxide-sintering targets. If metal targets are adopted, then oxygen gas must be first introduced into the chamber to form a thin-film oxide through chemical reactions. However, this method does not easily yield stable quality deposited film. Therefore, a powder oxide-sintering target is preferred [119]. Three conventional methods

viz. using a hot press, a hot isostatic press and normal sintering, exist for making powder oxide sintering targets.

ZnO powder (99.99 %) obtained from Sigma-Aldrich (U.S.A.) is used to prepare i-ZnO target. ZnO powder is dry-pressed or palletized by applying a force of 5 ton for three minutes in 51 mm diameter stainless steel die using droplets of acetone as binding material. The resultant disc shaped pellet (target) has 50 mm (± 1 mm) diameter. The target is first sintered at 400 °C temperature in an electric furnace at atmospheric pressure. The heating rate of furnace is kept at 4 °C per minute. The target is maintained at elevated temperature for six hour after which the temperature of the furnace is allowed to cool down to the laboratory temperature at the same rate. The shrinkage of the target is developed. Therefore, the target is crushed to powder using pestle and mortar. The sintered powdered material is then used to prepare the pellet (target) again. The target is sintered at 1150 °C for twenty-four hours. The sintered target is then ready for the deposition. The crystalline structure of i-ZnO target is investigated by X-ray diffraction (XRD) analysis in 2θ range from 20° to 100°. Figure 6.10 shows the XRD pattern of i-ZnO target. All major peaks for Zinc Oxide are identified in the XRD and agree well with the JCPDS data card no. 36-1451.

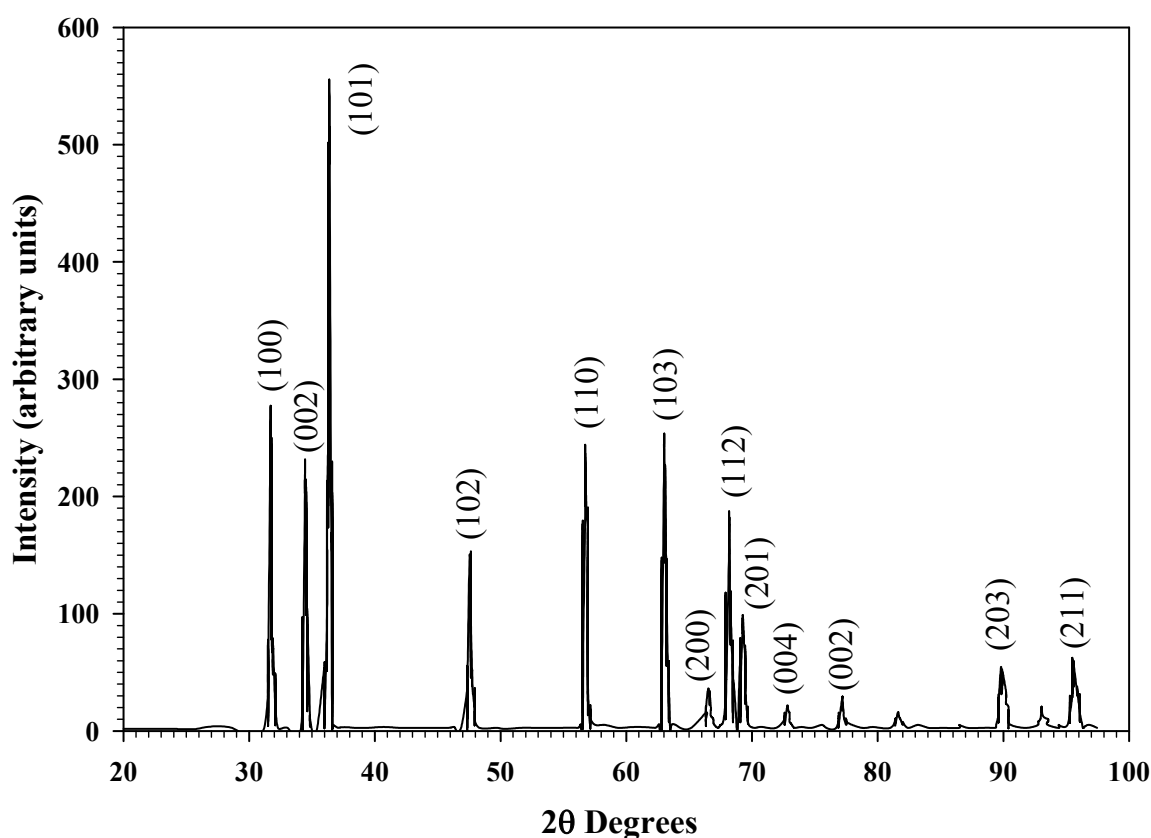


Fig. 6.10 XRD spectrum of i-ZnO target.

i-ZnO Thin Film Preparation: The front contact of CIGS based thin film solar cell consists of a highly conductive AZO layer on top of a highly resistive layer of i-ZnO. The very thin high resistive layer of i-ZnO prevents a shunt path between the molybdenum back contact and the aluminum doped zinc oxide front contact. For CIS based solar cell device application thickness of i-ZnO layer and its' resistivity are important parameters. The correlation of the cell performance of CIS based solar cells with the thickness of highly resistive i-ZnO layer had been studied in detail by S. Ishizuka et al. [120]. Their study reveals that the efficiency of CIGS based thin film solar cell depends on i-ZnO thickness, and the highest efficiency is achieved when the thickness of i-ZnO layer is about 70 nm. In the case where i-ZnO layers are thinner than 40 nm, a slight degradation in cell performance was observed and cell efficiency reproducibility worsened. On the contrary, when i-ZnO layers were thicker than 70 nm, cell efficiency again degraded. In this study, we have deposited i-ZnO thin film of 70 nm thickness on glass substrates. We set the target substrate distance 50 mm, sputtering power is 100 W, deposition pressure is 1 mTorr. The deposition is carried out under the argon environment and no pre-heat treatment given to the substrate before deposition. The resistivity of i-ZnO thin film is $4.7 \times 10^5 \Omega\text{cm}$. The value of resistivity is close to the reported value for CIGS solar cell application by researchers [121]. The structural, morphological, and optical properties of i-ZnO thin film are investigated.

6.5.1 Structural Characterization

The crystalline structure and orientation of the i-ZnO thin film is investigated by X-ray diffraction (XRD) analysis, in 2θ range 20° - 80° at a scan rate $0.05^\circ \text{ s}^{-1}$ with Cu K_α ($\lambda= 0.154$ nm) radiation source. Figure 6.11 shows the XRD pattern of i-ZnO thin film deposited on glass substrate. Major peak is observed at diffraction angle $2\theta = 34.421^\circ$. This diffraction angle corresponds to (002) plane of reflections. JCPDS data card (file 36-1451) reveals that the film has strong c-axis orientation and hexagonal structure.

6.5.2 Optical Characterization

Figure 6.12 depicts transmission spectrum of i-ZnO layer. In order to obtain highly resistive i-ZnO layer deposition is carried out at higher deposition pressure. It is seen that i-ZnO layer exhibited very high transmission (above 85 %) in the visible range. The optical band gap of the film is calculated using plot of $(\alpha h\nu)^2$ vs. $h\nu$ (shown in Fig. 6.13). The value of energy band gap for i-ZnO thin film can be estimated by extrapolating the linear portion of the absorption edge with energy axis to find the intercept. Energy band gap of i-ZnO thin film

using the linear fit is 3.25 eV. It is in good agreement with the reported value by researchers using different deposition techniques [122, 123, 124].

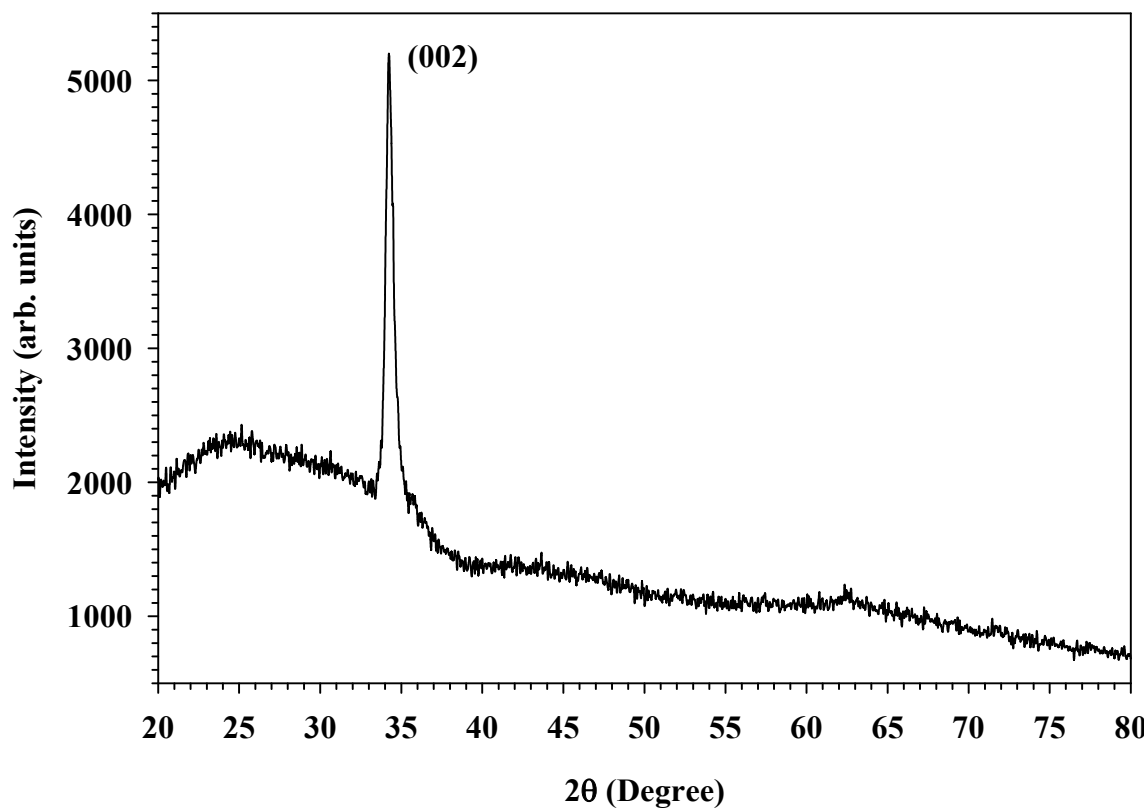


Fig. 6.11 X-ray diffraction pattern of i-ZnO thin film shows the preferred orientation of (002) plane.

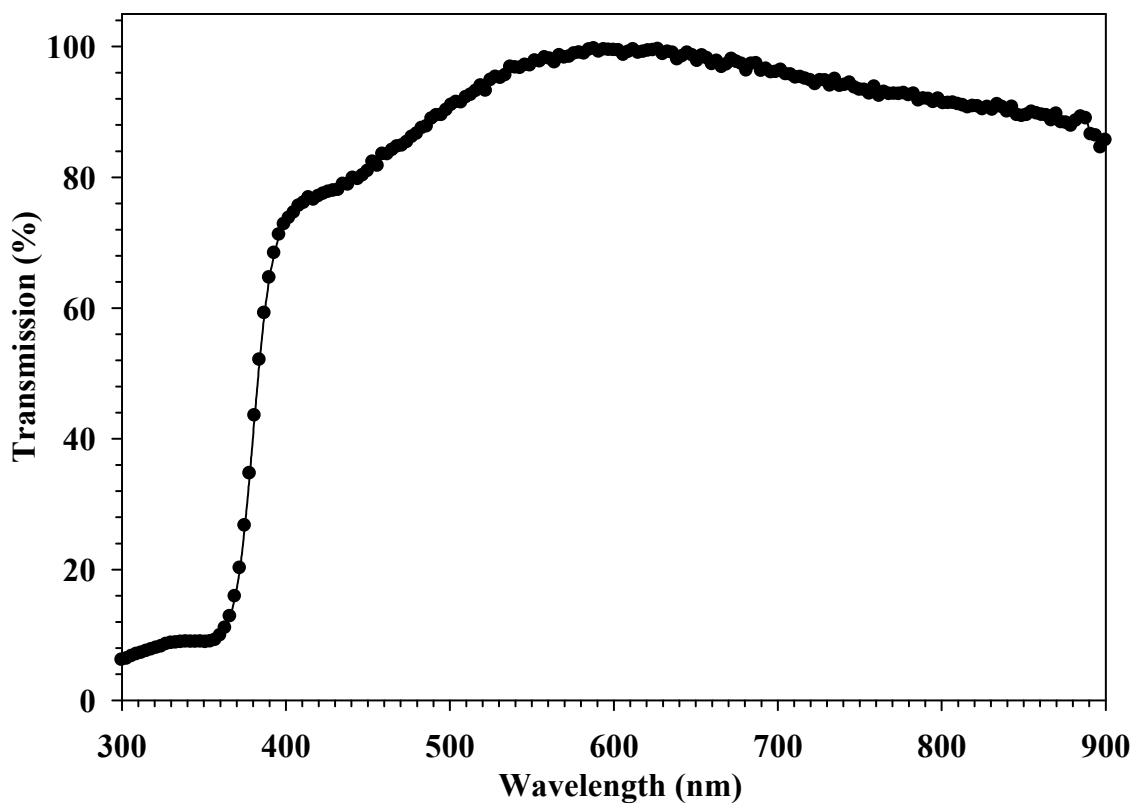


Fig. 6.12 Transmission spectrum of i-ZnO thin film showing the >95 % of transmission in visible range.

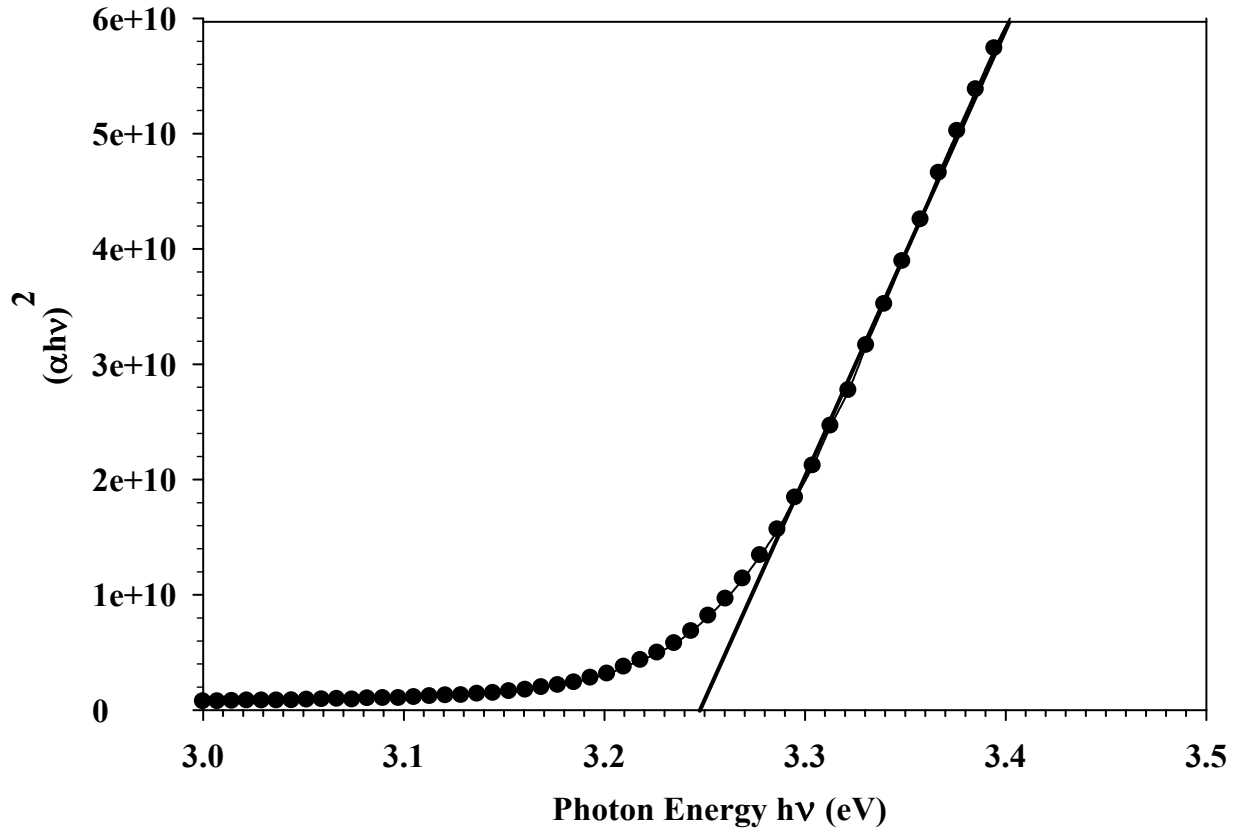


Fig. 6.13 Energy band gap of i-ZnO thin film. Sharp transition observed at 3.25 eV of photon energy.

6.5.3 Morphological Characterization

The morphological characteristic of i-ZnO thin film is studied using atomic force microscope. Figure 6.14 shows two and three-dimensional AFM images of i-ZnO thin film. AFM image of the film reveals a structure with dense grains. The irregular shape of the grains suggests that the kinetic energy of molecules reaching the substrate is not sufficient for the coalescence of the grains. The surface roughness of the film approximated from AFM analysis is 4 nm.

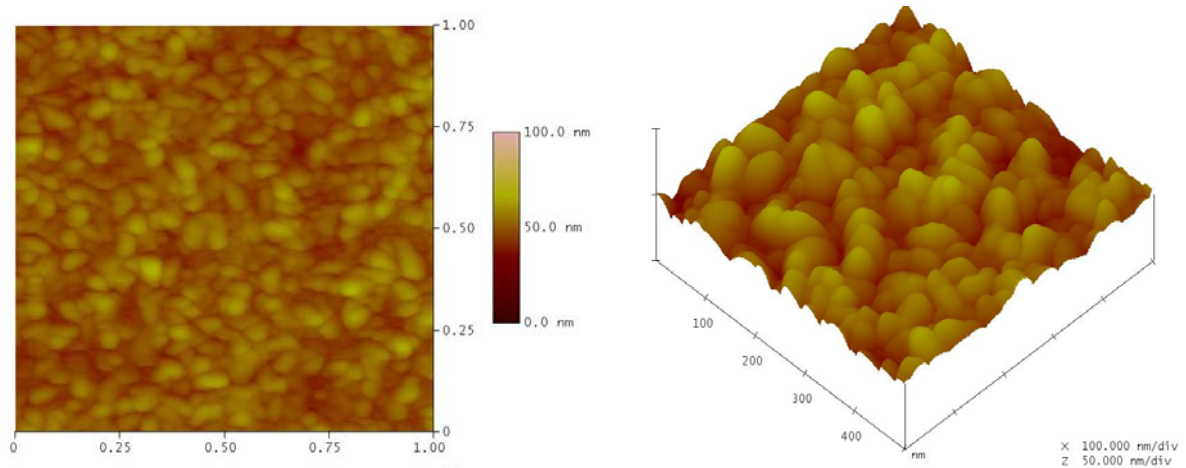


Fig. 6.14 AFM image of i-ZnO thin film showing the rough morphology with identical shaped grains.

6.6 CONCLUSIONS

AZO thin films have been obtained by RF-magnetron sputtering by varying the RF power and the working pressure. The structural, optical, electrical, and morphological properties of AZO thin films were analyzed. The obtained films were polycrystalline and had a preferred orientation with the c-axis perpendicular to the substrates. The lowest resistivity of $6.9 \times 10^{-4} \Omega\text{cm}$ is obtained at 100 W RF power and 10 mTorr working pressure. Transmission measurement shows that all films are highly transparent (~85%) in the visible region. Highly packed uniform grain structure was observed at 100 W at 10 mTorr working pressure. This work demonstrates the future use of Al doped zinc oxide (AZO) thin films as a window layer as well as a front-contact for the CIGS solar cell. Intrinsic ZnO (i-ZnO) layer also shows the preferred orientation as the AZO film shows. High resistive and above 85 % transmission in the visible region makes it most preferable to improve the performance of the CIGS thin film solar cell.

Chapter 7

**FABRICATION OF CIGS THIN
FILM SOLAR CELL DEVICE AND
ITS CHARACTERIZATION**

7. FABRICATION OF CIGS THIN FILM SOLAR CELL DEVICE AND ITS CHARACTERIZATION

The solar cell structure based on copper indium gallium diselenide (CIGS) as the absorber layer, cadmium sulfide (CdS) as a buffer layer un-doped (i) and Aluminium (Al) doped zinc oxide (ZnO) as a window layer was simulated using the one dimensional simulation program called analysis of microelectronic and photonic structures (AMPS-1D). The effect absorber thickness is been consider to check the performance of CIGS solar cell, demonstrated in the form of current-voltage (I-V) characteristics and quantum efficiency (QE). Fabrication part includes the deposition of each layer one by one on to the glass substrate. The structure of CIGS solar cell is already defined in the chapter 1. In this chapter, the influence of the thicknesses of i-ZnO and CdS layer has been observed. Also the influence of flash and evaporated CdS and the thermally evaporated CdS has been checked. The performance of fabricated CIGS thin film solar cell has been checked by the current-voltage (I-V) measurements and by the spectral response measurements.

7.1 SIMUALTON OF CIGS SOLAR CELL

The copper indium gallium diselenide, $\text{CuIn}_{1-x}\text{Ga}_x\text{Se}_2$ (CIGS), based solar cells have largest efficiencies on the laboratory scale [47] and as well as on the level of large-area modules [125]. In addition to high efficiencies, CIGS thin-film modules exhibit excellent outdoor stability [126] and radiation hardness [127, 128]. Therefore, this combination of high efficiency coupled with stability and radiation hardness makes CIGS a promising material for the low cost, high efficiency solar cells. Recently, Bloss et al. [129] have predicted a conversion efficiency (η) of 33.9% for CGS/CIS tandem solar cells at global air mass (AM) 1.5 illuminations. Song et al. have modeled a CGS/CIGS tandem solar cell and they have shown that η was 25% achievable when a high efficiency CGS top cell was used with an optimized CIGS bottom cell [130].

In this present work, a one dimensional simulation program called a analysis of microelectronic and photonic structures (AMPS-1D) [131] is used to simulate the $\text{CuIn}_{1-x}\text{Ga}_x\text{Se}_2$: $x=0.3$ solar cell structure. AMPS-1D developed at Pennsylvania State University and Electric Power Research Institute by S. Fonash et al. The software is designed

to simulate various photonic semiconductor structures, such as solar cells and photodiodes, and has the ability to introduce illumination with a defined photon spectrum and the electric biasing. The output data is generated through the numerical solution of the Poisson's equation for the charge distributions in semiconductor structures, and two continuity equations for the electron and hole currents flowing through the structures. Figure 7.1 shows the schematic of solar cell design studied in this work. The aim of the simulation of CIGS solar cell structure was to check the device performance by varying the thickness of the CIGS absorber layer. The device performance is mainly based on the material parameters, optical parameters, and electrical parameters of each layers used in the structure. In this simulation the required parameters of CIGS thin film having a thickness of 300 nm were taken from the elsewhere [132]. For the rest of the layers the standard parameters [133] were used.

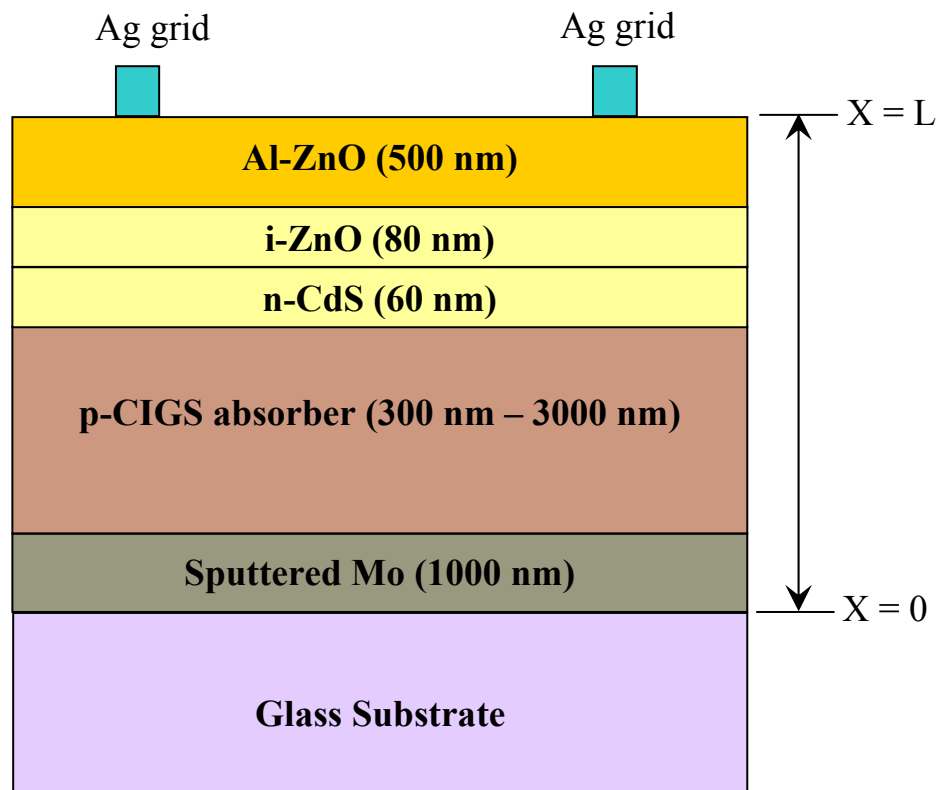


Fig. 7.1 CIGS solar cell device structure used for the simulation.

The thickness of the CIGS, in general, was kept ~2000 - 2500 nm [134, 135] in the commercial available solar cell device. In concern with that in this work, we simulate the solar cell structure by increasing the thickness of CIGS from 300 to 3000 nm. It was found from the simulated results that the η , and quantum efficiency (QE) were considerable influenced by the absorber layer thickness. As the thickness of the absorber layer increases

from 300 to 3000 nm, the value of η increases from 8.25 % to 10 % and the response of QE improves near to the band edge of CIGS.

7.1.1 MODEL DESCRIPTION

The AMPS software can operate in two distinct modes: the density of state (DOS) mode or the lifetime mode. A description of both modes can be found in the AMPS manual [131]; a comparative discussion is found in A.L. Fahrenbruch's work on CdTe solar cells [136]. In essence, the lifetime mode accepts inputs in the form of carrier lifetimes, which are assumed constant, independent of light and voltage bias, and does not address the underlying recombination processes. The DOS mode allows the definition of multiple defect states, using densities, energy distributions, and capture cross-sections. Based on this information, the recombination current and defect occupancy is calculated using the Shockley-Read-Hall formalism.

To model the charge transport processes in the present structure shown in Fig. 7.1, the drift-diffusion approach is used as a function of device length, x . The three main equations are: the Poisson's equation, continuity equation for free holes, and continuity equation for free electrons. Generally, the Poisson's equation is [1],

$$\frac{d}{dx} \left(-\varepsilon(x) \frac{d\Psi}{dx} \right) = q \left[p(x) - n(x) + N_D^+(x) - N_A^-(x) + p_t(x) - n_t(x) \right] \quad (7.1)$$

where, Ψ is the electrostatic potential, n , p are the concentrations of free electrons and holes, n_t , p_t are the concentrations of trapped electrons and holes, N_D^+ , N_A^- are the concentrations of ionized donors and acceptors, ε is the dielectric permittivity of semiconductor, and q is the electron charge.

The transport characteristics of an electronic device may be derived by the continuity equation for the holes and electrons. The continuity equations in steady state conditions are,

$$\frac{1}{q} \frac{dJ_n}{dx} = R_n(x) - G(x), \quad (7.2)$$

$$\frac{1}{q} \frac{dJ_p}{dx} = G(x) - R_p(x) \quad (7.3)$$

where, J_n , J_p are electron and hole current density, R_n , R_p are electrons and holes recombination velocities for direct band-to-band and indirect transitions, and G is the optical generation rate which is expressed as a function of x is,

$$G(x) = -\frac{d}{dx} \sum_i \Phi_i^{\text{FOR}}(\lambda_i) + \frac{d}{dx} \sum_i \Phi_i^{\text{REV}}(\lambda_i) \quad (7.4)$$

where, Φ_i^{FOR} and Φ_i^{REV} are, respectively, the photon flux of the incident light and the light reflected from the back surface at a wavelength, λ of i at some point x , depending on the light absorption coefficient, and the light reflectance in the forward and reverse direction. In our simulation, the reflection indices for the forward and reverse directions are 0 and 0.6, respectively. The governing equations 7.1, 7.2, and 7.3 must hold at every position in a device, and the solution to these equations involves determining the state variables $\Psi(x)$, the n-type quasi-Fermi level E_{Fn} , and the p-type quasi-Fermi level E_{Fp} or, equivalently, $\Psi(x)$, $n(x)$, and $p(x)$, which completely defines the system at every point x . Because the governing equations for $\Psi(x)$, E_{Fn} , and E_{Fp} are non-linear and coupled, they cannot be solved analytically. There must be boundary conditions imposed on the set of equations. The Newton-Raphson technique is used in AMPS-1D. To be specific, the solutions to equations 7.1, 7.2, and 7.3 must satisfy the following boundary conditions:

$$\begin{aligned} \Psi(0) &= \Psi_0 - V; \\ \Psi(L) &= 0; \\ J_p(0) &= -qS_{po}[p_o(0) - p(0)]; \\ J_p(L) &= qS_{pL}[p(L) - p_o(L)]; \\ J_n(0) &= qS_{no}[n(0) - n_o(0)]; \\ J_n(L) &= -qS_{nL}[n_o(L) - n(L)]. \end{aligned} \quad (7.5)$$

S_{po} , S_{pL} , S_{no} , and S_{nL} appearing in those conditions are effective interface recombination speeds for holes and electrons at $x = 0$, and $x = L$.

AMPS-1D solves three coupled differential equations each subject to boundary conditions (Equation 7.5) and then calculates the electrostatic potential and the quasi-Fermi level for holes and electrons at all point in the solar cell. Once these values are known as a function of depth, it is straightforward to calculate the carrier concentrations, electric fields and currents, and device parameters like the open-circuit voltage (V_{oc}), short-circuit current density (J_{sc}), fill-factor (FF), and the efficiency (η). These parameters define the performance of a solar cell. The grid spacing was selected to be denser in the thinner top layers of the device, where more rapid changes are to be expected in the band structure. The grid point does not exceed the maximum limit of 400. Selected biases were entered as necessary; by default AMPS calculates QE and band structure for thermodynamic equilibrium, maximum power point, and under open-circuit conditions.

7.1.2 Simulation Parameters

In this study, a one-dimensional numerical analysis tool, AMPS-1D, is used to create various solar cell models and obtain its results. In AMPS-1D, four different layers are required for the modeling. More layers can be added as long as the grid points do not exceed the limitation, viz. 400-grid points. The four layers that are used in this modeling is the n-type Al doped ZnO, i-ZnO, CdS and CIGS. Table 7.1 show the description for the parameters used in the simulation and the base parameter that are used throughout the presented simulation [133].

Table 7.1 Parameters used for the CIGS thin film solar cell simulation.

Parameters \ Layers	n ⁺ -ZnO	n-[i-ZnO]	CdS	CIGS
Thickness (nm)	500	80	60	300*- 3000
Dielectric constant, ϵ	9	9	10	13.6
Electron mobility, μ_n (cm ² /Vs)	50	50	6	300
Hole mobility, μ_p (cm ² /Vs)	5	5	3	36*
Carrier density, n or p (cm ⁻³)	n:1.70E+19	n:5E+16	n:6E+16	p:2.0E+17*
Optical band gap, E_g (eV)	3.3	3.3	2.4	1.20*
Effective density, N_c (cm ⁻³)	1.00E+19	1.00E+19	1.00E+19	3.00E+18
Effective density, N_v (cm ⁻³)	1.00E+19	1.00E+19	1.60E+19	1.50E+19
Electron affinity, χ (eV)	3.9	3.9	3.75	4.15

* Parameters of CIGS thin films grown by flash evaporation method on soda lime glass substrate [132].

The front and back contacts are solely defined by their work function and the reflectivity of the contact-semiconductor interface: work function for front contact is 0 eV i.e. at the Fermi level, E_F , and the reflectivity is 0.3. Similarly 0.9 eV work function i.e. above E_F and reflectivity is 0.8. The AM 1.5G photon flux was used for the illumination (Fig. 7.2). The number of incident photons/(cm²/s) was entered for wavelengths between 250 nm to 2500 nm, with a step size of 2 nm. The front panel of AMPS-1D simulation for CIGS solar cell structure is shown in Fig. 7.3.

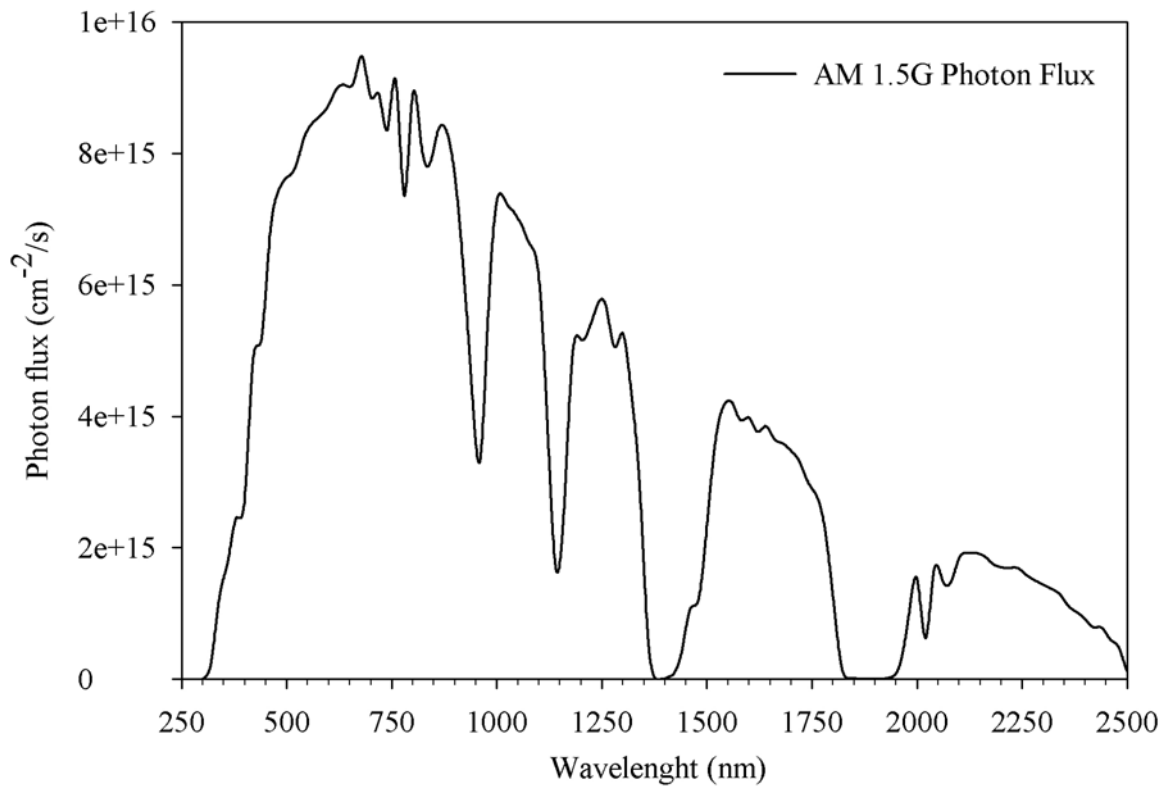


Fig. 7.2 AM1.5G photon flux used as the illumination condition in the simulation.

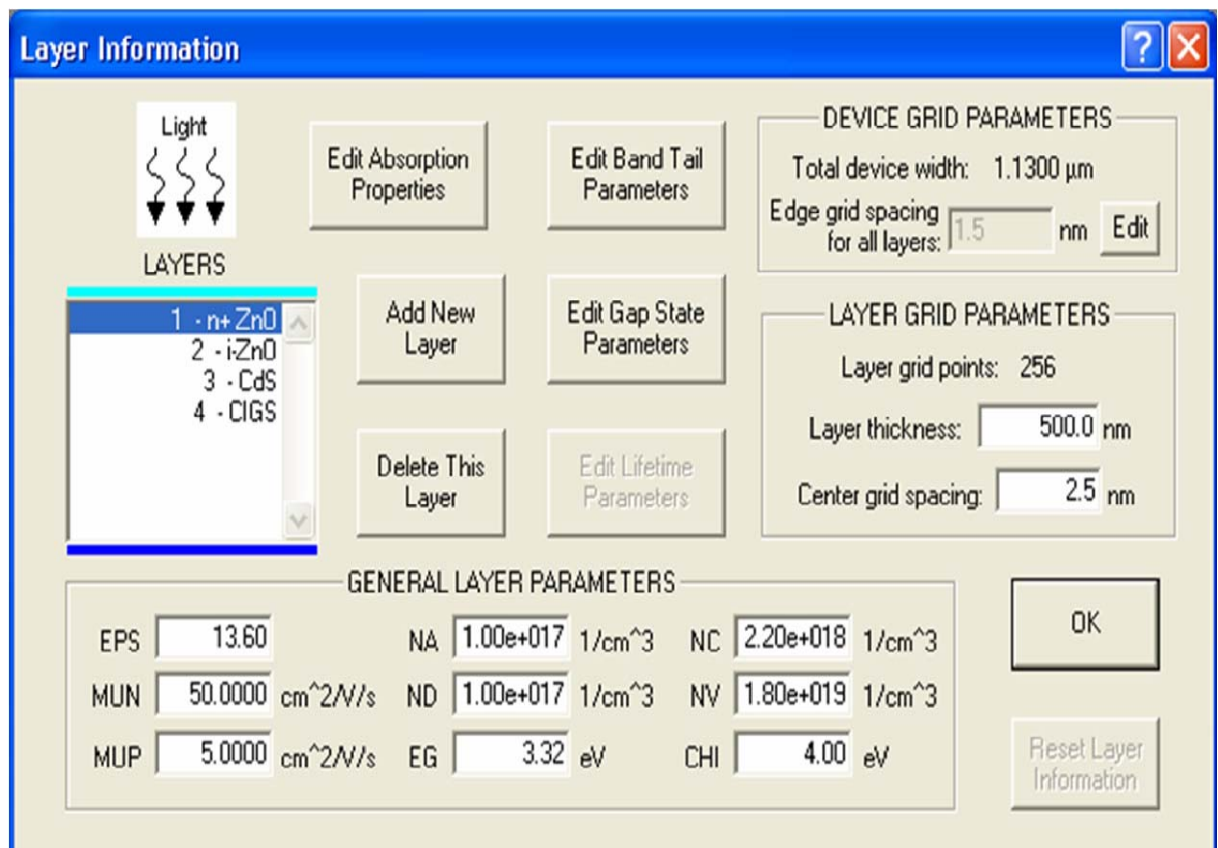


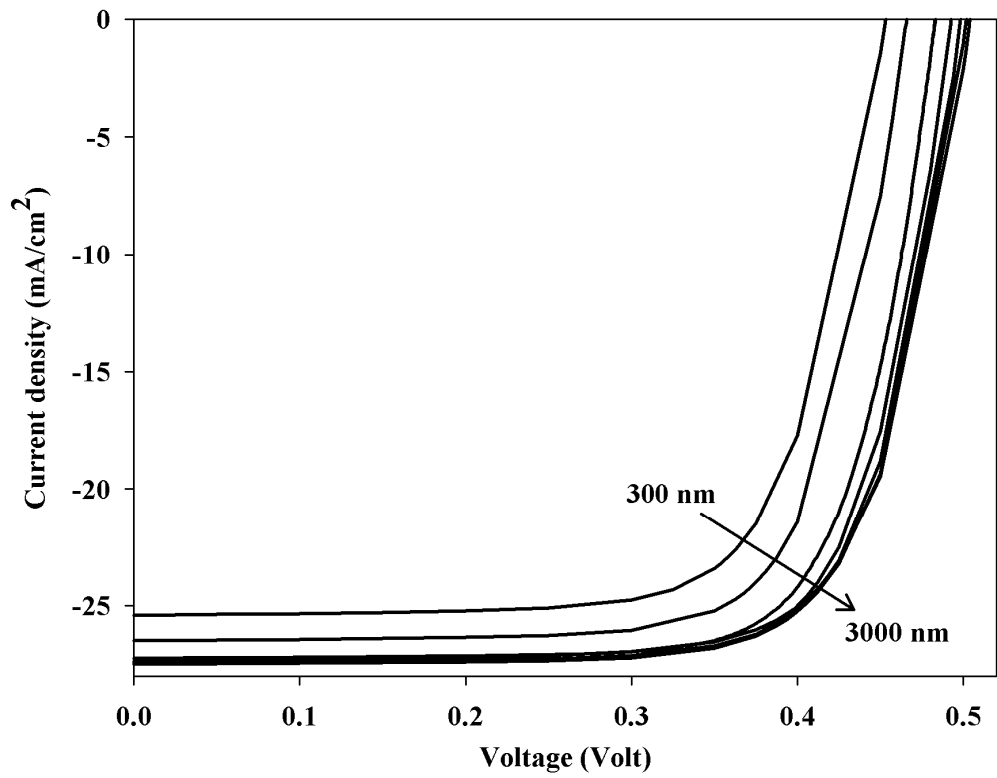
Fig. 7.3 AMPS simulation front panel contains the device and layer grid parameters, and general layer parameters.

7.1.3 Results and Discussions of Simulation

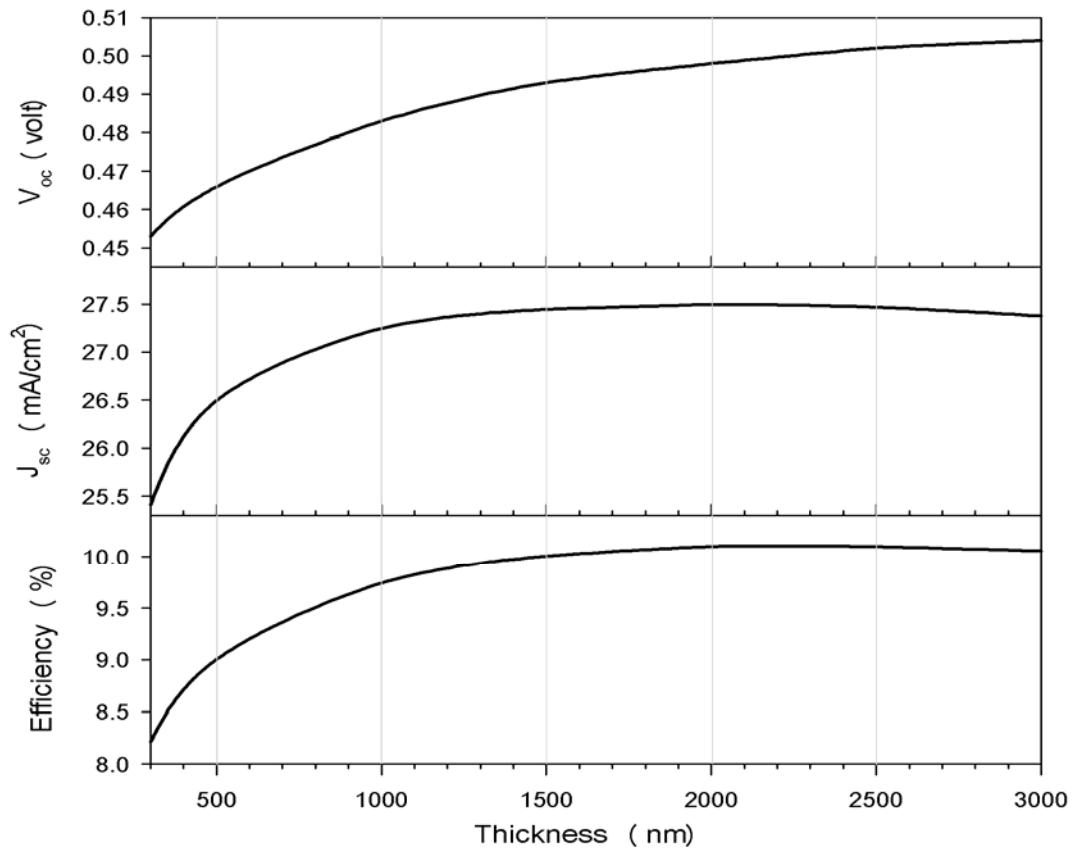
CIGS solar cells have a complex multilayer structure. Cell analysis is also complexed by a complicated window structure, consisting of a thin buffer layer (CdS or an alternative) and a double TCO layer (e.g. nominally undoped ZnO followed by Al doped ZnO).

It is clear that numerical modeling is necessary to evaluate quantitatively the effect of a set of assumed input parameters. Figure 7.4 (a) shows the J-V characteristic, using AMPS-1D, of the CIGS solar cell structure having a different thickness of CIGS absorber layer. As the thickness of the layer increases from 300 nm to 3000 nm, the conversion efficiency increases from 8.25 % to 10 %. Figure 7.4 (b) shows the variation in the V_{oc} and I_{sc} including η as a function of absorber thickness. It indicates that below 1500 nm thickness of absorber the cell shows the sharp decrease in the V_{oc} , J_{sc} and therefore decrease in the η . The cell having a 300 nm thickness of CIGS shows the values of V_{oc} and J_{sc} is 0.452 volt and 25.4 mA/cm² respectively.

The spectral response shown in Fig. 7.5 indicates the absorber having a lower, 300 nm, thickness loose a part of J_{sc} near to the band edge (~ 1000 nm) of the CIGS. As the thickness of the absorber layer increases, the recombination probability of the photon-generated carriers with back-contact is decreases. Recombination is mainly depending on the junction depth. As the thickness of the layer increases, the junction depth decrease relative to the thickness of the layer. Therefore, the photo-generated carriers are collected efficiently at higher thickness of the absorber layer. QE spectra shown in Fig. 7.5 suggest that at higher thickness of the CIGS absorber layer the maximum photon generated carriers are being collected and gives maximum ~ 70 % photon conversion efficiency.



(a)



(b)

Fig. 7.4 (a) J-V spectra for different CIGS thicknesses and, (b) Variation in the V_{oc} , J_{sc} , and efficiency as a function of CIGS thickness.

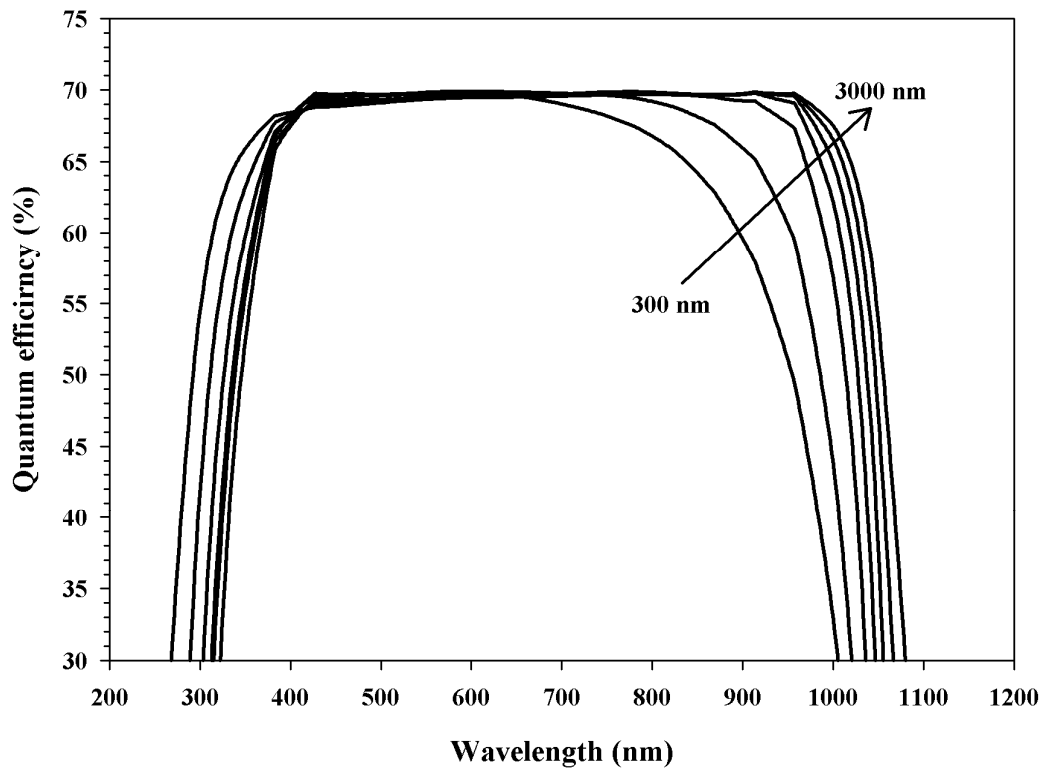


Fig. 7.5 Quantum efficiency spectra for different CIGS thickness show that higher thickness absorbs more photons which improve the overall efficiency of the device.

7.2 FABRICATION OF CIGS THIN FILM SOLAR CELL DEVICE

The fabrication part of CIGS solar cell includes the layer by layer growth of each individual layer on a glass substrate. Figure 7.6 shows the structure of the CIGS thin film solar cell fabricated in our laboratory. A frame-shaped shadow mask for each layer having a different area of exposing is used to avoid short-circuiting between the different layers from the edge. During the deposition of the different layers of the CIGS solar cell device, the structure is taken out from the vacuum chamber to change the source material and the shifting mask. The final active area of the device is 0.16 cm^2 .

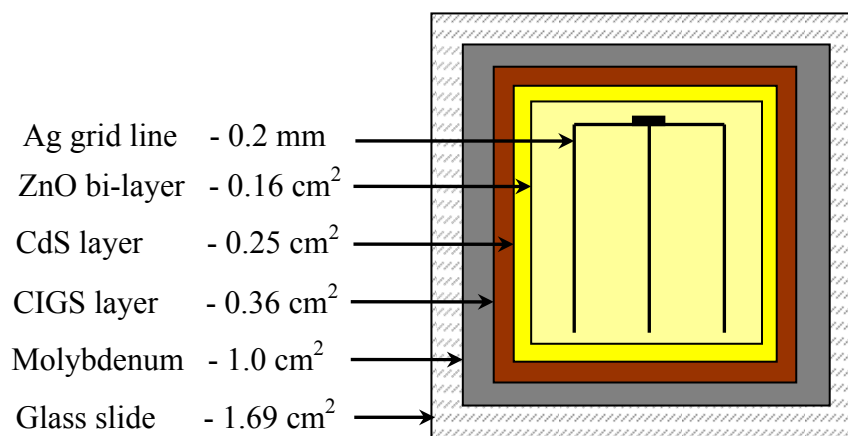


Fig. 7.6 A schematic diagram of the CIGS solar cell structure with a frame-shaped shadow mask.

Each layer in the solar cell structure plays an important role in the fabrication of p-n junction. In the CIGS thin film solar cell the p-n junction is formed between the CIGS and the CdS. ZnO bi-layer act as the conducting top window layer. The Molybdenum thin film acts as a back contact. Silver metal is used for the top contact as in finger type geometry. After each layer of deposition we had checked the behavior of the solar cell device for the confirming the goodness of the junction. In the summary we fabricated the CIGS thin film solar cell by varying the thickness of of CdS and i-ZnO layer. In addition we also use the thermal and flash evaporation method for growing the CdS layer. The performance of the CIGS solar cell was checked by the J-V measurements and the spectral response measurements.

7.2.1 Effect of Thermally Evaporated CdS Film Thickness on the performance of CIGS solar cell

In the CIGS thin film solar cell, the junction between CIGS and CdS plays the crucial role in the carrier generation and the recombination mechanism. In the fabrication process of CIGS solar cell, we have tried to optimize CIGS/CdS junction parameters by varying the thicknesses of CdS layer from 50 to 150 nm. Minimum series resistance and approach of ideality factor near to unity is the prime requirement for better pn junction. Figure 7.7 shows the dark J-V curve of CIGS/CdS junction with varying the thicknesses from 50 nm to 150 nm of CdS layer.

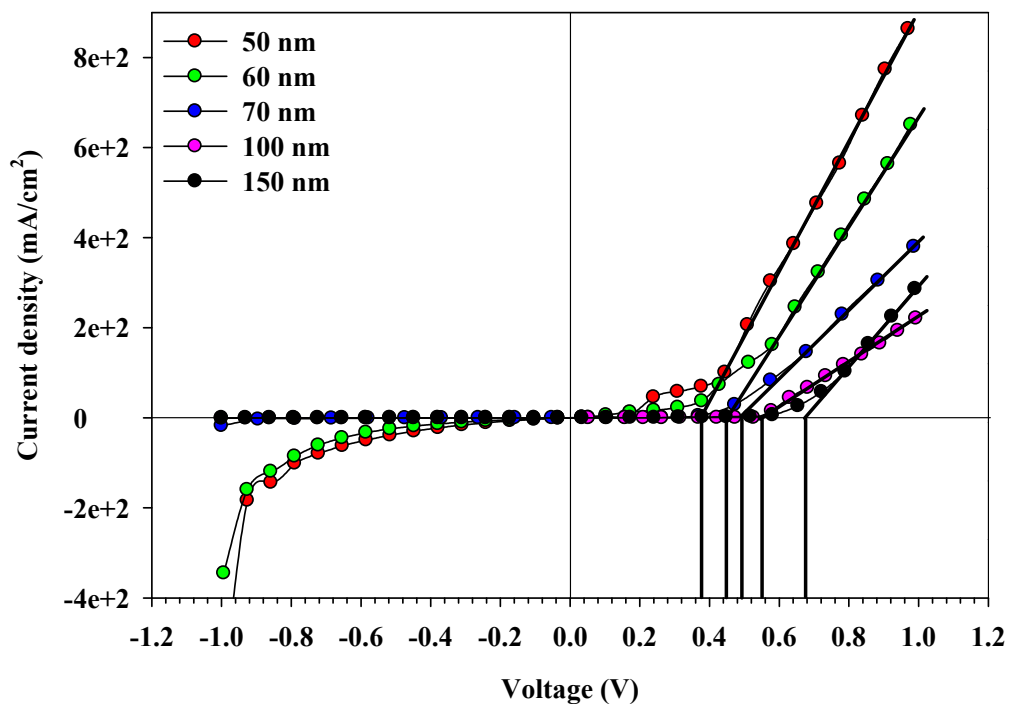


Fig. 7.7 The dark J-V characteristics of CIGS/CdS hetero-junction having different thicknesses of CdS layer.

The dark J-V curve of CIGS/CdS junction clearly indicates that as the thickness of CdS increases the slope of the curve is decreases, and then series resistance decreases. The lowest series resistance of 4.1 Ω and ideality factor of about 1.32 is observed for the 50 nm thickness of CdS layer. Table 7.2 shows the measured values of series resistance, ideal factor and the reverse saturation current density of CIGS/CdS junction for different thicknesses of CdS layer. It was observed that by reducing the CdS layer thickness from 150 nm to 50 nm, the series resistance reduces from 14.2 to 4.1 Ω and reverse saturation current density varies from 9.6×10^{-10} to 3.6×10^{-11} mA/cm². Lower reverse saturation current density, observed for thin CdS layer, may be responsible for the tunneling or shorting of the photo-generated carriers to the back contact. The value of ideality factor varies from 1.78 to 1.32 as the thickness of CdS reduces (Table 7.2). Still there is need to improve these values listed in Table 7.2. S. Nishiwaki et al. have observed near by values for stacked CGS based solar cells. According to their results of poor junction characteristics of CGS/ITO was observed [137].

Table 7.2 The series resistance, reverse saturation current density, and ideality factor of CIGS/CdS hetero-junction having a different thicknesses of CdS layer.

CdS thickness (nm)	Series resistance (Ω)	Reverse saturation current density (mA/cm ²)	Ideality factor
50	4.1	3.6×10^{-11}	1.32
60	6.4	7.5×10^{-11}	1.41
70	8.2	8.6×10^{-11}	1.55
100	9.2	4.2×10^{-10}	1.63
150	14.2	9.6×10^{-10}	1.78

Effect of Heat soaks on CIGS/CdS hetero-junction

Cd diffusion into CIGS surface and bulk layer occurs easily through Cu-deficient surface layer of CIGS. The Cd-doping is known to induce a type conversion of p-CIGS surface layer of about 5 to 10 nm thickness yielding n-CIGS/p-CIGS homo-junction [138], which may benefit photovoltaic performance due to the reduced interface recombination. Formation of this type of homo-junction need to be improve by means of thermal annealing [139]. Instead of annealing up to certain temperature, soaking pulse having a temperature of 200 °C was given to the CIGS/CdS junction and the effect of it was observed for different time intervals. The thickness of CdS was kept 70 nm, though it shows the higher value of series resistance, but it shows better surface coverage of film compared to the 50 nm thick CdS, which has a

lower series resistance. The dark J-V characteristics of CIGS/CdS junction, heat soaked for different time viz. 20 s, 40 s and 60 s is shown in Fig. 7.8.

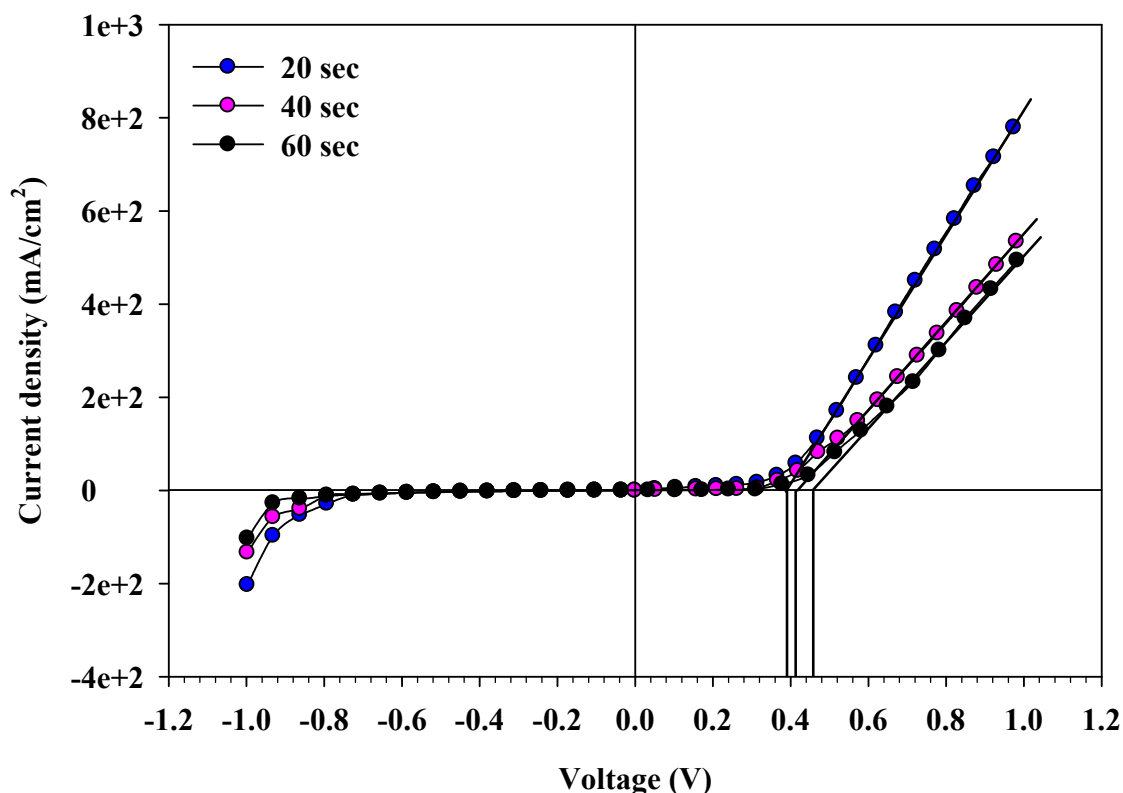


Fig. 7.8 The dark J-V characteristics of CIGS/CdS heterojunction heat soaked for different time.

As seen from the Fig. 7.8, the heat soak for less time interval, 20 s, shows significant improvement in the sharpness of the J-V. The threshold voltage for 20 s heat soak is 0.39 V and 0.44 V without heat soak as shown in Fig. 7.7. The series resistance is 3.4 Ω for 20 s heat soak CIGS/CdS junction, while it is 8.2 Ω without heat soak (Table 7.2).

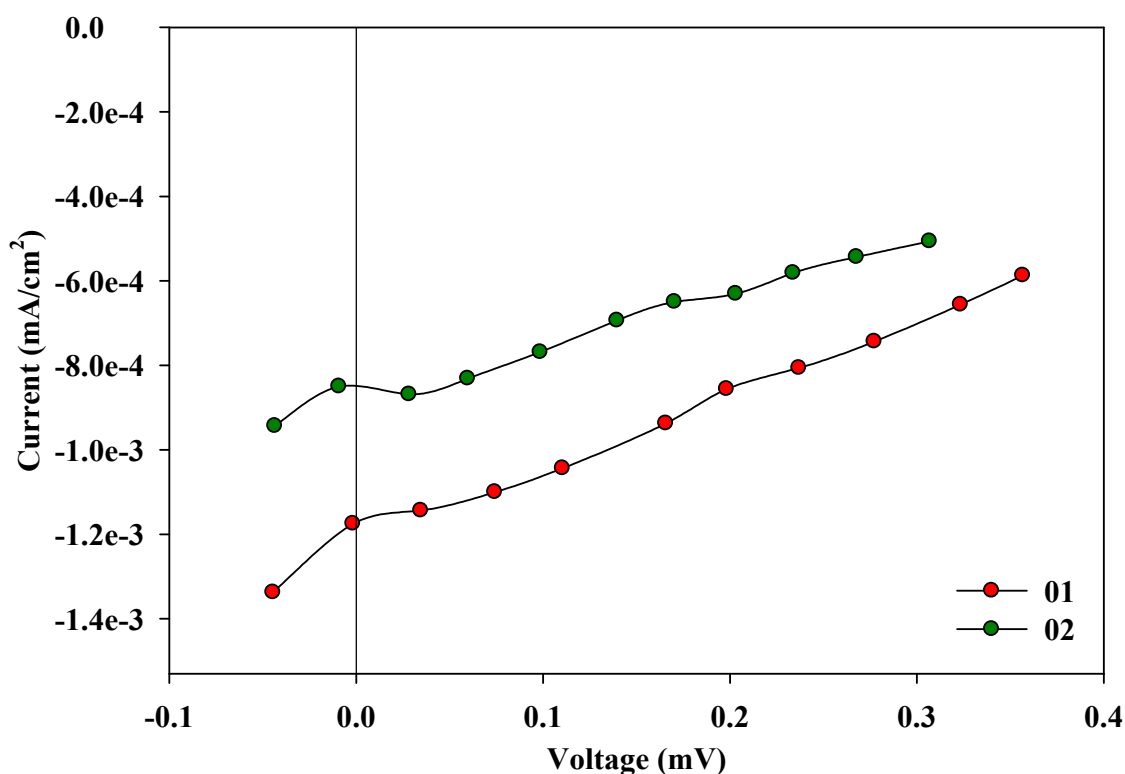
Table 7.3 The series resistance, reverse saturation current density, and ideality factor of CIGS/CdS hetero-junction having a different heat soak time.

Heat soak time (s)	Series resistance (Ω)	Reverse saturation current density (mA/cm^2)	Ideality factor
20	3.4	2.4×10^{-11}	1.19
40	7.2	6.3×10^{-11}	1.32
60	9.3	2.6×10^{-10}	1.52

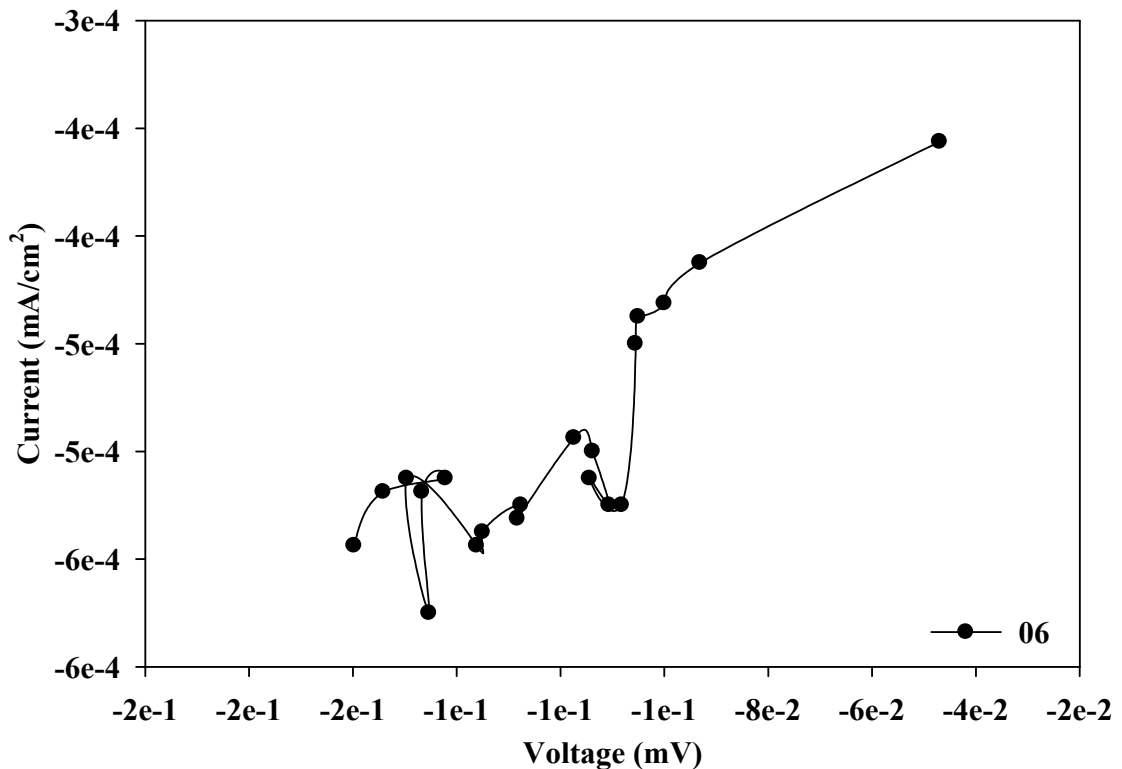
This reduction in the series resistance and threshold values shows the clear indication of the improvement of CIGS/CdS by applying the heats soak for 20 s. By increasing the soak time the series resistance value increases. It reached to 9.3 Ω for 60 s heat soak pulse. The values

of series resistance, reverse saturation current density, and ideality factor for different heat soak pulse is shown in Table 7.3.

The light J-V measurements in the light (100 mW/cm^2) are carried out after the ZnO bi-layer (intrinsic and Al-doped ZnO) deposition, on CdS layer. The layer of i-ZnO of about 70 nm is deposited on CdS and then the 450 nm thick AZO. After the ZnO bi-layer deposition the Al grid is deposited by thermal evaporation at room temperature. Couple of solar cells with Al grid did not show any photovoltaic effect. By microscopic observation of prepared CIGS solar cells, we observed blackish colored Al grid strips that may be due to the shadow effect of mask or Al diffusion into the AZO layer. Another couple of CIGS cell with similar kind of photovoltaic effect confirms the shorting of the junction due to the Al deposition. To overcome thus, we deposited the Silver (Ag) grid on AZO layer by thermal evaporation method at room temperature. Thin film of Ag, in the form of grid, shows nice appearance of reflecting silvery surface. The CIGS solar cells having an Ag grid shows V_{oc} of about 0.35 mV and J_{sc} about $1 \mu\text{A/cm}^2$. The light J-V characteristic is shown in Fig. 7.9.



(a)



(b)

Fig. 7.9 Light J-V characteristics of CIGS solar cell with Ag grid. Some of them show minor photovoltaic effect, (a) and some of them wont (b).

Many research groups have observed and discussed about the shorting of the p-n junction due excess Cd atoms on the surface of CIGS [140]. A part of CdS adjacent at the CdS/CIGS interface and made a porous structure. In fact, it is a very thin layer rather than void. This porous structure may exist due to the evaporation loss of CdS at high temperature (>1400 °C) and locality of the material loss as well. Therefore, the pore evolution should be directly correlated with Cd and/or S diffusion out of CdS. The pore structure, i.e., excess Cd atoms may be reducing by controlling the surface composition of CdS layer. The flash evaporation was used instead of thermal evaporation technique of the deposition of CdS layer for improving the Cd and S composition.

7.2.2 Effect of Flash Evaporated CdS Film Thickness on the performance of CIGS solar cell

Flash evaporation technique is widely used by researchers to deposit binary/ternary semiconductor compound material owing to its simplicity and ease of operation. In this method, pulverized compound material is transported to an evaporation boat hot enough to provide a quick evaporation of the material, without splitting it into individual elements. The CdS layer is deposited by flash evaporation technique at the substrate temperature of 100 °C. We have varied the thickness of CdS from 120 nm to 180 nm. Below 120 nm the film's

appearance not seems to be uniform. So, we have started the growth of CdS layer from 120 nm on CIGS layer. After the deposition of CdS layer we try to observe the dark and light J-V analysis. Figure 7.10 shows the dark J-V characteristics of CIGS/CdS junction having different thicknesses of CdS layer.

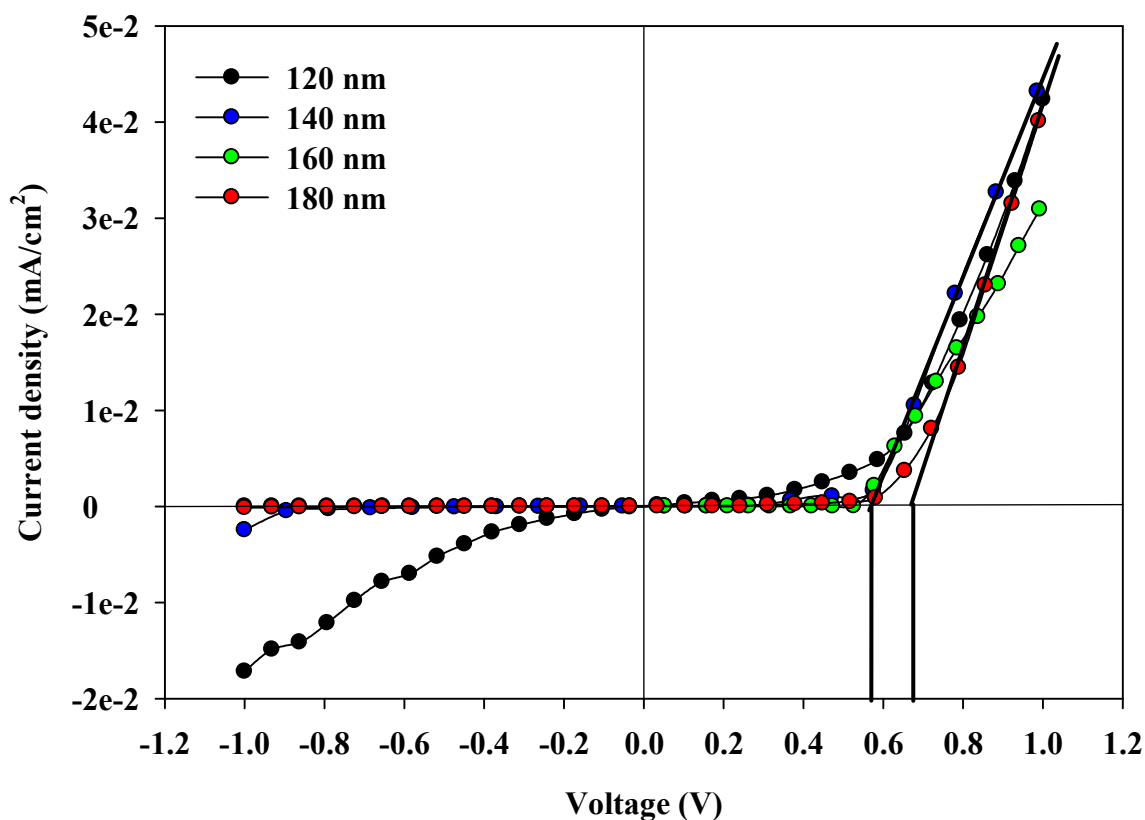


Fig. 7.10 The dark J-V characteristics of CIGS/CdS structure having a different thickness of flash evaporated CdS layer.

The dark J-V indicates that the threshold voltage is higher (~ 0.68 V) for the thicker CdS layer (180 nm). On the other hand the as thickness of CdS is decreases the threshold voltage is reduce and the reverse saturation current density increases. Higher values of reverse saturation current not been considered for the preparing the solar cell device. Physical the origin of this current can be due to extrinsic features related to the thin-film fabrication processes, such as the leakage path at the edge of the device, the presence of crystal defects or impurities, and pin holes [141]. All these factors are spatially non-uniform in nature, and thereby provide parasitic conduction paths. The values of the series resistance, reverse saturation current density and the ideality factor of the CIGS/CdS junction by varying the thickness of CdS is listed in the Table 7.3.

A light J-V measurement, Fig. 7.11, indicates that the 140 nm thickness has more V_{oc} and I_{sc} compared with other thicknesses of CdS. In the next part we have deposited i-ZnO layer (140 nm) on the CdS layer using the RF magnetron sputtering.

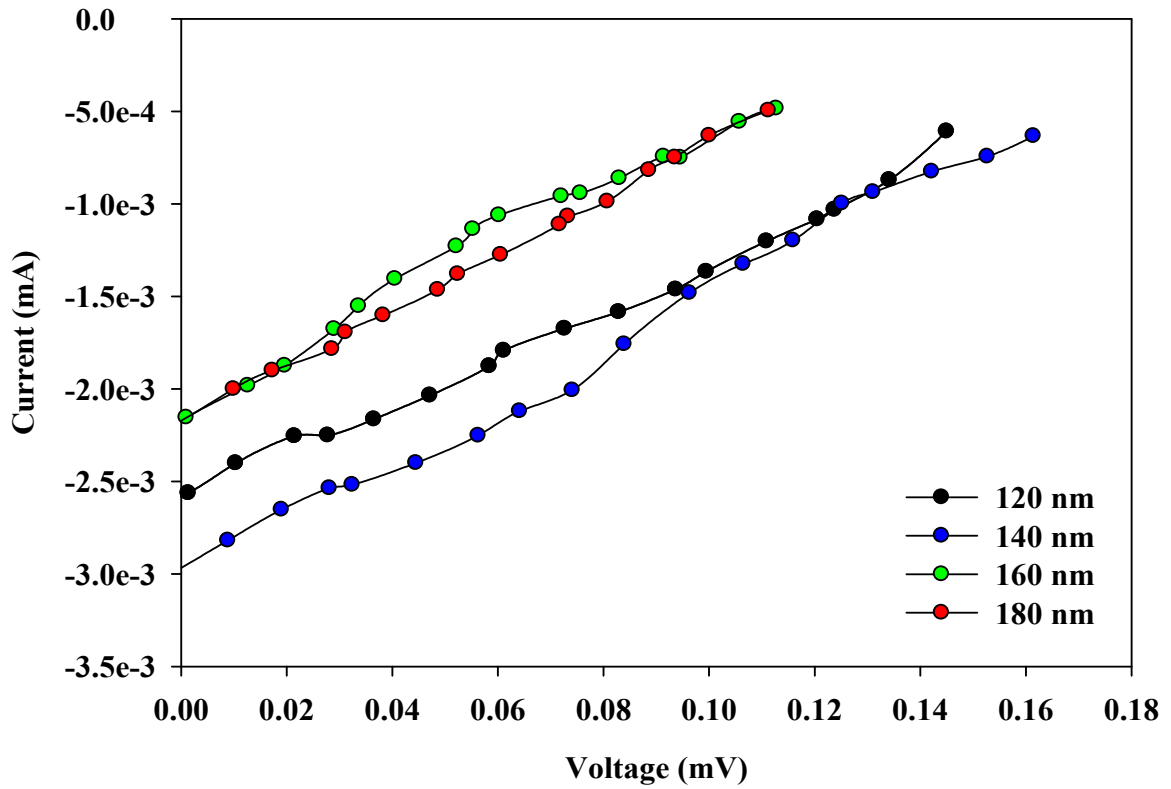


Fig. 7.11 The light J-V characteristics of CIGS/CdS structure having a different thickness of flash evaporated CdS layer.

Table 7.3 The series resistance, reverse saturation current density, and ideality factor of CIGS/CdS hetero-interface having different thicknesses of Flash evaporated CdS layer.

CdS thickness (nm)	Series resistance (Ω)	Reverse saturation current density (mA/cm^2)	Ideality factor
120	2.3	1.8×10^{-11}	1.13
140	2.2	8.5×10^{-11}	1.12
160	3.2	9.6×10^{-11}	1.19
180	5.3	1.2×10^{-10}	1.63

In the case of CIGS/CdS/i-ZnO structure also we measured the Dark and Light J-V. The dark J-V of the CIGS/CdS structure shows a noticeable Schottky behavior for the 140 nm thickness of CdS thin film. Figure 7.12 shows the dark J-V characteristics of CIGS/CdS/i-ZnO structure having different thicknesses of flash evaporated CdS layer. As the thickness of CdS decreases from 180 nm to 120 nm, the series resistance decreases from 400 Ω to 45 Ω and the diode ideality factor decreases from 3.8 to 1.6.

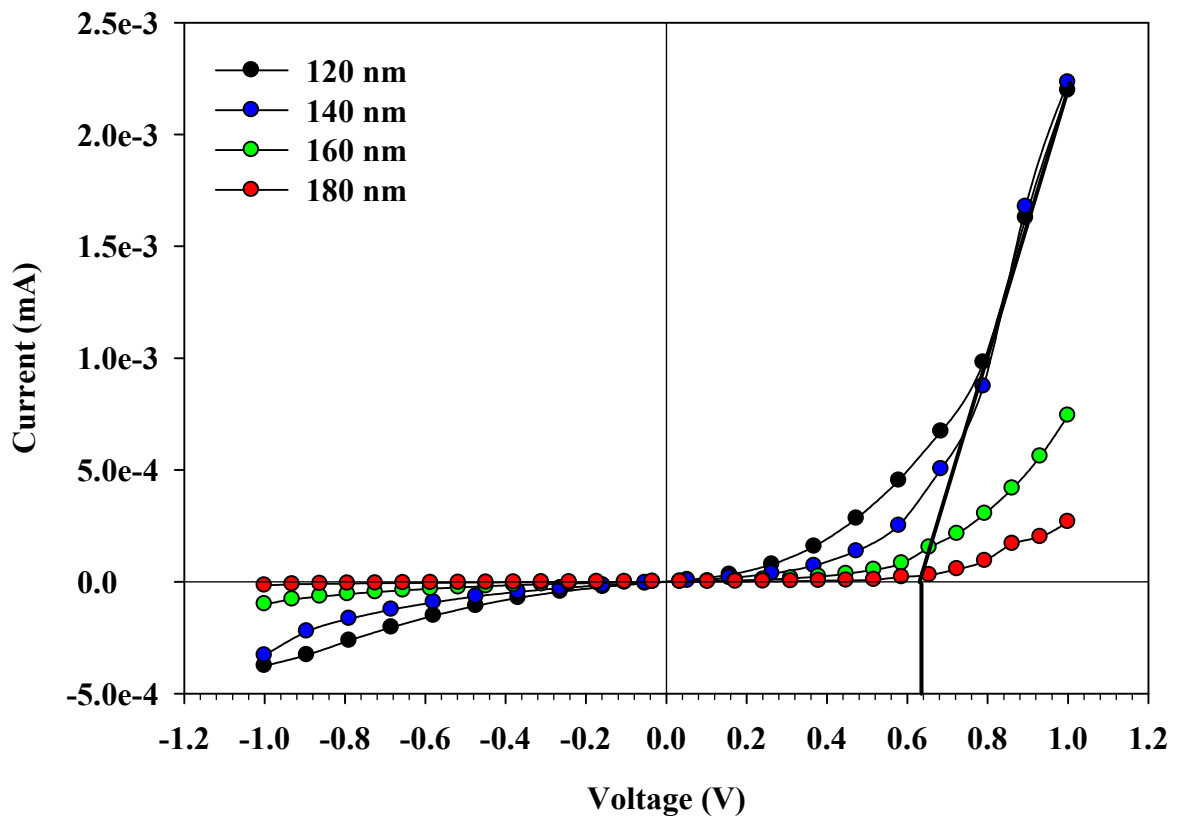


Fig. 7.12 The dark and J-V characteristics of CIGS/CdS/i-ZnO structure having different thicknesses of flash evaporated CdS layer.

After the deposition of i-ZnO layer, we deposited AZO layer using the RF magnetron sputtering. Figure 7.13 shows the dark and light J-V of a complete CIGS solar cell having different thicknesses of CdS layer. The dark J-V plot shows the linear relationship between the voltage and the current density. This indicates the shorting of the junction which may be due to the deposition of high energy AZO sputtering particles for a longer time. Light J-V curve show a maximum value of V_{oc} equal to 0.5 mV and I_{sc} of 30 μ A, which again confirms the major detrimental effect of AZO deposition.

The highly energetic particles can induce internal stresses and local defects [142, 143]. Moreover, the strong impact of oxygen may form aluminum oxide or excess oxygen inside AZO films. To reduce the internal stress we tried to reduce the thickness of i-ZnO layer and observed the performance of the solar cell device. The thickness of i-ZnO layer varied from 70 nm to 20 nm.

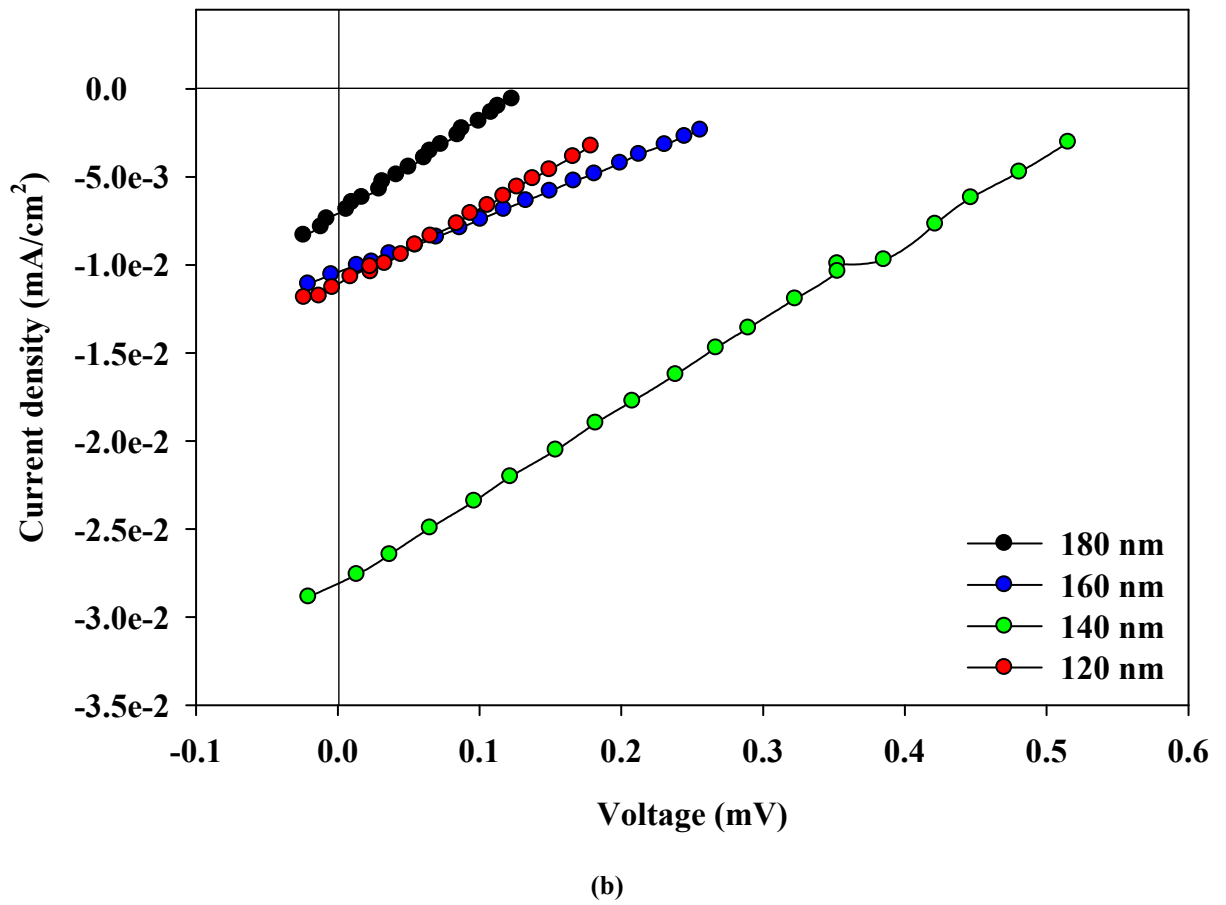
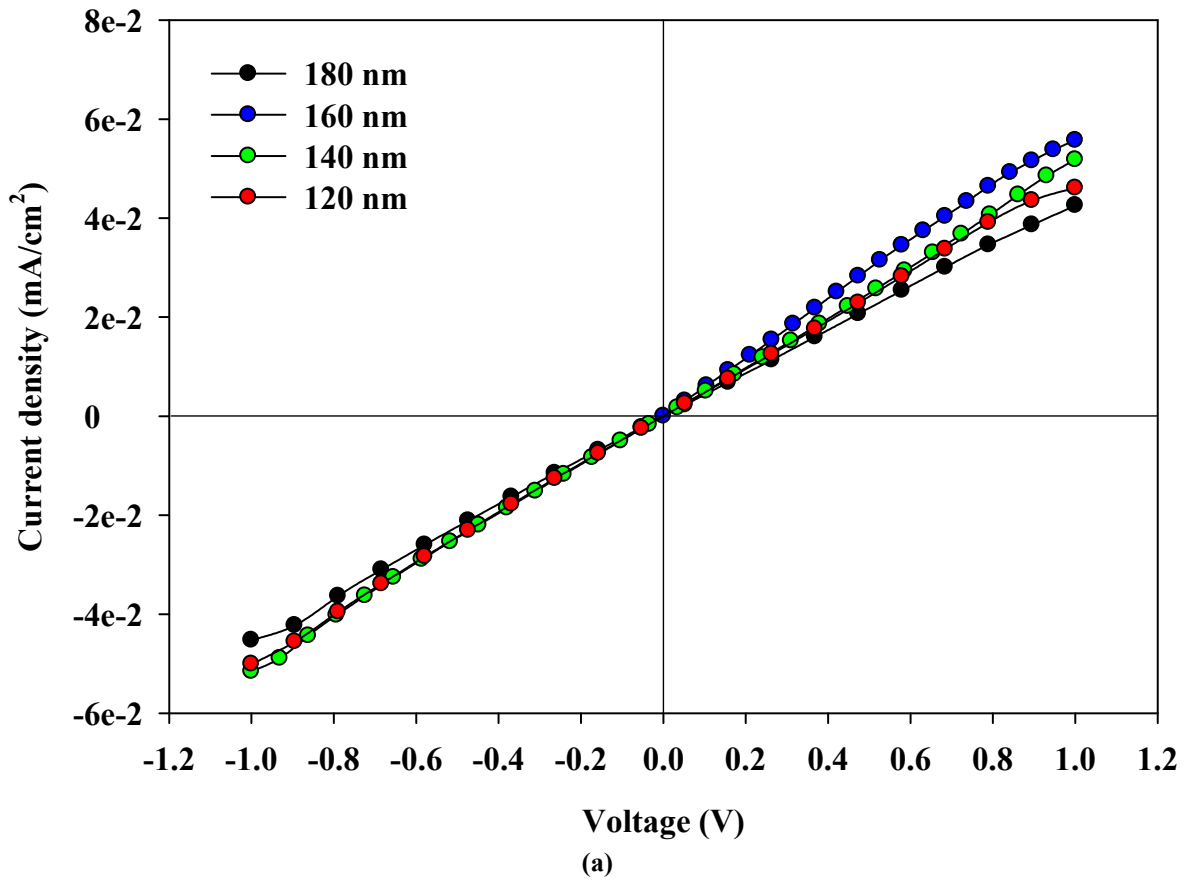


Fig. 7.13 (a) Dark and (b) Light J-V characteristics of CIGS complete solar cell having different thicknesses of flash evaporated CdS layer.

7.2.3 Effect of i-ZnO Film Thickness on the performance of CIGS solar cell

The dark J-V plots of CIGS/CdS/i-ZnO structure is shown in Fig. 7.14. It clearly shows a higher forward current after the threshold voltage (0.4 V) for 20 nm thin i-ZnO layer, compared to the film thickness of 35, 70 and 140 nm. This may be due to more optimal doping concentration and thus better conductivity across the junction. It also results the lowering the diode ideality factor. As seen from Fig. 14, the series resistance decreases from 96 Ω to 12.5 Ω as the thickness of i-ZnO reduces from 70 nm to 20 nm. The diode ideality factor also decreases from 1.5 to 1.23. On the other hand the reverse leakage current density increases as the thickness of i-ZnO decreases.

After observing the diode behavior, in the dark environment, up to i-ZnO layer, we have deposited AZO layer on to the i-ZnO layer and measured the dark and light J-V. Figure 7.15 (a) and (b) shows the dark and light J-V behavior of CIGS solar cell having a different thickness of i-ZnO layer, respectively. The dark J-V clearly shows that as the thickness of i-ZnO is reduced the diode behavior of CIGS solar cell improves. The value for the forward resistance of CIGS solar cell having a lowest thickness, i.e. 20 nm, of i-ZnO is 450 Ω and the reverse resistance is 491 Ω . In the case CIGS solar cells having a 35 nm and the 70 nm of i-ZnO the forward and reverse resistance is nearly same. That indicates the p-n junction has not been formed properly.

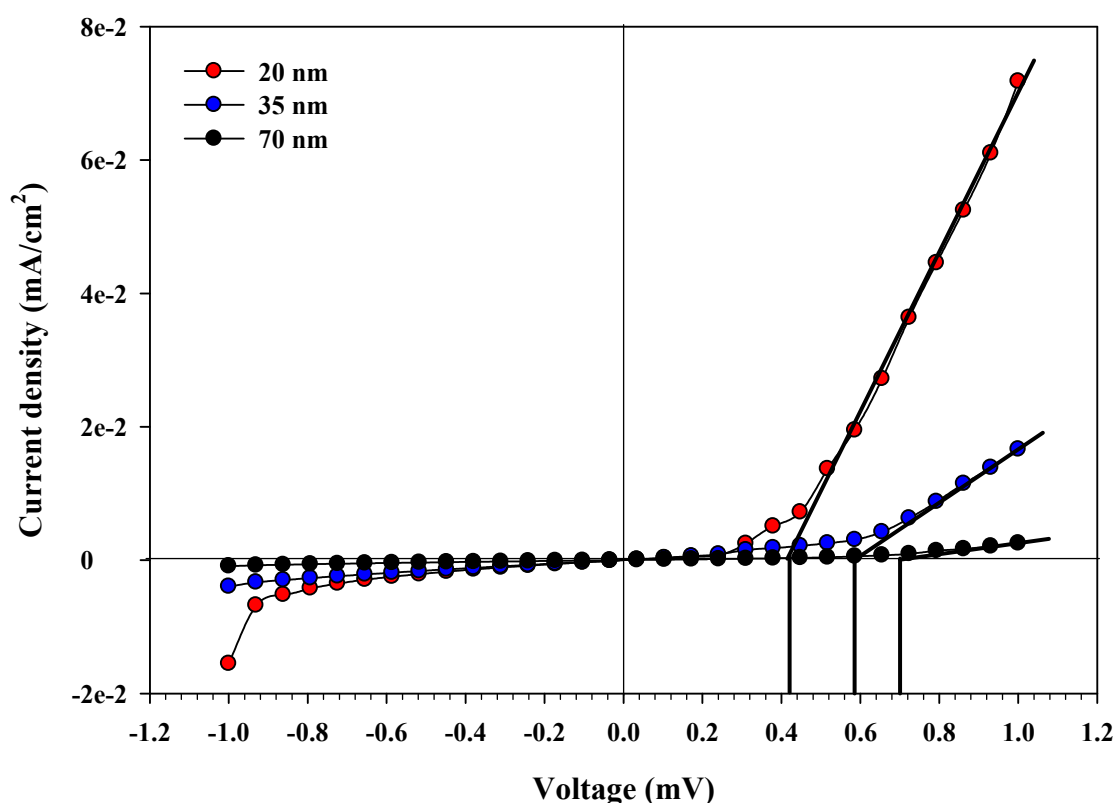
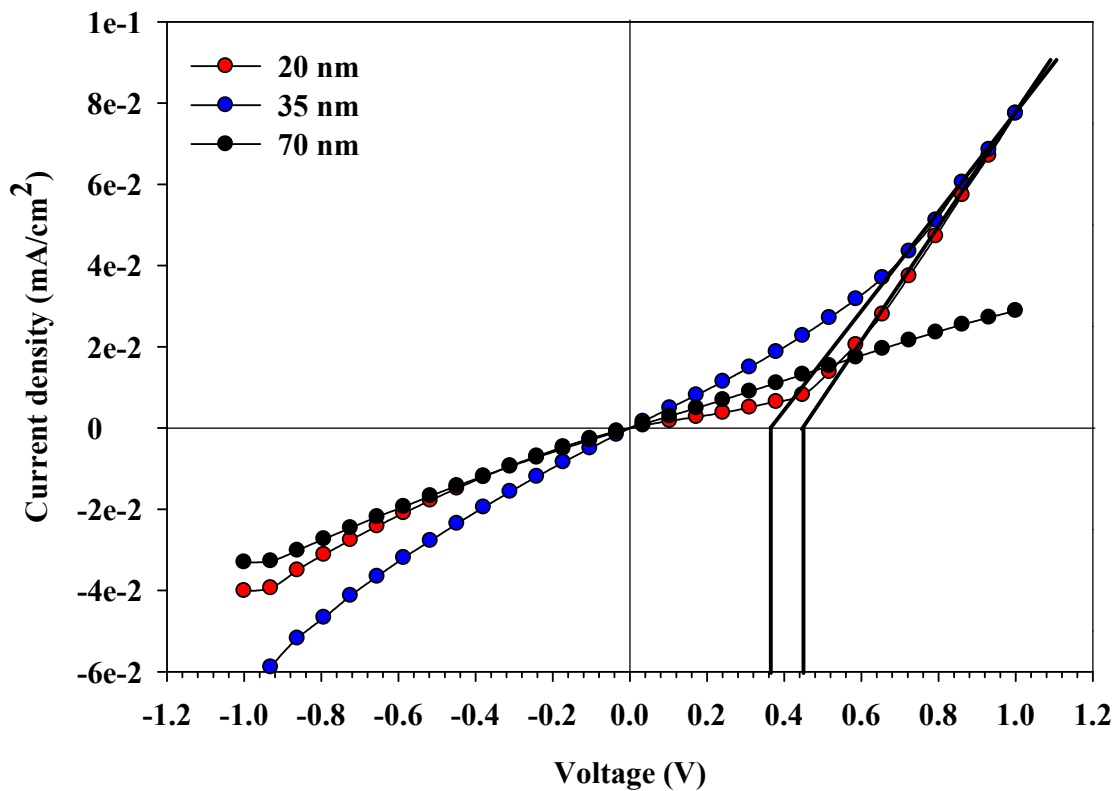


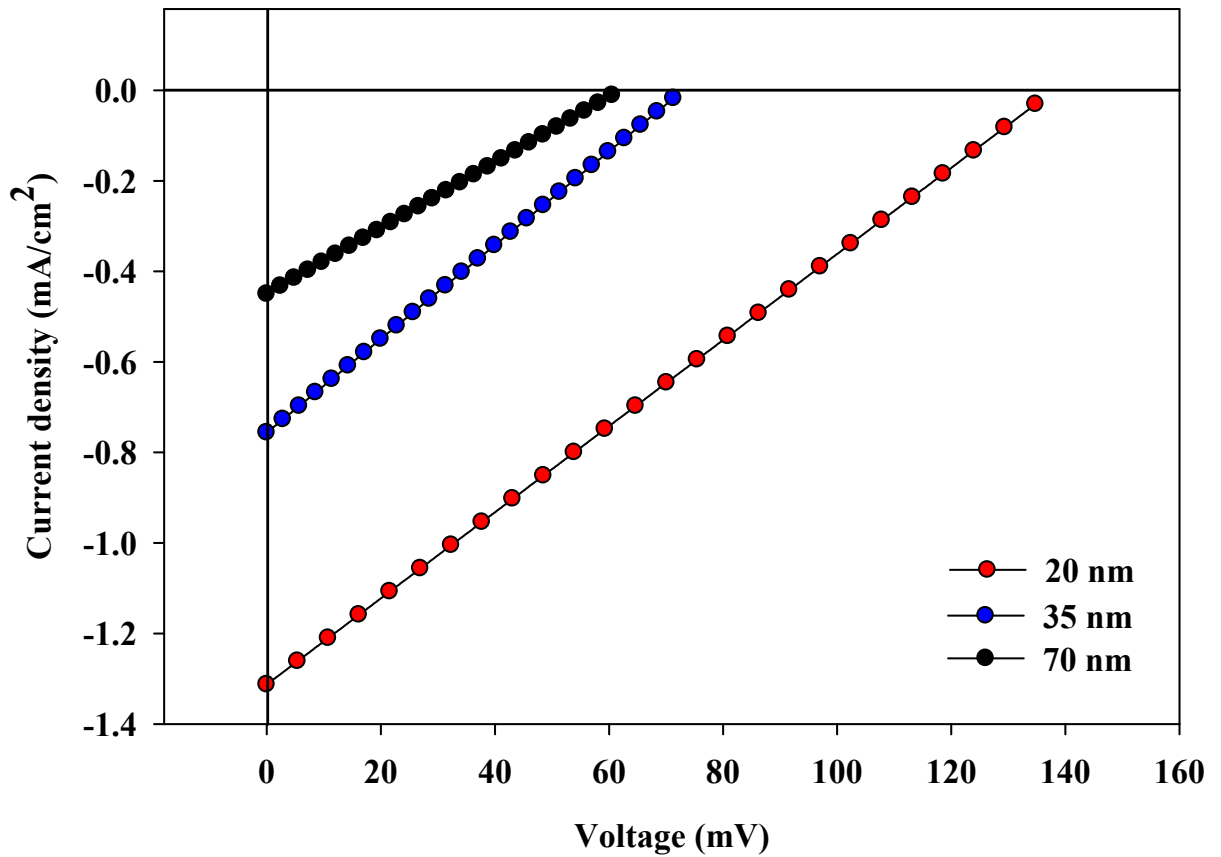
Fig. 7.14 The dark J-V of CIGS/CdS/i-ZnO structure having different thicknesses of i-ZnO layer.

For all three thicknesses of i-ZnO layer, the photovoltaic effect of CIGS solar cell has been observed. The maximum V_{oc} is of about 138 mV and the maximum J_{sc} is of about 1.3 mA/cm² has been observed for the CIGS solar cell having a thickness of 20 nm thickness of i-ZnO. As the thickness of i-ZnO increases the values of V_{oc} decreases, as shown in Fig. 7.15 (b). The possible reason for getting lower values of V_{oc} and J_{sc} is the higher reverse leakage current density, which indication the formation of the pore structure at the interface after the deposition of AZO layer.

The photo-current generation tells us the number of electron-hole pairs generation and distribution throughout the thickness of the device. The photo-generated current collection tells us the probability that these charge carriers will be collected by the external circuit, and therefore contribute to J_{sc} . This is generally expressed as a fraction and referred to as the collection efficiency. Depending on the depth within the device, different mechanisms are primarily responsible for photo current collection. Within the space-charge region (SCR) the built-in electric field sweeps electrons to the front of the device and holes towards the back, therefore collection is generally high. Outside of the SCR, carrier transport is limited by diffusion, and therefore collection is lower.



(a)



(b)

Fig. 7.15 The J-V characteristics, (a) in dark and, (b) in light of CIGS solar cell having different thicknesses of i-ZnO layer.

The influence of i-ZnO layer on the spectral response of CIGS solar cell has also been checked. The plot of spectral response for CIGS solar cell having different thickness of i-ZnO is shown in Fig. 7.16. The drop in spectral response below 520 nm wavelength is caused by the photon absorption in the CdS window layer (band gap $E_g = 2.4$ eV). The drop at higher wavelengths (~ 1100 nm) corresponds to the CIGS band gap of $E_g = 1.10$ eV. The CIGS solar cell having thin i-ZnO layer, i.e. 20 nm, shows maximum spectral response. As the thickness of i-ZnO increases from 20 nm the spectral response decreases. The experimental curve shows some optical interference in the range between 500 nm and 900 nm. AMPS simulation does not include interference effects and therefore the response will always give a smooth line.

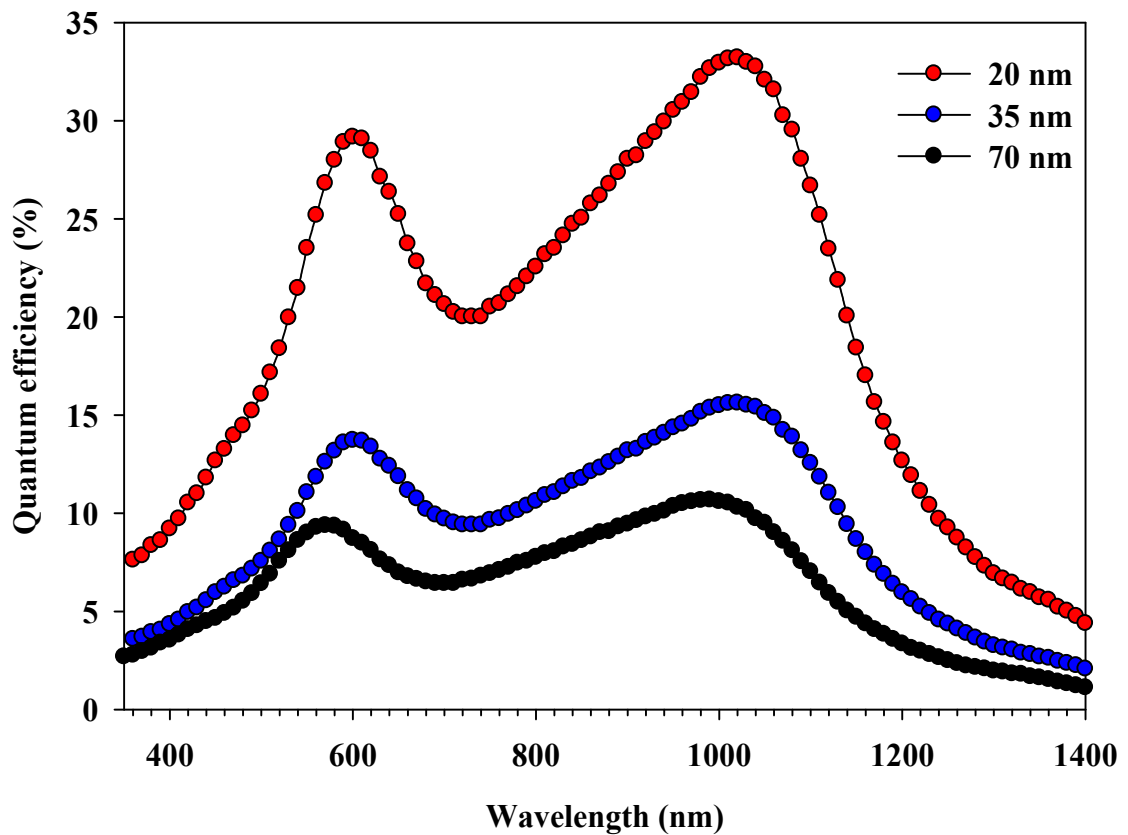


Fig. 7.16 Spectral response of CIGS solar cell having different thicknesses of i-ZnO layer.

After observing the photovoltaic effect of CIGS solar cell having a 20 nm i-ZnO layer, we again made CIGS solar cells having different thicknesses of CdS, i.e. 120 nm to 180 nm, by keeping constant the thickness of i-ZnO layer i.e. 20 nm. The dark J-V plots of CIGS/CdS/i-ZnO structure having different thicknesses of CdS is shown in Fig. 7.17. It shows that as the thickness of CdS layer decreases the reverse saturation current increases and the forward threshold voltage decreases.

The minimum reverse saturation current density and the minimum threshold value is observed for 140 nm of CdS film thickness. The higher forward current after the threshold voltage (0.42 V) is due to a more optimal conductivity across the junction. It also improve the diode ideality factor. The dark J-V of CIGS/CdS/i-ZnO structure having different thicknesses of CdS layer, as seen from the Fig. 7.17, shows that as the thickness of CdS layer decreases from 180 nm to 120 nm the diode behavior improves, so the series resistance is reduces from 33 Ω to 11 Ω .

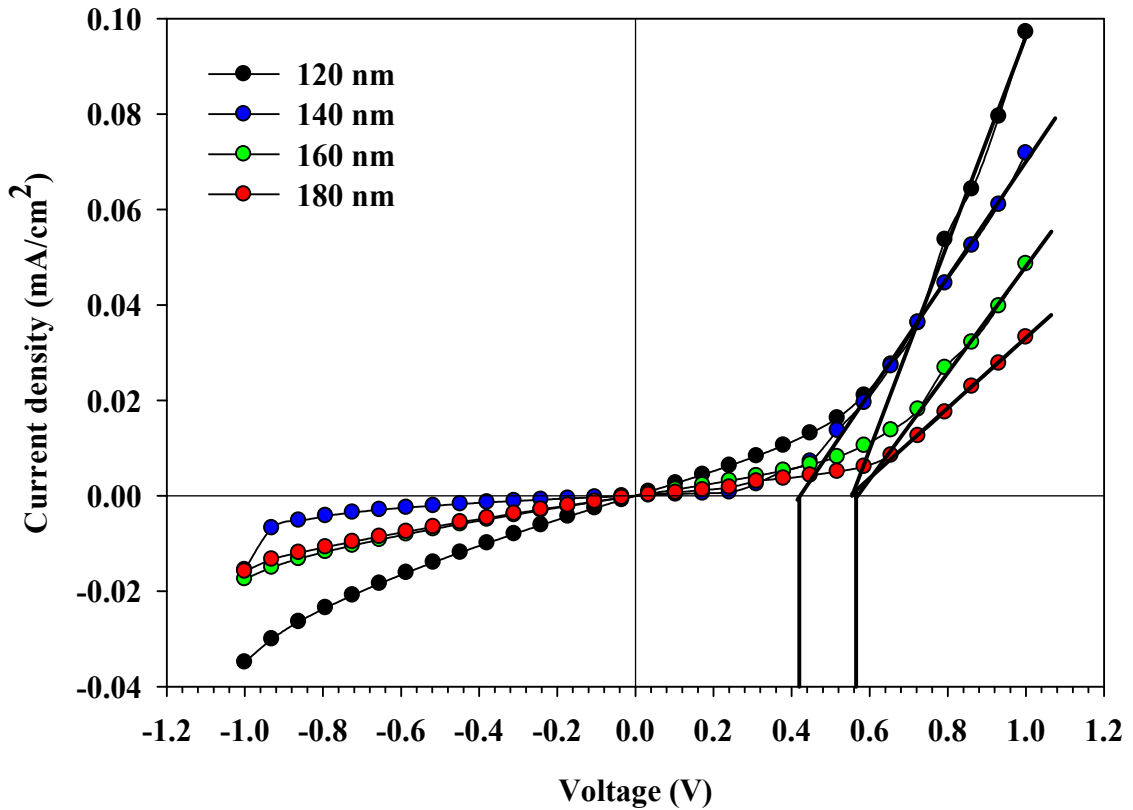
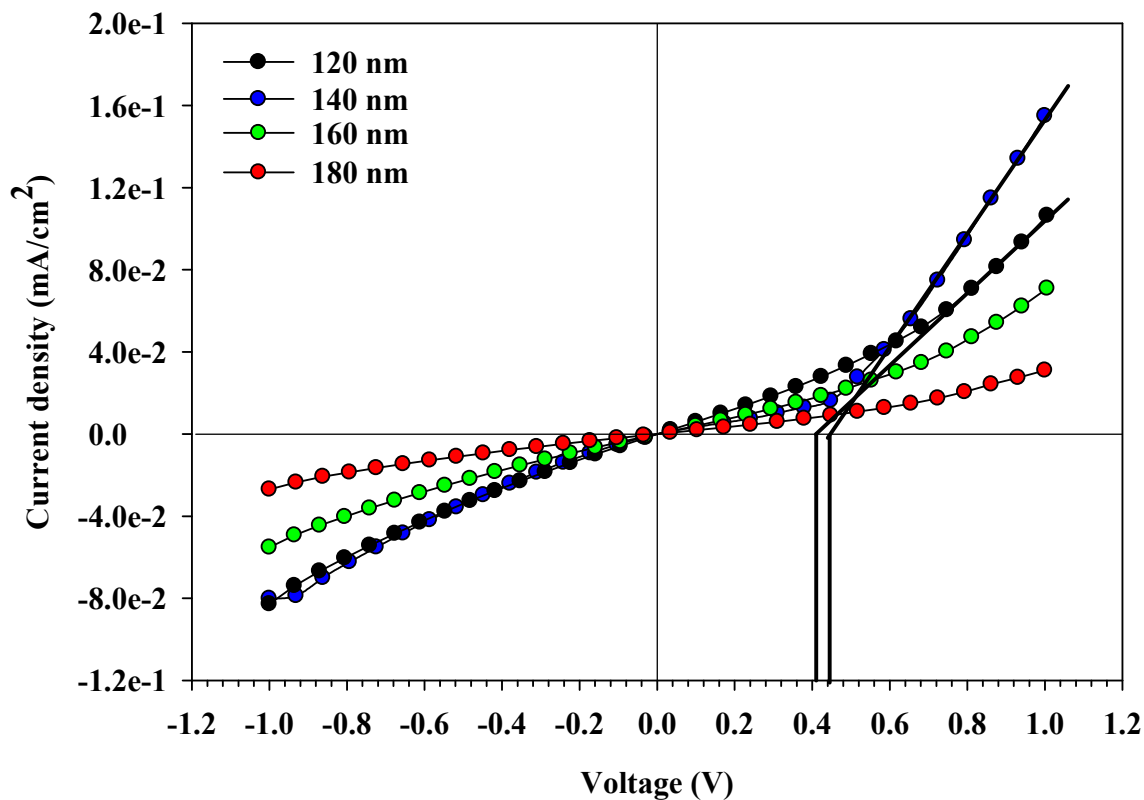


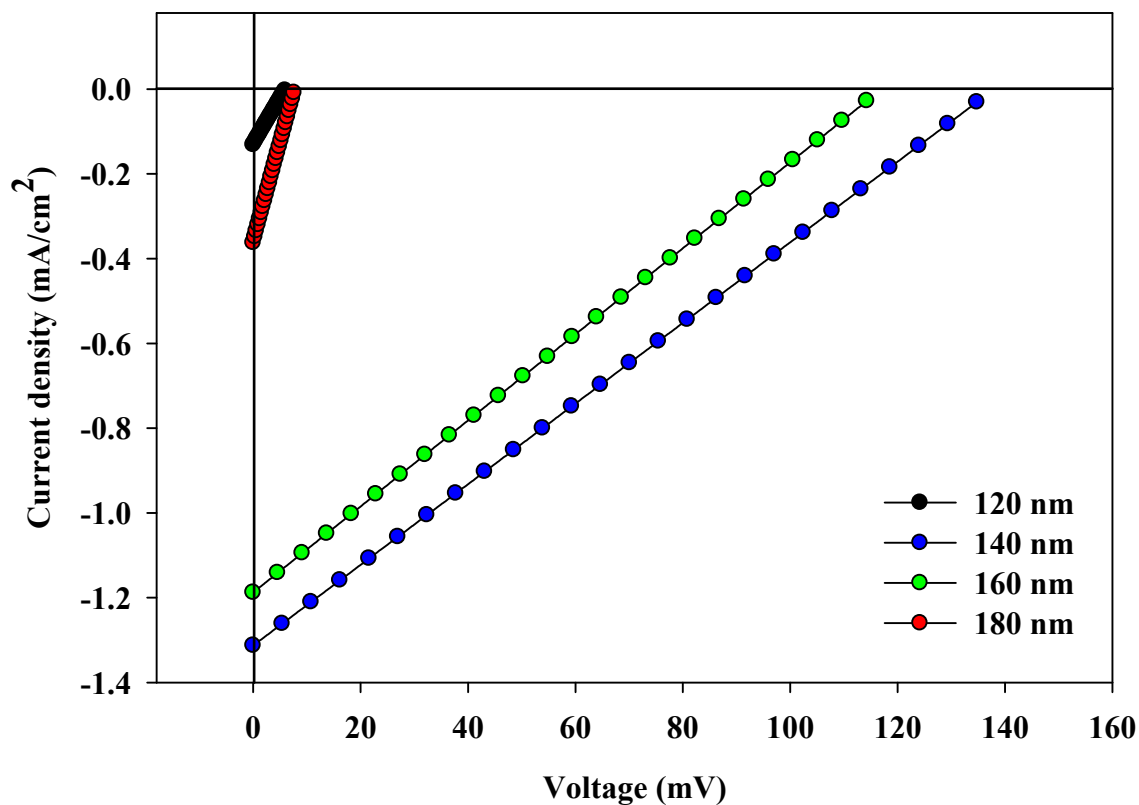
Fig. 7.17 The dark J-V of CIGS/CdS/i-ZnO structure having different thicknesses of CdS layer.

The deposition of AZO has been carried out on the i-ZnO layer. The dark and the light J-V characteristics of complete CIGS solar cell having different thicknesses of CdS is shown in Fig. 7.18 (a) and (b), respectively. The dark J-V of CIGS solar cells show that there is no diode like behavior of the junction which has the higher thickness of CdS films, viz. 160 and 180 nm. On the other hand, CIGS solar cell device having CdS thickness of 140 nm shows the diode behavior including the maximum reverse leakage current density. This diode behavior is responsible for getting the photovoltaic effect with the maximum V_{oc} of about 138 mV and the maximum J_{sc} of 1.3 mA/cm². There is no photovoltaic effect observed for 120 nm CdS, which may be because of the non uniform CdS layer, providing the shunt path for the photo-generated carriers.

At higher thickness of CdS (180 nm), the forward voltage threshold has not observed from the dark J-V plot. Also there has been a minor photovoltaic effect is observed for 180 nm thickness of CdS. It is possible that the thicker high resistive CdS does not allows passing the photo-generated carriers. Similarly, the maximum spectral response has been observed for CIGS solar cells having 140 and 160 nm thickness of CdS layer as shown in Fig. 7.19. Finally, the fabricated CIGS solar cell is shown in the Fig. 7.20.



(a)



(b)

Fig. 7.18 Dark (a), and light (b), J-V characteristics of CIGS solar cell device having different thicknesses of CdS layer.

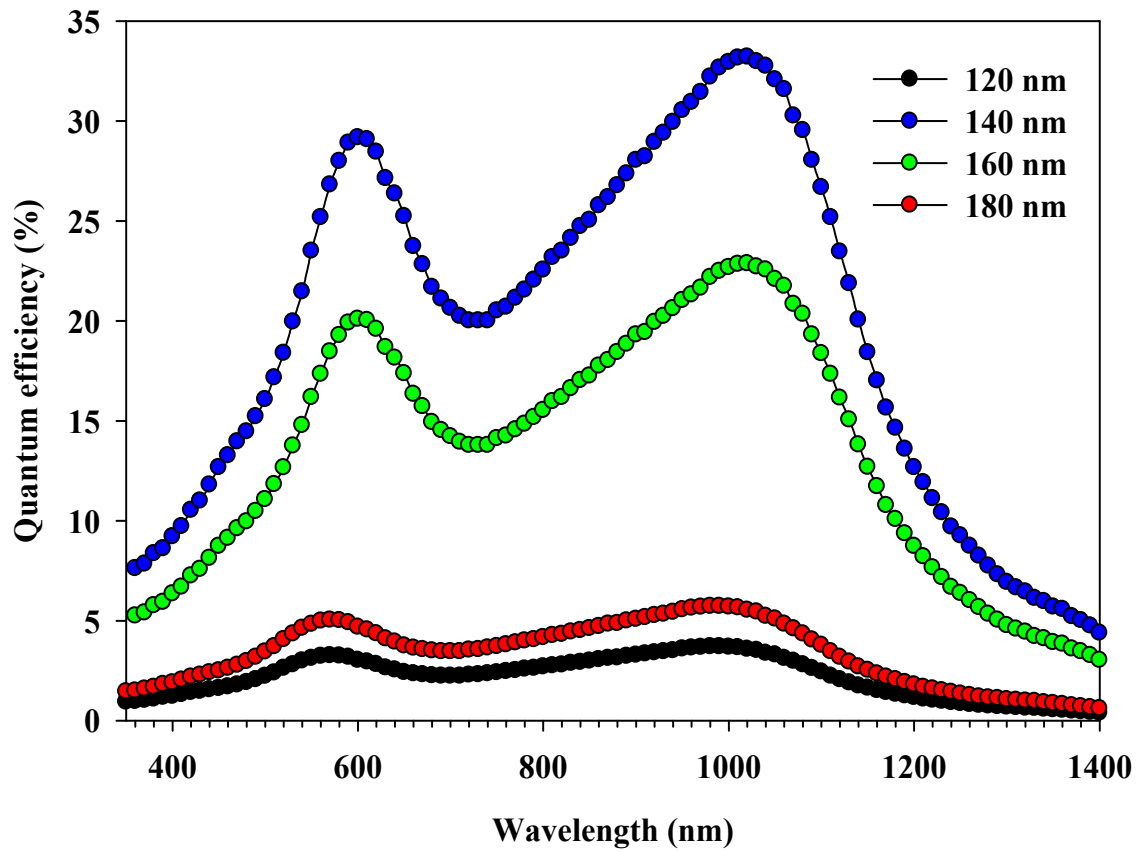


Fig. 7.19 Spectral response of CIGS solar cell having different thicknesses of CdS layer.

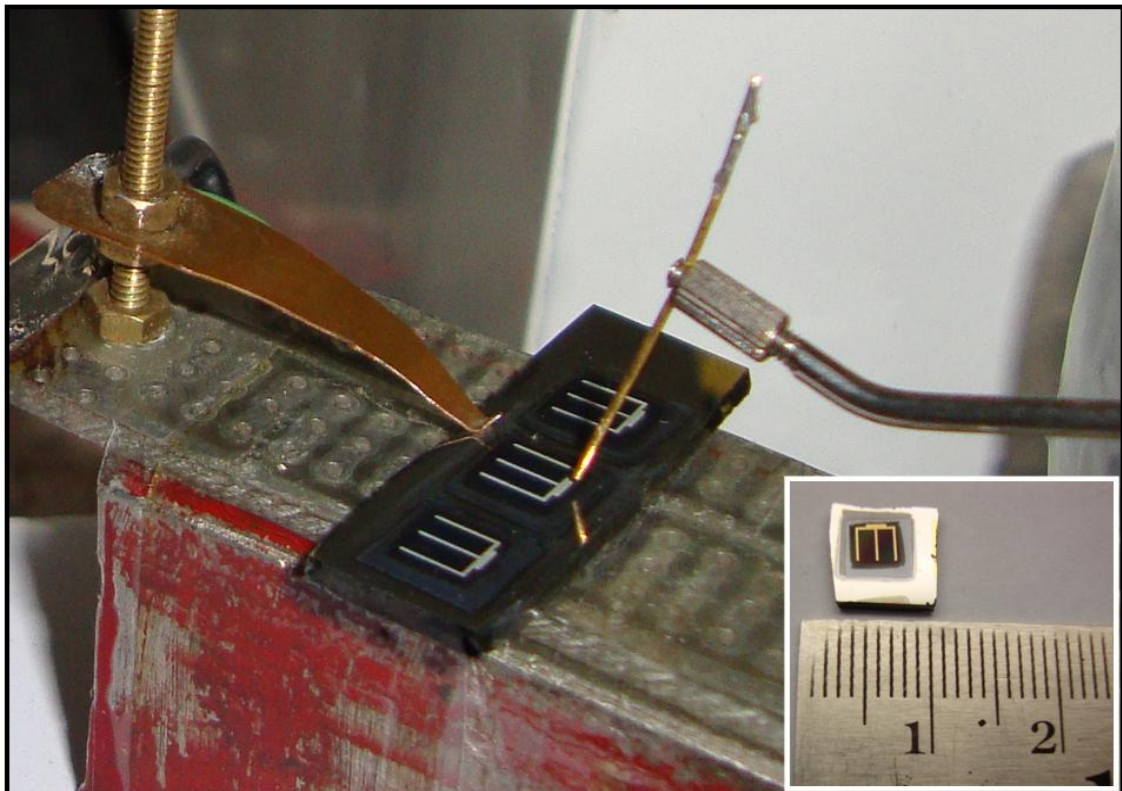


Fig. 7.20 The photograph of a complete CIGS solar cell with the measurement probe: Gold wire, a top contact on Ag grid and copper strip, a pressure contact on Molybdenum thin film. The inset photograph shows closer look of a single CIGS solar cell.

7.3 CONCLUSIONS

AMPS-1D is used to simulate the CIGS solar cell device. The simulated results suggested that the conversion efficiency increased until the thickness reached at around 2 μm . Further increase in the thickness of the films does not show any improvement in the efficiency. The maximum energy conversion efficiency of about 10 % has been observed. These observation leads to the conclusion that for the optimum performance of the solar cell device the thickness of the absorber layer plays an important role. By fixing up the absorber layer thickness, i.e. 1 μm , we fabricated the CIGS solar cell. The variation with the thicknesses of i-Zno and CdS is observed. At 140 nm thickness of CdS and 20 nm thickness of i-ZnO, we observed maximum V_{oc} and J_{sc} of CIGS thin film solar cell is about 138 mV and about 1.3 mA/cm^2 . The influence of the thickness of i-ZnO and the CdS thin film has also been observed on the spectral response of CIGS thin film solar cell.

Chapter 8

SUMMARY AND FUTURE OUTLINE

8. SUMMARY AND FUTURE OUTLINE

SUMMARY

The present thesis is based on the fabrication of Copper indium, gallium diselenide (CIGS) thin film solar cell. In comparison with the commercial crystalline Silicon (Si) solar cell, polycrystalline CIGS solar cells are substantially cheaper due to much lower material cost and potentially lower fabrication cost. CIGS based thin film solar cell is a multilayered heterojunction. The overall performance of this kind of solar cell is depends on the properties of the individual thin film layers. Thus, it is necessary to optimize each individual thin film layer of material, as it plays an important role in solar cell. In this present work, each individual thin film is optimized on a single glass substrate using physical vapor deposition (PVD) technique before proceeds to the fabrication of CIGS solar cell. In addition to that a numerical simulation is carried out using the AMPS-1D to check the future performance of the CIGS solar cell.

The Mo thin film, prepared by RF magnetron sputtering, is used as a metallic low resistance, of about $1 \Omega/\square$, back-contact for CIGS solar cell. On Mo thin film CIGS, an absorber layer, is deposited using flash evaporation. The effects of substrate temperature, film thickness and heat treatment (rapid thermal annealing) are analyzed for optimize the device quality thin film. Thin film of cadmium sulphide (CdS) is deposited using thermal evaporation on CIGS thin film. The influence of substrate temperature is observed. Using RF magnetron sputtering method bi-layer of Zinc Oxide (ZnO), i.e. intrinsic and aluminum doped ZnO, as a Transparent Conducting Oxide (TCO), front contact for CIGS based solar cells is deposited and optimized. Finally, the silver (Ag) grid is deposited on ZnO layer for better collection of photo-generated electrons. The width of the each grid line is 0.2 mm.

In the fabricate part of CIGS thin film solar cell device, we used the best optimized condition of each individual thin film layer. The initial performance of these fabricated devices is less compared to the standard values of commercially available solar cells. The data from all the experiments indicate the importance of CdS layer. As the thickness of CdS gets lower, the performance of solar cell gets demises. Thin CdS layer is responsible for shorting the layer of ZnO and CIGS. Thick CdS able to protect the junction from the high energy sputtered particles. Some of the devices become electrically shunted due to stress generation during the AZO coating at higher pressure. By varying the thickness of i-ZnO and the CdS layer the internal stress can be reduced. Finally we have successfully fabricated the CIGS solar cell having a V_{oc} and J_{sc} of about 138 mV and 1.30 mA/cm^2 .

FUTURE OUTLINE

- Study of Cadmium free buffer layer for more environment friendly renewable energy.
- Performance of CIGS solar cell having a less than 1 μm thickness of absorber layer helpful to fabricate the flexible thin film solar cell.
- Need more cost effective thin film preparation method compare to the vacuum based evaporation methods.
- Replacement of Indium and gallium material in CIGS solar cell for reducing further the fabrication cost of solar cell.

REFERENCES

- [1] S.M. Sze, *Physics of Semiconductor Devices (2nd edition)*, John Wiley and Sons, Inc., USA (2004).
- [2] A.E. Becquerel, *Comptes Rendus de L'Academie des Sciences*, **9** (1839) 145.
- [3] Su-Huai Wei, S.B. Zhang, A. Zunger, *Applied Physics Letters*, **72** (1998) 3199.
- [4] M.A. Green, K. Emery, D.L. King, Y. Hishikawa, W. Warta, *Progress in Photovoltaics: Research and Applications*, **15** (2007) 35.
- [5] A. Lique, S. Hegedus, *Handbook of Photovoltaic Energy Conversion and Engineering*, John Wiley & Sons Inc., England (2003).
- [6] National Renewable Energy Laboratory (NREL) “*Best Research-Cell Efficiencies.*” Golden, CO: NREL, August 2012 (http://www.nrel.gov/nepv/images/efficiency_chart.jpg).
- [7] <http://www.solarthermalmagazine.com/solar-power-in-india/>
- [8] http://en.wikipedia.org/wiki/Gujarat_Solar_Park
- [9] P. Jackson, D. Hariskos, E. Lotter, S. Paetel, R. Wuerz, R. Menner, W. Wischmann, M. Powalla, *Progress in Photovoltaics: Research and Applications*, **19** (2011) 894.
- [10] R. Caballero, C.A. Kaufmann, T. Eisenbarth, M. Cancela, R. Hesse, T. Unold, A. Eicke, R. Klenk, H.W. Schock *Thin Solid Films* **517** (2009) 2187.
- [11] W. Shockley, H.J. Queisser, *Journal of Applied Physics*, **32** (1961) 510.
- [12] <http://www.renewableenergyfocus.com/view/24219/solar-frontier-reaches-17-8-efficiency-with-cis-solar-thin-film/>
- [13] M.A. Contreras, K. Ramanathan, J. AbuShama, F. Hasoon, D.L. Young, B. Egaas, R. Noufi, *Progress in Photovoltaics: Research and Applications*, **13** (2005) 209.
- [14] R. Noufi, R. Axton, C. Herrington, S.K. Deb, *Applied Physics Letters*, **45** (1984) 668.
- [15] A.O. Pudov, *Ph.D. Thesis*, Colorado State University, Colorado (2005).
- [16] R.N. Bhattacharya, M.A. Contreras, B. Egaas, R.N. Noufi, A. Kanevce, J.R. Sites, *Applied Physics Letters*, **89** (2006) 253503.
- [17] S.H. Wei, A. Zunger, *Applied Physics Letters*, **63** (1993) 2549.
- [18] Stephen Fonash, *Solar Cell Device Physics (2nd Edition)*, Academic Press, USA (2010).
- [19] *IEC 60904-3. Photovoltaic devices - Part 3: Measurement principles for terrestrial photovoltaic (PV) solar devices with reference spectral irradiance data*, International Electrotechnical Commission (1989).
- [20] U. Rau, A. Jasenek, H.W. Schock, F. Engelhardt, T. Meyer, *Thin Solid Films*, **361-362** (2000) 298.
- [21] Mary D Archer, Robert Hill, *Clean Electricity from Photovoltaics*, Imperial College Press, United Kingdom (2001) 277-345.
- [22] J. Malmström, J. Wennerberg, M. Bodegård, L. Stolt, *Proceedings 17th European Photovoltaic Solar Energy Conference*, 1265 (2001).
- [23] M.A. Green, *Solar Cells: Operating Principles, Technology and System Applications*, The University of New South Wales, USA (1982).

- [24] Solveig Roschier, *Development of Procedures for performance and Lifetime Testing of Thin Film Photovoltaic Devices*, Dissertation, Helsinki University of Technology, Finland.
- [25] T.J. Coutts, J.D. Meakin, *Current Topics in Photovoltaics*. Academic Press, USA (1985).
- [26] U.P. Singh, Surya P. Patra, *International Journal of Photoenergy*, **2010** (2010) art. no. 468147.
- [27] A. Romeo, M. Terheggen, D. Abou-Ras, D.L. Bätzner, F.-J. Haug, M. Kälin, D. Rudmann, A.N. Tiwari, *Progress in Photovoltaics: Research and Applications*, **12** (2004) 93.
- [28] I.V. Bodnar, B.V. Korzun, A.I. Lukomskii, *Physica Status Solidi B*, **105** (1981) K143.
- [29] D.S. Albin, J.R. Tuttle, G.D. Mooney, J.J. Carapella, *Proceedings of the IEEE Photovoltaics Specialists Conference*, 1990.
- [30] V. Mertens, J. Parisi, *Journal of Applied Physics*, **101** (2007) 1045077.
- [31] O. Lundberg, M. Bodegard, J. Malmstrom, L. Stolt, *Progress in Photovoltaics: Research and Applications*, **11** (2003) 77.
- [32] H.S. Ullal, K. Zweibel, B.G. von Roedem, *28th IEEE Photovoltaic Specialists Conference*, (2000) 418.
- [33] Charles A. Bishop, *Vacuum Deposition onto Webs, Films, and Foils (2nd Edition)*, Elsevier, USA (2011).
- [34] Donald M. Mattox, *Handbook of Physical Vapor Deposition (PVD) Processing*, Noyes Publications, USA (1998).
- [35] Krishna Seshan, *Handbook of Thin-Film Deposition Processes and Techniques*, Noyes Publications, USA (2002).
- [36] René Guinebrière, *X-ray Diffraction by Polycrystalline Materials*, ISTE Ltd., USA (2007).
- [37] Samuel H. Cohen, Marcia L. Lightbody, *Atomic Force Microscopy/Scanning Tunneling Microscopy 3*, Kluwer Academic Publishers, London (2002).
- [38] A. Adachi, A. Kudo, T. Sakata, *Bulletin of the Chemical Society of Japan*, **68** (1995) 3283.
- [39] F. Demichelis, G. Kaniadakis, A. Tagliferro, E. Tresso, *Journal of Applied Optics*, **26** (1987) 1737.
- [40] J.I. Pankove, *Optical Processes in Semiconductors*, Prentice-Hall, New Jersey (1971).
- [41] L.J. van der Pauw, *Philips Research Reports*, **13** (1958) 1.
- [42] Edwin Hall, *American Journal of Mathematics*, **2** (1879) 287.
- [43] S. Raud, M.A. Nicolet, *Thin Solid Films*, **201** 361 (1991).
- [44] A.A. Kadam, N.G. Dhere, P. Holloway, E. Law, *Journal of Vacuum Science and Technology A*, **23** (2005) 1197.
- [45] L. Assmann, J.C. Bernede, A. Drici, C. Amory, E. halgand, M. Morsli, *Applied Surface Science*, **246** (2004) 159.
- [46] Y.G. Wu, E.H. Cao, Z.S. Wang, J.M. Wei, W.X. Tang, L.Y. Chen, *Applied Physics A: Materials Science & Processing*, **76** (2003) 147.
- [47] I.Repins, M.A. Contreras, B.Egaas, C. DeHart, J. Scharf, C.L. Perkins, B. To, R. Noufi, *Progress in Photovoltaics: Research and Applications*, **16** (2008) 235.
- [48] Zhao-Hui Li, Eou-Sik Cho, Sang Jik Kwon, *Applied Surface Science*, **257** (2011) 9682.
- [49] G.T. West, P.J. Kelly, *Surface and Coatings Technology*, **206** (2011) 1648.
- [50] H. Khatri, S. Marsillac, *Journal of Physics: Condensed Matter*, **20** (2008) 055206.

- [51] G. Hass, R.E. Thun, *Physics of thin films*, Academic press, New York and London (1966).
- [52] S. Govindarajan, J.J. Moore, B. Mishra, D.L. Olson, *Surface and Coatings Technology*, **68/69** (1994) 45.
- [53] G. Gordillo, F. Mesa, C. Calderon, *Brazilian Journal of Physics*, **36** (2006) 982.
- [54] J.A. Thortrou, D.W. Hoffman, *Journal of Vacuum Science and Technology*, **14** (1977) 164.
- [55] A.D. Compaan, I. Matulionis, S. Nakade, *Final Technical Progress Report*, NREL/SR-520-24842 (1998).
- [56] K.L. Chopra, *Thin Film Phenomenon*, McGraw-hill, New York (1969).
- [57] C. Solanki, *Solar Photovoltaics: Fundamentals, Technologies and Applications*, PHI Learning Pvt. Ltd., New Delhi (2009).
- [58] K.L. Chopra, I. Kaur, *Thin Film Device Applications*, Plenum Press, New York (1983).
- [59] V. Ramanathan, L.A. Russell, C.H. Liu, P.V. Meyers, *Solar Cells*, **28** (1990) 129.
- [60] J.G. O'Dowd, N.R. Johnson, R.S. Oswald, F. Willing, *Proceeding 23rd IEEE Photovoltaic Specialists Conference*, 926 (1993).
- [61] R. Arya, *Solarex Final Technical Report. NREL*, contract ZN-I-19019-4 (1995).
- [62] W.M. Steen, J. Mazumder, *Laser Material Processing*, Springer-Verlag London Ltd., New York (2010).
- [63] M. Richter, C. Schultz, J. Bonse, H.-U. Pahl, H. Endert, B. Rau, R. Schlatmann, V. Quaschnig, B. Stegemann, F. Fink, *Proceedings of 26th European Photovoltaic Solar Energy Conference and Exhibition*, 2540 (2011).
- [64] <http://www.tsmc-solar.com/technology/cigs-technology>
- [65] B.D. Cullity, *Elements of X-ray diffraction*, Addison-Wesley Publishing Company, Inc., USA (1956).
- [66] Miguel A. Contreras, John Tuttle, Andrew Gabor, Andrew Tennant, Kannan Ramanathan, Sally Asher, Amy Franz, James Keane, L. Wang, John Scofield, Rommel Noufi, *1st World Conference on Photovoltaic Energy Conversion*, Hawaii (1994).
- [67] R.W. Birkmire, J.E. Phillips, W.N. Shafarman, E. Eser, S.S. Hegedus, B.E. McCandless, *NREL Annual Report*, 24 August 1998-23 August 1999.
- [68] G. Gordillo, C. Calderón, W. Bolaños, E. Romero, *Superficies y Vacío*, **16** (2003) 12.
- [69] Li Zhang, Qing He, Wei-Long Jiang, Fang-Fang Liu, Chang-Jian Li, Yun Sun, *Solar Energy Materials and Solar Cells*, **93** (2009) 114.
- [70] J.R. Tuttle, D.S. Albin, R. Noufi, *Solar Cells*, **30** (1991) 21.
- [71] H. Zachmann, S. Heinker, A. Braun, A.V. Mudryi, V.F. Gremenok, A.V. Ivaniukovich, M.V. Yakushev, *Thin Solid Films*, **517** (2009) 2209.
- [72] J. Bekker, *Solar Energy Materials and Solar Cells*, **93** (2009) 539.
- [73] J.R. Ray, M.S. Desai, C.J. Panchal, Bharati Rehani, *AIP Conference Proceedings*, **1451** (2012) 251.
- [74] C.J. Hibberd M. Kaelin, S.E. Dann, G. Bilger, H.U. Upadhyaya, A.N. Tiwari, *Thin Solid Films*, **517** (2009) 2235.
- [75] Erees Queen B. Macabebe, Charles J. Sheppard, Vivian Alberts, E. Ernest van Dyk, *Thin Solid Films*, **517** (2009) 2380.

- [76] D. Abou-Ras, *Thin Solid Films*, **517** (2009) 2218.
- [77] D. Liao, A. Rockett, *Journal of Applied Physics*, **91** (2002) 1978.
- [78] T. Gödecke, T. Haalboom, F. Ernst, *Z. Metallkd.* **91** (2000) 635.
- [79] A.F.D. Cunha, F. Kurdesau, D. Rudmann, P.M.P. Salome, *Journal of Non-Crystalline Solids*, **352** (2006) 1976.
- [80] R. Caballero, C. Guille'n, M. T. Gutie'rrrez, C. A. Kaufmann, *Progress in Photovoltaics: Research and Applications*, **14** (2006) 145.
- [81] Y.C. Lin, Z.Q. Lin, C.H. Shen, L.Q. Wang, C.T. Ha, Chris Peng, *Journal of Materials Science: Materials in Electronics*, **23** (2012) 493.
- [82] L. Kazmerski, *Renewable and Sustainable Energy Reviews*, **1** (1997) 71.
- [83] Hongyong Zhang, Naoto Kusumoto, *United States Patent No. 5352291* (1994).
- [84] S.B. Zhang, S.H. Wei, A. Zunger, *Physical Review Letters.*, **21** (1997) 78.
- [85] S.A. Dinca, E.A. Schiff, B. Egaas, R. Noufi, D.L. Young, W.N. Shafarman, *Physical Review B*, **80** (2009) 2352011.
- [86] Ping Fan, Guang-Xing Liang, Xing-Min Cai, Zhuang-Hao Zheng, Dong-Ping Zhang, *Thin Solid Films*, **519(16)** (2011) 5348
- [87] G. Arreola-Jardón, L.A. González, L.A. García-Cerda, B. Gnade, M.A. Quevedo-López, R. Ramírez-Bon, *Thin Solid Films*, **519** (2010) 517
- [88] K.J. Salwan, Al-Ani, A. Raid, Ismail, F.A. Hana, Al-Ta'ay, *Journal of Materials Science: Materials in Electronics*, **17** (2006) 819.
- [89] M.E. Calixto, P. J. Sebastain, *Solar Energy Materials and Solar Cells*, **59** (1999) 65.
- [90] G. Sasikala, R.Dhnasekaran, C. Sbramanian, *Thin Solid Films*, **302** (1997) 71.
- [91] A.I. Oliva-Avilé, R. Patino, A.I. Oliva, *Applied Surface Science*, **256** (2010) 6090.
- [92] S.A. Al Kuhaimi, *Vacuum*, **51** (1998) 349.
- [93] D. Sreekantha reddy, B. Kang seong-cho yu, K.R. Gunasekhar, K. Narasimha rao, A. Divya, P. Sreedhara reddy, *Journal of optoelectronics and advanced materials*, **9** (2007) 3747.
- [94] A. Yamada, S. Chaisitsak, Y. Ohtake, M. Konagai., *Proceeding of 2nd World Conference on Photovoltaic Energy Conversion*, **1** (1998) 1177.
- [95] C.Y. Yeh, Z.W. Lu, S. Froyen, A. Zunger, *Physical Review B*, **46** (1992) 10086.
- [96] M. Tomakin, M. Altunbaş, E. Bacaksiz, Ş. Çelik *Thin Solid Films*, **520** (2012) 2532.
- [97] A. Mandoza-Galvan, G. Martinez, R. Cozda- Morales, *Journal of Applied Physics*, **80** (1996) 3333.
- [98] A. Adachi, A. Kudo, T. Sakata, *Bulletin of the Chemical Society of Japan*, **68** (1995) 3283.
- [99] C.T. Tsai, D.S. Ohuu, G.L. Chen, S.L. Yang, *Journal of Applied Physics*, **79** (1996) 9105.
- [100] N.Lovergine, R.Cingolani, A.M.Mansini, *Journal of Crystal Growth*, **118** (1992) 304.
- [101] B. Su, K.L. Choy, *Thin Solid Films*, **359** (2000) 160.
- [102] A. Ashour, N. El-Kadry, S.A. Mahmoud, *Thin Solid Films*, **269** (1995) 117.
- [103] L.L. Kazmerski, W.S. Berry, C.W. Allen, *Journal of Applied Physics*, **43** (1972) 3515.
- [104] R.L. Petritz, *Physical review*, **104** (1956) 1508.
- [105] T. Nakada, Y. Ohkubo, A. Kunioka, *Japanese Journal of Applied Physics*, **30** (1991) 3344.

- [106] O. Kluth, G. Schöpe, B. Rech, R. Menner, M. Oertel, K. Orgassa, H.W. Schock, *Thin Solid Films*, **502** (2006) 311.
- [107] P. Nunes, D. Costa, E. Fortunato, R. Martins, *Vacuum*, **64** (2002) 293.
- [108] X.T. Hao, J. Ma, D.H. Zhang, Y.G. Yang, H.L. Ma, C.F. Cheng, X.D. Liu, *Material Science and Engineering B*, **90** (2002) 50.
- [109] Powder Diffraction File, Joint Committee on Powder Diffraction Standards, ASTM (1998) (Card no. 36-1451).
- [110] L.V. Azaroff, *Elements of X-ray Crystallography*, McGraw-Hill, New York (1968).
- [111] Milton Ohring, *Materials Science of Thin Films (2nd Edition)* Academic press, USA (2006).
- [112] W. Yang, Z. Liu, D.-L. Peng, F. Zhang, H. Huang, Y. Xie, Z. Wu, *Applied Surface Science*, **255** (2009) 5669.
- [113] A. Adachi, A. Kudo, T. Sakata, *Bulletin of the Chemical Society of Japan*, **68** (1995) 3283.
- [114] T.S. Moss, *Proceedings of the Physical Society*, **67** (1954) 775.
- [115] E. Burstein, *Physical Review*, **93** (1954) 632.
- [116] D. Song, *Applied Surface Science*, **254** (2008) 4171.
- [117] D.C. Look, J.W. Hemsky, J.R. Sizelove, *Physical Review Letters*, **82** (1999) 2552.
- [118] D.C. Look, C. Coskun, B. Clafin, G.C. Farlow, *Physica B*, **340/342** (2003) 32.
- [119] Chung Ping Liu, Gwo Rou Jeng, *Journal of Alloys and Compounds*, **468** (2009) 343.
- [120] S. Ishizukaa, K. Sakuraia, A. Yamadaa, K. Matsubaraa, P. Fonsa, K. Iwataa, S. Nakamura, Y. Kimurab, T. Babab, H. Nakanishib, T. Kojimaa, S. Niki, *Solar Energy Materials & Solar Cells*, **87** (2005) 541.
- [121] J.S. Oyola, J.M. Castro, G. Gordillo, *Solar Energy Materials and Solar Cells*, **102** (2012) 137.
- [122] S.T. Tana, B.J. Chena, X.W. Suna, X. Hub, X.H. Zhang, S.J. Chu, *Journal of Crystal Growth*, **281** (2005) 571
- [123] T. Prasada Rao, M.C. SanthoshKumar, S. Anbumozhi, M. Ashok, *Journal of Alloys and Compound*, **485** (2009) 413.
- [124] F.K. Shan, Y.S. Yu, *Journal of the European Ceramic Society*, **24** (2004) 1869.
- [125] C. Lombardi, (http://www.miasole.com/sites/default/files/Cnet_Dec_02_2010.pdf)
- [126] H. S. Ullal, K. Zweibel, B.V. Roedern, *Proceedings of the 26th IEEE Spec.Conference, IEEE*, art. no. 2012 (1997).
- [127] M. Yamaguchi, *Journal of Applied Physics*, **78** (1995) 1476.
- [128] H.W. Schock, K. Bogus, in: J. Schmid, H.A. Ossenbrink, P. Helm, H. Ehmann, E.D. Dunlop (Eds.), *Proceedings of the 2nd World Conference on Photovoltaic Energy Conversion, E.C. Joint Research Centre, Luxemburg*, art. no. 3586 (1998).
- [129] W.H. Bloss, J. Kimmererele, F. Pfisterer, H.W. Schock, *Conference Record of the 17th IEEE PVSC*, art. no. 715 (1984).
- [130] J. Song, S.S. Li, C.H. Huang, T.J. Anderson, O.D. Crisalle, *NCPV and Solar Program Review Meeting*, art. no. P874 (2003).

- [131] S.J. Fonash, *A manual for One-Dimensional Device Simulation Program for the Analysis of Microelectronic and Photonic Structures (AMPS-1D)*, The Center for Nanotechnology Education and Utilization, The Pennsylvania State University, University Park, PA 16802.
- [132] J. Ray, C.J. Panchal, *Symposium on Condensed Matter Physics (CMDAYS 09)*, art. no. P-090413 (2009).
- [133] M. Gloeckler, A.L. Fahrenbruch, J.R. Sitesm, *Proceedings of 3rd World Conference on Photovoltaic Energy Conversion*, art no. 491 (2003).
- [134] O. Lundberg, M. Edoff, L. Stolt, *Thin Solid Films*, **480** (2005) 520.
- [135] S. Ishizuka, A. Yamada, K. Matsubara, P. Fons, K. Sakurai, S. Niki, *Current Applied Physics*, **10** (2010) S154.
- [136] A.L. Fahrenbruch, R.H. Bube, *Fundamentals of Solar Cells*, Academic Press, NewYork (1983).
- [137] S. Nishiwaki, S. Siebentritt, P. Walk, M. Ch. Lux-Steiner, *Progress in Photovoltaics: Research and Applications*, **11** (2003) 243.
- [138] T. Nakada, *Thin Solid Films*, **361–362** (2000) 346.
- [139] Soon-Yong Park, Eun-Woo Lee, Sang-Hwan Lee, Sang-Wook Park, Woo Kyoung Kim, Sung Ho Lee, Wan-Gyu Lee, Boung Ju Lee, Hee Kyung Bae, Jung Ho Yoo, Chan-Wook Jeon, *Current Applied Physics*, **10** (2010) S399.
- [140] L.L. Kazmerski, O. Jamjoum, P.J. Ireland, *Journal of Vacuum Science and Technologies*, **21** (1982) 486.
- [141] P.G. Muzykov, A.V. Bolotnikov, T.S. Sudarshan, *Solid-State Electronics*, **53** (2009) 14
- [142] I. Petrov, V. Orlinov, A. Misiuk, *Thin Solid Films*, **120** (1984) 55.
- [143] J. Hinze, K. Ellmer, *Journal of Applied Physics*, **88** (2000) 2443.

LIST OF SYMBOLS

ΔE_c	Conduction-band offset	n_t	Concentrations of trapped electrons
A	Absorption	n_s	Density of electrons
Å	Angstrom	P_{in}	Input power
at%	Atomic percent	P_{max}	Maximum power point
d	Distance	p_s	Density of holes
D	Crystalline size	p_t	Concentrations of trapped holes
e	Electron charge	θ	Angle
E	Young modulus	R	Reflection
E_A	Activation energy	ρ	Resistivity
E_f	Fermi energy	$R(x)$	Recombination at x
E_g	Energy band gap	R_n	Electron recombination velocities
FF	Fill factor	R_p	Holes recombination velocity
G	Gauss	R_s	Series resistance
$G(x)$	Photo generation at x	R_{sh}	Sheet resistance
η	Efficiency	R_{shu}	Shunt resistance
I_{DUT}	Current of device under test	R_{STD}	Responsivity of standard device
I_{max}	Maximum current	s	Second
I_{sc}	Short circuit current	σ	Conductivity
I_{std}	Current of standard device	S_n	Recombination speed of electrons
j_0	Reverse saturation current	S_p	Recombination speed of holes
J_n	Electron current density	T	Temperature
J_p	Hole current density	T	Transmission
J_{rec}	Recombination current	t	Film thickness
J_{sc}	Current density	υ_f	Poisson ration
k	Boltzmann constant	V	Applied voltage
K	Kelvin	V_{max}	Maximum voltage
λ	Wavelength	V_{oc}	Open circuit voltage
μ	Mobility	W	Watt
mA	Milliampere	Ψ	Electrostatic potential
min	Minute	Φ_1^{FOR}	Photon flux of the incident light
n	Ideality factor	Φ_1^{REV}	Photon flux reflecting from back surface
n_i	Order of reflection		

ABBREVIATIONS

AFM	Atomic Force Microscopy
AM	Air Mass
AMPS-1D	One Dimensional Analysis of Microelectronic and Photonic Structures
AR	Anti-Reflection
Ar	Argon
BHEL	Bharat Heavy Electrical Limited
BSF	Back-Surface Field
CBD	Chemical Bath Deposition
CEL	Central Electronics Limited
CRT	Cathode Ray Tube
CVD	Chemical Vapor Deposition
EDS	Energy Dispersive Analysis of X-ray
FWHM	Full Width Half Maxima
GIXRD	Grazing Incidence X-ray Diffraction
GPIB	General Purpose Interface Bus
ISIT	India Solar Investment & Technology Summit
JCPDS	Joint Committee on Powder Diffraction Standards
LabVIEW	Laboratory Virtual Instrument Engineering Workbench
LECVD	Laser Enhanced Chemical Vapor Deposition
MOCVD	Metal-Organic Chemical Vapor Deposition
N ₂	Nitrogen
PECVD	Plasma Enhanced Chemical Vapor Deposition
PV	Photovoltaic
PVD	Physical Vapor Deposition
QE	Quantum Efficiency
RF	Radio Frequency
RTA	Rapid Thermal Annealing
SAD	Selected Area Diffraction
SCR	Space Charge Region
SEM	Scanning Electron Microscopy
SSR	Solid State Relay
STC	Standard Test Condition
TCO	Transparent Conductive Oxide
TEM	Transmission Electron Microscopy
UV-VIS	Ultraviolet Visible
XRD	X-ray Diffraction

LIST OF PUBLICATIONS

➤ International Journals

- 1. Molybdenum back-contact optimization for CIGS thin film solar cell**
J. R. Ray, N.M. Shah, M.S. Desai C.J. Panchal
Journal of Nano- Electron Physics, **3(1)** (2011) 766
- 2. Magnetron sputtered Al-ZnO thin films for photovoltaic applications**
J. R. Ray, M.S. Desai, C.J. Panchal, P.B. Patel
Journal of Nano- Electron Physics, **3(1)** (2011) 755
- 3. Simulation of CIGS thin film solar cells using AMPS-1D**
J. R. Ray, C.J. Panchal, M.S. Desai, U.B Trivedi
Journal of Nano- Electron Physics, **3(1)** (2011) 747
- 4. Laser scribing optimization of RF magnetron sputtered molybdenum thin films**
V.B. Padhiar, A.L. Patel, **J. R. Ray**, M.S. Desai, C.J. Panchal
Journal of Nano- Electron Physics, **3(1)** (2011) 9
- 5. Impact of annealing on CuInSe₂ thin films and its schottky interface**
U. Parihar, **J. R. Ray**, N. Kumar, R. Sachdeva, N. Padha, C.J. Panchal
Journal of Nano- Electron Physics, **3(1)** (2011) 1086
- 6. Influence of substrate temperature on structural, optical and electrical properties of evaporated cadmium sulphide thin films**
N. M. Shah, **J. R. Ray**, M. S. Desai, C. J. Panchal
Journal of optoelectronics and advance materials, **12(10)** (2010) 2052
- 7. Structural, optical and electrical properties of flash evaporated Copper Indium Diselenide thin films**
N. M. Shah, **J. R. Ray**, C. J. Panchal, V. A. Kheraj, M. S. Desai
Journal of Material Science, **44** (2009) 316

8. Structural, electrical and optical properties of copper indium diselenide thin films prepared by thermal evaporation method

N. M. Shah, **J. R. Ray**, K. J. Patel, V. A. Kheraj, M. S. Desai, C. J. Panchal, Bharti Rehani

Thin Solid Films, **517** (2009) 3639

9. Growth, Structural and optical properties of copper indium diselenide thin films deposited by thermal evaporation method

N. M. Shah, C. J. Panchal, V. A. Kheraj, **J. R. Ray**, M. S. Desai

Solar Energy, **83** (2009) 753

➤ **Conference Proceedings**

1. The influence of the CIGS film thickness on its growth and optical properties

J.R. Ray, M.S. Desai, C.J. Panchal, Bharati Rehani

AIP Conference Proceedings **1451** (2012) 251

Indian Vacuum Society Symposium on Thin Films: Science and Technology at IIT Mumbai, Mumbai, 9–12 November, 2011

2. Synthesis and Characterization of copper indium gallium diselenide (CIGS) powder for solar absorber

J. R. Ray, M. S. Desai, C. J. Panchal

Proceedings of the 54th DAE Solid State Physics Symposium (2009) 447

54th DAE Solid State Physics Symposium at The M. S. University of Baroda, Vadodara, (Gujarat), 14 – 18 December, 2009

3. Optical and structural characterization of copper indium diselenide thin films prepared by direct thermal evaporation of the compound material

N. M. Shah, K. J. Patel, V. A. Kheraj, **J. R. Ray**, Bharti Rehani, V. J. Rao, M. S. Desai, C. J. Panchal

Proceedings of The International Conference on Solar Cells (2008) 272

The international conference on solar cells (IC-SOLACE) at Cochin University of science and technology, Cochin (Kerela) 21 – 23 January, 2008

➤ **Conference Oral Presentation**

- 1. Automated measurement of current-voltage (I-V) characteristic to evaluate the parameters for solar cells applications**

National Symposium on Vacuum Technology and its Application to Electronic Device and Systems (IVSNS 2009),

Central electronics engineering research institute (CEERI), Pilani, Rajasthan, 11- 13 November, 2009

➤ **Conference Poster Presentation**

- 1. Morphological, optical, and electrical properties of CIGS thin films for solar cell applications**

Condense Matter Days (CMDAYS 09),

Department of physics, Jadavpur University, Kolkata, 26 - 28 August, 2009